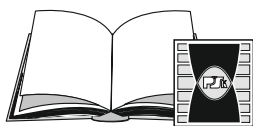


**MONOGRAFIE, STUDIA, ROZPRAWY**

**M19**

**SELECTED PROBLEMS  
OF MODELING AND CONTROL  
IN MECHANICS**

edited by  
**Stanisław Adamczak  
Leszek Radziszewski**



**WYDAWNICTWO**  
POLITECHNIKI ŚWIĘTOKRZYSKIEJ  
W KIELCACH

Kielce 2011

## **MONOGRAFIE, STUDIA, ROZPRAWY NR M19**

### **Redaktor Naukowy serii**

#### **NAUKI TECHNICZNE – BUDOWA I EKSPLOATACJA MASZYN**

prof. dr hab. inż. Stanisław ADAMCZAK, dr h.c.

### **Reviewers:**

Stanisław Adamczak – Kielce University of Technology

Andrzej Ambrozik – Kielce University of Technology

Mircea Barglazan – Politehnica University of Timisoara Romania

Artur Bartosik – Kielce University of Technology

Józef Gacek – Military Technical Academy Warszawa

Marek Idzior – Poznań University of Technology

Dariusz Janecki – Kielce University of Technology

Zenon Jędrzykiewicz – Academy of Science and Technology Kraków

Gennadiy Lvov – National Technical University Kharkiv Ukraina

Andrzej Neimitz – Kielce University of Technology

Dariusz Ozimina – Kielce University of Technology

Małgorzata Suchańska – Kielce University of Technology

Jerzy Szalapko – Chmielnitcky National University Ukraina

Zbigniew Szcześniak – Kielce University of Technology

Zbigniew Wesołowski – Kielce University of Technology

Włodzimierz Zowczak – Kielce University of Technology

### **Redakcja techniczna**

Irena PRZEORSKA-IMIOŁEK

### **Projekt okładki**

Tadeusz UBERMAN

© Copyright by Wydawnictwo Politechniki Świętokrzyskiej, Kielce 2011

Wszelkie prawa zastrzeżone. Żadna część tej pracy nie może być powielana czy rozpowszechniana w jakiegokolwiek formie, w jakiegokolwiek sposób: elektroniczny bądź mechaniczny, włącznie z fotokopiowaniem, nagrywaniem na taśmy lub przy użyciu innych systemów, bez pisemnej zgody wydawcy.

PL ISSN 1897-2691



25-314 Kielce, al. Tysiąclecia Państwa Polskiego 7, tel. 41 34 24 581  
[www.tu.kielce.pl/organizacja/wydawnictwo](http://www.tu.kielce.pl/organizacja/wydawnictwo) e-mail: [wydawca@tu.kielce.pl](mailto:wydawca@tu.kielce.pl)

# Contents

Introduction .....	7
Career biography of Prof. Jan Wojciech Osiecki .....	9
<b>1. DYNAMIC MODELING OF PHYSICAL STRUCTURES .....</b>	<b>11</b>
1.1. DYNAMIC MODELING OF HYDROSTATIC TRANSMISSIONS WITH SECONDARY CONTROL ( <i>Ryszard Dindorf</i> ) .....	11
1.1.1. Hydrostatic transmissions with secondary control .....	12
1.1.2. Application of MSM in modelling and simulation of secondary control .....	13
1.2. DYNAMIC ELEMENTS OF A MOTOR VEHICLE WHICH IS A CARRIER OF THE ANTI-AIRCRAFT MISSILE LAUNCHER ( <i>Zbigniew Dziopa</i> ) .....	19
1.2.1. Motor vehicle physical model .....	21
1.2.2. Mathematical model of the motor vehicle .....	25
1.2.3. Numerical simulation of the motor vehicle motion during the operation of the anti-aircraft missile assembly .....	26
1.3. CONTROLLED GYROSCOPES FOR PRECISION DESTRUCTION MUNITIONS ( <i>Zbigniew Koruba</i> ) .....	31
1.3.1. The control of the scanning and tracking gyroscopic system on board of an aerial vehicle .....	33
1.3.2. A gyroscope in an unmanned aerial vehicle .....	36
1.3.3. A gyroscope in a guided bomb .....	39
1.3.4. A gyroscope in a self-guided missile .....	42
1.4. THE MODEL OF BELLOWS SEAL WITH CONTROLLED CLOSING FORCE ( <i>Czesław Kundera</i> ) .....	44
1.4.1. Description of the seal .....	45
1.4.2. Dynamic model and equations of motion .....	46
1.4.3. Analysis of the model and examples of solutions .....	49
1.5. ANALYSIS OF INJECTION PROCESS IN DIESEL ENGINES ( <i>Andrzej Bąkowski, Leszek Radziszewski</i> ) .....	52
1.5.1. Experimental results .....	54
1.5.2. A mathematical model of the injection process .....	56
1.5.3. The model verification .....	58
1.6. LOCATION AND NEUTRALIZATION OF OVERHEAD HIGH VOLTAGE TRANSMISSION LINES IN WARFARE CONDITIONS ( <i>Janusz Tuśnio</i> ) .....	63
1.6.1. Emission of low-frequency electromagnetic radiation by overhead transmission lines .....	65
1.6.2. Detection and measurement of a 50 Hz electromagnetic field .....	67
1.6.3. Location of the angular position of transmission lines .....	71
1.6.4. Neutralization of transmission lines .....	73
References .....	76

<b>2. MODELING IN SURFACE ENGINEERING</b> .....	81
2.1. ANALYTICAL MODELS OF THE LASER BENDING PROCESS AND ITS EFFICIENCY ( <i>Zygmunt Mucha</i> ) .....	81
2.1.1. Analytical model for buckling mechanism .....	82
2.1.2. Model for temperature gradient mechanism .....	85
2.1.3. Experiments .....	90
2.1.4. Efficiency of laser forming process .....	93
2.2. APPLICATIONS OF LASER FORMING IN MICRO TECHNOLOGIES ( <i>Jacek Widłaszewski</i> ) .....	96
2.2.1. New concept of assembly and adjustment using a laser beam .....	96
2.2.2. Touch-less positioning of electric contacts .....	97
2.2.3. Laser adjustment of reed switches .....	98
2.2.4. Adjustment of magnetic heads in audio and video devices .....	99
2.2.5. Laser adjustment in manufacturing of hard disk drives .....	99
2.2.6. Actuator with embossment .....	100
2.2.7. Bridge actuators .....	101
2.2.8. Thermal stability of positioning .....	105
2.3. MODELING OF FRICTION AND FLOW IN THE SLIDING PAIRS WITH MICROSTRUCTURE OF SURFACE ( <i>Bogdan Antoszewski</i> ) .....	106
2.3.1. Analysis of friction resistances .....	107
2.3.2. Modelling fluid flow in the clearance between one smooth and one porous surface .....	114
2.4. ANALYSIS AND VERIFICATION OF SURFACE ROUGHNESS CONSTITUTION MODEL IN THE METAL CUTTING PROCESS APPLYING TOOLS WITH DEFINED STEREOOMETRY ( <i>Edward Miko</i> ) .....	119
2.4.1. Model of surface roughness in metal cutting .....	120
2.4.2. Forecasting the parameter <i>Ra</i> for face milling with spherical tools .....	128
2.4.3. Verification of the mathematical model based on the example of face milling machining .....	131
2.5. THE ANALYSIS OF MECHANICAL CHARACTERISTICS OF FILAMENT BRUSH TOOL ( <i>Sławomir Spadlo</i> ) .....	135
2.5.1. Statics interactions and kinematics of a single filament of the circular brush .....	136
2.5.2. Dynamics of a single filament of a circular brush .....	144
2.6. ELECTRO SPARK DEPOSITION AND LASER TECHNOLOGY IN SURFACE ENGINEERING ( <i>Norbert Radek</i> ) .....	146
2.6.1. Methodology .....	149
2.6.2. Results and discussion .....	150
2.7. TRIBOLOGICAL PROPERTIES OF PLASMA AND HVOF SPRAYED COMPOSITE COATINGS ( <i>Wojciech Żórawski</i> ) .....	157
2.7.1. Experimental investigation .....	158
2.7.2. Results and discussion .....	161

2.8. ANALYSIS OF RESIDUAL STRENGTH AFTER FATIGUE IN FIBROUS COMPOSITE USING MARKOV CHAINS MODEL	
( <i>Rafał Chatys, Yury Paramonov, Mārtiņš Kleinhofs</i> ) .....	166
2.8.1. Model of accumulation of fatigue damages based on the markov chain theory, with account of matrix plasticity .....	168
2.8.2. Numerical example .....	174
References .....	177



## Introduction

This monograph, dealing with *Selected problems of modeling and control in mechanics*, is a special publication issued to commemorate Prof. Jan Wojciech Osiecki – a great scholar, a *honoris causa* doctor and an unforgettable academic teacher. His outstanding contribution to the development of the Kielce University of Technology was honoured by unveiling a memorial plaque and naming Lecture Hall 117 of the Kielce University of Technology the Prof. Jan Wojciech Osiecki Lecture Hall. The ceremony was held on 21 January 2010 to mark the first anniversary of death of Prof. Osiecki.

Prof. Jan Wojciech Osiecki, holding the rank of full professor and titles of *honoris causa* doctor from the Łódź Technical University and the Kielce University of Technology, was a distinguished researcher who became an authority in the fields of mechanics, mechanical design and maintenance. For many years, he was a member of the Scientific Committees of the Polish Academy of Sciences, the State Committee for Scientific Research of the Ministry of Scientific Research and Information Technology and numerous other scientific boards. He will be remembered as a man with a heightened sense of ethical values, recognized for his meritorious contribution to the development of higher education and the Świętokrzyski region, an outstanding teacher, mentor and supervisor to many researchers.

The ceremony, which was very moving, took place in the presence of numerous guests, friends, colleagues, and former students. The honorary guests included:

dr Hanna Osiecka-Samsonowicz,

Prof. Osiecki's daughter, with family

prof. dr hab. inż. Stanisław Adamczak, dr h.c.,

Rector of the Kielce University of Technology

prof. dr hab. Janusz Kowal,

Dean of the Faculty of Mechanical Engineering and Robotics,

AGH University of Science and Technology in Kraków

dr hab. inż. Leszek Radziszewski, prof. PŚk,

Dean of the Faculty of Mechatronics and Machine Design

prof. dr hab. inż. Wiesław Trąpczyński,

former Rector of the Kielce University of Technology

prof. dr hab. inż. Zbigniew Wesółowski,

member correspondent of the Polish Academy of Sciences.

During the ceremony, the regulation of the Senate of the Kielce University of Technology concerning the naming of Lecture Hall 117 the Prof. Jan Wojciech Osiecki Lecture Hall was read: "...On behalf of the Senate of the Kielce University of Technology I hereby name Lecture Hall 117 the Prof. Jan Wojciech Osiecki Lecture Hall...".

The memorial plaque with an effigy of Prof. Osiecki was unveiled by dr Hanna Osieckia-Samsonowicz. The inscription reads:

Prof. zw. dr hab. Jan Wojciech Osiecki (1930-2009)

honoris causa doctor of the Kielce University of Technology

- a distinguished researcher and academic teacher,
- an authority in the field of mechanics,
- a faculty member of the Kielce University of Technology from 1971 to 2007,
- the dean of the Faculty of Mechanical Engineering from 1971 to 1973,
- a mentor of many engineers and academic teachers of the Kielce University of Technology.

This monograph devoted to Prof. Jan Wojciech Osiecki contains papers by several academic teachers, who were once his students or colleagues. The authors propose solutions to important scientific problems. Prof. Osiecki's enormous kindness, influence on the people he cooperated with and great support in their research career development can be felt throughout the whole publication.

*Prof. dr hab. inż. Stanisław Adamczak, dr h.c.  
Rector of the Kielce University of Technology*



## Career Biography of Prof. Jan Wojciech Osiecki

Professor Jan Wojciech Osiecki was born on 18 August 1930 in Brest-upon-Bug into a teacher's family with strong traditions of patriotism and humanism.

He started his university education in 1948 at the Faculty of Mechanical Engineering of the Warsaw University of Technology. The years 1954-1963 were a period of close cooperation with Prof. Sylwester Kaliski of the Institute of Fundamental Technological Research of the Polish Academy of Sciences and the Military University of Technology in Warsaw. Supported by his mentor, he proved to be a hard-working, open-minded and creative young scientist. He devoted himself to the study of the propagation and reflection of stress waves in heterogeneous solids, which bore fruit in a number of publications (17 papers) and the defence of his doctoral thesis in 1960.

The next stage of Prof. Osiecki's career began in 1963, when he joined the Faculty of Industrial Machines and Vehicles of the Warsaw University of Technology. He undertook research on the dynamics of machines and mechanisms. His findings were presented in two books: *Fundamentals of Mechanical Vibration Measurements*, co-written with Prof. Stefan Zięba, and *Tensioned Cable Systems. Theory and Calculations*, co-written with Prof. Jerzy Hajduk.

Another area of Prof. Osiecki's interest was the kinematics and dynamics of mechanisms for transmitting drive from an engine to rail vehicle wheels. The problems were investigated as a research project for the degree of habilitated doctor, which was awarded to him in 1970.

In 1972, Prof. Osiecki was invited by Prof. Henryk Frąckiewicz to join the Kielce unit of the Kielce-Radom Higher School of Engineering. Two years later, soon after obtaining the title of professor, he was appointed Dean of the Faculty of Mechanical Engineering. Since then, he was actively involved in the development of the institution, which largely contributed to its transformation into the Kielce University of Technology. Being an experienced researcher and a talented leader, he also helped gain the rights to bestow doctorate degrees in mechanics.

The establishment of the Kielce University of Technology in 1974 was a great success ensuring a continuation of the long tradition of technical education in the Świętokrzyski Region. This tradition goes back to 1816, the year that Stanisław Staszic founded in Kielce the first Polish technical university – the Academic School of Mining.

In 1976, Prof. Osiecki started cooperation with the Simulation Tests Laboratory at the Warsaw-based Automotive Industry Institute, where he initiated and led research projects on vertical dynamics of motor vehicles.

Another problem investigated by Prof. Osiecki was active reduction of vibrations in mechanical systems and missile control. The studies were conducted in collaboration with the Research and Development Institute in Skarżysko and the Military University of Technology in Warsaw.

His impressive output comprises 18 monographs and course books, and over 150 papers in specialized journals and conference proceedings.

Prof. Osiecki was also greatly admired as a teacher. He initiated research projects for several dozens of doctoral theses; he acted as a supervisor for 31 doctoral theses and an internal and external examiner to about a hundred. He was also an examiner of fifty habilitation theses. Twelve of his postgraduate students and younger colleagues have gained the degrees of habilitated doctor, and two have been bestowed the titles of professor.

Prof. Osiecki was frequently elected to join various committees and self-governing bodies at a number of research institutions. His merits were fully appreciated; he was awarded with many of the highest Poland's decorations and honorary titles, including the honoris causa doctorates of the Łódź University of Technology (2001) and the Kielce University of Technology (2004).

Undoubtedly, Prof. Jan Osiecki made a considerable contribution to the establishment and growth of the Kielce University of Technology. He was a highly respected researcher, teacher, superior and colleague. Whatever he did, his enthusiasm and engagement were natural. He never expected praise or reward. Those who had the pleasure to know him will remember him for his sincerity, disinterestedness, and kindness. For many, he was an example to follow.

Personally, I knew Prof. Osiecki for twenty five years. I admired him for his knowledge and passion as a scientist, his talents and commitment as a leader, and his kindness and tact as an individual.

I am certain that he and his accomplishments will never be forgotten.

*dr hab. inż. Leszek Radziszewski, prof. PŚk  
Dean of the Faculty of Mechatronics and Machine Design*

# **1 DYNAMIC MODELING OF PHYSICAL STRUCTURES**

## **1.1. DYNAMIC MODELLING OF HYDROSTATIC TRANSMISSIONS WITH SECONDARY CONTROL**

*Ryszard Dindorf*

Hydraulic drives compete with mechanic, electric and pneumatic ones. Development of hydraulic drives is connected with lower costs of their production, modern energy-saving control technologies, integration of hydraulics with microelectronics, application of intelligent control systems, recovery and accumulation of energy in hydraulic accumulators, miniaturization of hydraulics and micro-hydraulics. In design of hydraulic systems technological, economic and ecological problems should be taken into account. Reduction of costs of energy consumption and minimization of power losses are the basic conditions for development of drive and hydraulic control. In hydraulic systems energy saving and minimization of power losses may be achieved by proper selection of control technology. Volumetric control is in this respect more effective than throttle control. Volumetric control consists in application of combination pumps, fixed displacement pump with frequency converter or variable displacement pump. In throttle control valves and technology control reducing power losses may be used. The effective reduction of power losses in hydraulic drives may be obtained by application of pump controlled system, proportional control valve, three way flow control valve, slip-in cartridge valve, automatic control system, adaptive control, secondary control, load sensing system, flow dividers, hydraulic intensifier, follow up control, pulse modulation, sequence control, as well as separation of low and high pressure circuits and introduction of pump's dead movement breakers. In hydraulic drives pump power should be adjusted to the actual power demand in receivers (motors, cylinders). To accumulate the energy recovered in hydraulic drives the electric, inertial (gyro) and hydraulic accumulators are used. In hydraulic systems of high power the hydro-pneumatic accumulators should be used as the secondary source of energy. The energy recovered in hydraulic drives is accumulated in accumulators and then used to satisfy the peak power demand in hydraulics actuators. Application of the energy recuperation in accumulators reduces the demand for power in the phases of starting a pump and acceleration of hydraulic motor. The efficiency of energy transformation during charging and discharging of the hydro-pneumatic accumulator depends on work cycle of hydrostatic drive (acceleration time, breaking time and steady motion) and upon energetic capacity and thermal time-constant of an accumulator.

### 1.1.1. HYDROSTATIC TRANSMISSIONS WITH SECONDARY CONTROL

Practically, every hydraulic system of any arbitrary hydrostatic drive system consists of pressure energy generators (pumps, accumulators), pressure energy actuators (motors, servo-motors), resistance elements (valves, conduits), auxiliary elements (filters, heat exchangers, tanks), and control elements. In hydrostatic drive systems hydraulic accumulators find application as: pressure generators, volume loss compensators, auxiliary or emergency supply sources, pressure pulsation and hydraulic shock dampers. Experiments have shown that from different types of accumulators, gas accumulators with bladder or diaphragm have the best dynamic properties. The hydraulic accumulator is a pressure vessel adjusted to storing the pressure energy of working fluid by making use of the difference between compressibility of fluid and gas [2]. The hydraulic accumulator should be characterized by a high energy capacity in terms of mass or volume unit, possibility of gaining high power, high efficiency of energy storing and processing. A general diagram of a hydrostatic transmissions system with a variable-displacement pump, hydraulic accumulator as a pressure generator and variable-displacement reversible drive unit with secondary control is presented in Figure 1.1.

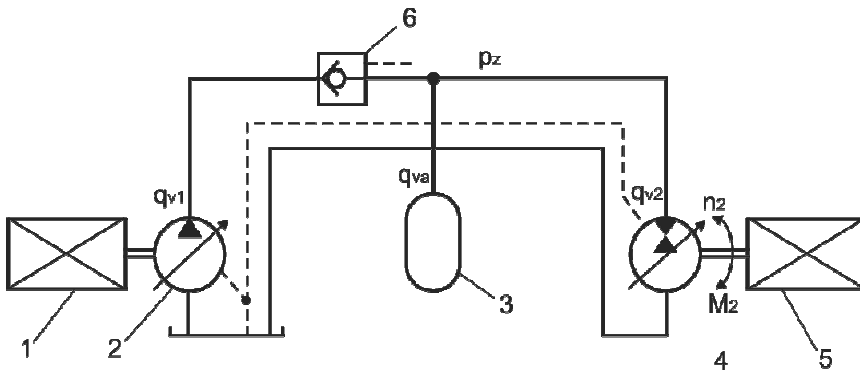


**Fig. 1.1.** General diagram of a hydrostatic transmission system: 1 – combustion engine, 2 – pump, 3 – hydraulic accumulator, 4 – reversible drive unit, 5 – driving mechanism, 6 – check power-operated valve

Three basic elements occur in this system, namely: pump (or a system of pumps) as the primary energy source, a hydraulic accumulator (or a battery of accumulators) as a secondary energy source and a reversible drive unit which can work either as an energy receiver (motor with rotating or linear movement) or as an energy generator (pump) of the same principle of operation. The most favourable method of pump control in such systems is control based on the principle of constant power ( $P_1 = \text{const}$ ). In this system the hydraulic pump is fed by a combustion engine. The hydraulic pump was provided with a regulation system depending on the combustion engine rotating velocity. The regulation system protects the combustion engine from overload and automatically adjusts the pump setting depending on the load of the combustion en-

gine. Regulation of reversible drive systems is realized in proportional technique which permits a high accuracy of regulation of rotating velocity  $n_2$  and torque  $M_2$  in the whole range of work, maintaining a constant torque  $M_2 = \text{const}$  irrespective of rotating velocity  $n_2$  and maintaining a constant rotating velocity  $n_2 = \text{const}$  irrespective of torque  $M_2$ . Reversible unit drives are additionally protected from uncontrolled change of rotating velocity  $n_2$ , i.e. the so-called over-speeding. In the hydrostatic transmission system represented in Figure 1.1 pressure  $p_z$  is maintained in dependence on the state of accumulator charge. It means that pressure  $p_z$  changes according to a proper characteristic of the accumulator depending on thermodynamical transformation and of flow rate  $q_{va}$  into the accumulator. Such a control system enables the accumulator to be charged to maximum pressure  $p_{\max}$  with small efficiency of the pump, whereas under a full load of the drive system the pump suffices to satisfy a mean power demand. With a peak demand of power the hydraulic accumulator is used. In the main line of supply of the discussed drive system there aren't any resistance elements. If a short supply line is additionally installed, transfer of pressure energy is effected without losses. A very important element of this type of hydrostatic drive systems is a reversible drive unit which, depending on work cycle, can transform hydraulic energy into mechanical one (steady state and acceleration) or mechanical energy into hydraulic one (delay). In order to fulfil its function well, the reversible drive unit must be provided with a proper system of regulation of torque  $M_2$  and rotating speed  $n_2$  which can be realized by means of the so-called "hydraulic weight" or in servo control with a power or position feedback. The condition of energy recuperation in hydrostatic drive systems is application of a hydraulic accumulator as a secondary energy source of two-directional flow. Application of the secondary energy source significantly decreases the demand for energy from the primary energy source (pumps) which leads to energy economy in hydrostatic drive systems. Hydrostatic transmission systems with secondary control find application in hydraulic fort-lift, heavy working machines, mining machines, dock levellers, cranes, vehicles.

### **1.1.2. APPLICATION OF MSM IN MODELLING AND SIMULATION OF SECONDARY CONTROL**

In modelling of dynamics of hydraulic systems, nonlinearities which may be classified as structural ones are taken into account. Structural nonlinearities result from physical nature of processes taking place in hydraulic systems. Unless the nonlinearities have got discontinuities they may be linearized by means of various methods, for example, by expansion into *Taylor* or *McLaurin* series. Linearization is carried out in justified cases, for instance, in testing of system stability around the balance point. In hydraulic systems nonlinearities may assume various forms, for example, may depend on one, two, or more variables or their derivatives, may be slow action (pump characteristics) or fast action (change of fluid compressibility in the function of pressure). Nonlinearities of the system are presented as a function or in the form of graphical function (steady-state characteris-

tics). In hydraulic systems numerous processes including fluid flow through throttling gap, hydrodynamic force, force of dry friction, fluid compressibility, fluid viscosity and thermodynamic phenomena are described by nonlinear functions whereas nonlinear static characteristics are taken into account in analysis of hydraulic valves, for example, servo-valves and proportional valves. The flow characteristics of the valves indicated possess both zone of insensitivity and saturation zone. Since modified structural matrices must be adjusted to dynamic modelling and testing of nonlinear hydraulic systems it is necessarily that the elements of matrix contain functions or nonlinear characteristics.

The modified structural matrices (MSM) is applied in modelling of both linear and nonlinear simulations of hydraulic control systems. The method is based upon the concise notation of matrix-vector product in the form of a table which enables ordinary notation of ordinary differential equations. For nonlinear systems MSM is written in the combined form allowing the separation of the submatrices of the linear and nonlinear parts. A nonlinear part contains the matrices of conjugations, coefficients and operators of nonlinear functions. The modified structural matrices enable a simple presentation of the system functional and dynamic structure as well as determining the relations between coordinates of state and between coordinates of state and input parameters (controlling, interfering and input). On MSM both the correctness of the system dynamic model and the flow of information signals can be easily checked. The usefulness of MSM was proved by means of modelling and digital simulation of secondary control. After linearization of nonlinearity the matrix was used in qualitative testing of the control system stability (parametric and structural). On the basis of the experiments conducted up to now it may be concluded that MSM can be applied in modelling dynamics and in quantitative and qualitative testing of the dynamic hydraulic systems and other physical systems including pneumatic, mechanical and electrical ones the paper concentrates on the principle of formation of modified structural matrices for linear and nonlinear control system by means of ordinary differential equations. The example showing the application of structural matrices in modelling dynamics and simulation of nonlinear system of secondary control does not provide sufficient information on usability of MSM in investigation of dynamic, linear control systems.

As an example modelling and simulation of reversible driving unit A2V107 type with secondary control is used [1]. The scheme of the hydraulics secondary control of reversible drive unit consisting of the servomechanism with the force-testing feedback is shown in Figure 1.2.

The reversible driving unit was incorporated into the hydrostatic transmissions system with the pressure generator ( $p_z = \text{const}$ ). The servo-motor is fed by the fluid flux of constant pressure  $p_o$ . In the system the tachometric pump feeding the measuring part of the system and consisting of throttle valve, flow control and servo-valve was used. The secondary control is applied to adjust the rotational speed  $n_2$  and momentum  $M_2$  of the driving unit to driving system loading and

operation, for example, during acceleration and stabilised motion the driving unit functions as an engine and during braking as a pump. During braking there is a possibility of energy recuperation and its subsequent accumulation in hydro-pneumatic accumulators. The application of secondary control systems in energy-saving driving systems of mining machines was a theme of the research project.

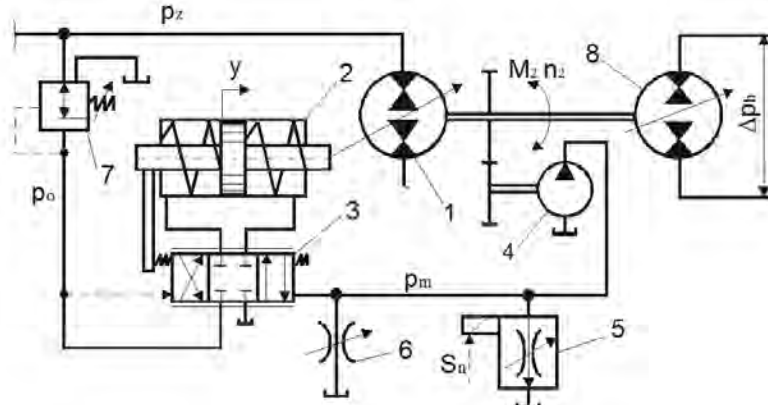


**Fig. 1.2.** Scheme of hydraulics secondary control system: 1 – reversible drive unit, 2 – servo-cylinder, 3 – servo-valve, 4 – tachometric pump, 5 – flow controller, 6 – throttle valve, 7 – reduction valve, 8 – reversible braking unit

A general dynamic model of the hydraulic secondary control system can be written in the form of the following ordinary differential equations:

$$\begin{cases} \dot{p}_m = a_{10} \dot{x} + a_7 \omega - a_8 f_1 - a_9 S_r \\ \ddot{x} + a_{16} \dot{x} + a_{17} x = -a_{18} p_m - a_{19} y + a_{18} p_o \\ \Delta \dot{p} + a_{22} \Delta p = -a_{21} \dot{y} + a_{20} f_2 \\ \ddot{y} + a_{11} \dot{y} + a_{12} y = -a_{14} x + a_{13} \Delta p - a_{15} F_{st} \\ \dot{\omega} + a_2 \omega = -a_4 p_m + a_1 f_3 - a_3 \Delta p_h - a_5 M_{st} \end{cases} \quad (1.1)$$

where:  $a_i$  – constant coefficients,  $\omega$  – angular velocity of the driving unit,  $p_m$  – pressure in the measurement system,  $y$  – displacement of the cylinder spool,  $x$  – displacement of the servo-valve control slider,  $\Delta p$  – pressure drop on the servo-motor,  $p_o$  – pressure behind the reduction valve,  $x_o$  – steady overlap of the control spool,  $S_n$  – steering parameter of the flow regulator,  $\Delta p_z$  – pressure drop on the braking unit is introduced as the input quantity,  $M_{st}$  – losses on net torque of the driving unit,  $F_{st}$  – losses of force in the servo-motor.

In order to write down nonlinearity on matrices the submatrix  $\mathbf{N}$  – the product of submatrix  $\mathbf{H}$  by submatrix  $\mathbf{F}$  is introduced:

$$\mathbf{N} = \mathbf{H} \times \mathbf{F} \quad (1.2)$$

where:

$$\mathbf{H} = \begin{bmatrix} -h_{11} & -h_{12} & \cdots & -h_{1n} \\ -h_{21} & -h_{22} & \cdots & -h_{2n} \\ \vdots & \vdots & \ddots & \vdots \\ -h_{n1} & -h_{n2} & \cdots & -h_{nn} \end{bmatrix}, \quad \mathbf{F} = \begin{bmatrix} f_{11} & 0 & \cdots & 0 \\ 0 & f_{22} & \cdots & 0 \\ \vdots & \vdots & \ddots & \vdots \\ 0 & 0 & \cdots & f_{nn} \end{bmatrix}$$

If submatrix  $\mathbf{N}$  is introduced into equation (1.2) the matrix-vector product of nonlinear system is represented as follows:

$$\overline{\mathbf{A}} \bar{\mathbf{x}} + \mathbf{N} = \mathbf{B} \mathbf{u} \quad (1.3)$$

The linear part of the indicated matrix does not differ from of modified structural matrix for linear system. It contains submatrices  $\overline{\mathbf{A}}$  and  $\mathbf{B}$ . Nonlinear part of the matrix includes diagonal submatrix  $\mathbf{F}$  and the submatrix of coefficients  $\mathbf{H}$ . Submatrix  $\mathbf{F}$  contains operators of nonlinear functions, for example, power, exponent, logarithmic, trigonometric, product of two or more variables. On the other hand, submatrix  $\mathbf{H}$  contains constant coefficients of nonlinear functions. The submatrices  $\mathbf{1}$  enable conjugation of linear part of the system with the  $\mathbf{N}$  submatrix of nonlinear functions. A concise notation of matrix-vector product (1.3) is obtained by means of modified structural matrix (Table 1.1). It is a combined notation of modified structural matrix consisting in separation from hydraulic secondary control system of its linear and nonlinear terms represented by respective submatrices.

**Table 1.1.** Modified structural matrix of hydraulics secondary control system

$p_m$	$x$	$\Delta p$	$y$	$\omega$	$N_1$	$N_2$	$N_3$	$p_z$	$p_o$	$x_o$	$\Delta p_h$	$S_r$	$M_{st}$	$F_{st}$
D	$a_{10} D$			$a_7$	$-a_8$							$-a_9$		
$-a_{18}$	$D^2+a_{16}D+a_{17}$		$-a_{19}$						$a_{18}$					
	n	$D+a_{22}$	$-a_{21} D$			$a_{20}$			n	n				
	$-a_{14}$	$a_{13}$	$D^2+a_{11}D+a_{12}$											$-a_{15}$
$-a_4$			n	$D+a_2$			$a_1$	n			$-a_3$		$-a_5$	
1					$f_1$									
	1	1				$f_2$			1	1				
			1				$f_3$	1						

On the modified structural matrix (Table 1.1) three nonlinear functions can be distinguished:

$$f_1 = \sqrt{p_m} \quad f_2 = (x_o - x) \sqrt{\frac{1}{2}(p_o - \Delta p)}$$

$$f_3 = p_z y (1 + a_6 \text{sign} \omega)$$

where:  $p_z$  – outlet pressure.

The dynamic model was applied and in accordance with the Table 1.1 the digital simulation of the secondary control system was carried out. The purpose of the simulation was to determine the run of the following parameters:  $\omega(t)$ ,  $p_m(t)$ ,  $y(t)$ ,  $v_y(t)$ ,  $x(t)$ ,  $v_x(t)$  i  $\Delta p(t)$  in relation to the change of coefficients  $a_i$ . After calculating the value of  $a_i$  coefficients an initial digital simulation determining the integration step and numerical method for the input action was introduced. Various numerical methods were tested but finally *Gear's* method of the order  $k = 2$  was selected. The integration step was determined as  $h = 0.0001$  s, integration range as  $t = 0 \div 1$  s and separation of results for every 0.005 s. The results of the initial digital simulation prove that the system investigated is numbered among the systems of stiff type. The simulation of the control system was conducted by means of a simulation program in *MATLAB* adapted to the structure of the modified structural matrices. The effect of the change of coefficients  $a_i$  upon stability of control system was carried out for input parameter  $\Delta p_h = 1 \times 10^6$  MPa. The system displayed stability in the initial state for the parameter indicated above.

In the simulation calculations the initial values of the control system coefficients were as follows:

$a_1 = 0.025 \text{ m}/(\text{Ns}^2)$	$a_2 = 97.006 \text{ 1/s}$	$a_3 = 0.001 \text{ m}^2/(\text{Ns}^2)$
$a_4 = 1.073 \times 10^{-4} \text{ m}^2/(\text{Ns}^2)$	$a_5 = 59.88 \text{ 1}/(\text{Nms}^2)$	$a_6 = 1.1$
$a_7 = 4.73 \times 10^6 \text{ N/m}^2$	$a_8 = 1.14 \times 10^5 \text{ N}^{1/2}/(\text{ms})$	$a_9 = 2.778 \times 10^7 \text{ N}/(\text{m}^2 \text{ s})$
$a_{10} = 8.333 \times 10^8 \text{ N/m}^3$	$a_{11} = 653.333 \text{ Ns}/(\text{kgm})$	$a_{12} = 1.28 \times 10^4 \text{ N}/(\text{kgm})$
$a_{13} = 4.667 \times 10^{-4} \text{ m}^2/\text{kg}$	$a_{14} = 0.667 \text{ 1/kg}$	$a_{15} = 0.667 \text{ 1/kg}$
$a_{16} = 525 \text{ Ns}/(\text{kgm})$	$a_{17} = 7.5 \times 10^5 \text{ N}/(\text{kgm})$	$a_{18} = 0.0015 \text{ m}^2/\text{kg}$
$a_{19} = 2.85 \times 10^{10} \text{ N}/(\text{kgm})$	$a_{20} = 1.021 \times 10^{10} \text{ N}^{1/2}/(\text{m}^2 \text{ s})$	$a_{21} = 9.589 \times 10^9 \text{ N/m}^3$
$a_{22} = 45.205 \text{ 1/s}$		

The following values of the control parameters were assumed:

$$x_o = 0.24 \times 10^{-3} \text{ m}, \quad p_z = 15 \text{ MPa}, \quad S_n = 5, \quad p_o = 4 \text{ MPa}.$$

Disturbance quantities included:  $M_{st} = 25 \text{ Nm}$  i  $F_{st} = 85 \text{ N}$ .

Simulations were conducted with only one coefficient changed (other coefficients remained constant). It was increased and decreased by 30%. After analysing the effect of various coefficients upon the system stability it may be concluded that some coefficients have a destabilising influence upon the run of all the parameters of the system, namely:  $a_1$ ,  $a_2$ ,  $a_7$ ,  $a_8$ ,  $a_9$ ,  $a_{18}$  i  $a_{19}$ . Other coefficients significantly affect only the run of particular parameters of the system, for example,  $\omega(t)$  angular

velocity is considerably affected by coefficients  $a_5 \pm 30\%$  and  $a_{20} - 30\%$ . The exemplary run of the function  $\omega(t)$  for coefficients  $a_5$  and  $a_5 \pm 30\%$  is presented in Figure 1.3 and for coefficients  $a_{20}$  and  $a_{20} - 30\%$  in Figure 1.4.

The run changes of the dynamic characteristics of the system resulting from the change of coefficients manifest themselves by the growth or decrease of amplitude and pulsation period in the transient state. As the result of digital simulations two kinds of output functions: strongly damped and unstable were obtained. The results of digital simulation are verified experimentally.

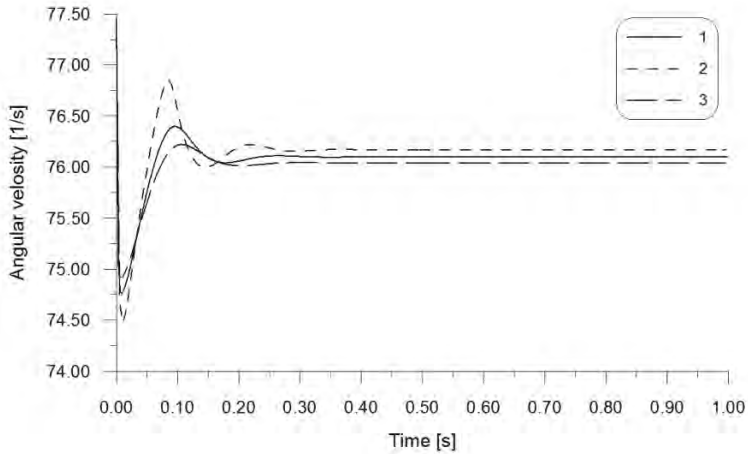


**Fig. 1.3.** Transient response of angular velocity  $\omega(t)$  for coefficients:  $a_5$  (1),  $a_5 + 30\%$  (2),  $a_5 - 30\%$  (3)

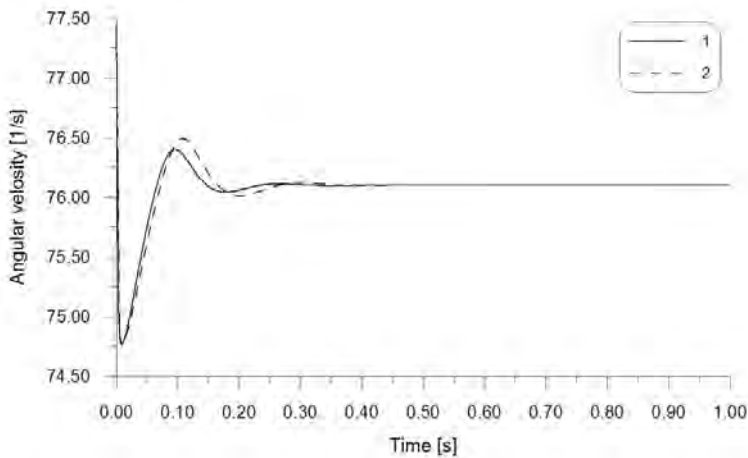


**Fig. 1.4.** Transient response of angular velocity  $\omega(t)$  for coefficients:  $a_{20}$  (1),  $a_{20} - 30\%$  (2)

The paper presents a dynamic model and results of digital simulation of hydraulic drive system with secondary control. The modified structural matrices (MSM) are used in modelling of the hydraulic secondary control system. The coefficients influence upon stability of secondary control system and quality indicators of dynamic characteristics are analysed. The modeling method is based upon the concise notation of matrix-vector product in the form of a table which enables ordinary notation of ordinary differential equations. The MSM obtained on the basis of *Shatihin's* structural matrices. The structural matrices are based upon the concise notation of matrix-vector product in the form of a table which enables ordinary notation of ordinary differential equations. The modified structural matrix in comparison with ordinary structural matrix contains differential operators  $D$ . For nonlinear systems modified structural matrix is written in the combined form allowing the separation of the sub-matrices of the linear and nonlinear parts. A nonlinear part contains the matrices of conjugations, coefficients and operators of nonlinear functions. The MSM enable a simple presentation of the system functional and dynamic structure as well as determining the relations between coordinates of state and between coordinates of state and input parameters (controlling, interfering and input). On MSM both the correctness of the system dynamic model and the flow of information signals can be easily checked. On the basis of the experiments conducted up to now it may be concluded that MSM can be applied in modelling dynamics and in quantitative and qualitative testing of the dynamic hydraulic systems.

## **1.2. DYNAMIC ELEMENTS OF A MOTOR VEHICLE WHICH IS A CARRIER OF THE ANTI-AIRCRAFT MISSILE LAUNCHER**

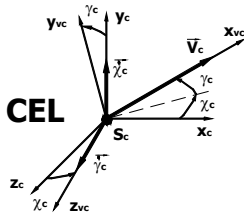
*Zbigniew Dziopa*

The discussed motor vehicle is one of the five basic elements of the self-propelled anti-aircraft missile assembly:

1. Combat vehicle.
2. Operator and driver in their seats.
3. Launcher with four missile guides.
4. Four missiles with gyroscope systems.
5. Target.

Each element is indispensable to performing the essential task assigned to the anti-aircraft assembly, which is the destruction of the target by the launched missile. The assembly elements are complex systems performing specific functions. Their geometry, structure, parameters values should be subject to the proper operation of the assembly as a whole.

# SELF-PROPELLED ANTI-AIRCRAFT MISSILE ASSEMBLY



**GYROSCOPE  $i$**  where:  $i=1,2,3,4$   
 $m_{ki} \ I_{kixw} \ I_{kiyw} \ I_{kizw}$

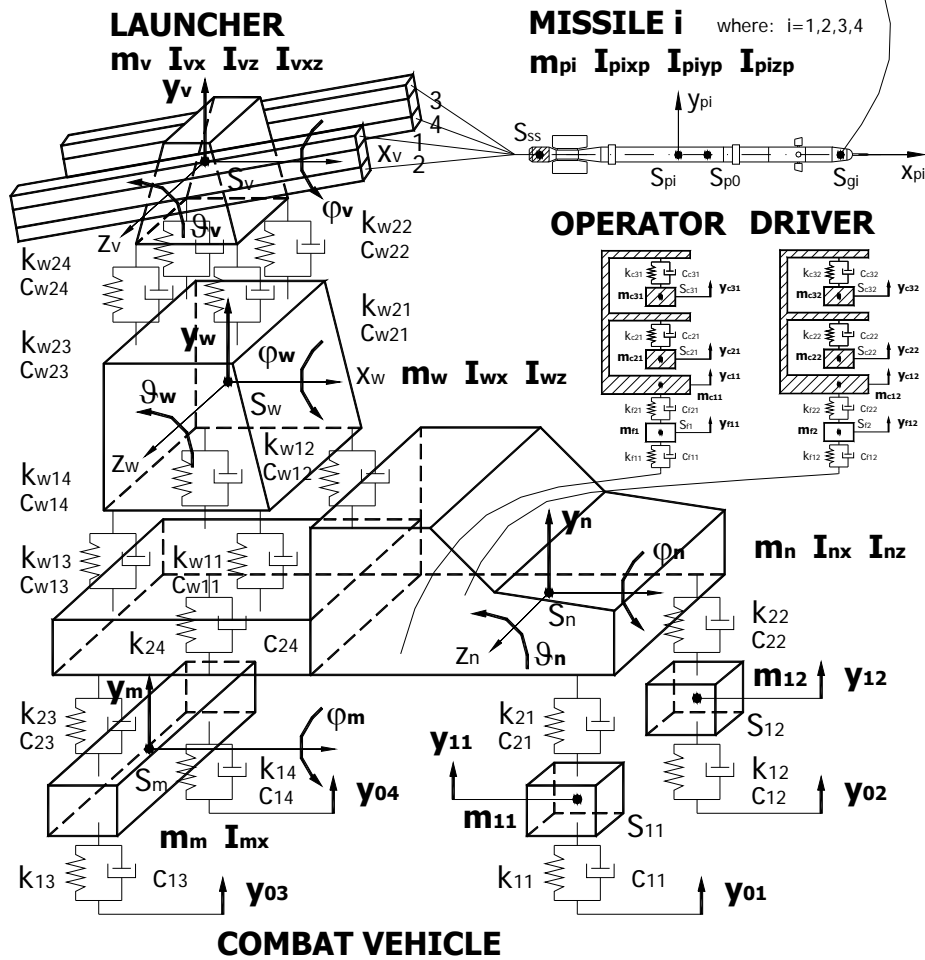
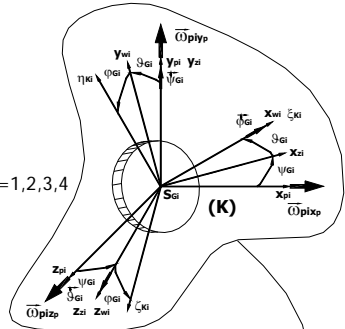


Fig. 1.5. Physical model of the self-propelled anti-aircraft missile assembly

The notion of the optimal structure of a particular element is linked, among others, to its harmless effect on other assembly elements. The interaction of the assembly objects is connected with the emission of disturbance generated by the individual element. If the disturbance does not affect the comfort of missile operation in a negative way then they are considered to be harmless. The functioning of the assembly is a continuous coincidence of the occurring processes. Therefore the right model design is fundamental to the anti-aircraft assembly analysis. It is necessary to take into consideration the structural details for the effectiveness of the numerical calculations and substantive indispensability evaluated in relation to the dynamic phenomena. The tasks performed by the assembly are not affected by the five assembly elements to the same degree. Their proper degeneration determines the preservation of the dynamic properties of an actual system by the constructed model.

The system is treated as one complex object [9, 14]. As the partial systems are not considered one may speak about the number of freedom degrees of the system as a whole. The notion of the number of freedom degrees is introduced in the study. It is a purely formal practice, which makes a clear presentation of the problem easier, however from the substantive interpretation point of few it is improper. The author points out the terminology inaccuracy, which in the case of complex system structure allows for accurate elaboration of the individual elements including the motor vehicle.

The self-propelled anti-aircraft missile assembly with one of its elements, the motor vehicle [4], presented in Figure 1.5.

### **1.2.1. MOTOR VEHICLE PHYSICAL MODEL**

The anti-aircraft missile launcher is mounted on a carrier which is a motor vehicle [3, 4]. Owing to that fact the assembly becomes mobile, which is essential for the modern battlefield. The possibility of a quick position change and a close interaction with an automated anti-aircraft defense system allow for locating the enemy and its elimination from battle. Depending on the type of risk and needs the application of the vehicle makes it possible for protecting the zone threatened with the enemy attacks. The vehicle can move into the threatened area and cover the troops and equipment stationed there. In the case of direct enemy attack from air an efficient location change of the assembly allows for neutralizing the opponent.

Shooting at a target can be carried out from a vehicle standing still as well as moving over a given surface. The elaborated model allows for conducting a numerical simulation in both cases. The vehicle standing still is a system in a stable equilibrium. Outer input does not affect the assembly. The disturbance generated within the system is solely linked to the launch of the first, and then the next missile. Another possible variant can be taken into consideration. The vehicle stands still while it is affected by the outer input from the side of the road. Such a model of input function suits the real conditions that can be created as a result of a nearby explosion occurring on the ground, which causes tectonic movement of the lithosphere in the direct vicinity of the standing vehicle. The function describing the

shape of such input can be assumed in accordance with the rule of intensive interaction of the disturbance source. On account of the determined presentation of the occurring processes such an assumption should be treated as a form of a test on the system under discussion. The application of the extreme input allows for drawing conclusions concerning the final effective application of the assembly in operational conditions. While formulating the vehicle model the interaction resulting from the work of the following elements of vehicle chassis: power transmission, steering, and braking systems as well as the engine, was ignored as these systems do not operate.

The general vehicle movement is usually treated as a combination of primary motion and primary motion disturbance. In the assumed model the primary vehicle motion is rectilinear and uniform. Therefore it is justifiable to introduce several simplifications into the vehicle structure. The steering system interaction with the running system vibration was considered as weak and thus ignored [11]. The braking system does not work while the power transmission system and the engine are so meticulously manufactured and balanced that they by no means can be considered to be the vibration source. The radius homogeneity of tyre rigidity is preserved and the wheels as an element of the running system are balanced. Apart from that the slight advance velocity of the vehicle justifies omitting the aerodynamic drag. In conclusion, you can state that the vehicle is not a source of internal input, but it is affected by the external input resulting from the movement of the vehicle wheels over vertical road surface irregularities. The interaction of the wheel tyre with the road surface can be an issue for a another study. In this paper it was assumed a priori that the input has a kinematic form determined by the course of the vertical relocation of the wheel contact with the road surface, and the vehicle model accounts for the radius deformability of the tyre. The input assumed in the discussion is a determined model of input signals of three different types. The first type is an ideally smooth road, i.e. the assembly is not affected by the external input. Such model allows for checking if under ideal conditions it is possible to launch effectively a missile off a running vehicle and at what advance velocity safety conditions and technical limitations are exceeded. A positive answer suggests that it is necessary to check the assembly performance in less favourable conditions. The limiting advance velocity determined in this way is the meter of the extreme assembly performance in the ideally created conditions and can be the reference point to the further research. The second type is the lateral, single hump located cross-wise the vehicle running direction. In this case it is a single pulse of a specific shape. The third type is a model accounting for the road surface profile. The model of the input signals reflects the road surface irregularities in the form of functions determined by well-known spectral power density characteristics [9]. On the basis of the existing road classification soft road surface was chosen.

Taking into consideration the formulated aim of the study and the above-mentioned assumptions the motor vehicle was modeled in the form of four masses and eight deformable elements [7, 8, 14], as presented in Figure 1.6.

The body of the car is ideally rigid with the mass  $m_n$  and moments of inertia  $I_{nx}$ ,  $I_{nz}$ . The vehicle chassis consists of the front independent suspension and the rear dependent suspension. The front axle of the vehicle along with the wheels is reduced to two concentrated masses  $m_{11}$  and  $m_{12}$ . The rear axle along with the wheels is reduced to a rigid body with the mass  $m_m$  and the inertia moment  $I_{mx}$ . The characteristics of the radius flexibility of the front wheels and rear wheels tyre and the characteristics of the front and rear suspension flexibility are the Voight-Kelvin linear models. Therefore the characteristics of the weightless deformable elements are represented by the following rigidity and damping coefficients:  $k_{11}$  and  $c_{11}$ , and  $k_{12}$  and  $c_{12}$  determine the front wheels tyre,  $k_{13}$  and  $c_{13}$ , and  $k_{14}$  and  $c_{14}$  determine the rear wheels tyre,  $k_{21}$  and  $c_{21}$  and  $k_{22}$  and  $c_{22}$  determine the front axle suspension,  $k_{23}$  and  $c_{23}$  and  $k_{24}$  and  $c_{24}$  determine the rear axle suspension.

## COMBAT VEHICLE

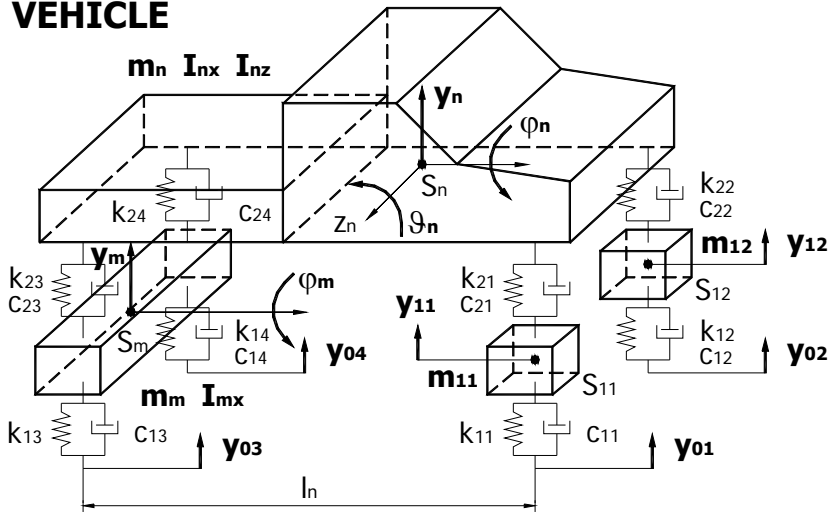


Fig. 1.6. Physical model of the combat vehicle

The vehicle inertia elements location at an optional moment are presented by a cartesian orthogonal dextrorotatory coordinates system [13]. The reference systems are the following coordinates systems:

- Coordinates system connected with the ground,
- Coordinates systems determining the vehicle body movement:
  - $0_n x_n y_n z_n$
  - $S_n x_n y_n z_n$
  - $S_n \xi_n \eta_n \zeta_n$

If the vehicle moves without the disturbance of the primary motion then the coordinates systems:  $0_n x_n y_n z_n$ ,  $S_n x_n y_n z_n$  and  $S_n \xi_n \eta_n \zeta_n$  overlap. The body

model as an element of the three-dimensional vibrating system performs in relation to the reference system  $0_n x_n y_n z_n$  complex motion consisting of the rectilinear centre of mass motion  $S_n$ . In accordance with the  $y_n$  coordinate change, rotary motion around the  $S_n z_n$  axis. In accordance with the inclination angle change  $\vartheta_n$  and rotary motion around the  $S_n x_n$  axis, in accordance with the tilting angle change  $\varphi_n$ ;

c) Coordinates systems determining the chassis movement:

c1) Coordinates systems determining the front axle motion:

$$- 0_{11} x_{11} y_{11} z_{11}$$

$$- S_{11} x_{11} y_{11} z_{11}$$

If the vehicle moves without the primary motion disturbance then the coordinates systems:  $0_{11} x_{11} y_{11} z_{11}$  and  $S_{11} x_{11} y_{11} z_{11}$  at any moment overlap. The first element of the front axle model in the form of a particle  $S_{11}$  in the case of vibration performs rectilinear motion towards the reference system  $0_{11} x_{11} y_{11} z_{11}$  and accordingly to the  $y_{11}$  coordinate change.

$$- 0_{12} x_{12} y_{12} z_{12}$$

$$- S_{12} x_{12} y_{12} z_{12}$$

If the vehicle moves without any primary motion disturbance then the coordinates systems  $0_{12} x_{12} y_{12} z_{12}$  and  $S_{12} x_{12} y_{12} z_{12}$  overlap at any time. In the case of vibration the second element of the front axle in the form of a particle  $S_{12}$  performs rectilinear motion towards the reference  $0_{12} x_{12} y_{12} z_{12}$  and accordingly to the  $y_{12}$  coordinate change;

c2) Coordinates systems determining the rear axle motion:

$$- 0_m x_m y_m z_m$$

$$- S_m x_m y_m z_m$$

$$- S_m \xi_m \eta_m \zeta_m$$

If the vehicle moves without any primary motion disturbance then the coordinates systems  $0_m x_m y_m z_m$ ,  $S_m x_m y_m z_m$  and  $S_m \xi_m \eta_m \zeta_m$  overlap at any moment. The rear axle model performs towards the reference system  $0_m x_m y_m z_m$  complex motion consisting of the rectilinear motion of the center of inertia  $S_m$  in accordance with the  $y_m$  coordinate change and rotary motion around the  $S_m x_m$  axis in accordance with the tilting angle  $\varphi_m$  change.

The number of the degrees of freedom resulting from a complicated structure of the motor vehicle model defining the primary motion disturbance in space equals seven.

## 1.2.2. MATHEMATICAL MODEL OF THE MOTOR VEHICLE

Seven independent coordinates determine the motion of the motor vehicle model:

- a) Motor vehicle body – ideally rigid body :  $y_n, \mathcal{G}_n, \varphi_n$
- b) Front axle and the wheels – concentrated mass :  $y_{11}$   
– concentrated mass :  $y_{12}$
- c) Rear axle and the wheels – ideally rigid body :  $y_m, \varphi_m$

**Motion equations:**

**The motor vehicle equations are one of the parts of the anti-aircraft assembly motion equations**

$$\begin{aligned}
 & m_n \ddot{y}_n + c_{21} \dot{\lambda}_{21} + k_{21} \lambda_{21} + c_{22} \dot{\lambda}_{22} + k_{22} \lambda_{22} + \\
 & + c_{23} \dot{\lambda}_{23} + c_{24} \dot{\lambda}_{24} + k_{23} \lambda_{23} + k_{24} \lambda_{24} + \\
 & - c_{w11} \dot{\lambda}_{w11} - c_{w12} \dot{\lambda}_{w12} - c_{w13} \dot{\lambda}_{w13} - c_{w14} \dot{\lambda}_{w14} + \\
 & - k_{w11} \lambda_{w11} - k_{w12} \lambda_{w12} - k_{w13} \lambda_{w13} - k_{w14} \lambda_{w14} + \\
 & - c_{f11} \dot{\lambda}_{f11} - k_{f11} \lambda_{f11} - c_{f12} \dot{\lambda}_{f12} - k_{f12} \lambda_{f12} + m_n g = 0
 \end{aligned} \tag{1.4}$$

$$\begin{aligned}
 & I_{nz} \ddot{\mathcal{G}}_n + c_{21} l_{n1} \dot{\lambda}_{21} + k_{21} l_{n1} \lambda_{21} + c_{22} l_{n1} \dot{\lambda}_{22} + k_{22} l_{n1} \lambda_{22} + \\
 & - c_{23} l_{n2} \dot{\lambda}_{23} - c_{24} l_{n2} \dot{\lambda}_{24} - k_{23} l_{n2} \lambda_{23} - k_{24} l_{n2} \lambda_{24} + \\
 & + c_{w11} l_{w1} \dot{\lambda}_{w11} + c_{w12} l_{w1} \dot{\lambda}_{w12} + c_{w13} l_{w2} \dot{\lambda}_{w13} + c_{w14} l_{w2} \dot{\lambda}_{w14} + \\
 & + k_{w11} l_{w1} \lambda_{w11} + k_{w12} l_{w1} \lambda_{w12} + k_{w13} l_{w2} \lambda_{w13} + k_{w14} l_{w2} \lambda_{w14} + \\
 & + c_{f11} l_f \dot{\lambda}_{f11} + k_{f11} l_f \lambda_{f11} + c_{f12} l_f \dot{\lambda}_{f12} + k_{f12} l_f \lambda_{f12} = 0
 \end{aligned} \tag{1.5}$$

$$\begin{aligned}
 & I_{nx} \ddot{\varphi}_n - c_{21} d_{np1} \dot{\lambda}_{21} - k_{21} d_{np1} \lambda_{21} + c_{22} d_{np2} \dot{\lambda}_{22} + k_{22} d_{np2} \lambda_{22} + \\
 & - c_{23} d_{nr1} \dot{\lambda}_{23} + c_{24} d_{nr2} \dot{\lambda}_{24} - k_{23} d_{nr1} \lambda_{23} + k_{24} d_{nr2} \lambda_{24} + \\
 & + c_{w11} d_{w1} \dot{\lambda}_{w11} - c_{w12} d_{w2} \dot{\lambda}_{w12} + c_{w13} d_{w1} \dot{\lambda}_{w13} - c_{w14} d_{w2} \dot{\lambda}_{w14} + \\
 & + k_{w11} d_{w1} \lambda_{w11} - k_{w12} d_{w2} \lambda_{w12} + k_{w13} d_{w1} \lambda_{w13} - k_{w14} d_{w2} \lambda_{w14} + \\
 & + c_{f11} d_{f1} \dot{\lambda}_{f11} + k_{f11} d_{f1} \lambda_{f11} - c_{f12} d_{f2} \dot{\lambda}_{f12} - k_{f12} d_{f2} \lambda_{f12} = 0
 \end{aligned} \tag{1.6}$$

$$m_{11} \ddot{y}_{11} + c_{11} \dot{\lambda}_{11} + k_{11} \lambda_{11} - c_{21} \dot{\lambda}_{21} - k_{21} \lambda_{21} + m_{11} g = 0 \tag{1.7}$$

$$m_{12} \ddot{y}_{12} + c_{12} \dot{\lambda}_{12} + k_{12} \lambda_{12} - c_{22} \dot{\lambda}_{22} - k_{22} \lambda_{22} + m_{12} g = 0 \tag{1.8}$$

$$\begin{aligned}
 & m_m \ddot{y}_m + c_{13} \dot{\lambda}_{13} + c_{14} \dot{\lambda}_{14} + k_{13} \lambda_{13} + k_{14} \lambda_{14} + \\
 & - c_{23} \dot{\lambda}_{23} - c_{24} \dot{\lambda}_{24} - k_{23} \lambda_{23} - k_{24} \lambda_{24} + m_m g = 0
 \end{aligned} \tag{1.9}$$

$$\begin{aligned}
& I_{mx}\ddot{\varphi}_m - c_{13}d_{m1}\dot{\lambda}_{13} + c_{14}d_{m2}\dot{\lambda}_{14} - k_{13}d_{m1}\lambda_{13} + k_{14}d_{m2}\lambda_{14} + \\
& + c_{23}d_{m1}\dot{\lambda}_{23} - c_{24}d_{m2}\dot{\lambda}_{24} + k_{23}d_{m1}\lambda_{23} - k_{24}d_{m2}\lambda_{24} = 0
\end{aligned} \tag{1.10}$$

where:

$$\begin{aligned}
\lambda_{11} &= y_{11} + y_{11st} - y_{01} \\
\lambda_{12} &= y_{12} + y_{12st} - y_{02} \\
\lambda_{21} &= y_n + y_{nst} + l_{n1}(\mathcal{G}_n + \mathcal{G}_{nst}) - d_{np1}(\varphi_n + \varphi_{nst}) - y_{11} - y_{11st} \\
\lambda_{22} &= y_n + y_{nst} + l_{n1}(\mathcal{G}_n + \mathcal{G}_{nst}) + d_{np2}(\varphi_n + \varphi_{nst}) - y_{12} - y_{12st} \\
\dot{\lambda}_{11} &= \dot{y}_{11} - \dot{y}_{01} \\
\dot{\lambda}_{12} &= \dot{y}_{12} - \dot{y}_{02} \\
\dot{\lambda}_{21} &= \dot{y}_n + l_{n1}\dot{\mathcal{G}}_n - d_{np1}\dot{\varphi}_n - \dot{y}_{11} \\
\dot{\lambda}_{22} &= \dot{y}_n + l_{n1}\dot{\mathcal{G}}_n + d_{np2}\dot{\varphi}_n - \dot{y}_{12} \\
\lambda_{13} &= y_m + y_{mst} - d_{m1}(\varphi_m + \varphi_{mst}) - y_{03} \\
\lambda_{14} &= y_m + y_{mst} + d_{m2}(\varphi_m + \varphi_{mst}) - y_{04} \\
\lambda_{23} &= y_n + y_{nst} - l_{n2}(\mathcal{G}_n + \mathcal{G}_{nst}) - d_{nt1}(\varphi_n + \varphi_{nst}) - y_m - y_{mst} + d_{m1}(\varphi_m + \varphi_{mst}) \\
\lambda_{24} &= y_n + y_{nst} - l_{n2}(\mathcal{G}_n + \mathcal{G}_{nst}) + d_{nt2}(\varphi_n + \varphi_{nst}) - y_m - y_{mst} - d_{m2}(\varphi_m + \varphi_{mst}) \\
\dot{\lambda}_{13} &= \dot{y}_m - d_{m1}\dot{\varphi}_m - \dot{y}_{03} \\
\dot{\lambda}_{14} &= \dot{y}_m + d_{m2}\dot{\varphi}_m - \dot{y}_{04} \\
\dot{\lambda}_{23} &= \dot{y}_n - l_{n2}\dot{\mathcal{G}}_n - d_{nt1}\dot{\varphi}_n - \dot{y}_m + d_{m1}\dot{\varphi}_m \\
\dot{\lambda}_{24} &= \dot{y}_n - l_{n2}\dot{\mathcal{G}}_n + d_{nt2}\dot{\varphi}_n - \dot{y}_m - d_{m2}\dot{\varphi}_m
\end{aligned} \tag{1.11}$$

Parameters of the studied model are presented in the monograph [6].

### 1.2.3. NUMERICAL SIMULATION OF THE MOTOR VEHICLE MOTION DURING THE OPERATION OF THE ANTI-AIRCRAFT MISSILE ASSEMBLY

On the basis of the elaborated mathematical model of the anti-aircraft assembly a computer program in the Borland C++ system was edited by the author. It allowed to conduct the numerical simulation of the formulated system operation [7, 12]. Owing to that the results of the motor vehicle performance during the anti-aircraft assembly operations can be presented. The analysis is limited solely to the mechanical interaction type and serves the purpose of evaluating their influence on the reachability of the manoeuvring target by the missiles at the time of launching.

The computer program allows for conducting a simulation of the anti-aircraft assembly operation from the moment the target becomes traced by the missiles

located on the launcher. The moment is selected by determining the initial target location towards the assembly for the time  $t = 0$ . The target performs independent movement, which can be treated as a defensive manoeuvre of the pilot. The configuration of the launcher turret results from the initial platform location and the guide system:  $\psi_{pv} = 45 \text{ deg}$  and  $\mathcal{G}_{pv} = 45 \text{ deg}$ .

Most often shooting at the target is carried out from a vehicle at rest. The spacial movement simulation of the assembly model will be discussed while taking into consideration additionally the disturbance coming from the nearby ground explosion. The mathematical model of such input is a virtual form resembling the drive of the vehicle over smooth surface with a hump, of a specific profile as presented in Figure 1.7, located crosswise. The case of input affecting the right side wheels of the vehicle is being discussed.

Due to the determined type of the analysis the introduction of the additional external input from the side of the road allows for the evaluation of the disturbance generated by the missiles while launching and gives an opportunity to test the performance of the gyroscope tracing systems.

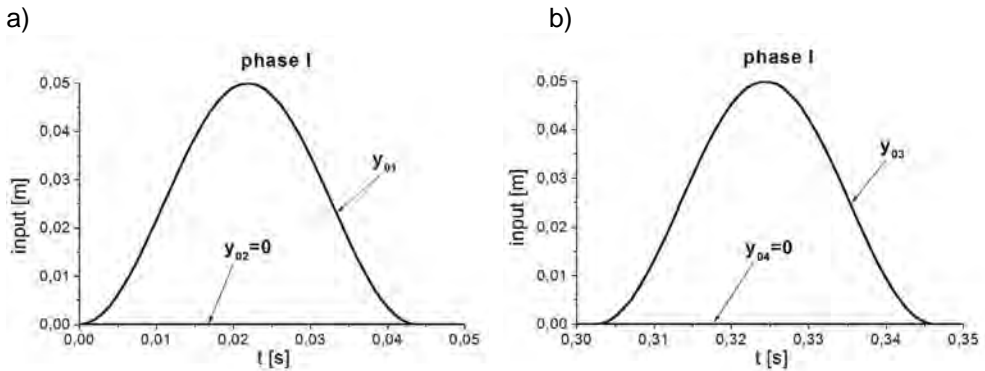


**Fig. 1.7.** Input from the side of the road affecting: a) front wheels of the vehicle, b) rear wheels of the vehicle

The launch of each of the four missiles significantly activates the linear vibration of the vehicle body. The missile movement along the launcher leads to the fast growth of the amplitude values of the course of the linear acceleration variability of the vehicle body Figure 1.8. On the basis of the acceleration variability course it is easy to determine the launching moments of the next missiles. The process of missile launching lasts about 0.1 s, and due to dynamic processes each missile stays at the launcher different amount of time. The moment of launching affects the characteristics of the initial flight parameters. The flight trajectory depends, among others, on these parameters values. The linear acceleration has the quality of continuous function in each motion phase.

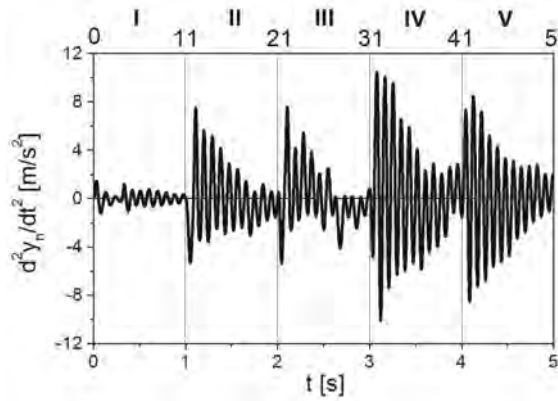


**Fig. 1.8.** Linear acceleration of the vehicle body

The standard deviation of the linear acceleration variation course of the vehicle body  $\ddot{y}_n$  equals  $\sigma_{\ddot{y}_n} = 2.8829 \text{ m/s}^2$ .

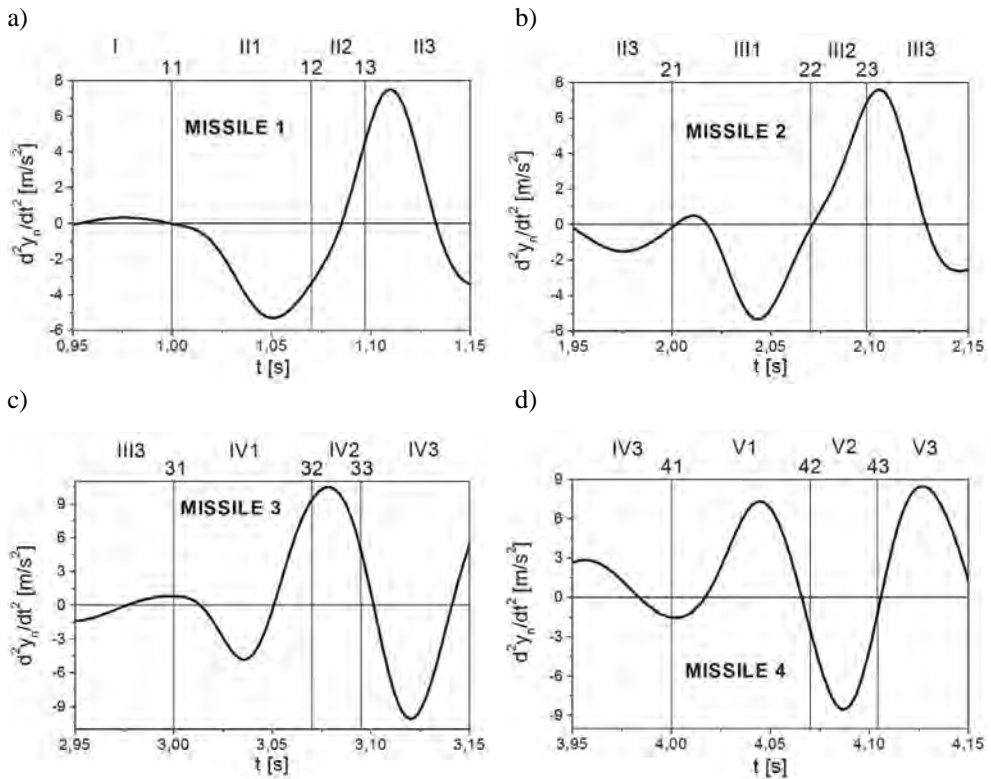


**Fig. 1.9.** Linear acceleration of the vehicle body while launching: a) missile 1, b) missile 2, c) missile 3, d) missile 4

Each missile leaves the guide with a different value of the linear acceleration of the body Figure 1.9. The moment the missiles leaves the launcher the initial flight parameters are determined, which are determined by the system dynamics and thus depend also on the reaction of the vehicle body to the propagation of disturbance.

The input coming from the road generates vibration of the vehicle body determined In phase I by the standard deviation with the lowest value Figure 1.10. The missile 3 launch In phase IV activates the body's vibration with linear acceleration, whose standard deviation is of the highest value.

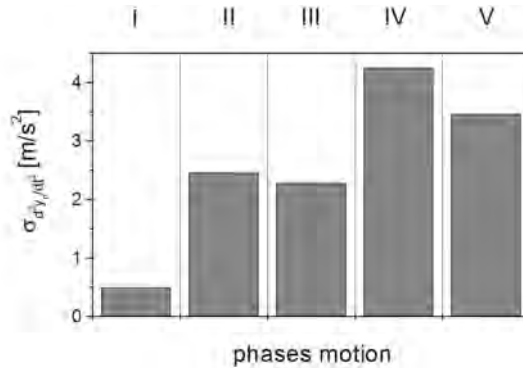


**Fig. 1.10.** Standard deviation of the linear acceleration variation course of the vehicle body

The launch of each of the four missiles significantly activates the vehicle body's angular vibration in the inclination motion, whereas in the tilting motion there is no such distinct regularity. The missile movement along the launcher guide leads to the rapid growth of the amplitude value (Fig. 1.11a) in the course of the angular acceleration variation of the body in the inclination motion. On the basis of the acceleration variation course it is easy to determine the moments of the next missiles launch. Whereas the missile launch is not distinguished clearly by a quick change of the course of the angular acceleration variation of the body in the tilting motion Figure 1.11b. It is difficult to determine the launching moments of the next missiles on the basis of the acceleration variation course.

The standard deviation of the angular acceleration variation course of the vehicle body is larger In the inclination motion than the tilting motion. It means that the body load caused by launching the missiles is larger in the direction of changing the  $\vartheta_n$  angle than in the direction of changing the  $\varphi_n$  angle.

The standard deviation of the angular acceleration variation course of the vehicle body  $\ddot{\vartheta}_n$  in the inclination motion equals  $\sigma_{\ddot{\vartheta}_n} = 2.8736$ .

The standard deviation of the angular acceleration variation course of the vehicle body  $\ddot{\varphi}_n$  in the tilting motion equals  $\sigma_{\ddot{\varphi}_n} = 1.6715 \text{ rad/s}^2$ .

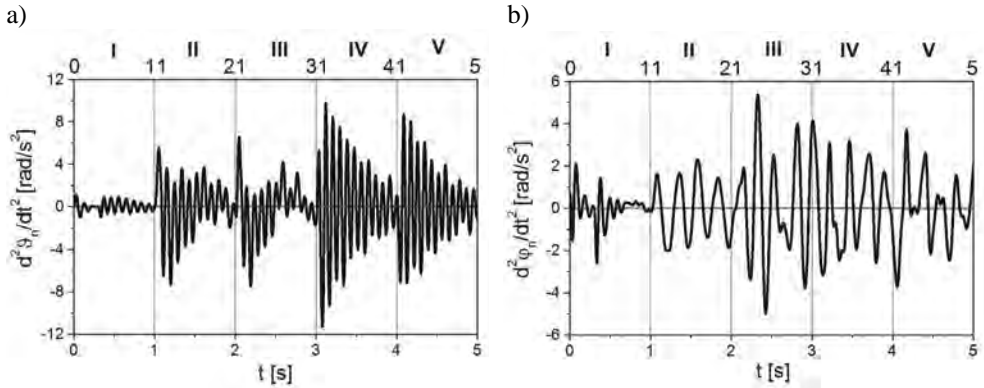


**Fig. 1.11.** Angular acceleration of the vehicle body: a) in the inclination motion, b) in the tilting motion

The acceleration in the inclination motion remains at the highest level after the launch of the 3 missile in the IV phase, whereas In the tilting motion after the launch of the 2 missile In III phase Figure 1.12.

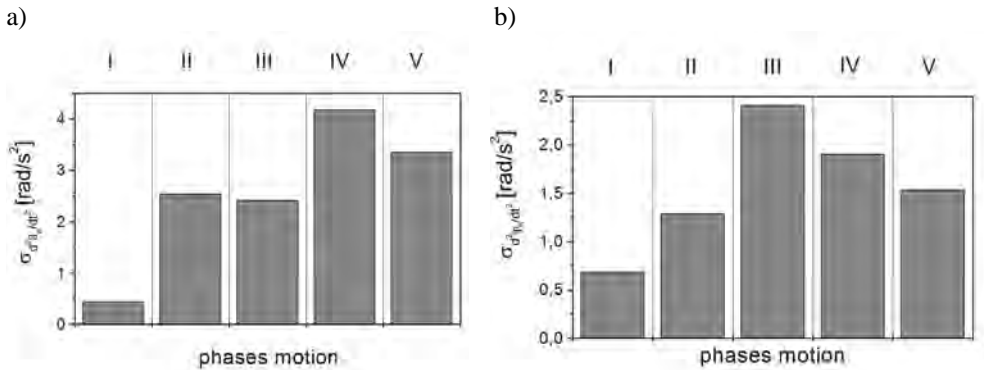


**Fig. 1.12.** Standard deviation of the angular acceleration variation course of the vehicle body: a) in the inclination motion, b) in the tilting motion

The presented acceleration variation courses characterizing vehicle's reaction to the input from the side of the road and caused by the launch of the four missiles have the quality of the continuous function in all the motion phases.

The article presents the variation courses of some physical variables characterizing the motor vehicle reactions to the selected launching conditions. The target performs a particular defensive manoeuvre. The vehicle does not perform the primary motion, but the external input from the side of the road is generated. The four missiles are launched at one-second intervals. Their movement along the launcher guide causes disturbance within the system.

The external input from the side of the road affects the right-side wheel. From the perspective of the determined analysis the extreme interactions are the most significant. In the studied case the input characteristic from the side of the road does not generate the maximal disturbance in the system. The input function is chosen in such a way as to allow for the evaluation of the individual anti-aircraft assembly elements vibration generated during the missile launch. The side-of-the-road input is transferred onto the human and it is felt as discomfort. The launch of the next missiles generates vibration of the individual inertia elements of the vehicle. The task of the vehicle is to isolate the people operating the anti-aircraft assembly and the launching missiles from the disturbance resulting from the road interaction.

The front and rear axle vibration are caused by the input from the side of the road and are transferred onto the other anti-aircraft assembly elements. The disturbance reaches the launcher turret and via the guides system affects the missiles movement. The acceleration fluctuation level of the turret is, in the studied case, lower than the level characterizing vibration caused by launching the next missiles. In real military operations, however, extreme side-of-the-road input conditions can be present, which will activate intensive turret vibration. This may lead to the negative parameters at the launch of missiles [5].

### **1.3. CONTROLLED GYROSCOPES FOR PRECISION DESTRUCTION MUNITIONS**

*Zbigniew Koruba*

In the last several decades, the gyroscope technology has undergone numerous transformations. State-of-the-art gyroscopes no longer resemble classic mechanical systems with a spinning rotor and suspension elements. In vibratory gyroscopes, for instance, the motion of the rotor can be in the form of progressive or angular vibrations. In vibratory hydrodynamic gyroscopes and vibratory magnetohydrodynamic gyroscopes, the rotor can be replaced by a spinning or vibrating fluid. In corpuscular gyroscopes, elementary particles – electrons, protons, neutrons, nuclei or atoms – are the carriers of angular momentum. In fact, all types of gyroscopes feature a carrier of angular momentum (kinetic moment).

In recent years, the basic definition of gyroscope as an instrument for measuring angular momentum or spin has been widened considerably. Nowadays, the term gyroscope is used for any device that allows autonomous measurement (no interaction with the environment) of the base rotation with respect to an inertial coordinate system. Examples include optical, laser, polarization-controlled gyroscopes, and ones based on de Broglie wave interference of elementary particles.

The name gyroscope was first used by the French physicist Foucault to describe a balanced high-speed rotor in a one- or two-axis Cardan suspension employed for

detecting and measuring the base rotation. The term was then used for all instruments with this property. The literature describes more than a hundred physical phenomena which can be applied to autonomously detect and measure a rotation by means of a gyroscope. Very few concepts, however, have been put to practice. Until recently, Foucault gyroscopes employing a rigid mechanical spinning rotor in a Cardan suspension were the most common. Now, hydrostatic (float) suspensions are frequently used to relieve the bearings. Equally popular are spherical gyroscopes with aerodynamic, electrostatic and magnetic suspensions. The latest models possess a cryogenic magnetic suspension, which makes use of superconductivity. An example of gyroscopes with no carrier of angular momentum are laser gyroscopes. Modern gyroscopic devices are frequently fitted on board of moving objects such as aircraft, ships, submarines, rockets and artificial Earth's satellites. Their task is to navigate the objects, establish their orientation with reference to some assumed systems, stabilize their motion with regard to the predetermined paths, automatically control these motions, and spatially stabilize the instruments on board.

Gyroscopic systems can be divided into spatial instruments for determining directions in a reference system (reference direction meters), and informative and measuring gyroscopes, which generate signals characterizing a measurement parameter of an object's motion (measuring gyroscopes). Group one includes gyrocompasses, vertical gyros, course gyroscopes, and free gyroscopes. The other includes gyroscopic tachometers (sensors of angular velocities), integrating gyroscopes, gyroscopic tachometers/accelerometers, and gyroscopic integrators of linear accelerations.

When fitted on board of a moving object, a gyroscope – an indicator of a reference direction – reproduces the spatial position of one of the reference axes of the coordinate system. It follows the direction of this axis via the spatial position of the gyroscope main axis. It is now easy and simple to measure one or two angles of deflection of the lenses with regard to the reference system in the form of angles of rotation of the object with respect to one or two gyroscope axes. The angles are measured in a natural scale with no dynamic errors.

Measuring gyroscopes are similar in the principle of operation and the method of input-to-output transfer to sensors used in the automation systems whose function is to convert electrical signals of various mechanical, thermal, and other non-electrical quantities. The coefficient of amplification of measuring gyroscopes, including instruments measuring the angle of the base rotation (integrating gyroscopes), is dependent on the instrument parameters. When designing measuring gyroscopes, engineers need to ensure the stability of dynamic parameters, particularly angular momentum, in order to achieve high accuracy of measurements. The output quantity of measuring gyroscopes is dependent not only on the value of the input quantity but also on the character of its changes. In other words, measuring gyroscopes are affected by dynamic errors.

The rapid development of gyroscopic systems has been due to the emergence of rocket and space vehicle technologies. Until recently, gyroscopic systems were divided into maritime and aerial. The systems in the first group were characterized



By omitting the moments of inertia of the gyroscope frames, we can write the equations describing the dynamics of an astatic gyroscope (with the centre of the gyroscope mass coinciding with the centre of the UAV mass) in the following form:

$$\begin{aligned} J_{gk} \frac{d\omega_{yg_2}}{dt} \cos \mathcal{G}_g + J_{gk} \omega_{gx_2} (\omega_{gz_2} + \omega_{gy_2} \sin \mathcal{G}_g) + M_k \sin \mathcal{G}_g + \\ - J_{go} \left( \omega_{gz_2} + \frac{d\Phi_g}{dt} \right) \omega_{gx_2} \cos \mathcal{G}_g + \eta_c \frac{d\psi_g}{dt} = M_c \end{aligned} \quad (1.12)$$

$$J_{gk} \frac{d\omega_{gx_2}}{dt} - J_{gk} \omega_{gy_2} \omega_{gz_2} + J_{go} \left( \omega_{gz_2} + \frac{d\Phi_g}{dt} \right) \omega_{gy_2} + \eta_b \frac{d\mathcal{G}_g}{dt} = M_b \quad (1.13)$$

$$J_{go} \frac{d}{dt} \left( \omega_{gz_2} + \frac{d\Phi_g}{dt} \right) = M_k - M_{rk} \quad (1.14)$$

where:

$$\omega_{gx_2} = P \cos \psi_g - R \sin \psi_g + \frac{d\mathcal{G}_g}{dt}$$

$$\omega_{gy_2} = (P \cos \psi_g + R \sin \psi_g) \sin \mathcal{G}_g + \left( \frac{d\psi_g}{dt} + Q \right) \cos \mathcal{G}_g$$

$$\omega_{gz_2} = (P \cos \psi_g + R \sin \psi_g) \cos \mathcal{G}_g - \left( \frac{d\psi_g}{dt} + Q \right) \sin \mathcal{G}_g$$

$J_{go}, J_{gk}$  – moments of inertia of the gyroscope rotor with respect to the longitudinal axis and the precession axis, respectively;

$\mathcal{G}_g, \psi_g$  – angles of rotation of the inner frame and the outer frame, respectively;

$M_k, M_{rk}$  – moments of the rotor driving force and the bearing friction force, respectively.

The control moments,  $M_b, M_c$  acting on the gyroscope fitted on board of a UAV, described by Eqs. (1.12)-(1.14), are:

$$M_b = \mathbf{\Pi}(t_o, t_w) \cdot M_b^P(t) + \mathbf{\Pi}(t_s, t_k) \cdot M_b^S \quad (1.15)$$

$$M_c = \mathbf{\Pi}(t_o, t_w) \cdot M_c^P(t) + \mathbf{\Pi}(t_s, t_k) \cdot M_c^S \quad (1.16)$$

where:  $\mathbf{\Pi}(\cdot)$  – rectangular pulse functions;  $t_o$  – start of space scanning;  $t_w$  – moment of target detection;  $t_s$  – start of target tracking process;  $t_k$  – end of target penetration, tracking and laser illumination.

The programmed control moments,  $M_b^p(t)$  and  $M_c^p(t)$ , ensure that the gyroscope axle moves with a desired motion; they are determined by solving the inverse problem of dynamics [17].

The tracking control moments,  $M_b^s(t)$  and  $M_c^s(t)$ , are responsible for making the gyroscope axis coincide with the line of sight [17].

The general concept of the control of a scanning/tracking gyroscope from board of an aerial vehicle is presented in Figure 1.14.

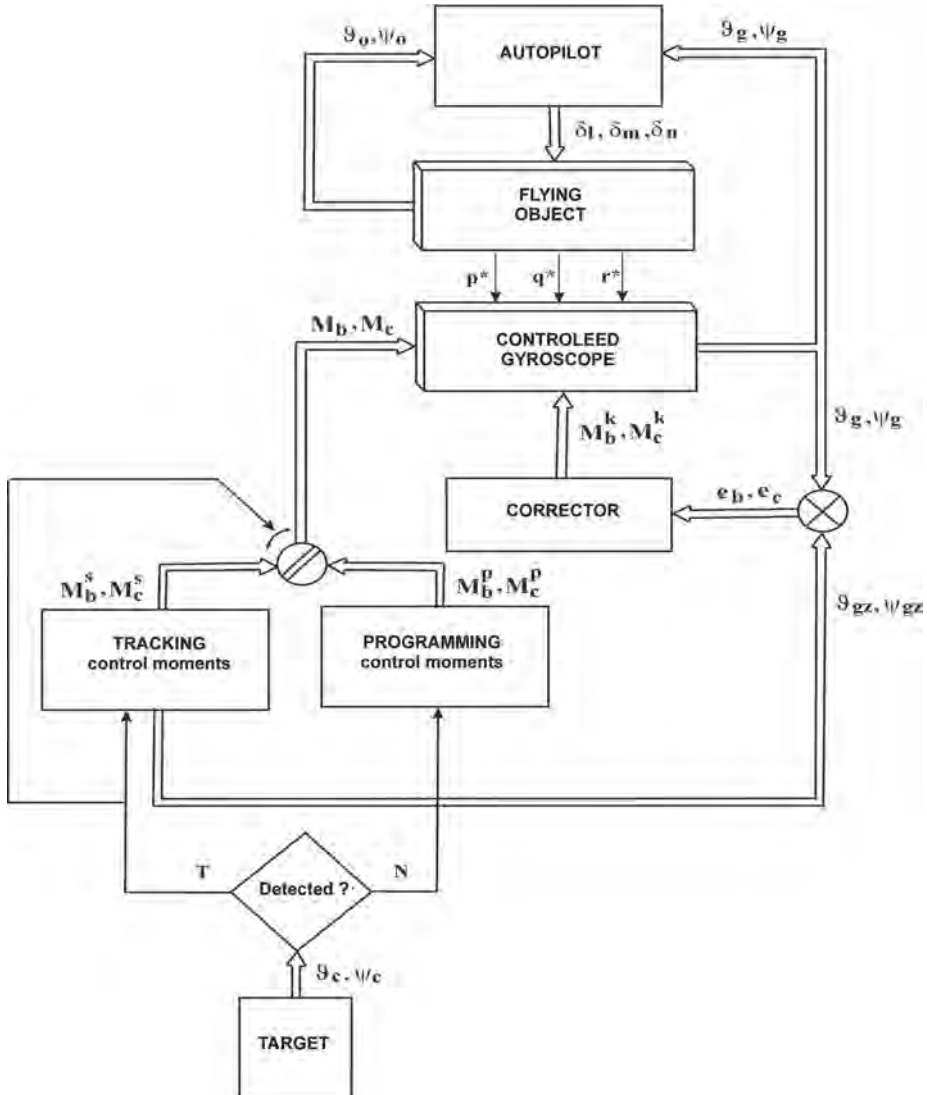


**Fig. 1.14.** Diagram of the target detection and tracking process using a gyroscope fitted on board of an aerial vehicle

During a target search controlled from board of an aerial vehicle (AV), the gyroscope axle should perform desired motions initiated by programmed control moments applied to the gyroscope frames. The optical system with a certain angle of view, which is fitted on the gyroscope axle, may detect a light or an infrared signal emitted by a moving object. It is thus necessary to properly select the kinematic parameters of the mutual motion of the AV board and the gyroscope axle to ensure the highest probability of target detection, tracking and, finally, attack.

After a target is located, i.e. a signal is received by the infrared detector, the gyroscope switches to the tracking mode. The spatial position of the gyroscope axis is then determined to enable missile guidance to the target, and the tracking control moments are applied to the gyroscope frames. Various disturbances, however, including the kinematic action of the vehicle board in the form of angular velocities  $P, Q, R$ , cause the occurrence of differences between the programmed motion and the real motion of the gyroscope axle. The automated gyroscope control system is equipped with a corrector, whose function is to reduce these differences. Basing on the motions of the gyroscope axle, the autopilot system generates control signals for the control surface displacements, which ensure that the motion is performed along the pre-determined vehicle flight trajectory.

### 1.3.2. A GYROSCOPE IN AN UNMANNED AERIAL VEHICLE

As a result of the rapid advances in the unmanned aerial vehicle technology, there is a need to conduct extensive research on gyroscopic platforms to be used for observation and tracking (Fig. 1.15). This section discusses the concept of target detection, tracking and laser illumination (TDTLI) on board of a UAV [18]. References [19, 20] provide a mathematical model of the process and the method for the generation of gyroscope control moments during target detection and tracking.

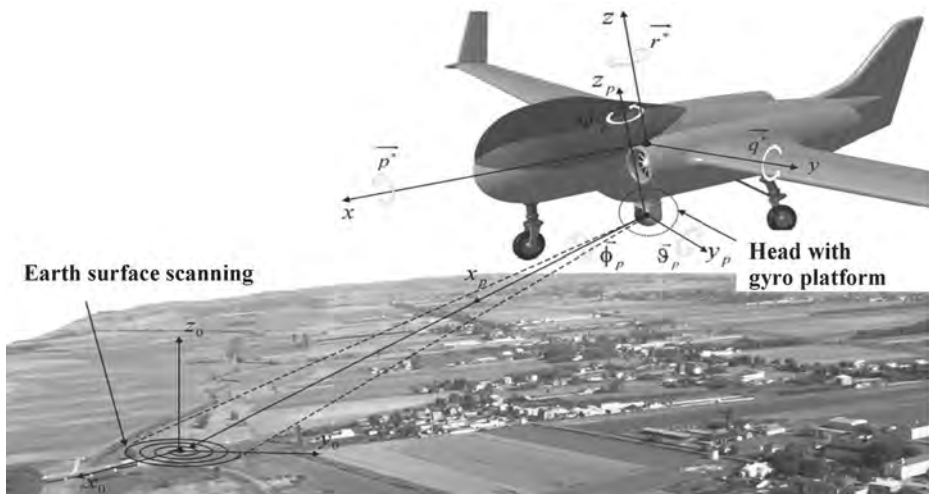


**Fig. 1.15.** General view of the Earth surface scanning by a UAV

The model can be used to analyze the dynamics of the controlled gyroscope as a drive unit of the TDTLI system, and the unmanned aerial vehicle itself, especially at the moment of target interception. The system is fully autonomous; it enables automatic changes in the UAV flight path after target detection. Optimal conditions for the tracking of an intercepted target are achieved by decreasing the angular deviations of the gyroscope axis.

It should be emphasized that the parameters of the gyroscope controller and the UAV autopilot need to be selected optimally due to a minimum time of the transition processes; otherwise, the intercepted target may escape out of the narrow seeker field of view.

Figure 1.16 shows example results of the simulation studies concerning the flight path of a hypothetical UAV and the gyroscope axis of the target detection, tracking and laser illumination system during the space scanning and the tracking of a moving ground target.

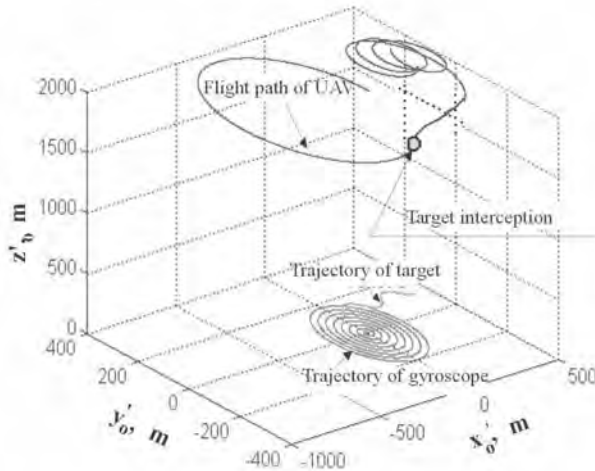


**Fig. 1.16.** Flight path of the UAV and the trajectories of gyroscope axis during the detection and tracking of a moving target

The theoretical considerations and the computer simulation results show that during Earth surface scanning from board of a UAV, the accuracy of the desired motion of the gyroscope axle is affected by the following factors:

- consistency of the initial conditions of the gyroscope axle motion with the pre-determined initial conditions. In order to bring the axis of the gyroscope to the proper starting position, additional time-independent controls need to be used [18];
- the values of the coefficients of the friction forces in the gyroscope frame bearings; although the coefficients play a positive role in the attenuation of the vibrations of the gyroscope axle, too large values cause the occurrence of additional displacements of the gyroscope axis, and, in consequence, a decrease in the precision with which the pre-determined motion is being performed;

- the effect of the non-linearity of the gyroscope motion model, which is particularly visible at considerable angular deflections of the gyroscope axis, for instance, during Earth surface scanning and target tracking.

The concept of a patrol flight by a UAV according to the program described in Refs. [18, 19], which involves Earth surface scanning by the TDTLI system around a circular cone has the following advantages:

- possibility to detect a target in an arbitrarily large area; the only limitation being the duration and range of a UAV flight;
- sufficiently precise scanning;
- simplicity of the Earth surface scanning program;
- relatively small values of the angles of deflection of the gyroscope axis from the vertical;
- possibility to change the UAV flight program after target detection, which helps ensure the most favourable conditions of target tracking by the TDTLI system; the smaller the angular deflections of the gyroscope axis, the higher the coincidence with the desired path; this causes that the probability of target escape out of the range of the field of view of the TDTLI system is reduced to a minimum;
- full autonomy of a UAV during search and laser illumination missions to reach a detected ground target; this prevents the ground control unit from being detected and destroyed by an enemy;
- operator's involvement in the control of a UAV can be limited only to cases when the vehicle completely gets off a course or a target moves outside a seeker field of view (wind gust, shell burst, etc.). It is essential that information about such events be automatically sent to the ground control unit so that the control of the UAV flight can be continued by an operator.

The basic drawback of this concept is that there needs to be constant cooperation between the automatic pilot and the target detection/tracking system. Another problem is the difficulty to determine the optimal program of the UAV flight and the Earth surface scanning that would allow immediate target detection. Moreover, it is necessary to develop a program for a minimum-time transition from the scanning mode to the target tracking mode, which would also ensure that the most favourite position for target laser illumination is reached in the shortest time possible.

The model of the UAV navigation and control describes a fully autonomous motion of a combat vehicle whose aim is first to detect and identify a ground target and then attack it. Prior to the attack, the target may be laser illuminated. The involvement of an operator in the control of a UAV can be limited only to cases when the vehicle completely gets off a course or the target moves outside a seeker field of view (wind gusts, missile bursts, etc.). It is essential that information about such events be automatically sent to the ground control unit so that the control of the UAV flight can be continued by an operator.

Further research including theoretical and computational investigations as well as simulation and experimental studies should aim at:

- determining an optimal program of a UAV flight,
- developing an algorithm for Earth surface scanning to ensure immediate detection of a target,
- developing a program for a minimum time transition from the programmed flight to the target tracking flight or self-guidance to a detected target according to the pre-determined algorithm.

### **1.3.3. A GIROSCOPE IN A GUIDED BOMB**

During a bomb attack, a target is usually known in the form of an image. It may emit electromagnetic waves or infrared radiation, but their intensity is usually too small to be useful. The target of a bomb attack should be visualized properly. At present, there are three groups of solutions applied in controlled bombs: laser-guided bombs, which require a separate source of laser illumination; self-visualization bombs with an in-built system for target visualization, and GPS-guided bombs. The major problem is always insufficient reliability and guidance precision owing to the minimum transition time and the flight path curvature. It is essential that a bomb be guided to a target at the right angle and along an optimal trajectory. A controlled gyroscope whose axis constitutes the line of sight for the bomb self-guidance system seems to be a suitable device. It should be noted that a gyroscope is not susceptible to disturbances and can replace a GPS system in emergencies.

A classic gyroscope suspended from a Cardan joint constitutes the executive unit responsible for controlling the line-of sight position in the coordinator of a self-guided aerial bomb. The optical system of the bomb head used for target detection and tracking is fitted on the gyroscope axle. Guidance precision is largely dependent on the gyroscope correction system, whose task is to minimize errors between the pre-determined motion, calculated immediately by the image analyzer, and the real motion. Gyroscope errors are associated mainly with the occurrence of friction in the suspension bearings and non-coincidence of the rotor mass centre with the point of intersection of the axes of the suspension frames. As a result, the gyroscope responds to the kinematic excitations of the gyroscope base, i.e. the angular motions and the changes in the linear velocity of an aerial bomb.

Following a bomb drop, the axle of the controlled gyroscope is put in the programmed scanning motion. Once a target is detected, the gyroscope axis is directed to the target and from now on it constitutes the line of sight (LOS), which is the reference for the bomb autopilot to follow the pre-determined guidance algorithm (Fig. 1.17).

A controlled gyroscope can be used in a TV-guided bomb used for destroying a ground target. The image of the target surroundings is transmitted to the operator's monitor via a telemetry channel or an optical fiber cable. The operator uses the monitor to determine the target to be attacked and, accordingly, the gyroscope axis. From now on, the bomb is guided automatically by following a pre-determined guidance algorithm.

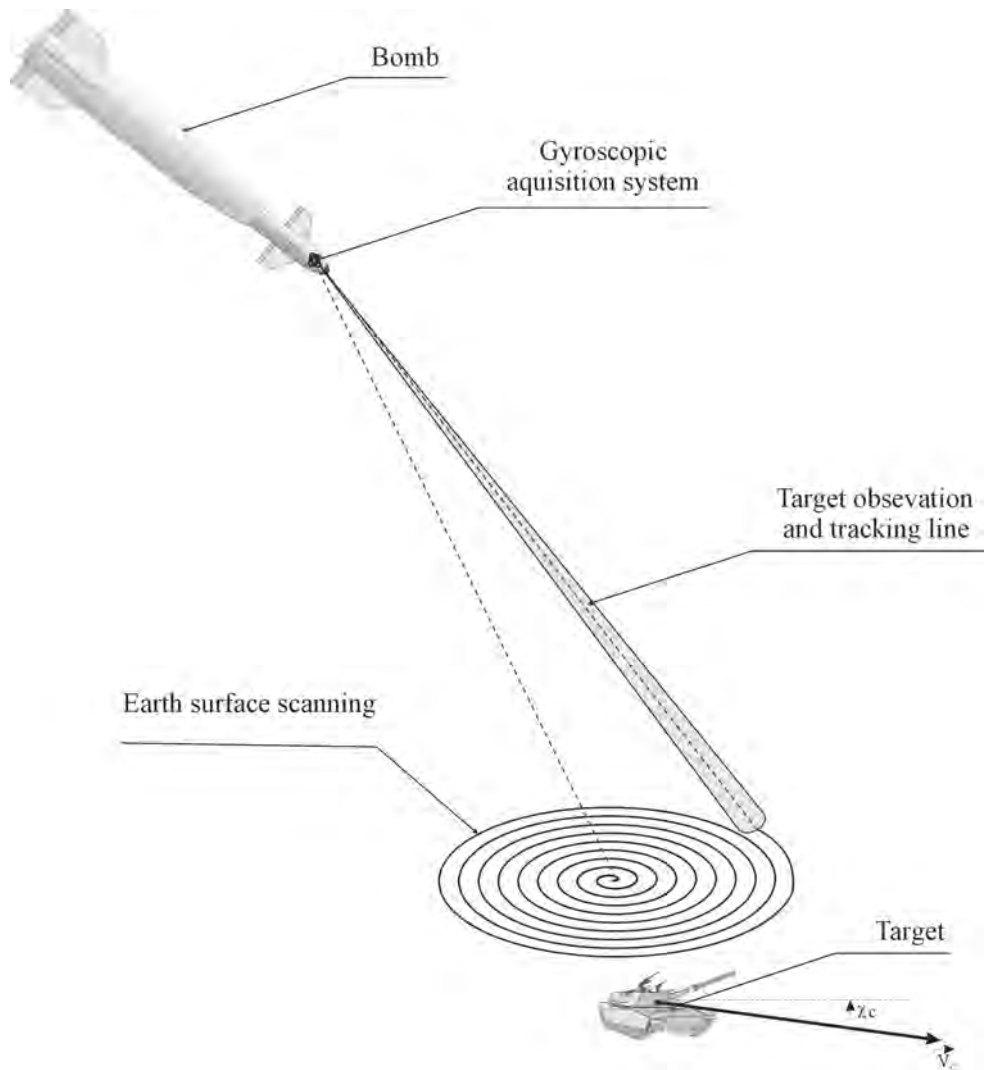


**Fig. 1.17.** General view of the Earth scanning and target tracking process for a guided bomb

Considerable changes in the parameters of the bomb flight occur at the initial phase of the self-guidance process, i.e. after the bomb is released, the target is detected or the guidance system switches on. The line of sight used as a reference for the guidance process may be determined with errors. If the gyroscope axis deflections from the pre-determined position are too large, then the target may escape out of the seeker field of view.

It is thus essential that the correction system and the gyroscope parameters be selected in an optimal way so that the influence of the base (aerial bomb board) vibrations on the position of the gyroscope axis can be minimized. Reference [17] proposes an algorithm based on the linear quadratic regulator (LQR) method.

Figure 1.18 presents the flight path of a bomb guided by using the analyzed gyroscope with an open-loop control system. The system, however, turns out to be insufficient to correctly operate, because the target is indicated inaccurately. This is particularly visible in the case of outer disturbances, as  $3.0 \text{ s} \leq t \leq 4.5 \text{ s}$ . The cause of the errors is the friction in the gyroscope suspension bearings. By applying an extra feedback in the automatic system for the control of the gyroscope axle motion with optimally selected parameters [18], it is possible to substantially improve the precision of determination of the line of sight (coincidence of the LOS with the gyroscope axis), and, accordingly, to minimize the differences between the pre-determined motions and the real motions of both the gyroscope and the guided bomb. This is well illustrated in Figure 1.19.

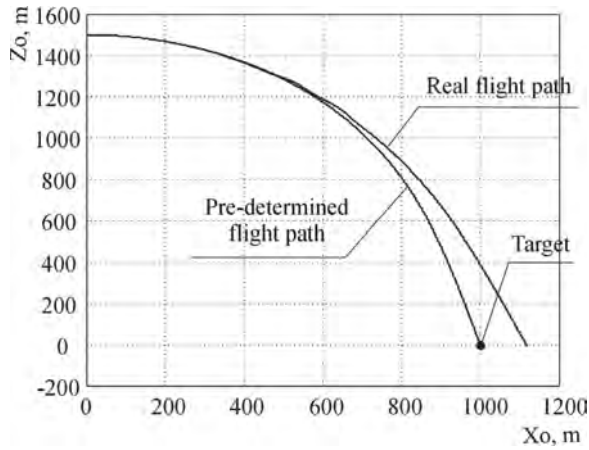


**Fig. 1.18.** Programmed and real bomb flight paths affected by disturbances before applying correction moments

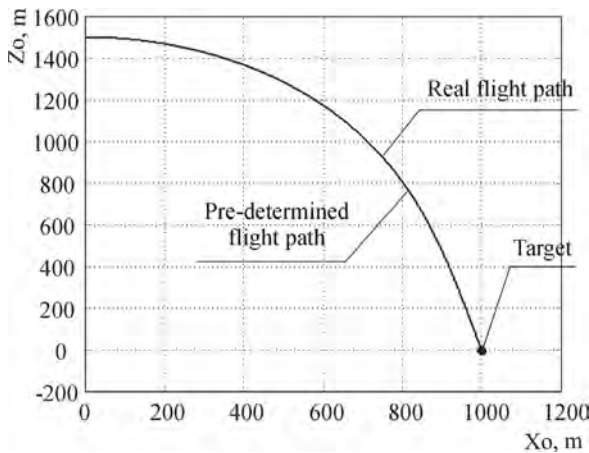
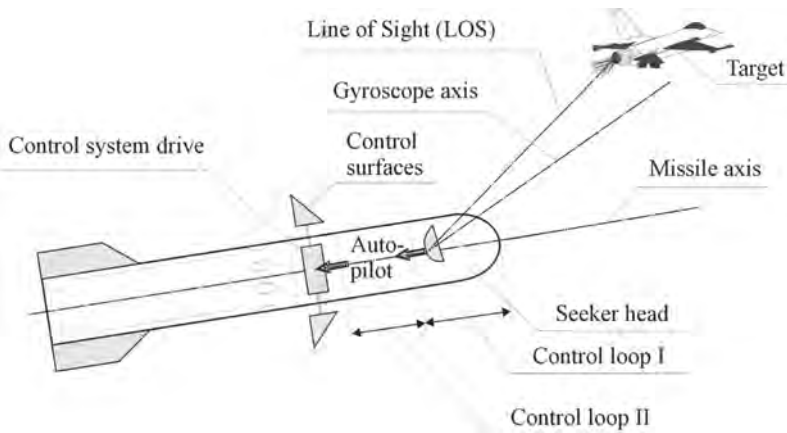


**Fig. 1.19.** Programmed and real bomb flight paths affected by disturbances, after applying correction moments

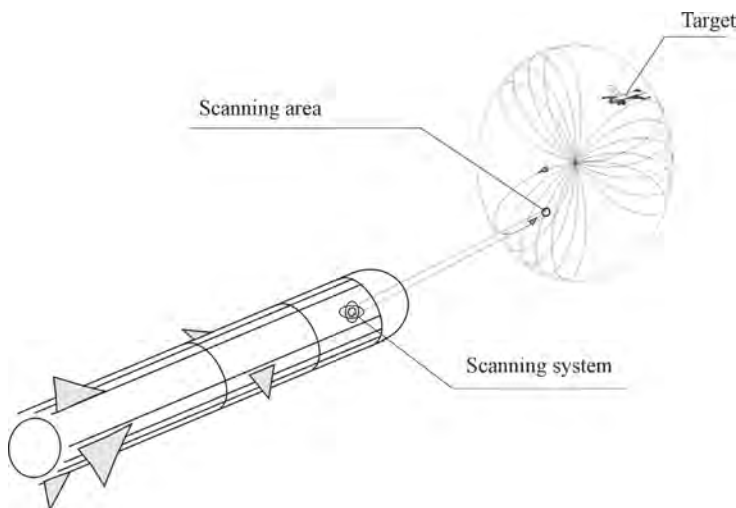
### 1.3.4. A GYROSCOPE IN A SELF-GUIDED MISSILE

Figure 1.20 shows a simplified diagram of the principle of self-guidance described in Ref. [17].

Modern target coordinators are equipped with scanning gyroscopes (Fig. 1.21), which allow immediate detection of an aerial target, even after missile launch [17, 18]. This solution makes a missile more resistant to such disturbances as decoy flares or false heat targets. In Ref. [18], this type of coordinator is driven by a flexibly suspended gyroscope, which is subjected to kinematic actions of the missile board (angular motions). The dynamic effects resulting from the gyroscope transition from the search mode to the tracking mode together with angular motions of the missile board may prevent the gyroscope axis from maintaining the pre-determined direction or moving with the pre-determined motion in space.



**Fig. 1.20.** Principle of self-guidance



**Fig. 1.21.** Self-guided missile with a scanning gyroscope

From the theoretical considerations and the numerical simulation studies it is clear that a space scanning/target detection system can be applied in a self-guided missile at the initial flight phase. By selecting optimal parameters of a gyroscope with a rotor flexibly mounted on the axle, which is a drive of the scanning coordinator, and by selecting optimal parameters of the missile control system, it is possible to reduce to a minimum the duration of the transition process [15], as soon as a target is detected. The optimal parameters of the gyroscopic system are responsible for stable, continuous target tracking, i.e. keeping a target in the field of view. This may be particularly important when a target is detected at a considerable angular deflection of the missile longitudinal axis from the line of sight. The optimal gyroscope controller minimizes also the deflection of the gyroscope axis resulting from the kinematic action of the missile board on the gyroscope suspension. Figures 1.22-1.24 show simulation results that confirm the above conclusions.

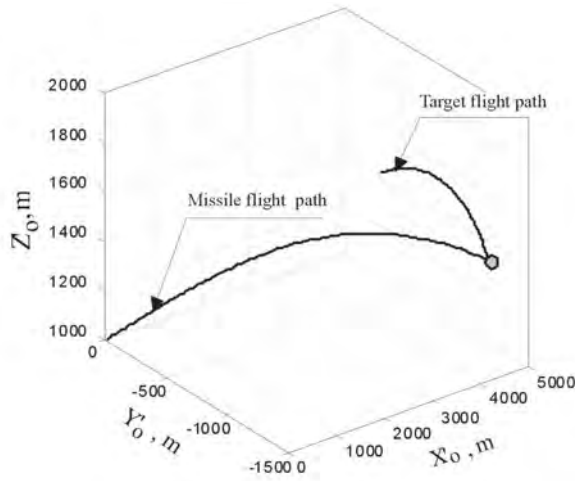


**Fig. 1.22.** The aerial target and the self-guided missile flight paths

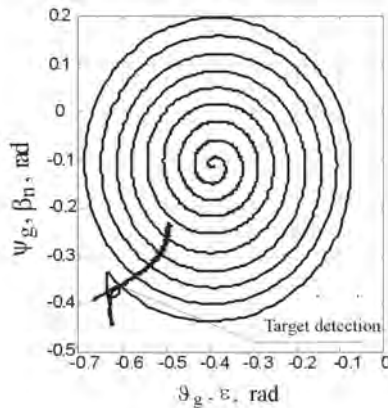


**Fig. 1.23.** The gyroscope axis and target axis paths during target detection and tracking – non-optimal parameters

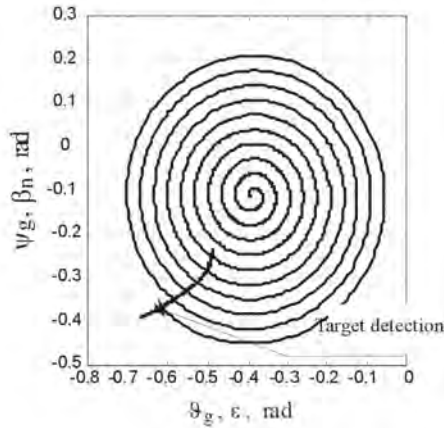


**Fig. 1.24.** The gyroscope axis and target axis paths during target detection and tracking – optimal parameters

It can be concluded that the most important factors affecting the precision of a controlled gyroscope used for the analyzed precision destruction munitions, i.e. self-guided missiles, guided bombs, and unmanned aerial vehicles, are: a) dry and viscous friction in the frame bearings, b) frame inertia, c) static and dynamic unbalance of the rotor with respect to the point of intersection of the frame axes – the centre of rotation, d) linear and angular accelerations of the base, e) flexibility of components, f) errors in the Cardan suspension, g) instability of the rotor drive, h) intersection of the frames at an angle other than the right angle, i) considerable angles and angular velocities of the deflection of the main axis of the gyroscope from the pre-determined direction, j) Earth's rotation.

Future research projects need to focus on solving the problem of the minimum-time between the position at the moment of target detection and the kinematic path calculated from the pre-determined flight algorithm. It is also necessary to conduct a study for an optimal design of the full control system taking account of the deformability of the units responsible for the execution of control in aerial vehicles.

## 1.4. THE MODEL OF BELLOWS SEAL WITH CONTROLLED CLOSING FORCE

*Czesław Kundera*

In the design of seals, it has been a rule to select parameters, such as mass, geometry of rings, initial load and dynamic coefficients of flexible attachment, to suit the operating conditions determined by the pressure and type (mainly properties) of

the sealed fluid and rotational speed of the shaft. Seals designed in this way are called **passive** or tuned to the desired frequency of excitation (i.e. rotational speed of the shaft) but they can become unreliable when, for example, the frequency coincides with the resonance frequency of the system.

A new method of improvement of reliability of seals involves an alteration of the seal construction by incorporating a system that will control force acting on the flexible mounted ring. These seals, being different from those applied so far, are generally called **active** or controlled ones.

The first suggestions to treat a seal as a controllable object were made were made in the experimental works [27-29] concerning mechanical contacting face seals. The investigations consisted in measuring the temperature or leakage rate and controlling the change in the force by applying an appropriate load on the sealing rings. Reference [30] reviews the most interesting theoretical as well as experimental findings in this field. An interesting experiment was described in Refs. [31, 32], where the clearance height was controlled by means of an electropneumatic transducer.

This paper discusses the construction of a contacting face seal with flexible bellows. An important operating parameter of such a seal is the value of the force closing the rings (i.e. value of contact pressure) dependent on the axial preset of the elastic element (i.e. bellows), medium pressure and rotational speed of the shaft. Therefore, the seal can operate properly only if the fluid pressure has the same value as that assumed in the constructional calculations.

One of the methods used for extending the range of operational parameters of self-regulated contacting seals is modifying the geometry of seal rings or the structure of their carrier. The modification usually requires applying an extra elastic element flexibly mounted in the ring carrier that will be responsible for regulating the value of contact pressure (and consequently the friction force) if there is any sudden increase in the fluid pressure above the permissible value.

A new qualitative method of increasing the reliability of contacting seals is applying in their construction a control system regulating the force closing the rings. An example of an active contacting face seal is discussed in this work.

#### **1.4.1. DESCRIPTION OF THE SEAL**

The construction of a contacting face seal with flexible bellows analysed in the paper is shown in Figure 1.25.

In real seal constructions, the flexible bellows – 3 are made of plastic or thin metal sheet. They function as an element pressing the seal rings. The seal ring – 2 is mounted flexibly enough to enable axial or angular (i.e. in the direction of the sliding velocity) displacement. The ring – 1, on the other hand, is fixed rigidly on the rotating shaft and represents its motion. For the purpose of this analysis it is assumed that the shaft has a defect in the form of a periodic displacement along the axis of rotation.

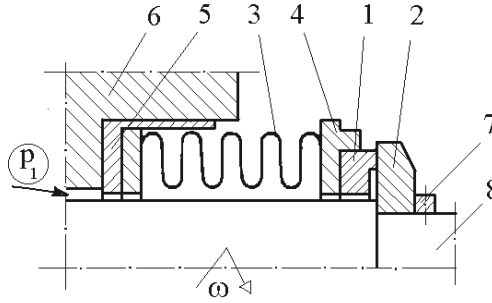


**Fig. 1.25.** Scheme of a contacting face seal: 1 – seal ring (stator), 2 – mating ring (rotor), 3 – bellows, 4 – seal ring carrier, 5 – bellows carrier, 6 – gland, 7 – clamping ring, 8 – shaft,  $p_1$  – pressure of sealed fluid,  $\omega$  – rotational speed of the shaft

### 1.4.2. DYNAMIC MODEL AND EQUATIONS OF MOTION

The analysis of seal dynamics is replaced by the analysis of the motion of the flexibly mounted ring, being dependent on the motion of the mating ring. The kinematics of the seal rings discussed above shows that the ring – 2 (Fig. 1.25) has two degrees of freedom.

The two-degree-of-freedom dynamic model, where the ring – 1 has a mass  $m$ , is suspended on linear stiffness and damping elements (see Fig. 1.26). The axial motion of the flexibly mounted ring – 1 denoted by the normal co-ordinate –  $y$ , is excited by an axial displacement of the mating ring. The angular motion, however, denoted by the tangential co-ordinate –  $x$ , is caused by the occurrence of friction force.

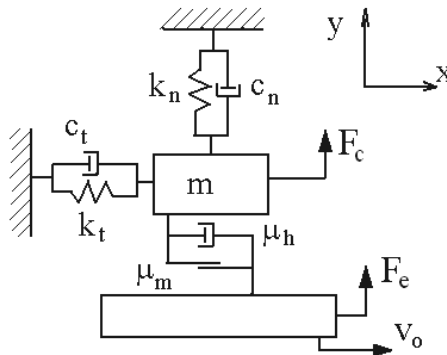


**Fig. 1.26.** Dynamic model of an active contacting seal (with control force)

The equations governing the motion of flexibly mounted ring shown in Figure 1.26 are expressed as:

$$\begin{aligned} m\ddot{x} + c_t\dot{x} + k_t x &= T(t) \\ m\ddot{y} + c_n\dot{y} + k_n y &= F_e(t) + F_c(t) \end{aligned} \quad (1.17)$$

where:  $m$  – mass of the ring;  $c_t, c_n$  – coefficients of tangential and normal damping;  $k_t, k_n$  – coefficients of tangential and normal stiffness;  $T(t)$  – friction force,  $F_e(t) = \xi k_e \sin pt$  – axial excitation force;  $F_c(t)$  – control closing force.

Introducing the following nondimensional transform:

$$\begin{aligned}\bar{x} &= \frac{x}{h_o}; \quad \bar{y} = \frac{y}{h_o}; \quad \tau = \omega_n t; \quad \omega_n = \sqrt{\frac{k_n}{m}} \\ \dot{\bar{x}} &= \omega_n h_o \bar{x}'; \quad \ddot{\bar{x}} = \omega_n^2 h_o \bar{x}'' \\ \dot{\bar{y}} &= \omega_n h_o \bar{y}'; \quad \ddot{\bar{y}} = \omega_n^2 h_o \bar{y}''\end{aligned}\tag{1.18}$$

where:  $h_o$  – nominal film thickness,  $\omega_n$  – natural frequency for normal motion.

Substituting the expressions (1.18) in Eq. (1.17), leads to the following set of governing equations:

$$\begin{aligned}\bar{x}'' + \psi_t \bar{x}' + \kappa \bar{x} &= \bar{T}(\tau) \\ \bar{y}'' + \psi_n \bar{y}' + \Omega_n^2 \bar{y} &= A \sin \nu \tau + \bar{F}_c\end{aligned}\tag{1.19}$$

where:  $\Omega_n^2 = \frac{k_n}{m \omega_n^2} = 1$ ;  $\Omega_t^2 = \frac{k_t}{k_n} = \kappa$  – dimensionless normal and tangential natu-

ral frequency;  $\psi_n = \frac{c_n}{\sqrt{m k_n}}$ ;  $\psi_t = \frac{c_t}{\sqrt{m k_n}}$  – dimensionless normal and tan-

gential damping;  $A = \frac{\xi k_e}{h_o k_n}$ ;  $\nu = \frac{p}{\omega_n}$  – dimensionless amplitude and fre-

quency of external harmonic excitation;  $p$  – frequency of excitation;

$\bar{T}(\tau) = \frac{T(t)}{h_o k_n}$  – dimensionless friction force.

Friction force in Eq. (1.18) is given as:

$$\bar{T} = \mu |\bar{W}(\tau)| \operatorname{sgn}(V_{rel})\tag{1.20}$$

where:  $\mu$  – friction coefficient;  $V_{rel} = \bar{v}_o - \dot{\bar{x}}$  – dimensionless relative sliding velocity;

$\bar{v}_o$  – dimensionless sliding velocity;  $\bar{W}(\tau)$  – loading force consisting of two components:

$$\bar{W} = \bar{W}_o + \bar{W}_{dyn} = \bar{W}_o + \bar{y}''(\tau)\tag{1.21}$$

where:  $\bar{W}_o$  – the static one, which results from the axial preset of the elastic element (bellows);  $\bar{W}_{dyn}$  – the dynamic one caused by normal displacements of the ring.

Friction force modelled (determined) in this way (see Eq. (1.20)) is the element coupling the two derived equations of motion (1.19). To describe coefficient of friction in the contact area of the face rings surfaces, the empirical model proposed by D.P. Hess [28] was used. In this model, the coefficient of friction is determined by two components containing the Stribeck modified parameter:

$$\mu = \mu_m + \mu_h = \frac{\mu_b}{1 + \frac{C_1 \eta^2}{W} V_{rel}^2} + \frac{C_2 \eta L}{W} V_{rel} \quad (1.22)$$

where:  $\mu_b$  – coefficient of friction in the boundary regime;  $C_1, C_2$  – empirical constants;  $W$  – normal load;  $V_{rel}$  – relative sliding velocity;  $\eta$  – fluid viscosity;  $L$  – contact length.

The first component of relation (1.22) describes mixed friction –  $\mu_m$ , whereas the other represents hydrodynamic (viscous) friction –  $\mu_h$ . The value of friction force depends on the relative sliding velocity, medium properties and loading force –  $W$ . In our further studies, the latter will be time-dependent.

In Figure 1.27, one can see examples of characteristics for the coefficient of friction in the function of relative sliding velocity calculated from relation (1.22) for constant values of the parameters  $C_1$  and  $C_2$  defined in Ref. [28]. The non-linear characteristics of friction force given in Figure 1.27 have minimum friction force at the boundary sliding velocity. It is clear that for relative sliding velocity smaller than the boundary value (the falling trend in the characteristics shown in Fig. 1.27), energy is supplied to the vibrating system, which leads to the occurrence of self-excited vibrations.

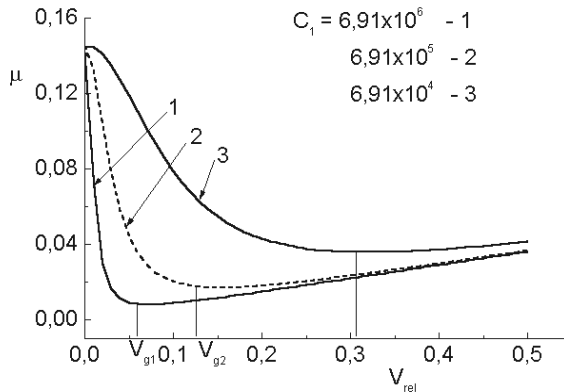


**Fig. 1.27.** Effect of parameter  $C_1$  on friction-velocity curves for  $W = 70$  [N]

In the model of the active seal presented in Figure 1.26, it is assumed that the controlling force should be dependent on the parameters of the tangential motion of the ring. Thus, the mathematical model of an active seal consists of the equations

of motion (1.18) conjugated with each other by means of two components: non-linear friction force and controlling force. Figure 1.28 shows a scheme of the proposed system for the control of the force loading the rings.

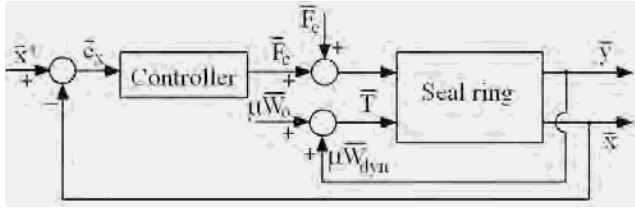


**Fig. 1.28.** Scheme of the control system

For this purpose, a classic linear controller was applied (1.21). The tangential displacement of the ring is the feedback signal in the control system (Fig. 1.28), while the normal displacement of its flexible carrier constitutes the controlling signal. The aim of the control system is to minimize tangential oscillations of the flexibly mounted ring when its contact with the mating ring is maintained.

$$F_c = \lambda_1 e_x + \lambda_2 \dot{e}_x + \lambda_3 \int e_x(\tau) d\tau; \quad (1.23)$$

$$e_x = \bar{x}^* - \bar{x}$$

where:  $\lambda_1, \lambda_2, \lambda_3$  – parameters of the controller;  $\bar{x}^*$  – desired tangential displacement;  $e_x$  – error.

The so obtained model was then numerically solved and a set of control parameters  $\lambda_1, \lambda_2, \lambda_3$  was achieved. To establish their values well known gradient method, valid for the assumed integral criterion.

### 1.4.3. ANALYSIS OF THE MODEL AND EXAMPLES OF SOLUTIONS

The controllability was checked only in the area of unstable vibrations observed when the relative sliding speed is smaller than the boundary value. In the characteristic of friction force (Fig. 1.27), it is the area with a negative inclination angle of the tangent at a given operating point determined by the desired sliding speed.

To fulfil the condition of maintaining the contact of the seal rings, it is necessary that the closing force be always positive. This requirement is of particular importance when excitation frequency coincides with resonance frequency. The numerical solution of the equations of motion (1.19) was checked for the following parameters:  $\psi_n = 3.53 \times 10^{-3}$ ;  $\psi_t = 1.76 \times 10^{-3}$ ;  $\kappa = 5 \times 10^{-3}$ ;  $A = 0.1$ ;  $\nu = 1$ ;  $\bar{\lambda}_1 = 0.25$ . Figure 1.29a and 1.29b show results of numerical integration of the equations of motion for different values of the initial tangential displacement of the flexible ring. In the calculations, it is also assumed that the frequency of axial vibrations of the mating ring constituting additional excitation coincides with the frequency of free vibrations of the flexible ring.

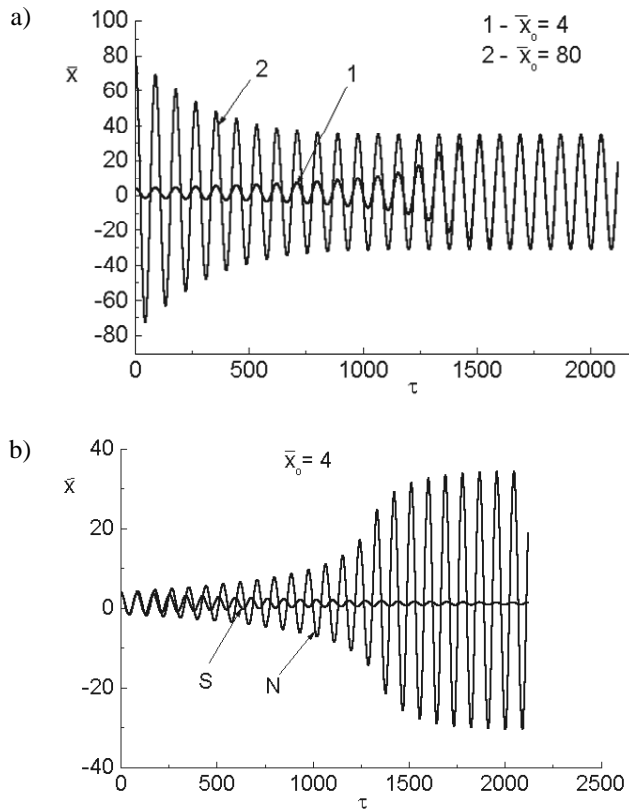


**Fig. 1.29.** Variation of the dimensionless tangential displacement –  $\bar{x}$  with dimensionless time –  $\tau$  for: a) two initial excitation: 1 –  $\bar{x}_0 = 4$ ; 2 –  $\bar{x}_0 = 80$ ; b) initial excitation  $\bar{x}_0 = 4$ , without control system – N and with control system – S

As can be seen in Figure 1.29a, the amplitude of tangential displacements of the ring stabilizes and reaches the boundary value after a short period of time regardless of the initial value of excitation. The application of the controlling signal (Fig. 1.29b) causes a quick decrease in the amplitude and stabilisation of vibrations. The changes in the force closing the seal rings shown in Figure 1.30 are of some interest too.

One can see that the closing (or loading) force during the operation of the rings remains positive, which points to the fact that the contact of the seal rings is maintained. It should be noted that at the same time there is an increase in the frequency of changes of the closing force. In this way, an additional aim of the usability of the control system is achieved. The parameters assumed for the calculations, especially the low value of the relative sliding velocity, show that the analysis concerns seals used in slow-speed fluid-flow machine. One should note that a small sliding velocity can be observed also under changeable operating conditions, e.g. when a machine is switched on or off.

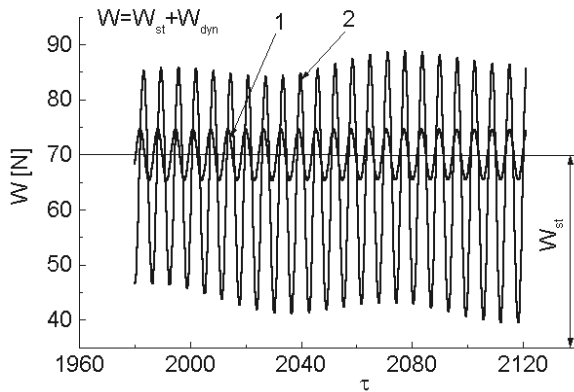
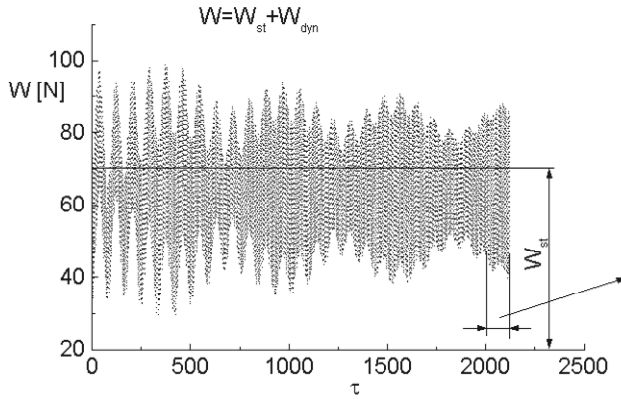


**Fig. 1.30.** Variation of the closing normal force with time: 1 – without control system; 2 – with control system

The results of numerical calculations confirm that it is possible to control tangential displacements of the flexibly mounted ring by adjusting the pressure force to maintain the contact of the seal rings. Therefore, it is possible to design reliable seals for optimal load of the rings. The presented digital calculations should be treated as an introduction to further theoretical analyses followed by experimental research. The theoretical mathematical model with non-linear friction force discussed in this paper can be linearized and on the basis of its analytical solution the stability analysis can be carried out.

## 1.5. ANALYSIS OF INJECTION PROCESS IN DIESEL ENGINES

*Andrzej Bąkowski, Leszek Radziszewski*

The fuel injection and atomization in the combustion chamber are dependent not only on their physical properties but also on the injection pressure and needle lift. By studying their characteristics, one is able to determine their effect on the unit amount of injected fuel for one cylinder and for one cycle of engine work as well the rate of delivery. The knowledge of the parameters is important while designing an injection system and an engine control system, and also while diagnosing the engine performance. Since the components and assemblies of an injection system are complex in design and their wear resistance may be different, it is necessary to develop models of injectors together with methods for their control [47]. The literature dealing with conventional injection systems, in which the amount of fuel and the injection advance angle are adjusted mechanically, is rich, this testifying to good recognition of the injection-related phenomena. Although the knowledge may seem sufficient, the injection process is still being investigated. Current studies concern, for example, the effective performance of electronically controlled injection systems, or the application of elements of conventional injection systems to modern pump-injectors or the so called common rail direct fuel injection systems. Moreover, it is desirable that the diagnosing of the injection phenomena be simple, immediate and reliable.

Engines with mechanically controlled injection pumps are commonly used in off-road vehicles, which can operate under extremely difficult conditions. An advantage of such pumps is that various fuels, including cheaper biofuels, can be used. A drawback, however, is that they do not cooperate with exhaust gas recirculation systems. Because of their high reliability, mechanically controlled injection systems are modernized by applying, for instance, electromagnetic valves instead of pressure valves. Changes in the injection parameters are made basing on the signals of the engine rotational speed, piston top dead centre, load, fuel temperature or pressure of the environment.

References [48] and [49] analyze the displacements of the piston and the pressure in the gap between the piston and the cylinder for a test injection pump to be used for a low-speed marine engine. The distribution of pressure in the injection pump was plotted against angular positions of the piston. It was found that the piston moved transversely around a closed circumference. In Ref. [39], pressure in the injection duct was calculated using the method of characteristics. Reference [50] discusses the results of measurement of fuel pressure in the injector port and the needle lift applied to calculate injection parameters. The relationship between the length of the injection duct and the injection parameters was studied in Ref. [44]. The results indicate that the length and bending angle of the duct affect mainly the occurrence and volume of the so called post-injection. The pressures in the pressure chamber, the nozzle valve, and the injector inlet were analyzed in Ref. [45]. Of interest were also the needle lift

and cavitations wear. Reference [46] deals with the calculation of injection parameters using measured pressure in the injector port, the needle lift and the active cross-section of the nozzle outlet under cavitations conditions. Reference [38] describes dilatometric studies of nozzles. The results were applied to assess the suitability of materials used for their production. It was found that the deformations of the injector body originating from fuel pressure combined with the assembly and thermal deformations may lead to needle blockage or loss of free movement. The distribution of pressure along the length of the annular slot for different imperfectly made needles and orifices in the nozzle body was analyzed in Ref. [36]. Of interest was also the action of forces in the nozzle causing the motion of the needle in directions transverse to the axis of symmetry.

In conventional injection systems, the pressure of fuel is usually measured in the fuel supply port, i.e. at the joint with the high pressure duct, the so called injection pressure. The measurements can be conducted under laboratory conditions using a test bench or during engine operation. Measuring pressure at other points is technically difficult and even impossible without sophisticated apparatus. Such measurements were described in Refs. [40, 51] and some of the results will be used for this analysis. The pressures in the injector port, the pressure chamber, and the nozzle valve differ in instantaneous values. An increase in pressure is reported to be different at different points, with the lowest in the pump, becoming higher in the injector port, and reaching the highest value in the nozzle valve. In the W1B01 injector and the D1LMK 140/2 nozzle, for example, the maximum pressure in the port and in the pressure chamber at the rotational speed of the injection pump shaft of 600 rev/min, was 38 MPa and 36.5 MPa, respectively. The pressure in the valve at the same rotational speed was 32.8 MPa. Similar drops in fuel pressure occurred at other speeds [51]. It can be assumed that before the fuel is injected, and while the pressure in the chamber is equal to that of the atmospheric air, the nozzle is under the action of a force of 350 N exerted on the needle so that it is pressed against the cone seat. The force originates from the initial deflection of the nozzle spring used to control the opening pressure of 17 MPa. As the fuel pressure in the nozzle chamber increases, there occurs a gradual release of the needle from the seat. The initial displacement of the needle of approx. 7  $\mu\text{m}$  recorded by means of inductive motion sensors is caused by the removal of the initial stresses and strains affecting the seat and the injector needle. The moment corresponds to the start of the dynamic opening of the nozzle. Once the needle is lifted off the nozzle seat, the fuel flows out of the pressure chamber into the nozzle valve, which is accompanied by an instantaneous decrease in pressure in the pressure chamber. It is clear that the start of the needle lift measured by means of an inductive sensor does not coincide with the dynamic opening of the nozzle needle. In a similar way, the moment defining the start of the needle opening, is not always coincident with the start of fuel delivery. Fuel injection begins with an increase in the fuel pressure in the needle valve. It is commonly assumed that the position of the first local maximum pressure measured in the injector port determines the dynamic opening of the nozzle

needle, the timing (start of injection) and the injector needle lift. Experimental results, however, do not confirm the hypothesis. Furthermore, the pressure at this point does not correspond to the pressure of the dynamic opening. The dynamic pressure is higher than the static pressure, and this is due to the fact that the friction forces and the inertia of the needle need to be overcome. By comparing the experimentally determined fuel injection rate in the pressure chamber and in the injector port, one can conclude that the amount of injected fuel is different in each case. The difference between the calculated amounts of injected fuel is approx. 10%, which is also dependent on the rotational speed of the shaft of the injection pump. The size of the nozzle gap (in a cross-section) changes during the injection process due to elastic deformations of the nozzle body. Deformations may reach up to 30% of the radial spray. The analysis of the fuel pressure distributions in the cross-sections perpendicular to the axis of symmetry of the needle shows that the needle moves transversely as well as longitudinally. The production accuracy of the cone seat and the needle cone, as well as the area of contact between the needle and the cone affect the process of determination of a skewed or eccentric position of the needle relative to the body orifice before or after injection. It is probable that the position of the needle while it reaches the bumper is the same as that when it leaves the seat. During the subsequent impinging, the needle is pressed against the generatrix of the body orifice or even rotated about its own axis due to non-symmetrical distribution of pressure in the gap. As a result, the needle settles in the seat, where it assumes another instantaneous inclination of the axis. Another factor affecting the position of the needle is also a nonsymmetrical distribution of pressure in the fuel duct between the cone and the leading part to the needle. In non-conventional, for example, common rail injection systems, the transverse motions of the needle are eliminated by changes in the design and production stages [51].

The aim of the study was to analyze the changes in the pressure and motions of the needle of injector in order to determine their relationships with some of the processes and phenomena occurring in the injection system and the combustion chamber of the diesel engine. Analytical studies were conducted using the results of the experimental research to achieve the following objectives: to calculate the pressure in the injector valve, to determine the displacement of the injector needle, to define the effect of the injection pressure on the fuel flow parameters and to determine the non-repeatability of the unit amount of injected fuel for one cylinder and for one cycle of engine work.

### **1.5.1. EXPERIMENTAL RESULTS**

The experimental studies [41] were carried out at a laboratory facility consisting of a Perkins AD3.152 UR three-cylinder diesel engine, a hydraulic brake and a control panel. The fuel used was diesel oil. The injection pressure ( $p_w$ ) was measured at the injector port by means of piezoelectric transducers, while the needle lift was determined using an inductive displacement sensor. The pressure and the needle lift

were recorded in the function of the crank angle ( $\alpha$ ) expressed in degrees ( $^\circ$ ). The angle of rotation was registered using a rotary-pulse transducer and a system for marking and synchronizing the crankshaft position. The measurements were conducted for an engine operating at full load at the crankshaft speed ( $n$ ) ranging from 1000 rev/min to 2000 rev/min. The pressure values were registered every 1.4 degrees of the crank angle (512 measurements per one cycle). Fifty measurements were taken for each position of the crankshaft. The tests were performed using series-produced injection systems. The results illustrating the repeatability of values were described in Ref. [35]. Figure 1.31 illustrates averaged values of the injection pressure, the combustion pressure, and the displacements of the injector needle at  $n = 1800$  rev/min in the whole range of the crank angle for one cycle of diesel work.

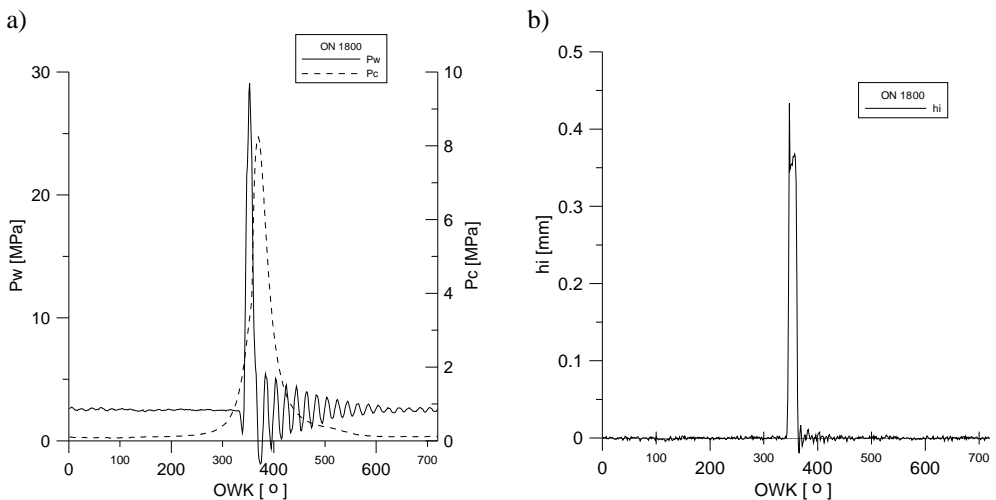


**Fig. 1.31.** Averaged experimental values obtained at  $n = 1800$  rev/min: a) injection and cylinder pressure, b) injector needle lift

As can be seen from Figure 1.31a, the fluctuations in the injection pressure in the final stage of injection confirm the oscillatory character of the process.

The mathematical and simulation models of the injector work were developed using the MATLAB/SIMULINK software. By developing a structural model of an injector, one will be able to describe its operation and then calculate the parameters and coefficients necessary for the process simulation. The model required formulating analytical relationships and using experimental data [41, 42]. A schematic cross-section of the injector with a nozzle is shown in Figure 1.32. The injector features a classic design with a rod and a spring fitted to the upper part of the body. It was selected to act as a representative sample, because the design is typical of high-speed direct-injection diesel engines. The injector opening pressure was 17 MPa.

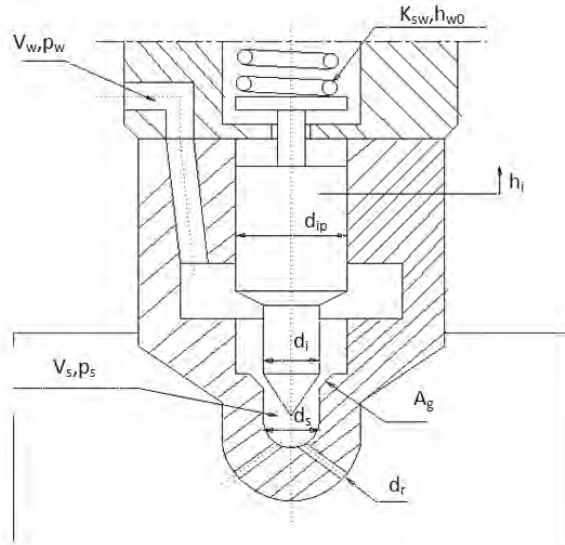


**Fig. 1.32.** Schematic cross-section of a multi-orifice injector [42];  $p_w, p_s, p_k$  – pressures in the injection duct, the nozzle valve, and the cylinder, respectively;  $V_w, V_s$  – volumes of the chamber and the valve, respectively,  $A_g$  – cross-sectional area of flow through the seat,  $h_i$  – injector needle lift,  $d_{ip}, d_i$  – diameter of the needle,  $d_r$  – diameter of the orifice.

### 1.5.2. A MATHEMATICAL MODEL OF THE INJECTION PROCESS

The schematic diagram in Figure 1.33 shows the algorithm for the calculations of the parameters related to the fuel injection. The quantities used for the calculations are the pressures measured in the injection port of the injection duct,  $p_w$ , and in the combustion chamber,  $p_k$ . Basing on the model, it is possible to determine the injector needle lift  $h_i$ , the pressure in the injector valve, and the amount of injected fuel  $V$ .

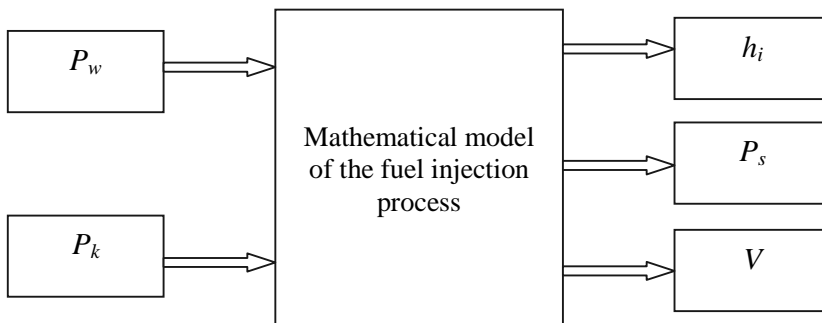


**Fig. 1.33.** Schematic diagram of the calculations

The following equations were used to develop the mathematical model of the needle motion:

- the continuity equation describing the flow of fuel through the injector valve:

$$\frac{V_s}{E_s} \frac{dp_s}{dt} = \text{sgn}(p_w - p_s) \mu_g A_g \sqrt{\frac{2}{\rho_s} |p_w - p_s|} - \varepsilon_s \mu_r A_r n \sqrt{\frac{2}{\rho_s} |p_s - p_k|} - \frac{dV_s}{dt} \quad (1.24)$$

where:

$$\varepsilon_s = 1 \text{ for } p_s \geq p_k, \quad \varepsilon_s = 0 \text{ for } p_s < p_k,$$

$p_w, p_s, p_k$  – pressures in the injection port of the injection duct, the nozzle valve, and the combustion chamber, respectively [Pa],  $\frac{dV_s}{dt}$  – change in the volume of the nozzle valve in the function of time resulting from the needle lift

$$\Delta V_s = \frac{1}{3} \pi r^2 H - \left( \frac{r}{H} (H - h_i) \right)^2 (H - h_i)$$

where:  $r, H$  – constants relating to the needle dimensions.

$A_g$  – cross-sectional area of flow through the seat, defined by the following relationship:

$$A_g = \frac{\pi}{2} \left( d_s - \frac{\sqrt{3}}{4} h_i \right) h_i$$

- dynamic equation of motion of the injector needle:

$$m_w \frac{d^2 h_i}{dt^2} = -\beta_w \frac{dh_i}{dt} - k_{sw} (h_i + h_{w0}) + p_w (A_{ip} - A_i) + p_s A_i - T \quad (1.25)$$

where:

$T = f(p_s) = p_s (A_i - A_s)$  – other forces of resistance of the injector needle;

- relationships used to determine the rate of fuel delivery and unit amount of fuel for one cycle of engine work:

$$U_p = \mu \sqrt{\frac{2\Delta P}{\rho_s}} \quad V = 4 \int_{tpw}^{tkw} U_p A_r dt \quad Q = 4U_p A_r \quad V = \int_{tpw}^{tkw} Q dt \quad (1.26)$$

where:  $U_p$  – initial rate of injection [m/s],  $Q$  – volumetric flow rate [m<sup>3</sup>/s],  $V$  – unit amount of fuel for one cylinder and for one cycle of engine work [m<sup>3</sup>],  $t_{pw}$  – start-of-injection time [s],  $t_{kw}$  – end-of-injection time [s].

Equations (1.24) and (1.25) are nonlinear, and this nonlinearity is due to the relationships between the following parameters:  $V_s = f(h_i)$ ,  $A_g = f(h_i)$ ,  $A_g = f(h_i)$ ,  $E_s = f(p_s)$ ,  $\rho_s = f(p_s)$ . The non-repeatability coefficient [35] of the unit amount

of injected fuel for one cylinder and for one cycle of engine work was calculated from Eq. (1.27)

$$X_V = \frac{\sigma(V)}{\bar{V}} \quad (1.27)$$

where:  $\bar{V} = \frac{1}{k} \sum_{i=1}^k V_i$  – mean of the unit amount of injected fuel for one cylinder and

for one cycle of engine work,  $\sigma(V) = \sqrt{\frac{1}{k} \sum_{i=1}^k (V_i - \bar{V})^2}$  – standard deviation

of the unit amount of fuel,  $V_i$  – unit amount of fuel delivered in the  $i$ -th cycle to cylinder,  $k$  – number of measurement cycles.

It should be noted that the non-repeatability coefficient  $X_V$  will be used as a parameter with a defined value, dependent on the selected range of the crank angle. The analysis was performed in the following range: from  $\alpha_{pw}$ , an angle corresponding to the start of injection, to  $\alpha_{kw}$ , an angle corresponding to the end of injection. It was assumed that injection occurs in the range for which the needle lift satisfies the condition:  $h_i \geq 0.04$  mm.

The model was validated assuming that the parameters have the following values:

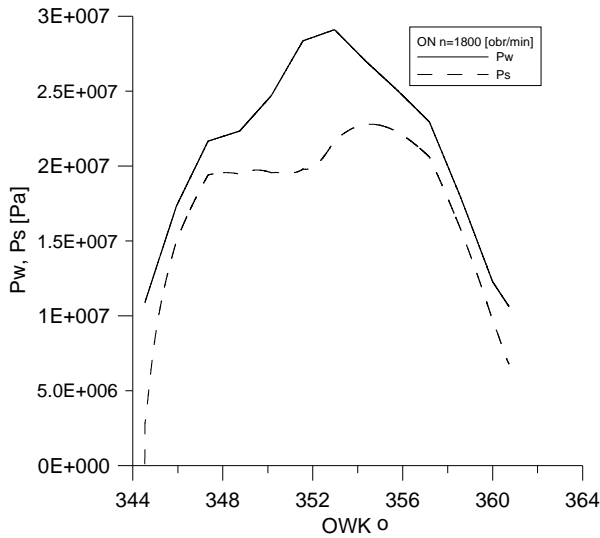
- $V_s = 1.3e-9$  m<sup>2</sup> – volume of the injector valve with  $d_s = 1.2e-3$  m,  $l_s = 1.16e-3$  m,
- $E_s = 1.8e+9$  Pa – elastic modulus of fuel,
- $d_s = 1.2e-3$  m – diameter of the valve seat,
- $A_i = 7.07e-6$  m<sup>2</sup> – cross-sectional area of the needle for  $d_i = 3e-3$  m,
- $A_{ip} = 2.8e-5$  m<sup>2</sup> – cross-sectional area of the upper, leading part of the needle for  $d_{ip} = 6e-3$  m,
- $h_i$  – needle lift [m],
- $h_{ow} = 0.65e-3$  m – initial deflection of the nozzle spring,
- $\mu_g, \mu_r$  – coefficients of flow [40] equal to 0.7,
- $\beta_w = 25$  Ns/m – coefficients of resistance of the needle,
- $k_{SW} = 2.4e+5$  N/m – spring constant,
- $A_r = 6.15e-8$  m<sup>2</sup> – cross-sectional area of one orifice in the injector for a diameter of  $0.28e-3$  m,
- $n = 4$  – number of orifices,
- $m_w = 0.00835$  kg – injector needle mass.

### 1.5.3. THE MODEL VERIFICATION

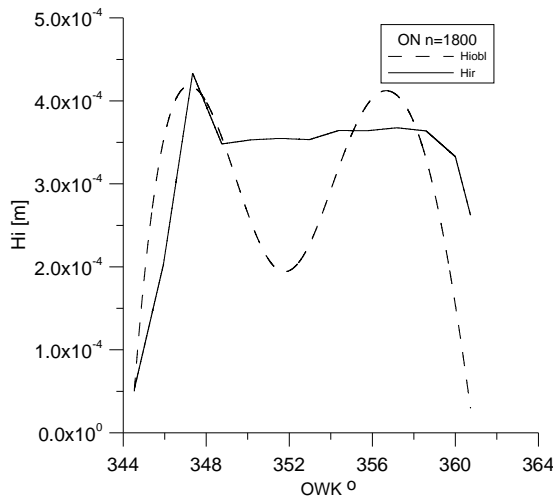
The simulation model was developed basing on the proposed mathematical model and using the Matlab/Simulink software. An advantage of the package is that the calculations are easy to perform, they are reliable and can be immediately visualized. The Matlab/Simulink package was used for solving the system of equations (1.24) and (1.25). The diagram of the model developed with Simulink is shown in Figure 1.34.



Figure 1.35 compares the experimental values of injection pressure with the analytical values of the fuel pressure in the valve in the function of the crank angle at  $n = 1800$  rev/min. One can clearly see that for each position of the crankshaft the calculated pressure in the valve is lower than the pressure measured in the port. The highest differences of up to 25% were reported for crank angles ranging from  $347^\circ$  to  $358^\circ$ . The mean of the difference for the whole range of the angle for which fuel injection occurs is approx. 19%; this is close to the data presented in Ref. [51].



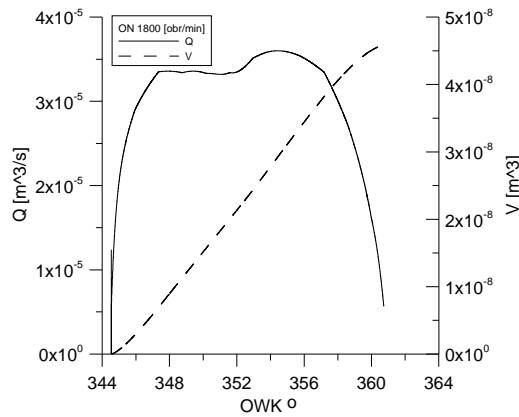
**Fig. 1.35.** Comparison of the measured injection pressure with the calculated pressure in the injector valve vs the crank angle at  $n = 1800$  rev/min



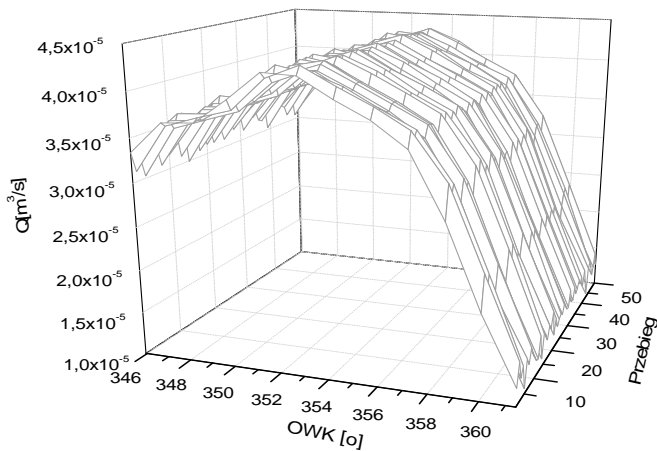
**Fig. 1.36.** Relationship between the injector needle lift and the crank angle at  $n = 1800$  rev/min (model and experimental curves)

Figure 1.36 shows a curve of the injector needle lift determined experimentally and analytically using Eq. (1.25). By comparing the two curves, one can notice that the proposed model is suitable for determining the total injection time and the first phase of the needle lift for the crank angles less than  $349^\circ$ . In the central part, there are clearly visible differences between the two curves. The measurements show that the needle at this phase of motion is stable or slightly displaced upwards. The model calculations, however, testify to the oscillating motion characterized by low frequency and high attenuation. The divergence, calculated as the difference in the area under the distribution curves, is 10%.

The volumetric flow rate and the amount of fuel injected into the engine one cylinder shown in Figure 1.37 were determined analytically for  $n = 1800$  rev/min. As can be seen, the amount of fuel per cycle is approx.  $4.6 \cdot 10^{-8} \text{ m}^3$ . When the needle is at the top position, the changes in the volumetric flow rate are small.



**Fig. 1.37.** Volumetric flow rate and amount of fuel injected into the engine cylinder at  $n = 1800$  rev/min



**Fig. 1.38.** Volumetric flow rate vs the crank angle at  $n = 1800$  rev/min in 50 cycles

In Figure 1.38 we can see that the changes in the volumetric flow rate over one or many cycles (both maximum values and the rate in the function of the crank angle) are non-uniform. One of the causes of this non-uniformity is a disturbance in the real motion of the injector needle, with the real motion being considerably different from the theoretical motion.

Changes in the amount of injected fuel for  $n = 1800$  rev/min are shown in Figure 1.39. The average amount is  $5.07e-8$  m<sup>3</sup>, the standard deviation is  $5.09e-10$  m<sup>3</sup>, the median is  $5.07e-8$  m<sup>3</sup>, and the variance is  $2.59e-19$  m<sup>3</sup>.

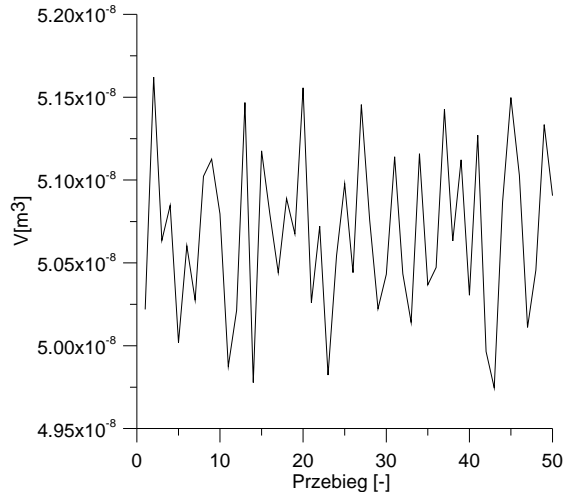


**Fig. 1.39.** Fuel injection volume at  $n = 1800$  rev/min in 50 cycles

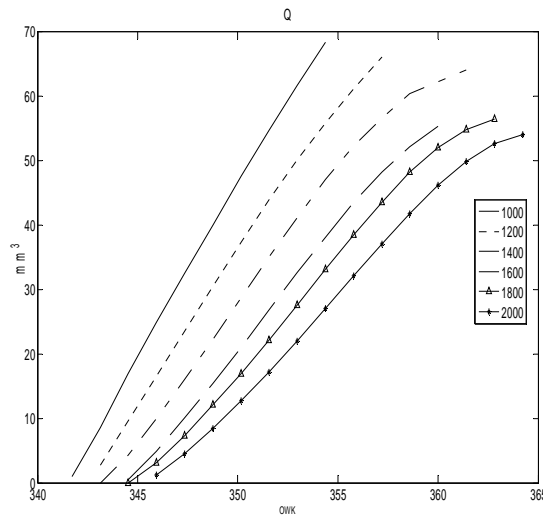


**Fig. 1.40.** Relationship between the amount of fuel injected into the engine cylinder and the crank angle for different rotational speeds

The non-repeatability coefficient of the amount of injected fuel,  $X_v$ , calculated from Eq. (1.27) is 0.01. We have to know that for the properly work of engine it is important not only the non-repeatability coefficient of the amount of injected fuel but also the non-repeatability of the phase of injection. This parameter was not analyzed in the paper. An increase in the rotational speed of the crankshaft causes a decrease in the volume and a reduction in injection duration, which is visible in Figure 1.40. The relationship between the amount of injected fuel and the speed of the crankshaft is nonlinear.

The proposed model of injection process is suitable for determining the total injection time and the first phase of the needle lift for the crank angles less than  $349^\circ$ . In the central part of crank angle, there are clearly visible differences between the experimental and analytical curves. The divergence, calculated as the difference in the area under the distribution curves, is 10%. One can observe changes in the volume of injection in the subsequent cycles. When the rotational speed of the crankshaft was 1800 rev/min, the average volume was  $5.07e-8 \text{ m}^3$ , the standard deviation  $5.09e-10 \text{ m}^3$ . The non-repeatability coefficient of the amount of fuel injected in the consecutive cycles for  $n = 1800 \text{ rev/min}$  was:  $X_v = 0.01$ . An increase in the rotational speed of the crankshaft caused a decrease in the volume and duration of injection. The relationship between the amount of injected fuel and the speed of the crankshaft is nonlinear. The experimental and analytical model of a fuel injector was used to determine the pressure of the fuel in the injector valve. As compared with the pressure measured in the injector port, the highest drop in pressure was 25% and corresponded to the crank angle ranging from approx.  $347^\circ$  to approx.  $358^\circ$ . The average difference of 19% reported for the whole range in which injection occurs is similar to the literature data.

## **1.6. LOCATION AND NEUTRALIZATION OF OVERHEAD HIGH VOLTAGE TRANSMISSION LINES IN WARFARE CONDITIONS**

*Janusz Tuśnio*

In the last few decades, electricity demand has increased substantially as a result of the rapid advances in the mechanization and automation of manufacturing processes, the development of public transport and household appliances as well as higher living standards. To meet the demand, more and more lines are being constructed and the existing ones are being extended.

Transmission lines are structures strategically important to a state's safety. Their failure or disruption to energy transmission may lead to business shutdowns, disruption to traffic, and general inconvenience to daily life, e.g. no lightning, and lifts, air-conditioning or household appliances not working. This year, severe winter weather has caused similar problems, i.e. frequent power outages.

A very important problem related to electric power transmission is the threat that overhead lines pose to the health of people living in the immediate neighborhood [55]. Although it is now possible to transfer electrical energy via high-voltage underground cables, the conversion of the existing networks would be too expensive. It is thus clear that during the next several decades energy transmission via overhead lines will predominate.

During warfare, transmission lines and other electric power systems become targets of air and other forces. The first aerial attacks on transmission lines were made during the first war with Iraq in 1990, following Iraq's attack on Kuwait. The experiences gathered by the US army during that time made it possible to improve munitions technology and methods of attack, and apply the solutions during the Kosovo War (1999). Transmission lines and similar structures can be attacked from the air using aerial bombs, especially cluster ones, missiles or unmanned aerial vehicles. Such structures are likely to be defended intensively, therefore it is desirable that the weapons used for an attack be guided automatically at least at the final stage of flight, using special systems for detecting, locating and tracking targets that emit low-frequency electromagnetic radiation. The targets include transmission lines, and switching and transformer stations.

Electric lines are generally attacked using cluster bombs releasing bomblets stuffed with spools of fine conductive fiber, which, dispersed by the wind, settle on line conductors producing short circuits. The effects are expensive and difficult to remove, especially in hard-to-reach areas, for instance, woods or swamps. Repair work may last up to several tens of hours. Although the number of casualties reported for attacks with cluster bombs is much smaller than for classic attacks, their effects are very painful economically. An effective attack on a transmission line with multiple simultaneous explosions requires using bombs or other means of aerial attack capable of precisely detecting and locating a target.

There needs to be sufficient time to detect and locate a high-voltage structure so that it can be effectively attacked or safely bypassed by an aerial vehicle. Aerial attack means, for instance, bombs or missiles, move with a velocity of the order of several meters per second; in the case of unmanned aerial vehicles, the velocity is smaller. The time required for automatic guidance of small flying objects to a target is of the order of several seconds; it is, therefore, assumed that a target to be attacked needs to be detected and located at a distance of at least 1000 meters. The velocities of aerial vehicles such as powered hang gliders or small sports and passenger aircraft are even smaller, which is due to the fact that they are generally steered manually. Their larger dimensions and higher inertias cause that the time required for performing a desired maneuver is longer. Again, it is assumed that 1000 meters is a minimum distance necessary to detect and locate an obstacle.

A target (obstacle) is detected when the monitoring system receives a 50 Hz signal; this testifies to the presence of an active high-voltage line or some other electric power system at a close distance. To accurately locate a point target, it is essential to know the direction from which the wind is blowing (and accordingly from which the signal emitted by the target is coming) and the target distance from the monitoring device. To detect a target, we use an ordinary receiving antenna, and to locate it, we need a set of at least two antennas with directional properties.

### **1.6.1. EMISSION OF LOW-FREQUENCY ELECTROMAGNETIC RADIATION BY OVERHEAD TRANSMISSION LINES**

Overhead transmission lines emit low-frequency electromagnetic radiation, which consists of electric and magnetic field components. An electromagnetic field extends through three basic zones:

- the near or Fresnel zone, an area surrounding a source of electromagnetic radiation; its range is smaller than the wavelength  $\lambda$ ,
- the transition zone, an area where the distance from a radiation source is close to the wavelength  $\lambda$ ,
- the far or Fraunhofer zone, an area where the distance from a radiation source is many-fold longer than the multiple wavelength  $\lambda$  and the source size.

A transmission line conducting an alternating current generates an alternating electromagnetic field, and in consequence, emits higher- or lower-frequency electromagnetic waves. However, if the length of the line is shorter than the wavelength,  $\lambda = 2\pi c/\omega$  (low frequency of current oscillations), then the radiation is negligibly low, because the electromagnetic fields generated by the individual elements of the system with the same current rate but reverse current directions attenuate each other. The intensity of the resultant, changeable electromagnetic field becomes rapidly lower as the distance from the system increases until the transmission line no longer emits electromagnetic waves. The current with a frequency of 50 Hz corresponds to a wavelength of 6000 km, and the losses in radiation in the conductors where current flows are negligibly small [57].

Each conductor or circuit, whether live is a source of an electric field. The intensity of an electric field around a transmission line is dependent mainly on the distance between the phase conductors and the ground. Generally, the intensity of an electric field is reported to be the highest in the middle of a span, where the distance of the cable to the ground is the smallest. The intensity of the field drops rapidly when the distance from the line axis becomes larger, or the distance to the tower is smaller, with the latter being due to the scanning properties of the tower. Most objects permanently located in the vicinity of power lines, such as trees, bushes or buildings, have scanning properties; as a result, the intensity of an electric field may fall considerably. The slack due to high temperature of air in the summer or heat generated by large currents is also responsible for the changes in the intensity of an electric field on the ground surface. At a distance of about

23÷28 m from the axis of a 400 kV double-circuit line, the intensity of an electric field falls below 1 kV/m [55].

Figure 1.41 illustrates an example relationship between the intensity of an electric field and the distance from a 110 kV high-voltage line at different measurement altitudes. The intensity of the electric field significantly declines when the distance from the line axis is larger or the height above the ground level is smaller.

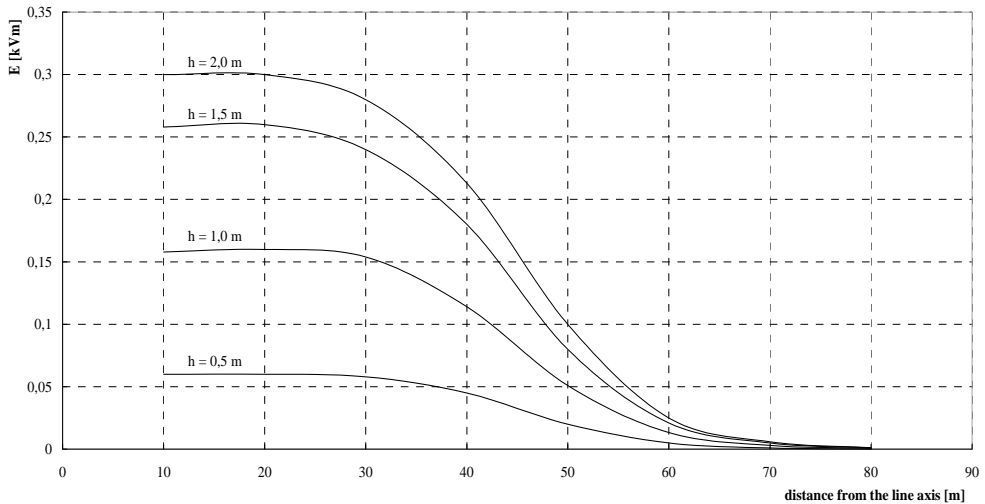


**Fig. 1.41.** Relationship between the electric field intensity  $E$  [kV/m] and the distance from the line axis for different line types dependent on the measurement altitude [59]

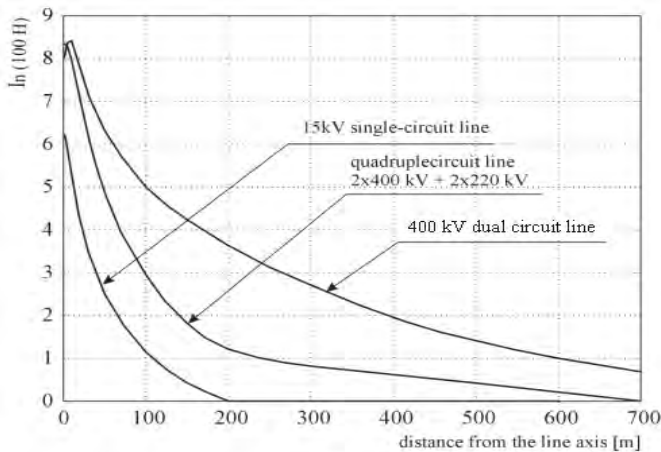


**Fig. 1.42.** Compressed (logarithmic) values of the magnetic field intensity  $H$  [A/m] versus the distance from the line axis for different line types (on the basis [56])

The intensity of a magnetic field near transmission lines, even highest voltage lines, is small. The magnetic field under and near the line changes with the current

flowing through it; the higher the current value, the higher the intensity. In a similar way, if the distance from the line axis becomes larger, the intensity of the magnetic field drops rapidly. Unlike an electric field, a magnetic field penetrates a majority of materials and objects not causing any deformation. This means that the direction of the magnetic lines passing through various objects is maintained. There is no significant change in the intensity either, even if the field passes through a number of objects [55]. Example relationships between the magnetic field intensity and the distance from the line axis are presented in Figure 1.42.

### 1.6.2. DETECTION AND MEASUREMENT OF A 50 HZ ELECTROMAGNETIC FIELD

Detecting and measuring the components of an electromagnetic field requires selecting a suitable converting system. Different sensors are applied to measure a field close to the electric component. These include ground-referenced meters, especially ones with flat surface electrodes and asymmetric rod antennas. Other examples are free-body meters with symmetric dipole antennas, which are less sensitive to parasitic feedback [52].

The principle of operation and structure of an electric field sensor together with an alternate diagram are presented in Figure 1.43. The voltage induced in the antenna represents a source, whose  $SEM = ea$ . The source is coupled with the rest of the system via the antenna capacity.  $C_a$ ,  $C_p$  and  $L_p$  represent the parasitic capacities and inductance, respectively; they are related to improper assembly and imperfection of elements. In the range of low frequencies of the order of 50 Hz, the influence of these factors is negligible.  $C_f$  and  $R_f$  are elements of a low-pass filter, which allow modeling the sensor frequency characteristic particularly in the range of high frequencies. Capacity  $C$  and resistance  $R$  represent the detector parameters [Bieńk].

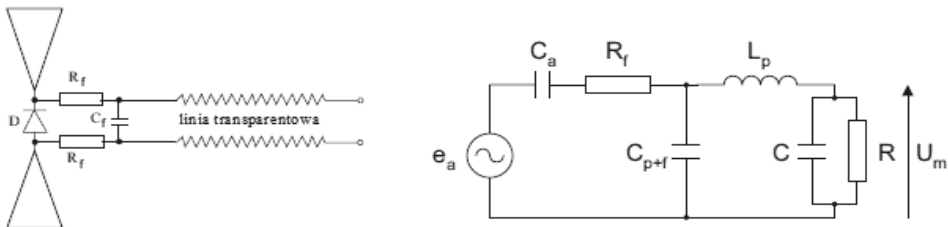


**Fig. 1.43.** Electric field sensor and an alternate diagram [52]

The principle of measurement described above can be used only when a radiation source is at a small distance, i.e. where the electric field intensities are higher. If overhead electromagnetic structures are to be detected from a further distance, we need to apply a special measuring system with amplification of at least 140 dB, which is particularly important in military operations.

The system needs to be characterized by low voltage supply, little power consumption and considerable resistance to high and low temperatures. The first element of the system is an initial amplifier, whose schematic diagram is presented in Figure 1.44.

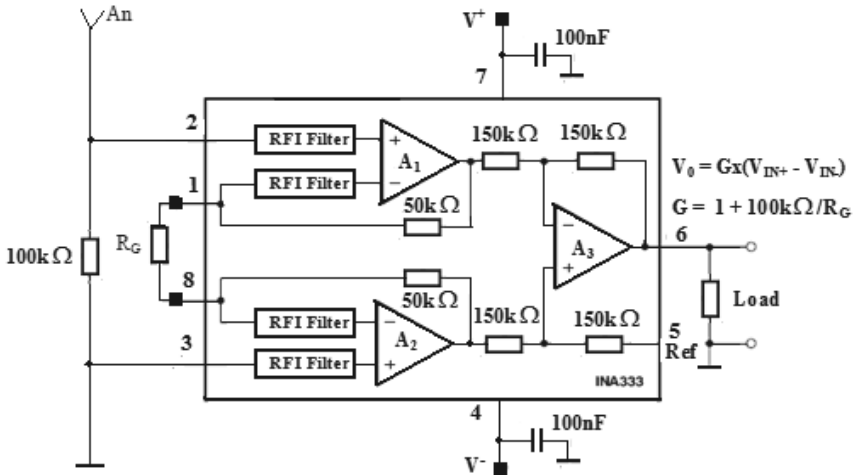


*Fig. 1.44. Diagram of the initial amplifier designed basing on the INA 333 system*

The requirements concerning low voltage supply and power consumption are perfectly met by the INA128, and particularly the INA333, measuring amplifiers. The INA333 amplifier is characterized by a very good signal/noise coefficient, very low disequilibrium voltage, and the drift; it operates at a minimum voltage supply of 1.8 V, consuming a current of the order of 75  $\mu$ A. It utilizes the zero drift technology developed by Texas Instruments, using a switched-capacity barrier filter protected by patent law, which eliminates pulse disturbances and assures a very low level of input voltage noise reaching 50 nV/rt-Hz, a low disequilibrium voltage of 25  $\mu$ V and a small temperature drift of 0.1  $\mu$ V/ $^{\circ}$ C, which assures perfect accuracy and long-term stability [61].

The asymmetrical rod antenna “An” was connected to the reversing input of the INA333 amplifier, while the non-reversing input was connected to the system mass and via the resistor ( $R_1 = 100$  k $\Omega$ ) to the reversing input. The amplifier may also cooperate with a magnetic field sensor, which features directional properties and includes a coil wrapped around a ferromagnetic core. In this case, the coil is connected directly to the amplifier inputs.

As suggested by the producer, the maximum amplification of the device shown in Figure 1.44 is 80 dB. In practice, however, this value causes that the system becomes unstable. It is thus recommended that 70 dB or sometimes even 60 dB be used. Because of a very low value of the voltage signal on the rod antenna (below 1  $\mu$ V), the system reaches the desired sensitivity following an amplification of the order of 140 dB and more. Obtaining such a value requires applying one or even

two additional degrees, with the total amplification being 80-100 dB. Increasing amplification implies using high-quality operational amplifiers, e.g. OP90 or double OP290. Because the amplification is considerable, amplifiers with capacity coupling need to be employed.

The tests for the measuring amplifier with an asymmetrical rod antenna and a magnetic field sensor were conducted at rest at a small distance from a transmission line. The results show that the system operated correctly. Then, the tests were carried out for the system in motion. This time, some disturbances were reported. The further from the line, the more difficult the measurements were; when the distance was considerable, the disturbances made the measurements impossible. Some of the disturbances had a frequency of several Hz, which corresponded to sudden spatial displacements of the sensors with an initial amplifier and some disordered disturbance signals featured a frequency of the order of several hundred Hz. At a distance of several hundred meters from the line, the disturbance signal amplitude was many fold higher than the useful signal amplitude.

When the experiments were conducted in conditions of rapid motion and vibrations of the model, the disturbances occurring at the output of the measurement system had a low but difficult-to-define frequency and an amplitude many fold higher than the useful signal amplitude. At a distance of about 60 meters from an overhead 110 kV line, the disturbance amplitude was nearly 100 times higher than the useful signal amplitude. Under laboratory conditions, the system was found to be susceptible to disordered electrostatic-charge-related disturbances, which were due to the friction of the fabric against the casing inside which the device was placed and due to the friction of the air stream released through the nozzle against the casing. Other disturbances that may affect the operation of a system fitted on board of an aerial vehicle include disturbance signals with a frequency different from that of the useful signal, i.e. 50 Hz, which can be reduced by using active filters [59].

A filter in the form of a natural resonance circuit LC tuned to a frequency of 50 Hz was introduced to the initial system in order to reduce the disturbances affecting the operation of the magnetic field sensor. The amplitude characteristic shows that because of the value of the sensor coil resistance,  $R = 1.4 \text{ k}\Omega$  (approx. 10000 turns of  $\phi 0.08 \text{ mm}$  Cu wire), and the value of the system capacity,  $C = 1.5 \text{ }\mu\text{F}$ , its goodness-of-fit  $Q$  and selectivity are very small. Better results were obtained, when, according to the concept presented in patent [52], we applied active and simulated inductances in the input system by means of a gyrator [60].

The preliminary studies show that there is still another type of disturbances that cannot be reduced using electric methods. It is reported that the value of a signal at the output of the measuring system is largely dependent on the angle of inclination of the sensor with respect to the horizontal plane; this inconvenience causes that gyroscopic systems are used for stabilizing the sensor position [58].

There are many methods used for the measurement of the magnetic field intensity [53] The most sensitive low field sensor is the Superconducting Quantum Interference Device (SQUID). The SQUID magnetometer has the capability to sense a field in the range of several fempto-tesla (fT) up to 9 tesla.

Other more common measurement methods include:

- earth field sensors (1 microgauss to 10 gauss),
- fluxgate (1 microgauss to 100 gauss),
- magnetoinductive (repeatable to within 4 miligauss),
- magnetotransistor (0.01 gauss to 10000 gauss),
- magnetodiode (1 gauss to 10000 gauss).

To detect a source of an alternating electromagnetic field, it is sufficient to use a single receiving antenna, while to locate it, a system of at least two antennas with directional properties.

Transmission lines can be detected and located using various methods and apparatus for the measurement of a magnetic field, for example, fluxgate magnetometers and magnetoinductive magnetometers.

Fluxgate magnetometers were developed around 1928 and later refined for detecting submarines [53]. This device involves two coils, a primary and a secondary, wrapped around a common highpermeability ferromagnetic core. The magnetic induction of this core changes in the presence of an external magnetic field. A drive signal is applied to the primary winding at frequency  $f$  (e.g. 10 kHz) that causes the core to oscillate between saturation points. The signal at the terminals of the secondary winding is affected by any change in the core permeability and appears as an amplitude variation in the sense coil output. Signal processing requires using a phase sensitive detector, the sense signal can be demodulated and low pass filtered to retrieve the magnetic field value. Fluxgates can measure both magnitude and direction of static magnetic fields and have an upper frequency band limit of around 1 kHz – due to the drive frequency limit of around 10 kHz [53].

To avoid a direct current component (magnetizing current) at the primary winding, it is necessary to provide a symmetrical signal to the winding, which is possible by applying for instance a divisor divided by 2 based on the 555 system. One can also use a 4541 programmable oscillator timer with a 4050 buffer or a 4066 quad bilateral switch. Applying a buffer or a switch to support the 4541 system is necessary because the output current of the ordinary CMOS gates is too small.

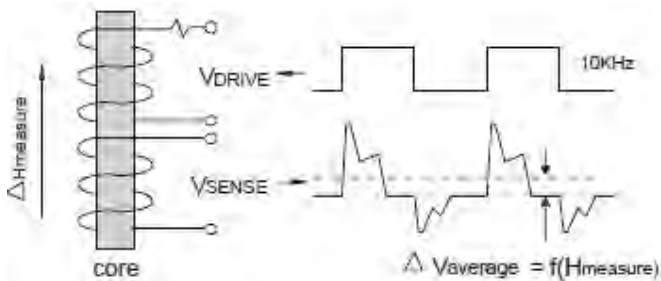


**Fig. 1.45.** Fluxgate Magnetometer Operation [53]

Magnetoinductive magnetometers are relatively new with the first patent issued in 1989. The sensor is simply a single winding coil on a ferromagnetic core that

changes permeability within the Earth's field. The sense coil is the inductance element in a  $L/R$  relaxation oscillator. The frequency of the oscillator is proportional to the field being measured. The observed frequency shift can be as much as 100% as the sensor is rotated 90 degrees from the applied magnetic field [53].

### 1.6.3. LOCATION OF THE ANGULAR POSITION OF TRANSMISSION LINES

Locating a power line involves determining the line direction and the distance from the measurement system, and accordingly, establishing precisely the line voltage. Figure 1.46 shows a diagram of an example system for the detection and initial location of a transmission line [54]. The electric signal induced in the sensor is filtered, the disturbances are attenuated, and the alternating signal with a frequency of a transmission line (60 Hz in the US and 50 Hz in Poland) is converted in the analog-digital (A/D) transducer. The signal values obtained during further processing are memorized and then compared with those registered in previous measurements. Even if a transmission line is not detected, it is possible to determine whether an aircraft equipped with the above mentioned measurement system is approaching or moving away from such a line. Directional properties of the system allow determining the angular position of the source of electromagnetic radiation. It is necessary, however, for the system to assume a position at which the signal reaches a maximum. The direction from which the signal induced in the coil comes is assessed correctly only when the measuring system is at rest with respect to the signal source; rapid motions towards the source make such measurements inaccurate.

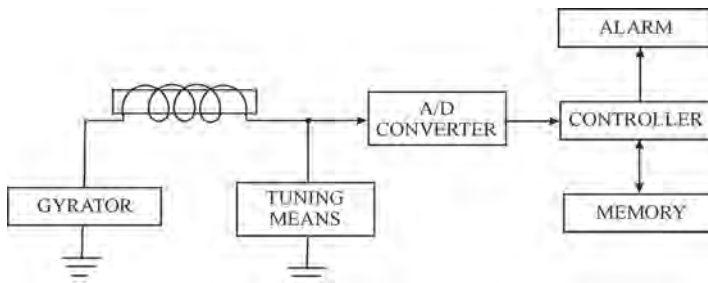


**Fig. 1.46.** Block diagram of the system for detecting high-voltage transmission lines [54]

Reference [62] discuss the concept and simplified mathematical models of a system for the location of the angular position of a point and linear source of electromagnetic radiation. The system consists of two mutually perpendicular sensors with directional properties, as shown in Figure 1.47.

The signal from the outputs of the measurement amplifiers is delivered to the system of band-pass filters with a medium frequency of 50 Hz [60]. 8th order Butterworth filters with a goodness-of-fit,  $Q$ , of the order of 10, made up of monolithic MF10-type integrated circuits, were used in the tests. The filtered alternating voltage signal with a frequency of 50 Hz is further amplified, rectified in a full-wave linear

rectifier, and finally filtered (AC/DC converted) using a low-pass filter. The effective voltage values obtained at the filter outputs are dependent, for instance, on the distance from the detected transmission line and the value of the line voltage.

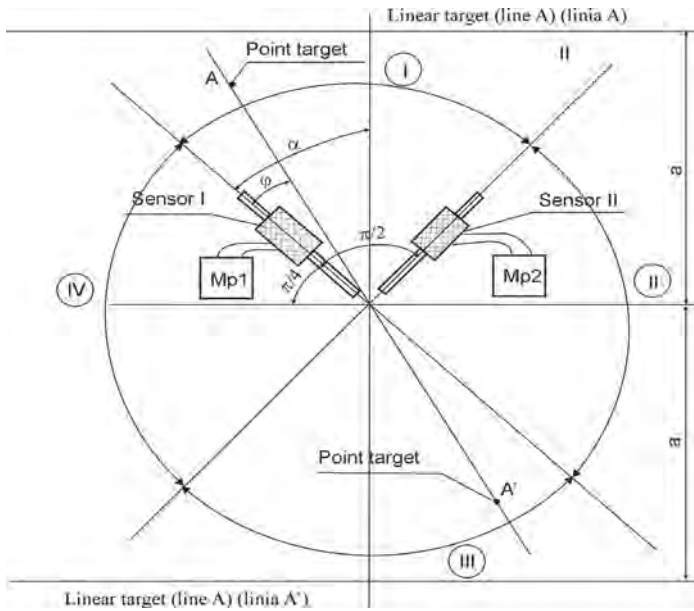


**Fig. 1.47.** System for locating the angular position of the line or point target consisting of two directional sensors [62]

If the target being located is linear in nature, e.g. a transmission line, the angles of the inclination of the sensors axes with respect to the straight line going through the point of intersection of these axes and the straight line perpendicular to the transmission line are  $\alpha$  and  $\pi/2 - \alpha$ , and then the effective voltages at the outputs of the measurement paths are:

$$U_1 = \frac{K_2}{a} (\alpha \cos \alpha + \pi \cos \alpha - 0.5 \cos \alpha \sin 2\alpha - \sin^3 \alpha) \quad (1.28)$$

$$U_2 = \frac{K_2}{a} \left[ \left( \alpha - \frac{\pi}{2} \right) \sin \alpha - \cos \alpha \right] \quad (1.29)$$

The voltage signals determined in accordance with relations (1.28) and (1.29) are further processed, and the  $U_1/U_2$  quotient and the  $\ln(U_1/U_2)$  logarithm are calculated; as a result, one can determine the angle of deviation,  $\alpha$ , which specifies the position of the transmission line with regard to the aerial vehicle path.

The simulation studies [60] show that the value of the  $\ln(U_1/U_2)$  logarithm is linearly dependent on the angle of deviation of the sensor from the normal to the high-voltage line.

#### 1.6.4. NEUTRALIZATION OF TRANSMISSION LINES

Attacks on transmission lines during war operations can be conducted by applying aerial cluster bombs, missiles containing cluster bomblets or unmanned aerial vehicles. On reaching a target, cluster bomblets disperse releasing reels of fine conductive composite fibers. In the easiest case, the flight of an attacking aerial vehicle or missile is performed along the shortest possible path in the line direction.

After being launched, the unmanned aerial vehicle achieves an altitude ( $H_s$ ) that is higher than the power line height. Then, the vehicle performs a horizontal flight at that altitude with a constant velocity,  $V$ . Once a 50 Hz electric field is detected and the pre-determined field intensity is achieved, a bomb is dropped. Being at a close distance to the line, the bomb disperses its filling (conductive fibers) causing the neutralization of the target line. Determining the moment of release and the moment of dispersion requires analyzing the problem in more detail.

An unmanned aerial vehicle needs to fly at altitude  $H_s$ , higher than the line height  $H$  by  $\Delta H$  ( $\Delta H = H_s - H$ ) [63]. Neglecting the drag, we can describe the motion of the cluster bomb released from board of the aerial vehicle by means of the horizontal projection relationship, where the reference level is the line height,  $H$ . The range of an independent flight of a cluster bomb  $Z$  (the horizontally measured distance between the point of release and the point of intersection of the flight path and the horizontal reference plane going through the transmission line) is:

$$Z = V\sqrt{2\Delta H / g} \quad (1.30)$$

where:  $g$  – acceleration of gravity ( $10 \text{ m/s}^2$ ).

When the flight velocity is, for instance, 140 km/h ( $\sim 40 \text{ m/s}$ ) and the difference between the flight altitude and the line height  $\Delta H$  is 20 m, the drop range of a bomb release is 80 m; it is recommended that the signal to release a cluster bomb by an unmanned aerial vehicle should be generated at a slightly greater distance, for example, at about 90 meters from the line.

Selecting a suitable fuze is an important problem in such cases. As the bomb is unlikely to hit a target transmission line with high precision, it is not advisable to apply a contact fuze. The choice is between a time fuze and a proximity fuze. Applying a time fuze is conditioned by possessing a fairly precise classic rangefinder or one with a GPS-based distance calculation system. Electronic time fuzes are used in small-diameter missiles, which are part of active marine defense systems and whose aim is to disperse clouds of fine air-floating metal needles acting as false targets. It should be noted that there exists fairly large tolerance in the distance between the ship and the false target. When a transmission line is attacked, the tolerance is only of the order of a dozen meters, assuming that the wind is favorable, i.e. it can carry the composite fibers onto the line conductors. In either case, it is important to establish the moment of bomb release, unless we decide to risk destroying the aerial vehicle by performing a flight at an altitude the same as the line height. The release and dispersion occur the moment the vehicle reaches the target.

The research described in Ref. [58] shows that it is not difficult to detect a 110 kV or higher voltage line from a distance of 400-500 m. Since the intensity of an electric field increases rapidly with the distance to the conductors, a proximity fuze will ensure reliable dispersion of a submunition at a distance of several meters from a power line.

The method of attack on a transmission line analyzed above enables the neutralization by applying short circuits along a short section (due to a small amount of conductive fibers in one bomb). Obviously, a multiple attack at different angles between the flight path and the transmission line is also possible; neutralization of a larger number of line sections will be more reliable and more effective.

To increase the attack effectiveness, it is essential that a line be destroyed at several points along as long a distance as possible. It is desirable that the attack be performed in hard-to-reach areas, which makes the repair work more difficult and time-consuming. The operation can be conducted by means of an unmanned aerial vehicle with cluster bombs or a missile. The flight of a bomb carrier needs to be performed above the transmission line and the dispersion should take place at the closest possible distance. It should be noted that the first cluster bomb hitting a target line causes short circuits and disruption of energy flow. Then, the guidance of the carrier to a target is not possible, and the application of proximity fuzes to disperse the other bombs is not recommended, because their operation bases on the effect of a magnetic or an electric field.

It is desirable that all clusters released should disperse at the same time when close to a transmission line, even if the line is conducting no current. A preliminary analysis of the concept shows that the operation would be difficult. When neglecting the drag of a bomb dropped from an AV, the vertical component of the velocity,  $V_z$  is:

$$V_z(t) = V_{0h} + gt \quad (1.31)$$

where:  $V_{0h}$  – initial velocity of the cluster bomb in the vertical direction (m/s);  $g$  – acceleration of gravity ( $9.81 \text{ m/s}^2$ );  $t$  – time following a cluster bomb release (s).

There exist several theoretical methods for ensuring a simultaneous multiple attack. It is necessary that the bombs be dropped more or less simultaneously at a short distance from the transmission line axis so that the release of a subsequent cluster can take place at the same altitude as the previous one and the vertical component of the initial velocity of each cluster can be equal to an instantaneous velocity. A preliminary analysis, however, shows that the option features too many drawbacks.

The major problem is that it is necessary to perform a dive with a rapidly increasing component  $V_z$ . For instance, if the horizontal component of the aircraft velocity is 50 m/s, and the attack is to be conducted with eleven cluster bombs at intervals of about 100 meters along a distance of 1 km, with the time between the drop of the first and the last bomb being 20 s. After the aircraft releases the last bomb, the vertical component of the velocity of the first bomb is:  $V_z = gt = 10 \text{ m/s}^2 \cdot 20 \text{ s} = 200$

m/s. It is an unlikely velocity to be reached by an unmanned aerial vehicle. Moreover, the distance that the first bomb covers in the vertical direction is  $s = 0.5 \cdot g t^2 = 2000$  m. Dropping bombs from a higher altitude is also ineffective because the attack would have little accuracy. An alternative solution would be to drop cluster bombs on small-size parachutes. This would lead to a decrease in the component  $V_z$  of the bomb flight velocity, and accordingly an undesirable decrease in the component  $V_z$  of the velocity of the vehicle performing a dive. This solution has two disadvantages. It can be conducted only when there is no wind; otherwise the bombs would be carried away from the transmission line. Parachutes would also add to an increase in the load mass, and accordingly, the operation cost.

It should thus be assumed that the most effective method for attacking transmission lines is to drop a series of cluster bombs from an unmanned aerial vehicle flying horizontally at an altitude of the order of several dozen meters above the line. If the first bomb hits the target line, the flow of energy will be disrupted, and the systems for power line detection and location fitted on board of the aerial vehicle will become useless. In a similar way, the application of proximity fuzes responding to an electric and a magnetic field will be ineffective.

All the above problems related to the ineffectiveness of target location systems after the target is reached with the first bomb can be solved by using a gyroscopic system for the stabilization of the flight path of the unmanned aerial vehicle. In such a case, the stages of an attack on a transmission line are as follows:

- detection of a transmission line,
- location of its angular position,
- approaching the line by the aerial vehicle, determining the flight path at a desired altitude above the line in the same direction as that of the line,
- stabilization of the flight path by means of the gyroscopic system,
- attacking the line with a series of cluster bombs (graphite bombs),
- switching off the flight path stabilization system after the release of the last cluster bomb, and transition to the next task.

A successful attack requires equipping a bomb with a fuze that will enable effective dispersion. Taking into account the above conditions, there are two types of fuzes that can be used for this purpose:

- altitude fuzes, whose task is to release a bomb at a pre-determined height above the ground,
- time fuzes, which are programmed to release a bomb using a single width-modulated pulse or a series of short pulses.

In time fuzes, non-contact programming is performed, for example, by means of an inductive loop or an optical coupling. The processor mounted on board of an aerial vehicle calculates the time of release basing on two parameters – the flight altitude and the desirable altitude of the bomb dispersion.

Under warfare conditions, neutralization of transmission lines in an enemy's territory is one of the major aims of military missions, especially those made by the air force. Such an operation requires detecting and locating the position of a power

line to be attacked, guiding an aerial munition to the target, and, finally, effective bombing. The most effective and economically painful is a multi-cluster bomb attack. It is essential that an aerial vehicle should fly immediately over the line axis and drop single clusters in hard-to-reach areas at intervals that make the repair work difficult and time-consuming. Using an unmanned aerial vehicle to conduct a bomb attack on a power line seems to be the most convenient and involves the least risk. It is assumed that an attack should be performed from above the line at the same altitude by dropping cluster bombs equipped with pre-programmed time fuzes. It is also significant that the flight be stabilized at an altitude slightly higher than the height of the transmission line by applying a special-purpose gyroscope.

## REFERENCES

- [1] Dindorf R.: *Modelling and simulation of non-linear elements and control systems of fluid power drives* (in Polish). Monograph 44. Politechnika Świętokrzyska, Kielce 2004.
- [2] Dindorf R.: *Fluid power drives. Fundamentals theory and calculation methods of hydrostatic and pneumatic drives* (in Polish). Academic textbook. Politechnika Świętokrzyska, Kielce 2009.
- [3] Dziopa Z.: *The dynamics of a rocket launcher placed on a self-propelled vehicle. Mechanical Engineering*, No. 3 (81), Lviv 2004, ISSN 1729-4959, s. 23-30.
- [4] Dziopa Z.: *Modelowanie ruchu pojazdu samochodowego z zainstalowaną wyrzutnią rakiet przeciwlotniczych*. Problemy Bezpieczeństwa w Pojazdach Samochodowych, Zeszyt Naukowy, Mechanika z. 84, Politechnika Świętokrzyska, Kielce 2006, ISSN 0239-4979, s. 179-186.
- [5] Dziopa Z.: *Ocena wpływu dynamiki pojazdu samochodowego na początkowe kinematyczne parametry lotu rakiety*. Teza Komisji Motoryzacji: Konstrukcja, Badania, Eksploatacja, Technologia Pojazdów Samochodowych i Silników Spalinowych, Zeszyt nr 29-30, PAN, Kraków 2005, ISSN 1642-1639, s. 115-122.
- [6] Dziopa Z.: *Modelling and examining the dynamic properties of the self-propelled anti-aircraft missile assemblies*, Politechnika Świętokrzyska, Kielce 2008, s. 313.
- [7] Genta G.: *Motor Vehicle Dynamics, Modeling and Simulation*. World Scientific Publishing, Singapore 1997.
- [8] Gillespie T.D.: *Fundamentals of Vehicle Dynamics*. Society of Automotive Engineers, Inc., Warrendale 1992, ISBN 1-56091-199-9.
- [9] Kortüm W., Lugener P.: *Systemdynamik und Regelung von Fahrzeugen*, Einführung und Beispiele. Springer-Verlag, Berlin-Heidelberg 1994.
- [10] Mitschke M., Wallentowitz H.: *Dynamik der Kraftfahrzeuge*. Springer-Verlag, Berlin-Heidelberg 2004.
- [11] Osiecki J., Gromadowski T., Stępiński B.: *Badania pojazdów samochodowych i ich zespołów na symulacyjnych stanowiskach badawczych*. Przemysłowy Instytut Badawczy, Warszawa 2006.
- [12] Osiecki J., Stańczyk T.L., Kałuża Z., Dziopa Z.: *System obliczeniowo-analizujący obciążeń dynamicznych samochodów ciężarowych*. Badania symulacyjne w technice samochodowej, Lublin 1991, s. 115-120.
- [13] Osiecki J.: *Dynamika maszyn*. WAT, Warszawa 1994.

- [14] Popp K., Schiehlen W., Teubner B.G.: *Fahrzeugdynamik, Eine Einführung in die Dynamik des Systems Fahrzeug-Fahrweg*. Stuttgart 1993.
- [15] Dubiel S.: *Rocket Construction. Part. 1 (edition 2) – Overloads* (in Polish), the Warsaw Military University of Technology Publishing House, Warsaw 1980.
- [16] Graffstein J., Krawczyk M., Maryniak J.: *Modelling the Dynamics of Automatically Controlled Unmanned Aerial Vehicle Flight with the Application of Non-holonomic Constraints Theory* (in Polish). Scientific Papers of the Chair of Applied Mechanics, vol. 4, XXXVI PTMTS Symposium "Modelling in Mechanics", Gliwice 1997.
- [17] Koruba Z., Osiecki J.W.: *Budowa, dynamika i nawigacja wybranych broni precyzyjnego rażenia*. Podręcznik akademicki, Wydawnictwo Politechniki Świętokrzyskiej, Kielce 2006, ISBN 83-88906-17-8, p. 484.
- [18] Koruba Z.: *Elementy teorii i zastosowań giroskopu sterowanego*. Monografie, Studia, Rozprawy M-7. Politechnika Świętokrzyska, Kielce 2008, p. 241.
- [19] Koruba Z.: *Dynamics and Control of Gyroscope on the Deck of Aerial Vehicle* (in Polish). Monographs, Studies, Dissertations No 25. Kielce University of Technology, Kielce 2001, p. 285.
- [20] Koruba Z.: *Unmanned Aerial Vehicle Flight Programme, Ground Surface Scanning and Laser Target Illumination*, Journal of Technical Physics, no. 4, 1999, Polish Academy of Sciences, Institute of Fundamental Technological Research, the Warsaw Military University of Technology, Warsaw.
- [21] Koruba Z.: *The Options of Terrain Penetration and Selected Object Tracking from Unmanned Aerial Vehicle Deck* (in Polish), Scientific Papers of Rzeszów University of Technology, Mechanics, vol. 45, pp. 357-364, Rzeszów 1995.
- [22] Koruba Z., Ładyżyńska-Kozdraś E.: *The dynamic model of combat target homing system of the unmanned aerial vehicle*, Journal of Theoretical and Applied Mechanics 50, 2, 2010.
- [23] Ładyżyńska-Kozdraś E.: *Modeling of flight dynamics for a missile under automatic control in the phase of guiding mode change i.e. when the beam guidance is replaced with the homing on to a maneuvering target*, Scientific Proceedings of Riga Technical University, Series 6 „Transport and Engineering. Transport. Aviation transport”, N27, Riga, RTU, 2008, pp. 159-170.
- [24] Mishin W.P.: *The Dynamics of rocket*. „Mashinostroyenie”, Moscow 1990.
- [25] Nizioł J.: *Technical Mechanics, Vol. II, The dynamics of mechanical system*, Publisher Mechanics Committee of Polish Academy of Sciences, IPPT Polish Academy of Sciences, Warsaw 2005.
- [26] Svetlitskiy W.A.: *The dynamics of objects flying off*. “Nauka”, Moscow 1963.
- [27] Salant R.F., et al.: *Development of an electronically controlled mechanical seal*. Proc. BHRA 11th Intl. Conf. on Fluid Sealing, Paper H-2, Cannes, France, 1987, pp. 576-595.
- [28] Kundera Cz., Rudolf F.: *Boundary state of a sliding ring seal*. Exploitation Problems of Machines. Polish Academy of Sciences. Issue 1-2 (69-70), 1987, pp. 75-90 (in polish).
- [29] Heilala A.J., Kangasneimi A.: *Adjustment and control of a mechanical seal against dry running and severe wear*. Proc. BHRA 11th Intl. Conf. on Fluid Sealing, Paper H-2, Cannes, France, 1987, pp. 548- 575.
- [30] Kundera Cz.: *Active sealing of vibrating and rotating elements*. Monograph No 15, Kielce University of Technology, Kielce, 1999, pp. 115 (in polish).

- [31] Min Zou, Green I.: *Clearance Control of a Mechanical Face Seal*. Tribology Transactions ASLE, Vol. 42, No. 3, 1999, pp. 535-540.
- [32] Kundera Cz., Michalski D.: *Experimental tests of clearance control in noncontacting face seals*. Hydraulika a Pneumatika. No. 1, 2005, pp. 12-14.
- [33] Hess D.P.: *Apparent multi-valued friction in lubricated contact systems from tangential dynamics*. Journal of Tribology, Vol. 119, No. 4, 1997, pp. 632-638.
- [34] Berger E.J., Krousgrill C.M., Sadeghi F.: *Stability of sliding in a system exited by a rough moving surface*. Journal of Tribology, Vol. 119, No. 4, 1997, pp. 672-680.
- [35] Bąkowski A., Radziszewski L.: *An experimental and analytical study of fuel injection in diesel engine, in Problems of maintenance of sustainable technological systems*, red. L. Powierża, tom I, s. 31-48, monografia Zespołu Systemów Eksploatacji SPE KBM PAN, Polskie Naukowo-Techniczne Towarzystwo Eksploatacyjne Warszawa 2010.
- [36] Cygan S.: *Niektóre przyczyny niewłaściwej pracy rozpylaczy w silnikach wysokoprężnych*, Silniki Spalinowe Nr 3/1987.
- [37] Falkowski H., Hauser G., Janiszewski T., Jaskóła A.: *Układy wtryskowe silników wysokoprężnych. Konstrukcja, modelowanie, sterowanie*. WKŁ, Warszawa 1989.
- [38] Gąsowski W., Idzior M., Ryś J., Wierszyłowski I.: *O przydatności badań dylatometrycznych dla podnoszenia jakości wtryskiwaczy silników wysokoprężnych*, Silniki Spalinowe Nr 1/1981.
- [39] Golec K.: *Wpływ zjawisk falowych na przebieg ciśnienia w przewodach wtryskowych silników wysokoprężnych*, cz. I i II, Technika Motoryzacyjna Nr 10 i 11/1970.
- [40] Kijjarvi J.: *Diesel fuel injection system simulation*, PhD Thesis, Helsinki University of Technology, 2003, JSBN 951-22-6657-1.
- [41] Kurczyński D.: *Wpływ paliw roślinnych i ich mieszanin z olejem napędowym na wskaźniki pracy silnika o zapłonie samoczynnym*, Politechnika Świętokrzyska, Kielce 2007, praca doktorska.
- [42] Monieta J., Siedlich S.: *Structural model of injector of medium speed marine diesel engine*, Kones 2006, Vol. 13, No. 4.
- [43] Orzechowski Z., Prywer J.: *Rozpylanie cieczy*, WNT, Warszawa 1991.
- [44] Pacut M.: *Wpływ długości i kształtu przewodu wtryskowego na przebieg wtrysku w silniku o zapłonie samoczynnym*, praca doktorska, Politechnika Łódzka, Filia w Bielsku Białej, 1980.
- [45] Prescher K., Schaffitz W.: *Verschleiss von Kraftstoff-Einspritzduesen fuer Dieselmotoren infolge Kraftstoffkavitation*, Motortechnische Zeitschrift Nr 4/1979.
- [46] Pischinger R., Staska G., Gao Z.: *Berechnung des Einspritzverlaufes von Dieselanlagen bei Kavitation*, Motortechnische Zeitschrift Nr 11/1983.
- [47] Rajewski M., Walentynowicz J.: *Methodology of durability test of diesel engine injection system*, Kones 2006, Vol. 13, No. 4.
- [48] Roehl L., Preshner K.: *Theoretische und experimentelle Untersuchung der Stroemung im Dichtspalt eines Einspritzpumpenelements*, Motor technische Zeitschrift Nr 10/1982.
- [49] Roehl L., Preshner K.: *Kolbenqerverlagerung im Dichtspaltilines Einspritzpumpenelements*, Motortechnische Zeitschrift Nr 1/1984.
- [50] Wyczółkowski M.: *Analiza porównawcza charakterystyk wtrysku paliwa na stanowiskach probierczych i do komory spalania silnika z zapłonem samoczynnym*, praca doktorska, Politechnika Łódzka, 1973.

- [51] Zbierski K.: *Studium przebiegów ciśnień paliwa i ruchów iglicy rozpylacza w układach wtryskowych silników o zapłonie samoczynnym*, Zeszyty Naukowe Nr 850, Politechnika Łódzka, Łódź 2000.
- [52] Bieńkowski P.: *Czujniki pola elektromagnetycznego na przykładzie sond pola elektrycznego małej częstotliwości.*: Mat. XXXVI Międzyuczelnianej Konferencji Metrologów MKM 04.
- [53] Caruso M.J., Smith C.H., Bratland T., Schneider R.: *A New Perspective on Magnetic Field Sensing*, Honeywell, Inc. 5/98.
- [54] Gaines R.B.: *Method and apparatus for detecting a power line*. United States Patent Number 5.548.279, Aug. 20, 1996.
- [55] Grupa kapitałowa Polskie Sieci Elektroenergetyczne SA, Operator SA. *Linie i stacje elektroenergetyczne w środowisku człowieka informator* wydanie 3, Warszawa 2005.
- [56] Habrych M., Jaworski M., Szuba M.: *Wzajemna odległość pomiędzy budynkami mieszkalnymi a liniami napowietrznymi wysokiego, średniego i niskiego napięcia różnych typów w aspekcie oddziaływania pola magnetycznego* www.elektro.info.pl Nr 3/2006.
- [57] Jaworski B., Dietlaf A.: *Procesy falowe, optyka, fizyka atomowa i jądrowa. Kurs fizyki Tom III* PWN, Warszawa 1969.
- [58] Koruba Z., Tuśnio J.: *Giroskop jako stabilizator położenia kąтового pokładowych czujników do wykrywania i lokalizacji napowietrznych linii elektroenergetycznych wysokiego napięcia*, Pomiar Automatyka Robotyka Nr 2, 2008, ISSN 1427-9126, pp. 763-772.
- [59] Szmitkowski J, et. al: *Metoda i urządzenie do monitorowania zagrożeń porażenia prądem elektrycznym w warunkach prowadzenia akcji ratowniczych*. Sprawozdanie z realizacji projektu badawczego, Szkoła Główna Służby Pożarniczej, Warszawa 2003.
- [60] Tuśnio J.: *Budowa i badania bloków funkcjonalnych układu do wykrywania i lokalizacji położenia linii przesyłowej wysokiego napięcia jako źródła promieniowania elektromagnetycznego małej częstotliwości* Przegląd Elektrotechniczny (Electrical Review), ISSN 0033-2097, R. 85 NR 11/2009, pp. 164-166.
- [61] Texas Instruments: *INA333 Micro-Power (50mA), Zero-Drift, Rail-to-Rail OutInstrumentation Amplifier SBOS445B–JULY 2008–REVISED OCTOBER 2008*.
- [62] Tuśnio J., Koruba Z.: *A concept design of a wide-view angle system mounted on board of an unnamed aerial vehicle used for locating the position of a low-frequency electromagnetic radiation source*. Scientific Proceedings of Riga Technical University, Series 6 “Transport and Engineering, Transport, Aviation Transport”, No 27. Riga, RTU, ISSN 1407-8015, 2008, pp. 269-276.
- [63] Tuśnio J, Krzysztofik I.: *Koncepcja ataku startującego z pokładu okrętu bezpilotowego aparatu latającego na elektroenergetyczną linię przesyłową wysokiego napięcia*, Zeszyty Naukowe Akademii Marynarki Wojennej, Publikacje z Zakresu Automatykacji i Eksploatacji Systemów Sterowania i Łączności, ISSN 0860-889X Zeszyt Nr 177B, Gdynia 2009, s. 223-230.



# 2 MODELING IN SURFACE ENGINEERING

## 2.1. ANALYTICAL MODELS OF THE LASER BENDING PROCESS AND ITS EFFICIENCY

*Zygmunt Mucha*

Laser forming is a method of non-contact changing the shape of an object by heating it with a laser beam. Permanent, thermally induced plastic deformation of the material occurs if its thermal expansion or contraction during thermal cycle is restricted by some internal or external factor. The internal cause is the non-linear distribution of temperature. Thermal forming of metal plates with moving heat source is an effective and economical method applied in production and repairs of different structures, including ships, trains, and air planes and for rapid prototyping.

Two fundamental mechanisms of elastic-plastic deformation of material under influence of heating with a laser beam have been defined: the Temperature Gradient Mechanism (TGM) and the Buckling Mechanism (BM) [1]. It is useful to introduce the coefficient of restraint rigidity for the heating and cooling periods [2], which describes conditions of restriction for thermal expansion during the heating period and for contraction during the cooling period.

Bending under the Temperature Gradient Mechanism results in the concave shape of the workpiece. The buckling mechanism is based on the local loss of stability of the plate under influence of thermal stresses induced by laser heating [1, 3-5]. As a result the metal sheet is bent. Buckling has the bifurcative character. Therefore the direction of buckling depends on additional factors, such as the initial residual stresses, curvature of the plate or material anisotropy. In the result the bent plate can be concave or convex.

The bend angle in both mechanisms depends on laser processing parameters and material constants. It will be shown, that there exist dimensionless parameters for the process mechanisms. They can be treated as similarity numbers of laser bending. Obtained results can be used for optimization of laser forming process and enable transformation of the laser processing conditions with respect to dimensional scale or material.

The method of laser forming has many advantages and some disadvantages. To the advantages of the method belong: lack of contact between tool and the processed material, lack of the spring back effect, possibility of forming hard and fragile materials and possibility of changing shape of moving objects. To disadvantages belong: relatively low efficiency of the process and some unwanted deformations, which accompany laser forming.

The efficiency of laser bending is defined as the product of bend angle after one pass of laser beam and the laser beam velocity. The aim of the paper is to present methods to effectively increase the process efficiency. It is possible on two ways: by increasing the bend angle resulting from one laser beam pass and by accelerating the laser beam velocity. Increasing of the bend angle is possible by application of the laser beam with rectangular cross section. Increase of laser beam velocity requires simultaneous increase of laser power and control of the material surface temperature under laser beam. Maximum value of the bend angle appears when processing with the maximum surface temperature close to the melting point.

### 2.1.1. ANALYTICAL MODEL FOR BUCKLING MECHANISM

It is taken in consideration of Euler's criterion for buckling of heated, by moving of laser beam, flat plate fixed in cold material. Dimensions of the buckled plate are  $h \times b \times l_{red}$ , where:  $h$  – thickness of the plate;  $b$  – width of the plate equal to laser beam width in laser beam direction;  $l_{red}$  – reduced length of buckled plate, assumed to be equal to the laser beam width  $l$  in perpendicular to laser beam direction. Critical stress for beginning of buckling effect of the strip is expressed by Euler's formula:

$$\sigma_{cr} = \frac{\pi^2 EI_{min.}}{l_{red}^2 F} \quad (2.1)$$

where:  $I_{min.} = bh^3/12$  – minimal value of momentum of inertia of the buckled plate cross section  $h \times b$ ;  $F = bh$  – surface of the cross section of the plate and  $E$  – Yung's module. The critical stress should be equal thermal stress of fixed plate in cold material. It can be written:

$$\sigma_{cr} = \frac{\pi^2 Eh^2}{12l^2} = R_r E \alpha_{th} \Delta T_{cr} \quad (2.2)$$

where:  $\Delta T_{cr}$  – is temperature of heated plat at which the buckling effect starts;  $\alpha_{th}$  – coefficient of thermal linear expansion and  $R_r$  – is restrain rigidity coefficient, which value is between limits:  $0 \leq R_r \leq 1$ , if  $R_r = 0$  – the heated plate is free (not fixed) and for  $R_r = 1$  – the plate is fixed in rigid way. In one dimensional state of stress, the coefficient is defined as follows [2, 6]:

$$R_r = -\frac{\sigma}{E \alpha_{th} \Delta T} \quad (2.3)$$

The restrain rigidity coefficient can be estimated theoretically or experimentally. From equations (2.2) one can find condition for laser beam width depends on plate thickness and plate temperature:

$$\left(\frac{l}{h}\right)^2 = L^2 \geq \frac{\pi^2}{12R_r\alpha_{th}\Delta T} \quad (2.4)$$

The plate temperature should be between critical temperature and melting temperature:

$$\frac{2\pi^2}{3\alpha_{th}L^2} = \Delta T_{cr} \leq \Delta T \leq \Delta T_m \quad (2.5)$$

Experimentally was found [7] that for mild steel and for plate temperature closed to melting point the buckling effect start for dimensionless diameter of laser beam  $\frac{l}{h} = 16.6$ . From (2.5) we get value of the coefficient  $R_r = \frac{1}{8}$ . So critical temperature is:

$$\Delta T_{cr} = \frac{2\pi^2}{3\alpha_{th}L^2} \quad (2.6)$$

On Figure 2.1 is shown that part of flat plate under moving laser beam which width is  $l$  after buckling effect change its shape into arc with length  $s$ . It is assumed that relative increasing of length of plate is caused by thermal expansion effect. From this diagram can be written relations:

$$\frac{\Delta l}{l} = \frac{s-l}{d} = R_r\alpha_{th}(T - T_{cr}) = R_r\alpha_{th}(\Delta T - \Delta T_{cr}) = \frac{R\alpha_b - 2R\sin\frac{\alpha_b}{2}}{2R\sin\frac{\alpha_b}{2}} \approx \frac{\alpha_b^2}{24} \quad (2.7)$$

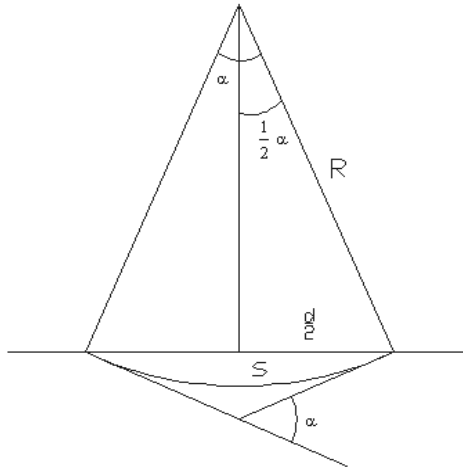


**Fig. 2.1.** Geometrical diagram for buckling effect of plate in perpendicular to laser beam direction, where  $d = l$

After using equation (2.6) and replace  $R_r = 1/8$ , bend angle of plate as a function of laser beam and material parameters can be written in following form:

$$\alpha_b = \sqrt{3n\alpha_{th}\Delta T - \frac{2\pi^2 h^2}{l^2}} = \sqrt{\frac{3n\alpha_{th}AP\kappa}{\lambda hlv} - \frac{2\pi^2 h^2}{l^2}} \quad (2.8)$$

where plate temperature heated by moving laser beam is:

$$\Delta T = \frac{AP}{\rho c_p v l h} = \frac{AP\kappa}{\lambda v l h} \quad (2.9)$$

where:  $P$  – laser beam power;  $A$  – absorption coefficient of laser beam;  $v$  – velocity of laser beam on plate surface;  $\lambda$  – coefficient of the thermal conductivity;  $\kappa = \lambda/(\rho c)$  – coefficient of thermal diffusivity;  $\rho$  – material density;  $c_p$  – specific heat of material at constant pressure;  $n$  – number of laser beam scans.

In experimental investigations of laser bending of plates, was used the CO<sub>2</sub> laser beam with power  $P$  for mod TEM 01\* is moved along plate surface with velocity  $v$ . The plate thickness  $h = 1$  mm, was made of low carbon steel St3 (max. 0.22% C, 0.1-0.35%Si, 1.2%Mn, max. 0.05%P. balance Fe). The bended plate was covered carbon absorption film ensured about 75% of laser beam absorption.

On Figure 2.2 is shown dependences of bend angle on beam diameter at constants material temperature according to formula (2.3). In this experiment  $\frac{P}{l} = 1325$  W/cm was kept constants.

Note that for  $l \approx 1.7$  cm ( $h = 1$  mm) or for  $l/h \approx 17$ , theoretical value of bend angle (2.8) drop to zero. But experimental data is about 4°. It is transition range from buckling mechanism of bending to temperature gradient mechanism, look at conditions (2.19) and (2.21).

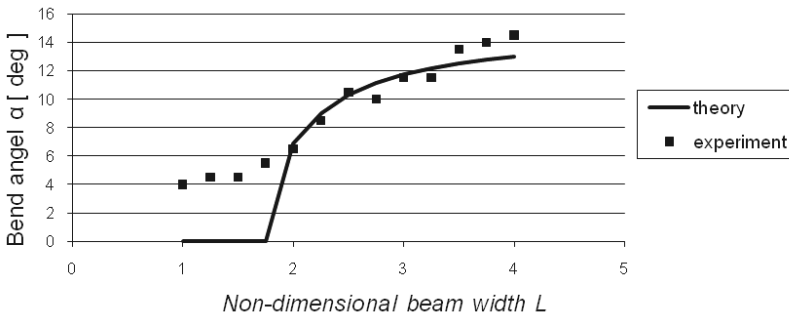


**Fig. 2.2.** Angle of bend depending on a laser beam width  $L = l/h$

## 2.1.2. MODEL FOR TEMPERATURE GRADIENT MECHANISM

Is considered bending under influence of temperature gradient mechanism TGM with moving rectangular cross-section laser beam which dimensions are  $b \times l$ . The source travels in the  $x$ -axis direction and coordinate system is fixed to the laser beam (Fig. 2.3). By heating the material by laser beam, is produced plastic strains zone. Because to thermal expansion restricted by the cooler elastic surroundings and material softening at higher temperature. Inherent strain zone of rectangular shape is assumed under the heat source path. Plastic material upsets during heating stage and thermal contraction of the zone during the cooling stage results bending of the plate. The depth of the inherent strain zone is assumed equal to the maximal depth of the isotherm  $T_{pl}$ . At this temperature material loses elastic properties, it is shown on Figure 2.4.

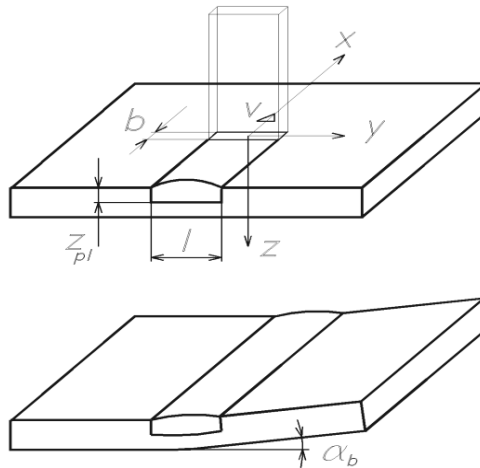


**Fig. 2.3.** Modelling of laser bending

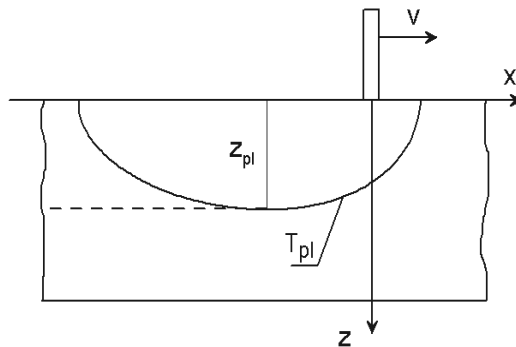


**Fig. 2.4.** The isotherm of the critical temperature

Other assumptions are:

- the temperature field is quasi-stationary in a co-ordinate system related to the heat source;
- material parameters are not depended on temperature, with the exception of the yield limit, which is assumed to drop to zero at critical temperature  $T_{pl}$ ;
- in the inherent strain zone is taken into account continuous distribution of temperature;
- the bend angle is small;
- the Fourier number is:  $F_O = (\kappa b) / (v h^2) < 1$ ;

where:  $h$  – thickness of plate;  $\kappa$  – thermal diffusivity coefficient;  $v$  – velocity of laser beam,  $b$  – dimension of the rectangular cross-section laser beam in direction of moving of laser beam.

Permanent deformation can be determined by the inherent strain method. The plate is modelled as the Bernoulli-Euler beam (mechanical beam). The stress distribution for elastic-plastic problem with imposed inherent strain due to material upsetting is described by the following equation

$$\sigma_{yy}(z) = ER_r^C (\varepsilon_{0y} + [z - (h_{cg} - z_{pl(cg)})]C + R_r^H \alpha_{th} \Delta T(z) H(z_{pl} - z)) \quad (2.10)$$

where:  $\varepsilon_{0y}$  – is the strain component characterizing material uniform elongation or shortening in the  $y$ -axis direction;  $[z - (h_{cg} - z_{pl(cg)})]C$  – is the strain component characterizing bending deformation; where  $C$  – is the plate curvature in  $y$  direction for the centre of gravity  $z = h_{cg}$ ;  $z_{pl(cg)}$  – center of gravity of depth of the inherent strain zone  $z_{pl}$  thickness. Centre of gravity for the plate, is:  $h_{cg} = h/2$  and  $z_{pl(cg)} = z_{pl}/2$ ;  $\Delta T(z) = T(z) - T_0$ ;  $H(z)$  is Heaviside's unit function ( $H(x) = 0$  for  $x < 0$ ;  $H(x) = 1$  for  $x > 0$ );  $R_r^H$  and  $R_r^C$  – are the restraint rigidity coefficient [1, 2] at the heating stage and the cooling stage, respectively.

The colder material in front of end on both sides of the heated area provides stiffness necessary for producing material thermal upsetting during heating stage. Converse the whole heat source path contracts during cooling, which results the deformation.

The following relation can express this effect:  $R_r^C \ll R_r^H$ . In the considered model  $R_r^H = 1$  is assumed.

The moving heat source for sufficiently high velocity  $v$  can be treated as a line heat source [8], which is thin in the direction of velocity and finite width in the perpendicular direction. In paper [9] was derived formula for distribution of peak

temperature in material for circular cross section of laser beam with assumption of fast moving of heat source. And in paper [6] in similar way was derived formula for dependence of peak temperature in material for rectangular cross section beam:

$$\Delta T(z) = T(z) - T_0 = \sqrt{\frac{2}{\pi e}} \frac{2AP}{\nu \rho c l \left( z + \sqrt{\frac{\kappa b}{2ev}} \right)} \quad (2.11)$$

where:  $A$  – the absorption coefficient;  $P$  – the power of the heat source;  $l$  – width of rectangular cross-section laser beam;  $\rho$  – density of material;  $c$  – specific heat;  $\lambda$  – thermal conductivity coefficient. For  $z = 0$  surface temperature  $T_S$  is:

$$\Delta T_S = \frac{2AP}{bl\lambda} \sqrt{\frac{\kappa b}{\pi v}} = \frac{2I}{\lambda} \sqrt{\frac{\kappa b}{\pi v}} \quad (2.12)$$

Note that if process parameters satisfy condition  $P/\sqrt{v} = \text{const}$  then the surface temperature becomes constant.

Equilibrium conditions for stress and momentum of stress through the plate thickness are described by equations:

$$\int_0^h \sigma_{yy}(z) dz = 0 \quad \int_0^h \sigma_{yy}(z) z dz = 0 \quad (2.13)$$

The two equations allow finding the strain  $\varepsilon_{cg}$  and curvature  $C$  after cooling the material. Solution for bend angle is:

$$\alpha_b = Cl = 3L\alpha_{th}\Delta T_{pl}\theta_S \sqrt{\frac{2}{e}} F_O \left\{ \ln \theta_S - \sqrt{\frac{2}{e}} F_O [\theta_S - \ln(e\theta_S)] \right\} \quad (2.14)$$

where: the Fourier number is:

$$F_O = \frac{\kappa b}{v h^2} = \frac{\tau_h}{\tau_d} \quad (2.15)$$

where:  $\tau_h = b/v$  is the interaction time of the heat source with the material,  $\tau_d = h^2/\kappa$  is time of heat diffusion thru thickness of the material. Dimensionless width of the rectangular laser beam is:

And surface temperature (2.12) written in dimensionless form is defined as:

$$\theta_S = \frac{T_S - T_0}{T_{pl} - T_0} = \frac{2AP}{l\lambda(T_{pl} - T_0)} \sqrt{\frac{\kappa}{\pi v b}} \quad (2.16)$$

The solution can be written in dimensional form:

$$\alpha_b = 6\sqrt{\frac{2}{e\pi}} \frac{\alpha_{th}AP\kappa}{\lambda\nu h^2} \left\{ \ln\theta_S - \sqrt{\frac{2\kappa b}{e\nu h^2}} [\theta_S - \ln(e\theta_S)] \right\} \quad (2.14')$$

The relationship for bent angle:  $\alpha_b \approx 3\frac{\alpha_{th}AP\kappa}{\lambda\nu h^2} = 3\frac{\alpha_{th}AP}{\rho c_p \nu h^2}$  is well known as analytical formula for bend angle in TGM mechanism [1, 4]. But dependence in brackets (2.14') plays very important role.

And solution for longitudinal shrinking  $\varepsilon_{0y} < 1$  in  $y$  direction or upsetting  $\varepsilon_{0z} > 1$  in  $z$  direction is found from conditions (2.13) written in form is:

$$\varepsilon_{0y} = -4\sqrt{\frac{2}{e\pi}} \frac{\alpha_{th}AP\kappa}{l\lambda h\nu} \left[ \ln\theta_S - \frac{3}{4}\sqrt{\frac{2F_O}{e}} (\theta_S - \ln e\theta_S) \right] = -\varepsilon_{0z} \quad (2.17)$$

where  $\varepsilon_{0z} = -\varepsilon_{0y}$  is strain of upsetting in thickness of plate, because strain along laser beam  $x$ -direction along the laser track  $\varepsilon_{0x} \ll \varepsilon_{0y}$ .

Note that laser thermal deformations are determined by three dimensionless parameters expressed by Esq. (2.4), (2.15) and (2.16). So these parameters play role of similarity numbers of laser thermal forming. These parameters help to transform parameters of laser bending from one scale or material to another.

This dependence (2.17) is useful for calculate of laser upsetting of plate. But solution (2.14) is used in laser forming technology.

Solutions (2.14) and (2.17) are valid if depth of the inherent strain zone not exceeds the thickness of the plate, which is  $Z_{pl} = z_{pl} / h \leq 1$ . From Esq. (2.11) and (2.12) this condition can be written as:

$$Z_{pl} = \sqrt{\frac{F_O}{2e}} (\theta_S - 1) \leq 1 \quad (2.18)$$

Permanent deformation of bend angle is  $\alpha_b > 0$  if  $T > T_{pl}$  or if  $\theta_S > 1$ .

Now question is how wide can be laser beam in TGM mechanism? Answer is that width of the laser beam should not experience buckling effect. Li and Yao [5] found on experimental way condition for buckling effect for low carbon steel is:

$$L_b = \frac{l}{h} \geq 16.3 \pm 0.3 \quad (2.19)$$

On Figure 2.2 the value is  $L_b \approx 17$  which is near to (2.19).

From relation (2.5) criterion for buckling mechanism is:

$$L \geq \sqrt{\frac{2\pi^2}{3\alpha_{th}\Delta T_{cr}}} \quad (2.20)$$

Because temperature of bended material is in range between melting temperature and temperature when material loses its elastic properties i.e.  $\Delta T_{pl} < \Delta T_{cr} < \Delta T_m$  so for low carbon steel is:  $26.4 > L > 16.6$ . One can see that Li and Yao take in account melting temperature. Conclusion is that in order to avoid buckling effect should be fulfilled condition opposite to (2.20) i.e.

$$L = \frac{l}{h} < \sqrt{\frac{2\pi^2}{3\alpha_{th}\Delta T_m}} \quad (2.21)$$

This condition has application for TGM mechanism as a criterion for maximal value of width of laser beam related to thickness of bent plates. From (2.17) is reasonable for beginning TGM mechanism to take the lowest value of the measured by W. Li and L. Yao [5], so width of the beam related to thickness of plate should be smaller than 16.0. It can be concluded that transition region between BM and TGM mechanism is for width of the laser beam is

$$17 > L > 16.0 \quad (2.22)$$

After founding analytical solutions for plate bending by use buckling and temperature gradient mechanism it is possible to formulate quantitative conditions for each kind of bending thermal mechanisms:

- Conditions for existence of buckling mechanism BM of plate bending:

$$\frac{2\pi^2 h^2}{3\alpha_{th} l^2} = \Delta T_{cr} \leq \Delta T = \frac{AP}{\rho c_p v h l} < \Delta T_m \quad \text{and} \quad F_O = \frac{\kappa b}{v h^2} > 1$$

- Conditions for temperature gradient mechanism TGM:

$$\Delta T_{pl} < \Delta T_S = \frac{2AP}{l\lambda} \sqrt{\frac{\kappa}{\pi v \kappa}} < \Delta T_m \quad \text{and} \quad F_O = \frac{\kappa b}{v h^2} < 1$$

- Conditions for upsetting mechanism UM:

$$\Delta T_{pl} \leq \Delta T = \frac{AP}{\rho c_p v h l} < \Delta T_{cr} = \frac{2\pi^2 h^2}{3\alpha_{th} l^2} \quad \text{and} \quad F_O = \frac{\kappa l}{v h^2} > 1$$

where:  $\Delta T_{pl}$  – temperature of material at which it lost elastic properties: for example for mild steel  $\Delta T_{pl} = 610^{\circ}\text{C}$ ; for stainless steel  $\Delta T_{pl} = 570^{\circ}\text{C}$ ; for aluminium  $\Delta T_{pl} = 180^{\circ}\text{C}$ ; for austenitic steel  $\Delta T_{pl} \approx 900^{\circ}\text{C}$ .

### 2.1.3. EXPERIMENTS

Experiments were carried out on samples made of plain carbon steel sheets St3. Rectangular plate of dimensions 150x100x3 mm were coated with graphite, which ensured approx. 77% absorption of the laser beam energy by the material. Laser beam was produced by TLF6000 TRUMPF CO<sub>2</sub> laser of 6 kW maximal power. The intensity distribution described by the Transverse Electromagnetic Mode pattern was TEM01\* in the case of circular laser beam. The rectangular laser beam was produced with a segmented mirror to dimensions 11x6.5 mm.

Set-up used in experiments is presented in Figure 2.5. The scanning CNC table was moving specimens along the straight line under the laser beam. Inductive displacement sensor LVDT mounted at some distance from the laser path measured deflection of the plate during bending process. The bend angle was calculated from deflection measurements. Bending deformation resulting from the first scan of every specimen was taken into considerations.

Material temperature in the laser spot was measured during processing. Two-colour fiber optic pyrometer Raytek FR1A CF1 was employed. Disturbance from the reflected laser radiation required application of a special filter. The necessary recalibration of the pyrometer resulted in shifting of the measured temperature range towards higher temperatures. A contact sensor (thermocouple) was applied to ensure the same initial material temperature for every specimen and irradiation.

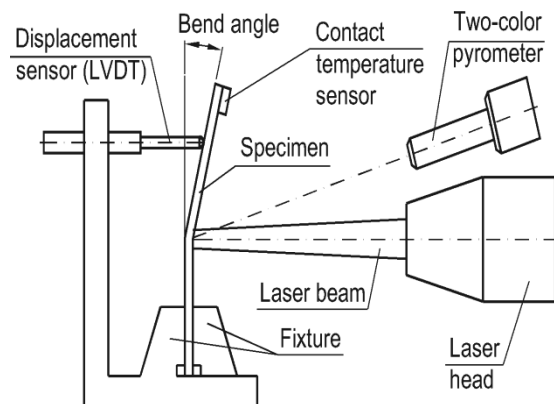


**Fig. 2.5.** The experimental set-up

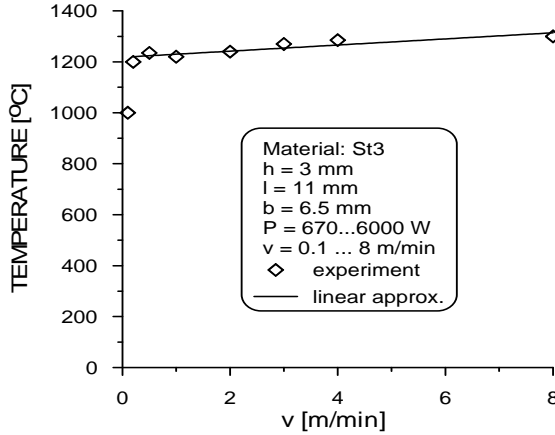


**Fig. 2.6.** Laser spot temperature programmed according to the condition  $T_S \propto P/\sqrt{v} = \text{const}$

The bend angle as a function of dimensionless surface temperature and Fourier number is shown on Figure 2.7 [10], where:  $\alpha_B = \alpha_b / (\alpha_{th} \Delta T_{pl})$ . On Figure 2.8 is shown experimental verification of the bend angle dependence Eq. (2.14) for plats thickness 2, 3 and 4 mm made of mild steel. Reasonable agreement of experimental and analytical results has been found. Interesting and useful result we can get from solution (2.17) with condition that the surface temperature  $\theta_S$  (2.21) is kept constant. The optimal value of the Fourier number with respect to the bend angle maximum is:

$$F_O^{opt} = \frac{e \ln^2 \theta_S}{8(\theta_S - \ln(e\theta_S))^2} \quad (2.23)$$

Assuming for mild steel, that surface temperature is close to melting condition  $\theta_S \approx 2.5$  we obtain  $F_O^{opt} = 0.837$ . We can see this point on Figure 2.7.

We can get the maximal value of the bend angle from (2.14) applying (2.23):

$$\alpha_b^{\max} = \frac{3L\alpha_{th}\Delta T_{pl} \ln^2 \theta_S}{4(\theta_S - \ln(e\theta_S))} \approx 2.7L\alpha_{th}\Delta T_{pl} = \frac{2.7l\alpha_{th}(T_{pl} - T_0)}{h} \quad (2.24)$$

Using condition  $\theta_S \leq 1$  in Eq. (2.16) the threshold heat source power for producing permanent deformation can be derived as:

$$P_{thres} = \frac{\lambda(T_{pl} - T_0)}{2A} \sqrt{\frac{\pi v b}{\kappa}} \quad (2.25)$$

In other hand the surface temperature should not exceed melting point. So conditions for surface temperature are:

$$1 < \theta_S < \theta_m = \frac{\Delta T_m}{\Delta T_{pl}} \quad (2.26)$$

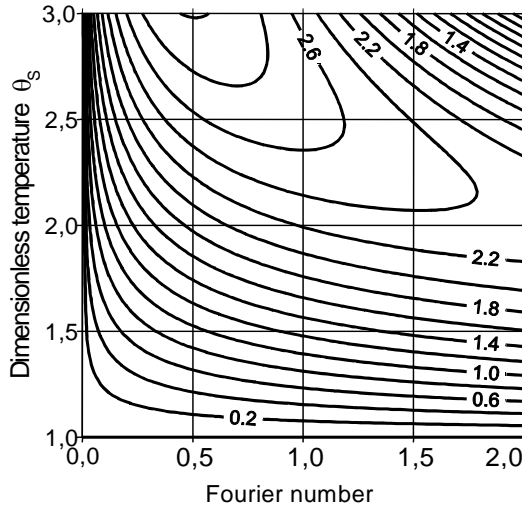


**Fig. 2.7.** Contour map of dimensionless band angle as a function of surface temperature and the Fourier number [10]

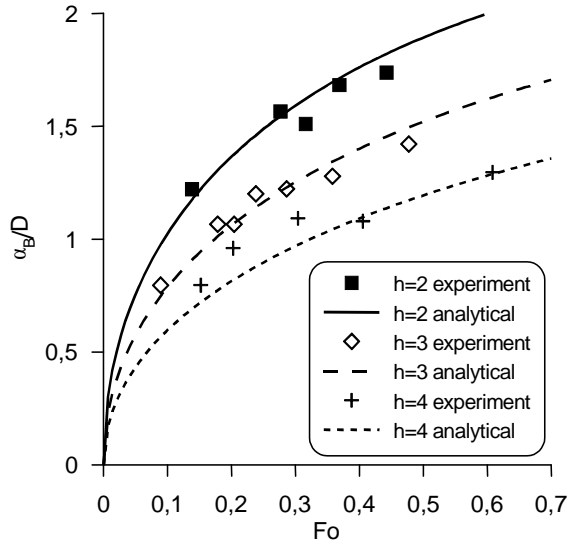


**Fig. 2.8.** Experimental and theoretical dependence of normalised bend angle on the Fourier number [10]

## 2.1.4. EFFICIENCY OF LASER FORMING PROCESS

Efficiency or capacity of the process of laser bending as economical parameter was defined in 1997 by F. Klocke and al. [11] as product of bending angle at one pass  $\alpha_b$  and velocity of laser beam on material surface  $v$  in units (deg·cm/sec):

$$E_P = \alpha_b \cdot v \quad (2.27)$$

In order to analyze the efficiency we are going to use analytical solution of bend angle for temperature gradient mechanism (2.14). Formula for the efficiency parameter is:

$$E_P = 3vL\alpha_{th}\Delta T_{pl}\theta_S \sqrt{\frac{2}{e}F_O} \left\{ \ln\theta_S - \sqrt{\frac{2}{e}F_O} [\theta_S - \ln(e\theta_S)] \right\} \quad (2.28)$$

with respect to condition (2.16). The formula written in dimensional units has form:

$$E_P(v) = 3\sqrt{\frac{2\kappa b v}{e}} \frac{l}{h^2} \alpha_{th}\Delta T_{pl}\theta_S \left\{ \ln\theta_S - \sqrt{\frac{2\kappa b}{evh^2}} [\theta_S - \ln(e\theta_S)] \right\} \quad (2.29)$$

where

$$\theta_S = \frac{2AP}{l\lambda(T_{pl} - T_0)} \sqrt{\frac{\kappa}{\pi v b}} = \text{const} \quad (2.30)$$

And after changing argument in (2.30) from velocity  $v$  into laser power  $P$  by using (2.30):

$$E_P(P) = 6\sqrt{\frac{2}{e\pi}} \frac{\alpha_{th}AP}{h^2\lambda} \left\{ \ln\theta_S - \sqrt{\frac{\pi}{2e}} \frac{lb\lambda\Delta T_{pl}\theta_S}{hAP} [\theta_S - \ln(e\theta_S)] \right\} \quad (2.31)$$

In case of multi pass forming or bending in this solution should be used assumption, that bend angle is proportional to number of scans.

On Figure 2.9 is presented experimental and theoretical dependence bend angle on the velocity of the rectangular laser beam at constant surface temperature according to formula (2.12). Maximal experimental value of bend angle is 2.8 deg. is for 3.3 cm/s and from this point the bend angle decreases according to (2.14), so is proportional to  $1/\sqrt{v}$ . On Figure 2.10 is shown the efficiency parameter (2.26) as a function of laser beam velocity et condition, when surface temperature is constants (2.12). Experimental results are represented by circular points but solid curve represents theoretical prediction. Note that efficiency parameter increases proportionally to  $\sqrt{v}$  in spite of bend angle decreases as  $1/\sqrt{v}$ .

After increasing velocity from value at which bend angle is maximal (2 m/min) to 30 m/min (50 cm/s) the efficiency parameter increases from 9 to 45 deg·cm/c that is factor 5. In order to keep constant surface temperature is necessary laser beam of about 8.5 kW power.

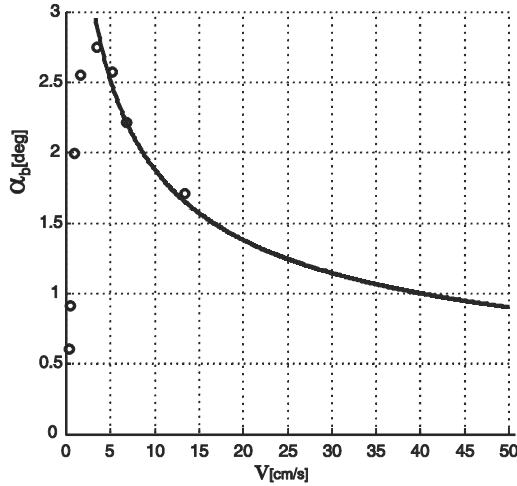


**Fig. 2.9.** Dependence of the bend angle on the velocity of the rectangular laser beam at constant surface temperature (2.30), where: points – experiment; line – theory (2.14)

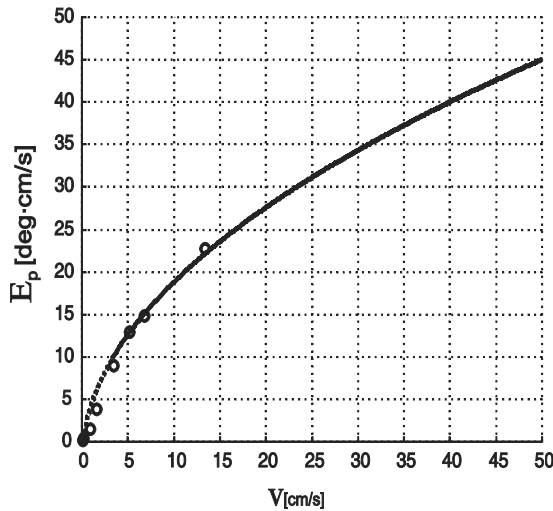


**Fig. 2.10.** Dependence of the efficiency parameter on the velocity of the rectangular laser beam at constant surface temperature (2.30), where: Points – experiment; line – theory (2.29)

On Figure 2.11 is presented efficiency parameter as functions of laser power (2.31) at constant surface temperature under the beam. The dependence illustrates effect that efficiency parameter increases proportionally to laser power.

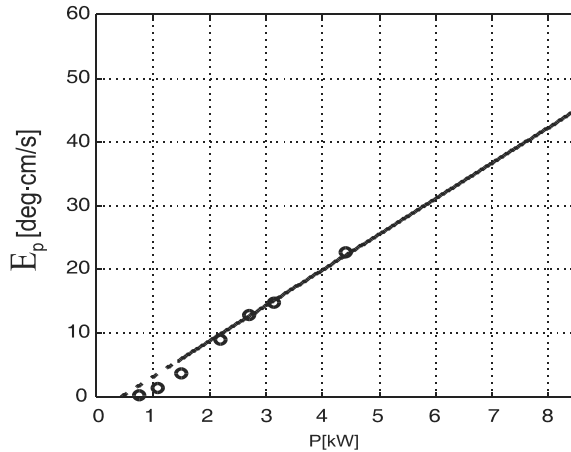


**Fig. 2.11.** Dependence of the efficiency parameter on the velocity of the rectangular laser beam at constant surface temperature (2.30), where: Points – experiment; line – theory (2.31)

For theoretical value of laser beam velocity 50 cm/s (30 m/min) on Figure 2.10 corresponds laser power 8.5 kW on Figure 2.11.

The present study shows that:

1. New theoretical model of laser bending of plates by use of thermal buckling mechanism is presented and results of this model was verified experimentally for low carbon plates.
2. The general strategy of laser forming should be assumed constants material temperature under laser beam.
3. In the paper are derived solutions for bend angle and upsetting of plates, for rectangular cross section of laser beam for TGM mechanism. The solutions depend on three dimensionless parameters: the Fourier number  $Fo$ , surface temperature  $\theta_s$  and dimensionless width of the laser beam  $L$ . These parameters play the role of similarity numbers of thermal forming processes.
4. The solution for bend angle describes characteristic effects observed experimentally: existence of the power threshold for thermal bending and existence of the maximum bend angle as a function of the Fourier number at constant surface temperature for each experimental points.
5. The solution for bend angle was helpful to analysis of the efficiency parameter of laser forming. In the paper was proved that efficiency parameter increases proportionally to laser power and to square root of beam velocity if surface temperature is kept constant. It is experimentally showed that efficiency of the process was increase of factor 2.
6. Rectangular cross – section of laser beam allows to control of laser bending process more flexible and to reach bigger bend angles then for circular beam, by independent controlling of laser track width and time of laser material interaction.

## **2.2. APPLICATIONS OF LASER FORMING IN MICRO TECHNOLOGIES**

*Jacek Widłaszewski*

Technology of laser micro-adjustment and alignment enables miniaturization of mechanic-optic-electronic micro-systems in optical and electronic industries. The required positioning accuracy is in the sub-micrometer range nowadays and adjustment in mass production must be obtained within seconds. Conventional methods applied in assembly and adjustment are inefficient in case of parts and subassemblies of overall dimensions within a few millimetres. Limited accessibility for mechanical tools makes it difficult to compensate for inaccuracies inherent to the production of individual elements and to methods of joining them together during the assembly stage. Limitations posed by mechanical, i.e. contact, methods of positioning and functional adjustment can be overcome by application of the laser forming method, which relies upon controlled producing of the work-piece deformation by heating it locally with a laser beam.

The method of bending or straightening structural steel members like beams, girders and plates using flame torches, known as flame bending or heat straightening [12-14], has been used in engineering since long ago, probably since the beginnings of welding [15]. Emergence of the laser as a well-defined heat source opened-up prospects for improvements in control, accuracy and automation of thermal forming processes [16, 17]. Among pioneers of the research on the laser forming method are Koichi Masubuchi [18], Yoshiharu Namba [19] and Polish scientists – Henryk Frąckiewicz and Zygmunt Mucha [20].

### **2.2.1. NEW CONCEPT OF ASSEMBLY AND ADJUSTMENT USING A LASER BEAM**

Conventional techniques applied in assembly of micro-parts include laser welding or gluing, followed by time-consuming alignment with expensive tools. Due to the undesirable thermo-mechanical deformations, the ultimate accuracy of high-precision laser welding in industrial applications is limited to several micrometers. The spring-back phenomenon is another factor limiting precision of mechanical alignment operations with external actuators. Application of laser induced deformations in automatic mass production of micro-parts has led to the laser adjustment technology, where the sub-assembly is at first “roughly” positioned during fixing, and afterwards is precisely aligned using the laser beam acting on a specially designed actuator, which is a part of the product. Research on the technology was sponsored by the European Community within the framework of the Brite-Euram project BE-1230 titled “Accurate Manipulation Using Laser Technology” (AMULET). The technology allows for improvement in positioning accuracy by one order compared to conventional methods, e.g.  $\pm 0.3$  micrometers versus  $\pm 3$  micrometers [21].

Non-contact precise manipulation, adjustment and alignment of miniature components are widely performed using the out-of-plane deformation induced by heating with a laser beam. The process is known as laser bending, and its characteristic feature is a steep temperature gradient in the material thickness direction. Hence, the involved mechanism of deformation is called the Temperature Gradient Mechanism (TGM) [22].

Another approach applied in touch-less micro-positioning is based on laser-induced material upsetting, possibly uniform on the element cross-section. With suitable laser processing parameters a tiny, but precise shortening of selected material areas is produced. The areas, which undergo deformation, are called bridges.

### 2.2.2. TOUCH-LESS POSITIONING OF ELECTRIC CONTACTS

Probably the first industrial application of laser forming [19] was in manufacturing of a miniature electric relay D2 by Siemens AG [23]. In the relay of overall dimensions approximately 20x15x10 mm there are pairs of electric contacts placed on so-called contact blades. The distance of contacts has to be set during the assembly of the relay with accuracy 0.01 mm or better. According to the invention by R. Martin and G. Kohler from the Siemens Company [24], a Nd:YAG pulsed laser beam is used to locally heat arms of the contact blades and produce tiny angular deformations of the arms (see Fig. 2.12). Initially the contacts are mounted with zero distance  $D$  between them, and during the adjustment process the distance  $D$  is increased up to the desired value by incremental bending of the contact arm. Bending towards the laser beam is used.

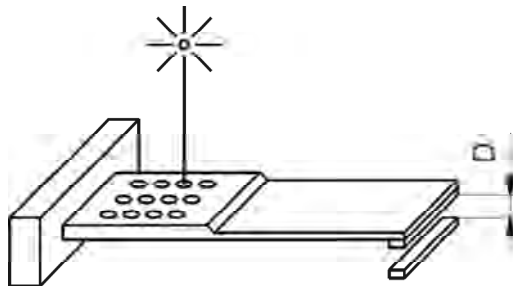


**Fig. 2.12.** Laser adjustment of the static distance  $D$  between contacts in an electric relay

The applied pulse energy is up to 19 J and pulse duration is up to 10 ms. Laser pulses cause melting of the contact blade material in spots, which are arranged in rectangular array. The magnitude of the angular deformation was controlled by computer-controlled selection of laser heating spots (melt pools). An example of the array is shown in Figure 2.12 and consists of 3x4 laser spots, each approximately 0.4 mm in diameter. Using a laser with pulse repetition 10 to 12 Hz, the process of laser shooting and the cooling period took approximately 1.5 second. Together with auto-

mated, optical determination of exact positions of contact blades before shooting, the adjustment process required 3 seconds. Depth of the heat-affected zone was estimated to 1/3 of the blade thickness. Response of the blade to the individual laser beam pulse had reproducibility of  $\pm 10\%$  concerning the angular deformation, even without additional cleaning of the blade surface. Due to the noncontact energy transfer to the work-piece and due to the automation of the adjustment process, very short production cycles were achieved, making the method ideal for mass production. For example, 13 millions of laser adjusted relays were produced in 1999 [25].

### 2.2.3. LASER ADJUSTMENT OF REED SWITCHES

A reed switch is an electric contact component. It consists of two metal contact plates hermetically sealed inside a glass tube. Position of plates is controlled by external magnetic field. The contact plates are made of magnetic material and attract each other in the magnetic field, thus allowing electric current to flow through the element. A schematic of a reed switch is shown in Figure 2.13.

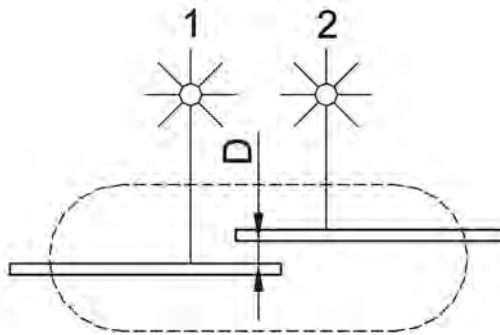


**Fig. 2.13.** Laser adjustment of the static distance  $D$  between contacts in a reed switch

The distance  $D$  between contacts should be set during the manufacturing process to the value 10-50 micrometers. Deviations of distance  $D$  adversely affect performance of the device, because the magnetic field strength necessary for the switching action strongly depends on the distance value.

Application of laser micro-bending enabled precise adjustment of reed switches with micron accuracy in mass production of the Philips Company [26-28]. Adjustment of the distance between contacts can be made on switches already assembled and sealed, through the glass enclosure. Appropriate selection of the laser source wavelength facilitates transmission of radiation through the walls of a glass tube. Argon-ion lasers operating at 454.5-514.5 nm wavelengths [27] and frequency-doubled Nd:YAG lasers with 532 nm wavelength [26] are suitable for the purpose. Bending in position 1 (see Fig. 2.13) with the Temperature Gradient Mechanism, i.e. towards the laser beam, results in decrease of the distance  $D$ , whilst laser heating in position 2 gives the opposite effect. The technology

allows for significant improvement in the economic aspect of production by reduction of waste products, which otherwise had to be rejected or sorted and stored for any future contracts.

#### 2.2.4. ADJUSTMENT OF MAGNETIC HEADS IN AUDIO AND VIDEO DEVICES

Potential of the laser forming method for the adjustment of recording heads of digital video and audio systems was intensively investigated by the leading manufacturers of the electronic industry – Matsushita Electric Industrial Co., Ltd. [29-31] and Philips Electronics N.V. [21], [32]. Read and write heads of the Digital Audio Tape (DAT) recorders were positioned using this method with a tolerance better than 0.1 micrometer [33], [34]. Adjustment of magnetic heads in video recorders was made “on the flight”, e.g. on heads rotating with 1800 rpm. Achieved positioning accuracy was better than 0.5 micrometer [28]. A variety of laser micro-bending applications, including adjustment of magnetic heads and micromechanical relays, have been reported to be implemented actually or to be under development in Japan [35].

#### 2.2.5. LASER ADJUSTMENT IN MANUFACTURING OF HARD DISK DRIVES

The read/write magnetic head in a computer hard disk drive (HDD) is located on a slider with an air-bearing surface. The slider is mounted on the so-called load beam, which in turn is connected to a base plate driven by an actuator to displace the head between disk tracks (see Fig. 2.14).

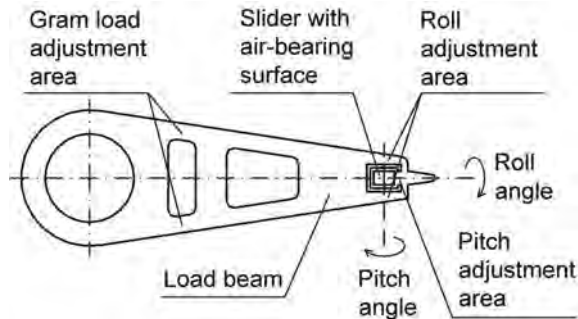


**Fig. 2.14.** A simplified view of the head suspension in a hard disk drive

When the disk rotates, the aerodynamic force generated on the air-bearing surface pushes the slider away from the disk surface. The head suspension assembly acts as a mechanical support and a spring, which counteracts the air-bearing forces. High density of the information storage on a magnetic medium requires very small (about 10 nm) height of flight of the head over the disk surface to be maintained. This distance is kept in a dynamic equilibrium and depends on a preload force called the gram load.

Laser-induced micro-deformations are widely applied for adjustment of the head suspension assembly and for shape correction of the air-bearing surface. The issues have been addressed in many patent applications of the leaders of the disk drive industry, e.g. [36-39]. For example, development of laser micro-bending technology at the Fujitsu company started in about 1993 [40]. Initially laser bending was used for rapid prototyping, but research results revealed that it is an excellent processing method for adjustment of high precision mechanism of a computer hard disk drive [38]. A Q-Switched YAG laser beam has been used to adjust angular position of the slider, i.e. to set the pitch angle and the roll angle.

Based on measurement results of the suspension in its initial state, several parameters of laser bending can be chosen to perform required shape correction: laser beam energy, pulse frequency, laser spot size, its location and irradiation time for spot adjustment, or scanning length, speed and pitch for scanning adjustment. Laser micro-bending has been applied by different HDD manufacturers to adjust the gram load (and so the flying height), the pitch and roll angular positions and to shape the air-bearing surface. Frequency-doubled Nd:YAG lasers are preferred with 532 nm wavelength or diode lasers with radiation wavelength less than 1100 nm, because they offer better efficiency of laser beam energy transfer into metals, as compared with sources of longer radiation wavelength. Using pulses of several nanoseconds duration time and energy below 100 mJ, local melts can be produced with the depth in the micrometer range. Temperature of the entire head suspension assembly is increased only by a few Celsius degrees after such heat pulse [37].

While local melts produce bending towards the laser beam, annealing of a bend, which is in a loaded state, can result in both increase or decrease of the bend angle, dependent on the load direction. The latter effect was utilized to decrease the gram load using infrared lamps, which can be replaced successfully with a laser heat source [37].

Correction of the air-bearing surface can be performed by laser-induced partial relaxation of residual stresses, that are left in the element after previous processing stages. The technique allowed making shape changes of  $\text{Al}_2\text{O}_3\text{-TiC}$  ceramics in a nanometer scale, beyond possibilities of conventional methods [35, 40, 41]. The Laser Curvature Adjust Technique (LCAT) has been implemented into high-volume manufacturing of ceramic sliders at the IBM Corporation [41].

### **2.2.6. ACTUATOR WITH EMBOSSEMENT**

Figure 2.15 presents design of an actuator, which can be made to bend either towards the laser beam, i.e. in the  $+z$  direction, or in the opposite direction. The concept is based on producing negative plastic strain above or below the neutral axis of the structure. Local heating of regions 1a and 1b, with suitable operating parameters, brings about material upsetting and shortening of the regions. As a result the free end of the actuator moves in the  $+z$  direction. If laser heating produces shortening of region 2, the structure bends in the  $-z$  direction, i.e. away from the laser beam. The design of an actuator with embossment has been developed for applications in CD players [28].

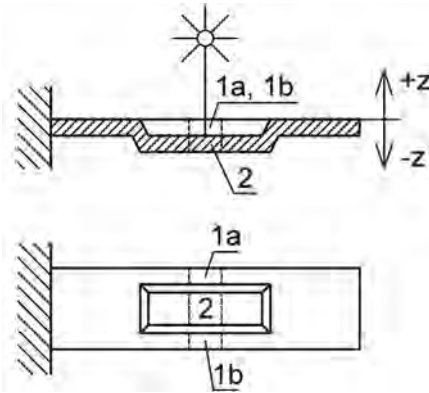


**Fig. 2.15.** An actuator with embossment

### 2.2.7. BRIDGE ACTUATORS

M. Koster and R. Semmeling of the Philips Electronics N.V. invented a method of mutually displacing two or more parts using an actuator, which undergoes plastic deformation through local heating [42]. The actuator consists of a number of bridges. Thermal elongation of a bridge during local heating is hindered by the stiffness of the rest of the actuator, in particular – of the other bridges. Decrease of the material yield stress with increase of temperature may result in a plastic deformation under compressive stress, i.e. material thermal upsetting in the heated bridge. After return to the initial temperature the bridge is shorter than before heating. Sequence of heat pulses applied to different bridges results in deformation of the whole actuator. Local heating conveniently can be accomplished with a laser beam.

One of the embodiments of the invention is the so-called truss or framework actuator, shown in Figure 2.16.

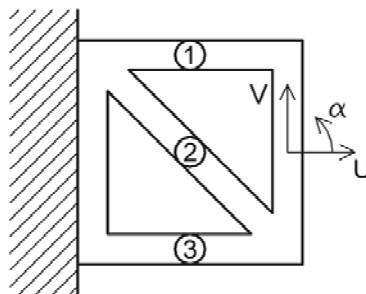


**Fig. 2.16.** The truss (framework) actuator

Shortening of the bridge 2 makes the segment shown on the right-hand side of Figure 2.16 to move in direction V, relative to the fixed, left-hand side of the actuator. If bridges 1 and 3 are shortened, a mutual displacement in the opposite direction is produced. Shortening of bridge 1 results in rotation of the right-hand side

segment in direction  $\alpha$ , while shortening of bridge 3 produces the opposite rotation. In fact, the induced deformations always have U, V and  $\alpha$  components more or less pronounced, but applications of the actuator for positioning can be designed in such a way, that the unwanted displacements are insignificant. The undesirable bending, i.e. out-of-plane deformation, can be minimized by a suitable choice of laser heating parameters. In order to minimize temperature gradient in the material thickness direction, time of heating should be large enough compared to the characteristic time of heat penetration through the material thickness. The Fourier similarity number value represents this condition and its value should be significantly greater than 1, if the temperature gradient is to be small.

The concept of the truss actuator was developed for positioning CCD chips, magnetic heads in Digital Compact Cassette devices and components of electron guns. Single laser pulse can produce linear displacement of few tens of micrometer or the angular displacement of a few milliradians [21], [42]. Using the truss actuator as a basic cell, more complex adjustment structures were designed. Two truss actuators were applied in an adjustment structure developed for positioning micro cylindrical lenses and its arrays in high power diode lasers [43].

Another embodiment of the Koster's and Semmeling's invention is the two-bridge actuator, wherein there is no bridge 2 of the truss actuator shown in Figure 2.16, and the bridges 1 and 3 usually are placed close one to the other. Alternate laser heating of bridges 1 and 3 results in shortening of such an actuator. A theoretical model of the two-bridge actuator is presented in [44].

Two-bridge actuators are combined in various configurations for different micro-positioning applications. An example is shown in Figure 2.17, where four two-bridge actuators enable angular positioning of the x-y plane with a sub-milliradian accuracy. Such designs have been developed for alignment of lenses in the optical pick-up units in CD and DVD players [28, 45, 46].

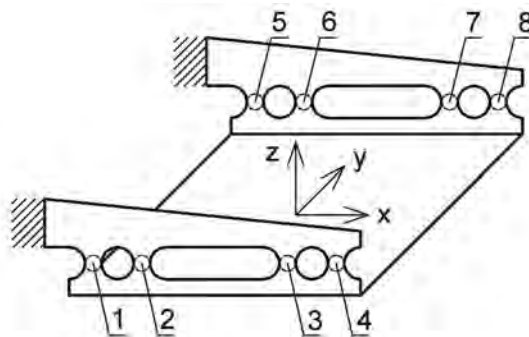


**Fig. 2.17.** Angular positioning of the x-y plane using four two-bridge actuators

Figure 2.18a shows an example of the so-called tube actuator, in which several two-bridge actuators are placed axisymmetrically on a tube-like structure. Such actuators were proposed for alignment of optical elements, e.g. lenses or fibers.

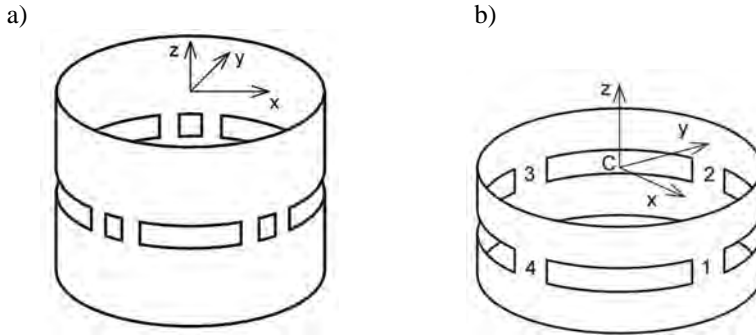


**Fig. 2.18.** Tube actuators: a) with three double bridges, b) with four single bridges

Shortening of bridges by pulsed heating with a laser beam enables precise positioning of a part or subassembly attached to one end of the actuator with respect to the other. Laser-induced deformation can be used to adjust the angular position of the x-y plane or to produce linear displacement in x and y directions [43, 47, 48]. A four-bridge axisymmetric actuator is presented in Figure 2.18b, while Figures 2.19 and 2.20 show possibilities of producing linear displacements with such an actuator [49].

Central point C of the top part of the actuator can be displaced (by  $\Delta x_C$  and  $\Delta y_C$ , as in Figures 2.19 and 2.20) with respect to the bottom part using different heating sequences. The examined structure was made of a stainless steel tube, 6 mm in diameter and 6 mm long. Deformations were produced with a Nd:YAG laser beam of power 76 W (Fig. 2.19) and 55 W (Fig. 2.20).

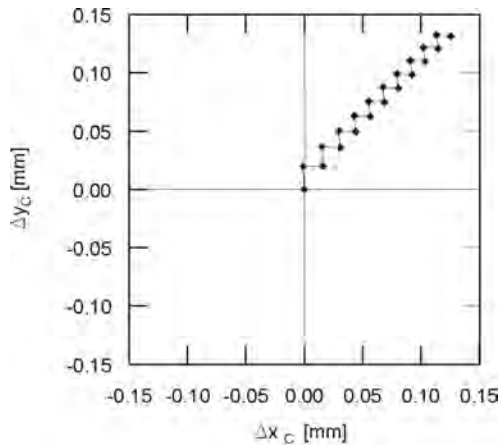


**Fig. 2.19.** Deformation of the four-bridge tubular actuator during sequential laser heating of bridges 1 and 2 (shown in Figure 2.18b) with the laser beam power 76 W

Optical communication networks require precision alignment of optical fibers with respect to lenses and laser diodes, e.g. the first lens has to be adjusted with respect to a semiconductor laser beam with an accuracy of  $\pm 0.5$  micrometer in a

lateral direction and  $\pm 2$  to  $\pm 5$  micrometer in the longitudinal direction. Various configurations of actuators have been developed to perform accurate adjustment of collimating optics during assembly of fiber optical devices. The tight positioning tolerances of optoelectronic components can be met by application of bridge actuators and angular actuators, which are based on laser micro-bending [50].

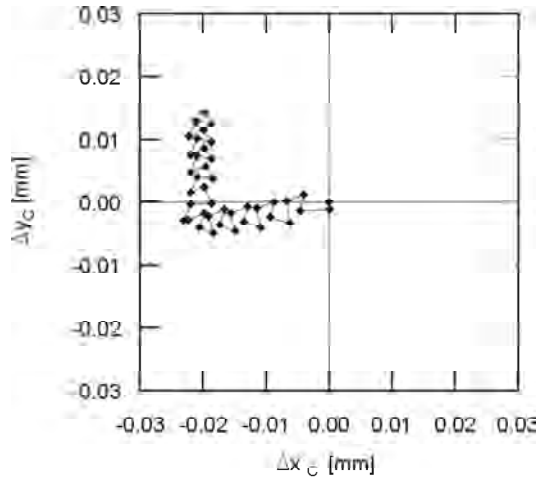


**Fig. 2.20.** Deformation of the four-bridge tubular actuator during sequential laser heating of all bridges (shown in Figure 2.18b) with the laser beam power 55 W

An array of three-bridge axisymmetric actuators (one actuator is shown Fig. 2.21) has been developed for applications in fiber-optical collimator arrays [51]. It enables precise alignment of fibers with respect to a micro lens array. An optical fiber located in the center of the actuator can be displaced by up to 10 micrometers in the x and y directions, with positioning precision better than 0.1 micrometer. Displacement results from shortening of a bridge (1, 2 or 3 in Fig. 2.21) locally heated by a laser pulse. The other bridges become stretched and distorted.

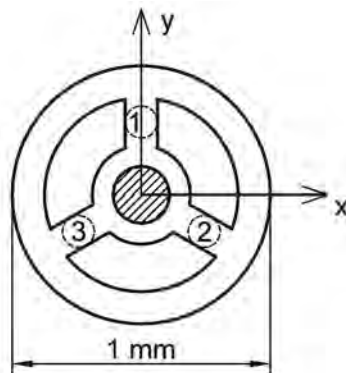


**Fig. 2.21.** A three-bridge axisymmetric actuator designed for positioning of optical fibers

## 2.2.8. THERMAL STABILITY OF POSITIONING

Laser forming processes, like many other thermo-mechanical processing methods, involve producing high stresses, up to the yield point value. Without any post-processing thermal treatment, the residual stress can also often have the level of the room temperature yield stress value. High residual stresses are disadvantageous taking into account thermal and long-term stability of alignment and positioning.

Solution to the problem is based upon the dependence of the material yield stress on temperature, i.e. the general for metals decrease of the yield stress value with increase of temperature. During heating of metals with locked-in stresses, increase of temperature to the value, at which material yield stress is lower than the initial residual stresses, results in the material plastic flow and reduction of stresses. The phenomenon is known as stress relief annealing and is widely exploited in metal working. In processes of laser forming, the heating preferably can be carried out using the same heat source, as is used for forming, i.e. with the laser beam, but with suitably changed operating parameters. Such a process can be called laser annealing. Due to dimensional changes, which occur during stress relieving, the steps of adjustment and annealing should be performed iteratively, or the adjustment step should produce an “overshoot” to be canceled during annealing.

Hoving and Verhoeven of the PHILIPS ELECTRONICS NV described high-precision micro-assembly using laser-adjustment method with local laser annealing [45]. While laser spot in adjustment steps applied to the actuator with embossment had the diameter 200 micrometers in their example, the local laser annealing spot was 600 micrometers in diameter.

Huber, Müller and Meyer-Pittroff presented a Finite Element Method (FEM) analysis of stress and strain changes in the two-bridge actuator under laser annealing [52]. They found the processing window, i.e. ranges of processing parameters necessary to perform laser annealing for the case they considered. Exemplary processing parameters for the adjustment were: pulse energy 0.2 J, pulse duration 1 ms and laser spot diameter 200 micrometers. Laser annealing was performed with pulse duration 5 ms and spot diameter 600 micrometers.

Müller, Ströl and Mehnert of the AIFOTEC AG Fiberoptics described in a patent application an adjustment method, especially suitable for adjusting micromechanical, optical or fiber optical components or subassemblies [48]. According to the invention, a laser beam or other high-energy beam is applied to induce plastic deformation of a bridge actuator. The adjustment steps are followed by heating the material, at least locally, to the so-called critical temperature, at which plastic flow process, resulting from the residual stress relieving, is sufficiently completed, so as to avoid unwanted deformations of the actuator during normal operation, i.e. within its operating temperature range (e.g. a range from -40 to +80 degree Celsius). The critical temperature is related to the material yield stress value at the upper limit of the operating temperature range. A Nd:YAG or diode lasers have been proposed to realize both the adjustment and annealing steps of positioning.

The unique features of the laser forming method, i.e. the lack of mechanical contact between the tool and the work-piece, the ease of the laser beam manipulation and application, particularly for processing micro-mechanical and optoelectronic micro-systems, and precise control of the applied energy, have been successfully used in a mass production of the electronic industry over last two decades. The laser adjustment can be realized with various actuators designed to meet specific positioning and adjustment demands. The up-to-date known industrial applications of the method exploit the temperature gradient mechanism and the upsetting mechanism of thermal forming. New perspectives emerge with the research on non-thermal laser forming, i.e. using laser pulses in the range of nanoseconds, which produce material deformation due to the propagation of laser-induced shock waves.

### 2.3. MODELING OF FRICTION AND FLOW IN THE SLIDING PAIRS WITH MICROSTRUCTURE OF SURFACE

*Bogdan Antoszewski*

Energy losses resulting from friction between contact surfaces in an internal combustion engine have been studied intensively by a considerable number of tribologists. Progress in this field has brought numerous economically effective solutions, which enable mass production of motor vehicles. Still, the automotive industry needs further improvements to reduce friction-related energy losses in engines and drive systems. For instance, the losses of energy generated in a piston-ring-cylinder system account for 45% of all the losses of energy due to friction in the whole engine. Numerous reports suggest that the problem can be solved by applying porous surfaces generated, for example, by laser surface texturing [55-57, 10] (Fig. 2.22).

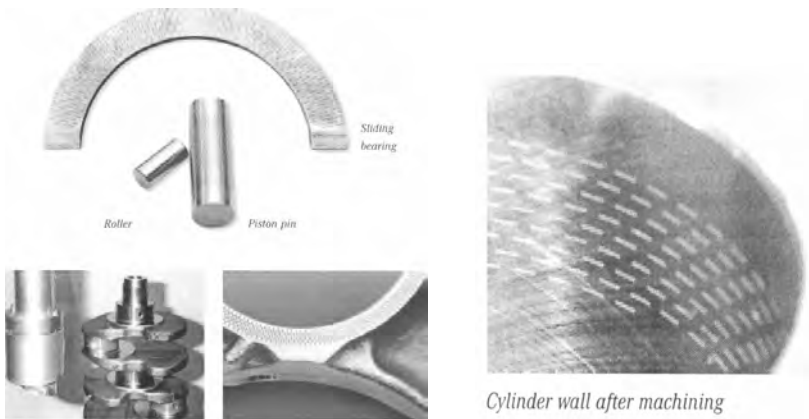


**Fig. 2.22.** Examples of application textured face in motorization [58]

### 2.3.1. ANALYSIS OF FRICTION RESISTANCES

Assuming the regularity of the cavities around the rubbing surfaces, we can develop a model of friction which takes into account both the area of flat surfaces and the area with cavities, here called the area of wavy surfaces. In the model, the flat surfaces are ideally flat, and the porous ones have roughness with equivalent parameters (see Refs. [56, 57]).

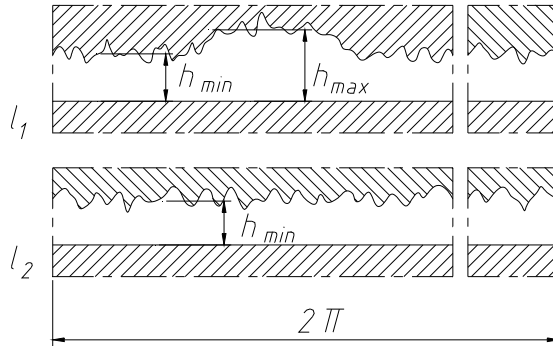


**Fig. 2.23.** Model of the clearance: fragment of surface with the cavitation area (upper part) and a fragment of surface without cavities (lower part)

In the general case, the total load force of a flat sliding pair with regular cavities around the opposing surfaces is expressed by the relationship:

$$W = W_m + W_h \quad (2.32)$$

where:  $W_m$  – mechanical component of the load force,  $W_h$  – hydraulic component of the load force.

The mechanical component of the load force resulting from the contact of the peaks of the microirregularities after taking into consideration the cavities [58] has the following form:

$$W_m = \alpha \cdot A \cdot P(H > h) \cdot p_g \quad (2.33)$$

where:  $A$  – area of microirregularities taking part in the transmission of loads,  $p_g$  – shearing strength of the softer material,  $P(H > h)$  – probability of the occurrence of the assumed clearance height.

Because of the surface heterogeneity, the load force of the fluid film has two components:

$$W_h = W_{h1} + W_{h2} \quad (2.34)$$

where:  $W_{h1}$  – load force of the fluid film in the areas with no cavities,  $W_{h2}$  – load force of the fluid film in the cavitation areas.

For areas without cavities, the relationship is:

$$W_{h1} = \frac{\mu \cdot U}{h^2} \alpha \cdot A \cdot L \cdot f(L, \Delta r) \quad (2.35)$$

where:  $f(L, \Delta r)$  – function determining the probability of occurrence of the fluid film [59],  $\mu$  – viscosity of the fluid in the clearance,  $U$  – sliding speed,  $L, \Delta r$  – length and width of the friction area.

For the cavitation areas, we adapt the relationship given by Lebeck [60]:

$$W_{h2} = (1 - \alpha) A \left[ \frac{k \cdot \mu \cdot \omega}{8\pi} \cdot \frac{(\Delta r)^2}{(h_{\min})^2} \cdot f_1 \left( \frac{h_a}{h_{\min}} \right) + \frac{p_0}{4} \right] \quad (2.36)$$

where, additionally:

$$f_1 \left( \frac{h_a}{h_{\min}} \right) = 1 - \frac{1}{\left( 1 + 2 \frac{h_a}{h_{\min}} \right)^2}$$

where:  $h_a$  – waviness amplitude,  $h_{\min}$  – minimum clearance height,  $\omega$  – rotational speed,  $p_0$  – fluid pressure in the clearance.

Finally, taking into account the above, we obtain the relationship for the load force of the flat sliding pair:

$$W = W_m + \frac{\mu \cdot U}{h^2} \alpha \cdot A \cdot L \cdot f(L, \Delta r) + (1 - \alpha) A \left[ \frac{k \cdot \mu \cdot \omega}{8\pi} \cdot \frac{(\Delta r)^2}{(h_{\min})^2} \cdot f_1 \left( \frac{h_a}{h_{\min}} \right) + \frac{p_0}{4} \right] \quad (2.37)$$

For simplicity, we shall consider a real case of a flat sliding pair, i.e. a pair of rings of a face seal, which is shown in Figure 2.24.

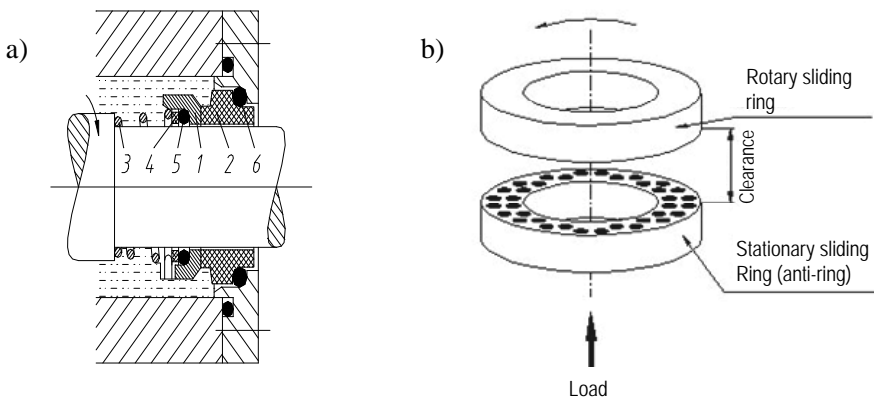


**Fig. 2.24a)** Schematic diagram of the face seal: 1 – axially shifted sliding ring, 2 – anti-ring, 3 – spring, 4 – clamping ring, 5,6 – secondary seals, b) model sliding pair with textured surface

## Case 1

Let us consider the case when  $h_{\min} > h_c$ , where  $h_c$  is the clearance height for which the peaks of the microirregularities are in contact. The clearance height is big enough so there is no contact of the microirregularities.

Since  $W_m = 0$ , relationship (2.37) can be written as:

$$W = \frac{\mu \cdot U}{h^2} \alpha \cdot A \cdot L \cdot f(L, \Delta r) + (1 - \alpha) A \left[ \frac{k \cdot \mu \cdot \omega}{8\pi} \cdot \frac{(\Delta r)^2}{(h_{\min})^2} \cdot f_1 \left( \frac{h_a}{h_{\min}} \right) + \frac{p_0}{4} \right] \quad (2.38)$$

In the general case, the friction force between the rubbing surfaces will be a sum of two components:

$$F = F_h + F_m \quad (2.39)$$

where:  $F_h$  – friction force of the fluid film,  $F_m$  – friction force of the peaks of the microirregularities in contact.

Thus, when  $h_{\min} > h_c$ ,  $F_m = 0$ .

The friction force of the viscous fluid,  $F_h$ , can be described by a known relationship:

$$F_h = A \frac{\mu \cdot U}{h} \quad (2.40)$$

Let us consider the case of complete fluid film with a variable thickness. If we base the considerations on the works by Stanghan-Batch and Ina [58] and Lebeck [60], we can calculate the coefficient of friction as follows:

$$f = \frac{\pi \cdot G \cdot r_m}{f_2 \cdot h_{\min}} \quad (2.41)$$

where:

$$f_2 = \sqrt{1 + 2 \left( \frac{h_a}{h_{\min}} \right)} \quad (2.42)$$

In relationship (2.41),  $h_{\min}$  is an unknown quantity, so it needs to be determined from other conditions. As the axial forces are in equilibrium, the load force in the clearance of the flat sliding pair of a face seal is counterbalanced by the external axial forces acting on the axially flexible element of the sliding pair. Thus, the condition of the equilibrium of the axial forces can be written as:

$$W = A \cdot p_0 \left( b + \frac{p_s}{p_0} \right) = A \cdot p_0 \cdot b' \quad (2.43)$$

where:  $p_s$  – spring tension,  $b$  – coefficient of load,  $b'$  – corrected coefficient of load,

$$b' = b + \frac{P_s}{p_0} \quad (2.44)$$

Comparing relationship (2.38) with (2.43) and including the size of the friction area, we can calculate the clearance height.

$$h_{\min} = \sqrt{\frac{\mu \cdot U \cdot \alpha \cdot L \cdot f(L, \Delta r) + (1 - \alpha) \frac{k \cdot \mu \cdot U}{8\pi \cdot r_m} \Delta r^2 f_1\left(\frac{h_a}{h_{\min}}\right)}{p_0 \cdot b' - (1 - \alpha) \frac{p_0}{4}}} \quad (2.45)$$

Using the definition of parameter  $G$ , we calculate the minimum clearance height:

$$C_1 = \sqrt{\frac{\frac{1 - \alpha}{4} k \cdot (\Delta r)^2 f_1\left(\frac{h_a}{h_{\min}}\right) + 4\alpha\pi^2 r_m^2 f(L, \Delta r)}{1 - \frac{1 - \alpha}{4b'}}} \quad (2.46)$$

where:

$$h_{\min} = C_1 \sqrt{G} \quad (2.47)$$

$$G = \frac{\mu \cdot U \cdot \Delta r}{W} \quad (2.48)$$

Substituting the calculated clearance height to relationship (2.41) and performing certain transformations, we obtain the value of the coefficient of friction.

$$f = \frac{\pi \cdot r_m \cdot \sqrt{G}}{f_2 \cdot C_1} \quad (2.49)$$

## Case 2

We consider a situation when there is a direct contact of the peaks of the microirregularities, i.e. when  $h_{\min} = h_c$ . The clearance height is known, as it results from the height of the microirregularities. Like in Refs. [61], [62], it is assumed that the distribution of the peaks of the microirregularities is the Gaussian distribution and the height of microirregularities in contact,  $h_c$ , is  $3\sigma$ , with  $\sigma$  being a standard deviation defined by the following relationship:

$$\sigma = \sqrt{\sigma_1^2 + \sigma_2^2} \quad (2.50)$$

where  $\sigma_1, \sigma_2$  – standard deviations of random variables representing the profiles of both surfaces.

Like in the previous case, the load force of the seal resulting from the fluid film is calculated according to formulas (2.35) and (2.36). The value of the friction force of the fluid film is given by relationship (2.39), while the friction force of the microirregularities in contact is defined by the following relationship:

$$F_m = f_b \cdot W_m \quad (2.51)$$

where  $f_b$  – coefficient of boundary friction.

Calculating  $W_m$  from relationship (2.38), we get:

$$W_m = W - \frac{\mu \cdot U}{h^2} \alpha \cdot A \cdot L \cdot f(L, B) - (1 - \alpha) A \left[ \frac{n \cdot \mu \cdot \omega}{8\pi} \cdot \frac{(\Delta r)^2}{(h_{\min})^2} \cdot f_1 \left( \frac{h_a}{h_{\min}} \right) + \frac{p_0}{4} \right] \quad (2.52)$$

Using relationships  $f = F/W$ , (2.38) and (2.52) and performing certain transformations, we obtain the following relationship for the coefficient of friction:

$$f = f_b \left[ 1 - G \cdot f(L, \Delta r) \cdot \alpha \cdot \frac{4 \cdot \pi^2 \cdot r_m^2}{h_{\min}^2} - \left( \frac{1 - \alpha}{4} \right) \left( G \cdot k \cdot f_1 \left( \frac{h_a}{h_{\min}} \right) \frac{(\Delta r)^2}{(h_{\min})^2} + \frac{1}{b'} \right) \right] + \frac{2\pi \cdot r_m \cdot G}{f_2 \cdot h_{\min}} \quad (2.53)$$

The model of friction assumes that the opposing surfaces are in contact or that there is no contact between them. The model can be used for the analysis of friction of seals with rings characterized by different geometries of surface heterogeneities.

The model was analyzed in a numerical example using the MATHCAD 7.0 program for the following data:

- dynamic viscosity of the medium  $\mu - 700 \cdot 10^{-6} \text{ Pa} \cdot \text{s}$ ,
- clearance height in the area of the flat surface  $h_c - 10^{-6} \text{ m}$ ,
- clearance height in the cavitation area  $h_a - 10^{-6} \text{ m}$ ,
- number of cavities per surface unit  $k - 3, 6, \dots, 12$ ,
- share of the flat surface  $\alpha - 0.2 \dots 0.8$ ,
- average ring radius  $r_m = 0.0205 \text{ m}$ ,
- ring width  $\Delta r = 0.005 \text{ m}$ .

The relationship between the coefficient of friction and parameter  $G$  was analyzed for different shares of the flat surface  $\alpha$  and different number of surface structures  $k$  in the friction area. It was necessary to define the influence of these parameters on the coefficient of friction for the following cases  $h > h_c$  and  $h = h_c$ .

Figures 2.25 and 2.26 show typical relationships between the coefficient of friction and parameter  $G$  both for the regime of mixed friction and that of fluid friction. As can be seen in Figure 2.25, in the mixed friction regime, the coefficient of friction decreases when there is a rise in parameter  $G$ . In the regime of fluid friction, an inverse relationship is observed (Fig. 2.26). This general relationship be-

tween the coefficient of friction and parameter  $G$  is not at all dependent on the number of cavities  $k$  or the share of flat surface  $\alpha$ . The influence of parameters  $k$  and  $\alpha$  is not analyzed in this paper.

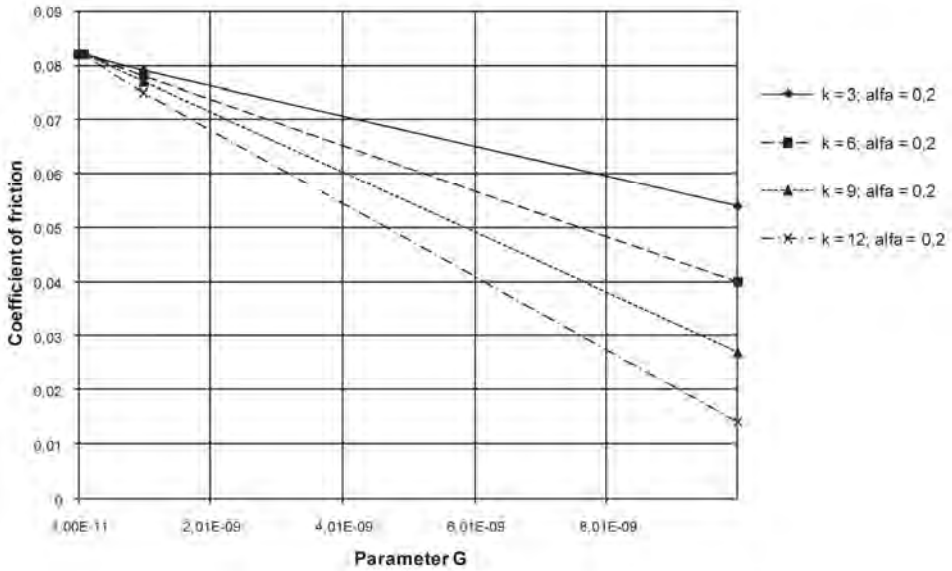


**Fig. 2.25.** Coefficient of friction between the face seal rings vs. parameter  $G$  in the regime of mixed friction for surfaces with a different number of cavities  $k$  and a constant share of flat surface  $\alpha$

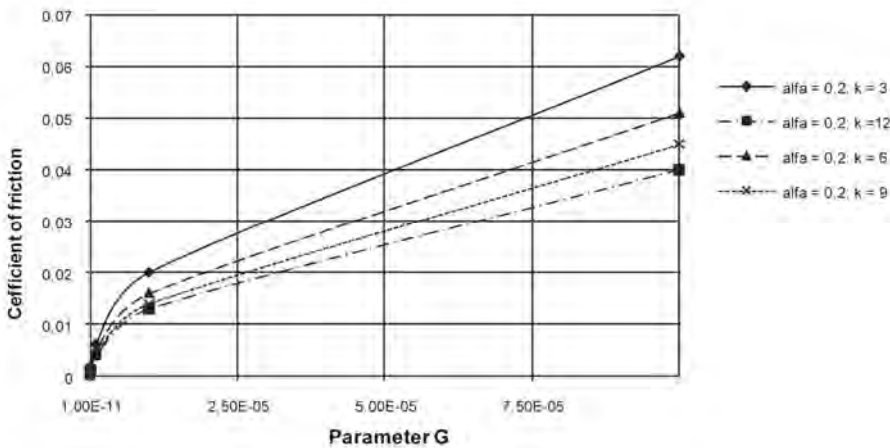


**Fig. 2.26.** Coefficient of friction between the face seal rings vs parameter  $G$  in the regime of fluid friction for surfaces with a different number of cavities

The proposed model of friction makes it possible to determine the values of the coefficient of friction and parameter  $G$  for which there is a transition from mixed friction to fluid friction. Figure 2.27 shows the values of the coefficient of friction

recorded for both regimes. The transition point is in the range of parameters  $G = 10^{-7} \div 10^{-8}$ . The exact position of the transition point is shown in Figure 2.28. The hypothetical values of the coefficient of friction  $f$  and parameter  $G$  at the transition point were established by comparing the mathematical model for mixed friction with that of fluid friction.

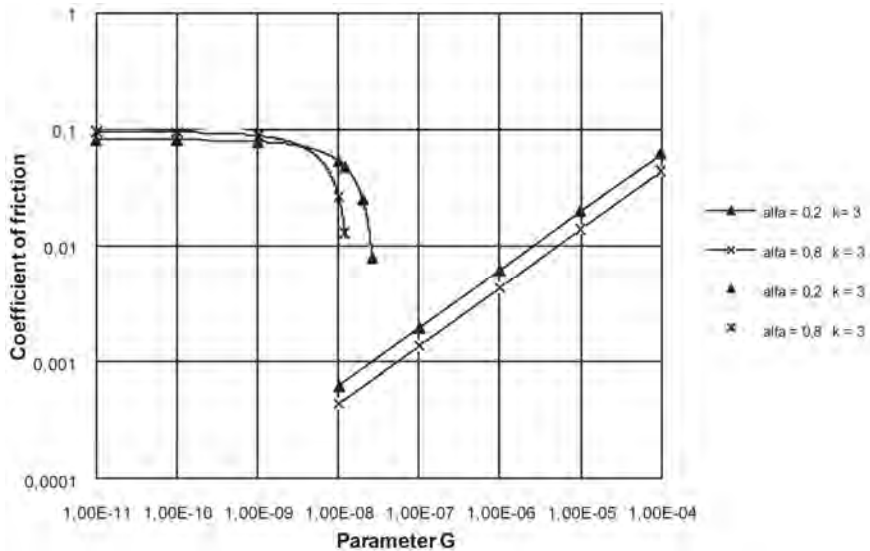


**Fig. 2.27.** Coefficient of friction between the face seal rings vs parameter  $G$  (logarithmic scale)

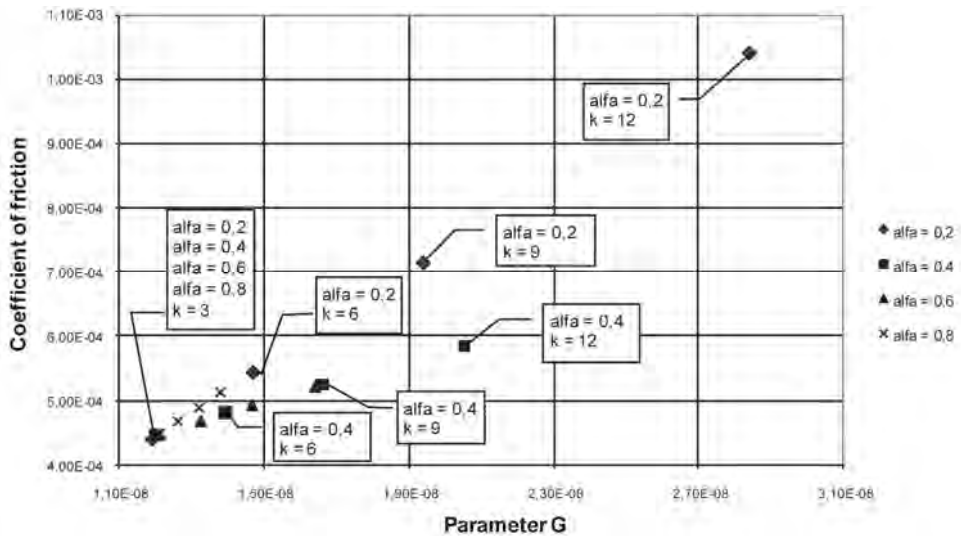


**Fig. 2.28.** Positions of the points of transition from mixed to fluid friction for the mating face seal rings

### 2.3.2. MODELLING FLUID FLOW IN THE CLEARANCE BETWEEN ONE SMOOTH AND ONE POROUS SURFACE

Effective numerical modelling of fluid flows in clearances of sliding pairs requires considering only the basic parameters of flow and neglecting the less important ones. The parameters that are crucial to this phenomenon can be selected on the basis of a dimensional analysis and general knowledge of physics. Considering all the parameters would mean having to solve full Navier-Stokes equations, which is impossible at the present state of knowledge and computer technology, even though the Reynolds number is very small. In the case of sliding pairs, we may need to consider a two-phase flow in areas where cavitation of the oil film occurs. Since it is generally known that all the hydrodynamic effects of interest, including the hydrodynamic force formation, are related to cavitation, the phenomenon cannot be omitted. The modelling, however, will have an approximate character, which is a significant problem in any simulation. The literature shows that different physical effects have been taken into account.

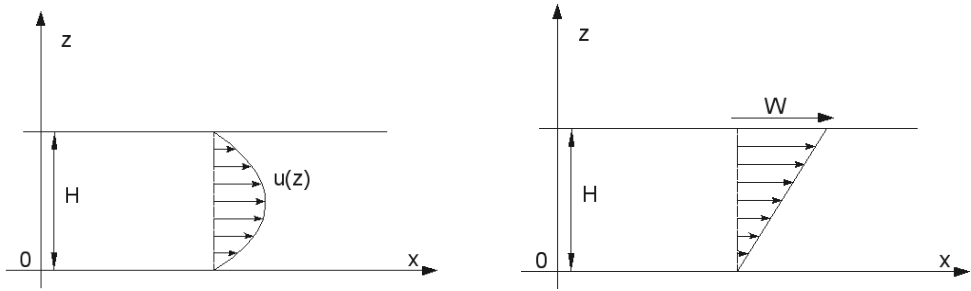


**Fig. 2.29.** Basic flows in the clearance: a) Poiseuille flow, b) Couette flow

If the changes in the  $x$  and  $y$  directions are much slower than those in the  $z$  direction (condition  $H \ll L$ ), one can assume that  $\vec{Q}$  is a superposition of the basic Poiseuille and Couette flows.

Thus, the equation derived for the oil film is:

$$\operatorname{div} \left( \frac{\rho H^3}{6\eta} \operatorname{grad}(p) \right) = \operatorname{div}(\rho H \vec{W})$$

where  $\rho$ ,  $\eta$ ,  $H$ ,  $p$  can be slowly-changing functions of  $x$  and  $y$ .

After integrating the equation in any domain  $\Omega$  (in the  $x, y$  plane), we obtain:

$$\int_{\Omega} \operatorname{div} \left( \frac{\rho H^3}{6\eta} \operatorname{grad}(p) \right) d\Omega = \int_{\Omega} \operatorname{div}(\rho H \vec{W}) d\Omega$$

Then, applying the Green formula, we have:

$$\int_{\partial\Omega} \frac{\rho H^3}{6\eta} \frac{\partial p}{\partial n} d\sigma = \int_{\partial\Omega} \rho H \vec{W} \vec{n} d\sigma$$

where:  $\partial\Omega$  – the boundary of the domain  $\Omega$ ,  $\vec{n}$  – external normal to that boundary.

Let the domain  $\Omega$  be an unit cell of a network covering the area of flow. The modelling will be performed using the example of a thrust bearing or a face seal as a friction pair.

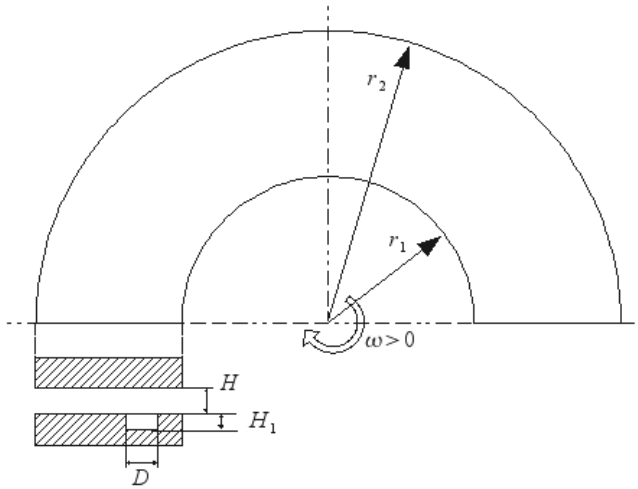


**Fig. 2.30.** Schematic diagram of the model clearance

If the coordinate system is related to the symmetry axis of the friction system, then:

$$\vec{W} = \omega r \hat{i}_0$$

where:  $\omega$  – the rotational speed,  $r$  – the radius vector,  $\hat{i}_0$  – the circumferential unit vector perpendicular to  $r$ .

In the above formulae, the clearance height  $H$  is a variable function of position used for describing the geometry of pores produced on the bearing races by laser surface texturing.

The equation for the oil film in the fluid flow area is solved to determine the pressure area,  $p(x,y)$ . The other elements are assumed to be known. The condition for pressure on the boundary of the domain is obvious, because the values of pressure around the inner and outer circumferences of the sliding ring are known.

It is assumed that the pressure in the cavitation area (where pressure falls below the boiling pressure  $p_{boil}$ ) is constant, and the pressure gradient is equal to zero. In this domain, the equation of the oil film is still valid. On the left-hand side, all the

terms disappear, while the right-hand side terms are used to calculate the unknown density area  $\rho(x,y)$ , and, accordingly, the amount of the fluid evaporated.

On the boundary of the cavitation domain, the following conditions are satisfied:

inlet: the pressure inside is continuous,  $\frac{\partial p}{\partial n} = 0$ ; the fluid fluxes inside and outside

are identical;

outlet: the density around the outer circumference is equal to the fluid density; the fluid fluxes around the inner and outer circumferences are equal.

The integral quantities of practical interest are:

**The hydrodynamic force**, which can be calculated from the formula:

$$F = \int_{r_1}^{r_2} \int_0^{2\pi} r(p - p_{atm}) d\Theta dr$$

where:  $r_1$  and  $r_2$  – inner and outer radii of the ring,  $p_{atm}$  – atmospheric pressure.

**The leakage** can be determined for any radius  $r$  using the following formula:

$$Q = \int_0^{2\pi} \frac{r\rho H^3}{12\eta} \frac{\partial p}{\partial r} d\Theta$$

it is desirable, however, to average the number by integration applying different radius to increase the accuracy of calculation:

$$Q = \frac{1}{r_2 - r_1} \int_{r_1}^{r_2} \int_0^{2\pi} \frac{r\rho H^3}{12\eta} \frac{\partial p}{\partial r} d\Theta dr$$

**The torque** representing the frictional resistance is determined as an integral of tangential stresses by means of the formula:

$$M = \omega \int_{r_1}^{r_2} \int_0^{2\pi} \frac{r\eta}{H} d\Theta dr - \frac{1}{2} \int_{r_1}^{r_2} \int_0^{2\pi} rH \frac{\partial p}{\partial \Theta} d\Theta dr$$

In numerical calculations, the hydrodynamic force  $F$  generated by a single element of the texture was replaced by:

$$P_{av} = \frac{F}{\pi D^2 / 4}$$

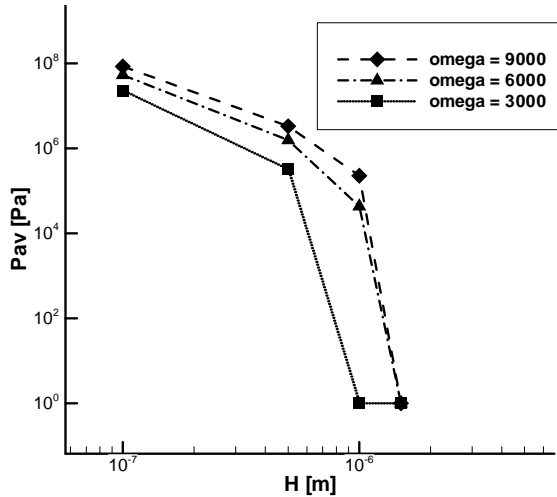
where the denominator corresponds to the pore surface area. Accordingly, the quantity  $P_{av}$  [Pa] corresponds to the average pressure acting on the etched part of the race. The total force acting on the seal is calculated as:

$$F_{total} = P_{av} \cdot S \cdot C$$

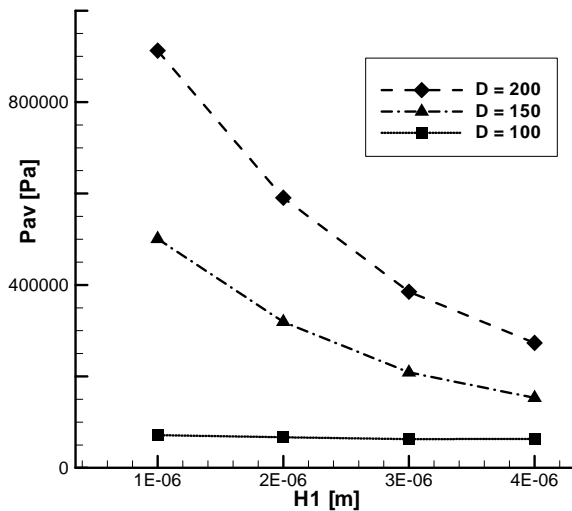
where:  $S$  – race area,  $C$  – dimensionless pore area coverage (percentage of pores in a whole surface).

Figure 2.31 indicates the variation of  $P_{av}$  in relation to the rotational speed  $\omega$  and the clearance height  $H$ . The other parameters are standard.

Figure 2.32 presents the relationship between  $P_{av}$ , the pore diameter [ $\mu\text{m}$ ] and the pore depth [m]. The other parameters are standard.



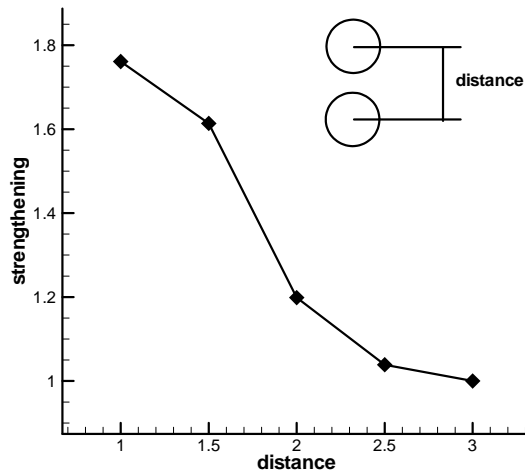
**Fig. 2.31.** Relationship between the average pressure, the clearance height and the rotational speed



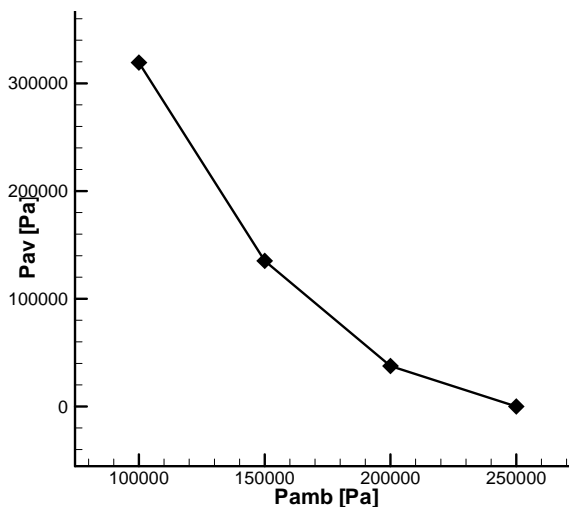
**Fig. 2.32.** Relationship between the average pressure, the pore depth and the pore diameter

Figure 2.33 illustrates the relationship between the hydrodynamic force amplification and the radial distance between the texture cavities. A multiple pore diameter is shown in the X-axis. The other parameters are standard. A decrease in the radial distance between cavities causes almost a double increase in the hydrodynamic force.

Figure 2.34 shows the effect of ambient pressure on the hydrodynamic force. In the previous diagrams, the ambient pressure corresponded to the atmospheric pressure. An increase in this pressure resulted in a considerable decrease in the hydrodynamic force. Technically, the pressures around the inner and outer edges of the friction elements are different, as is the case of face seals. Pores in the area of higher pressure will generate a hydrodynamic force that is smaller than those around the outer edge.



**Fig. 2.33.** Hydrodynamic force amplification versus radial distance between pores



**Fig. 2.34.** Average pressure versus ambient pressure

The following conclusions were drawn basing on the qualitative results of the simulations:

- as expected, the hydrodynamic force was greatly dependent on the rotational speed and the clearance height;
- on surfaces where pores were larger in depth and diameter, the pressure was higher and the hydrodynamic force was larger;
- the smaller the radial distance between the pores, the larger the hydrodynamic force;
- no such effect was observed in the circumferential direction;
- the greatest effect of surface texturing was reported in the low-pressure zone (around the outer circumference of the race).

Analyzing the above diagrams (Part 1), one can draw the following conclusions about face seal rings whose surfaces are partly flat  $\alpha$  and partly with cavities  $k$ :

- the greater the number of cavities  $k$  on the surface of a face seal ring, the lower the coefficient of friction both in the regime of fluid friction and that of mixed friction,
- the greater the area of the flat surface  $\alpha$ , i.e. the greater the share of the flat surface in the total area of friction in the regime of mixed friction, the greater the coefficient of friction; the relationship is true for all the considered number of cavities,
- for fluid friction, an increase in the share of the flat surface  $\alpha$  causes a decrease in the coefficient of friction, the exception being the case when  $k = 12$  for which the coefficient of friction rises slightly with an increase in  $\alpha$ ,
- a rise in the value of parameter  $G$  causes that the type of friction between the seal rings changes from mixed into fluid; the developed model makes it possible to assess the parameters of the transition point depending on the number of cavities and the share of the flat surface.

## **2.4. ANALYSIS AND VERIFICATION OF SURFACE ROUGHNESS CONSTITUTION MODEL IN THE METAL CUTTING PROCESS APPLYING TOOLS WITH DEFINED STEREOMETRY**

*Edward Miko*

Machining is still the most commonly used method of product formation of all manufacturing technologies. As it is also very expensive, it seems reasonable to select the most suitable conditions. The research on the metal cutting process as a di-

mensional and surface treatment aims at improving the cutting efficiency and, consequently, the technical quality of the outer layer of a machine part [77] and [73].

Machining – a basic production operation – is predicted to improve or at least maintain its position in the engineering industry, especially if precision is involved [65].

The increasing accuracy of metal cutting, particularly turning and milling, causes that surfaces sculptured in this way seldom require finishing, which has a positive effect on the properties of ready products. If ceramic or CBN cutters are used it has become a rule to replace grinding with turning or milling after casting or forging so as to obtain required dimensions and surface finish [66]. Therefore, the geometrical structure generation and the properties of the outer layer obtained in the course of machining are important problems of both theoretical and experimental studies nowadays. Roughness is an essential factor in tribology as it determines the quality of the outer layer and evaluates the cutting process [66].

Roughness, characterized by parameters determined by measuring its irregularities is said to be one of the most important factors affecting the operating properties of machine elements, expressed, among others, by friction conditions on contact surfaces, contact stresses, fatigue strength, corrosion resistance, tightness of joints, conditions of flow for fluids and gases, electrical and thermal contact resistance, superficial thermal radiation or magnetic properties [70].

The metal cutting process is generally accompanied by vibrations. These are mainly due to changeable forces produced by the tool, unbalance of rotating masses, performance of bearings, shafts, and toothed wheels, nonhomogeneity of the stock, etc. [66] and [68] to [76].

In the turning and milling operations, roughness is mainly a result of the stereometric and kinematical tool representation; also it is dependent on the unremoved fragment of the material, relative tool-workpiece vibrations, the tool runout, and, finally, the tool wear [72].

The mathematical models discussed in specialized literature focus on the quantitative influence of tool representation, and on one of the following factors: vibrations, cutter run-out, and sometimes tool wear.

Since roughness constitution is reported to be an extremely significant process, a number of researchers are involved in the study of the effects of the above mentioned factors on surface roughness in the metal cutting process. Their results as well as those obtained by the authors were used to develop a new model of surface roughness constitution [72].

#### **2.4.1. MODEL OF SURFACE ROUGHNESS IN METAL CUTTING**

In practice, a cutting edge is never ideally sharp, thus a certain rounded cutting edge radius  $r_n$  needs to be taken into account. During a metal cutting process, part of the allowance is removed, its thickness being greater than a certain threshold thickness called minimum undeformed chip thickness  $h_{\min}$  [65] and [72] to [74]. Generally, the process of metal removal is accompanied by relative tool-workpiece system vibrations that will be represented on the generated surface. It is crucial that

the process of constitution of lateral roughness (in the feed direction) represented by the parameters  $Ra$  and  $R_t$  be modeled for surfaces sculptured with a rounded cutting edge described by the equivalent radius  $r_z$ .

The model includes:

- the stereometric-kinematic representation of the cutting edges,
- the unremoved fragment of the material,
- relative displacements of the tool and the stock in the direction normal to the machined surface,
- the tool run-out in the direction normal to the machined surface and
- the tool wear.

Moreover, it was assumed that:

- the vibrations in the machining system occur irrespective of the tool run-out,
- the stock material is ideally elastic,
- the influence of other factors disturbing the ideal representation of the tool is negligible,
- the tool wear affecting the roughness of machined surfaces results in a change in the rounded cutting edge radius  $r_n$ ; this has an influence on the minimum undeformed chip thickness  $h_{min}$  and variations in relative displacements in the toolworkpiece (T-W) system [72].

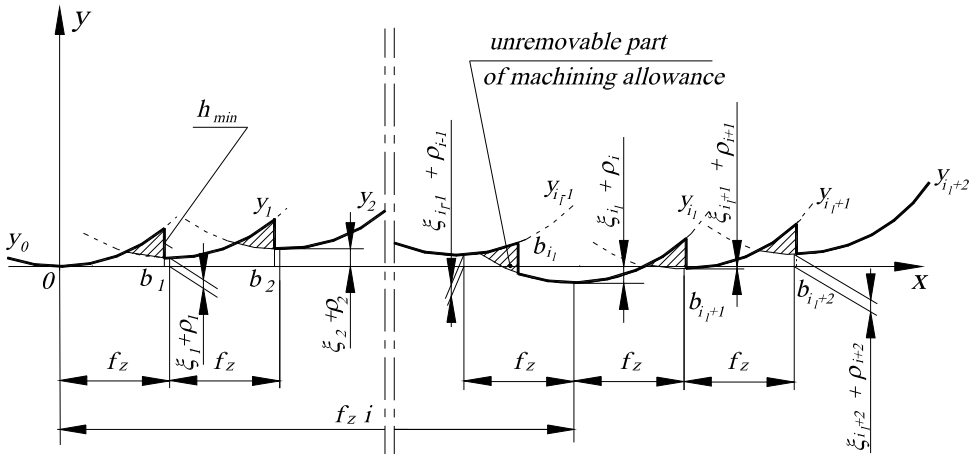


**Fig. 2.35.** Lateral roughness profile of a surface face-milled with the feed rate  $f_z$  with a milling head equipped with round corner cutters with the radius  $r_z$  due to relative displacements of the tool and the workpiece  $\xi_{il}$  and an instantaneous cutter position resulting from the face run-out  $\rho_i$

Figure 2.35 shows the lateral profile of a surface generated after a pass of the  $i$ -th cutter during the  $l$ -th revolution of a multicutter tool moving along the  $x$ -axis with a feed motion, performing vibrations and showing cutter runouts. A lateral profile of such a surface is described by the following relationship:

$$y_{i_l}(x) = \frac{1}{2r_z} \cdot (x - f_z \cdot i_l)^2 + \rho_i + \xi_{i_l} \quad (2.54)$$

for the range  $b_{i_l} < x \leq b_{i_l+1}$  (Fig. 2.35) while:  $i_l = z(l-1) + i - 1$  where:  $r_z$  – equivalent radius,  $f_z$  – feed per tooth  $\rho_i$  – instantaneous orientation of the  $i$ -th cutter in relation to the workpiece resulting from the face run-out,  $\xi_{i_l}$  – instantaneous relative displacement of the  $i$ -th cutter during the  $l$ -th revolution of a multicutter tool due to vibrations,  $z$  – number of cutters in the multicutter tool.

The instantaneous orientation of the  $i$ -th cutter in relation to the workpiece due to the face run-out  $\rho_i$  can be described using the relationship:

$$\rho_i \approx -e \cdot \cos \left[ (i-1) \cdot \frac{2\pi}{z} \right] \quad (2.55)$$

where:  $e$  – face run-out of the cutters. The range limits are given by:

$$b_{i_l} = f_z \cdot \left( i_l - \frac{1}{2} \right) + \frac{r_z}{f_z} \cdot (\rho_i - \rho_{i-1} + \xi_{i_l} - \xi_{i_l-1} + h_{\min}) \quad (2.56)$$

$$b_{i_l+1} = f_z \cdot \left( i_l + \frac{1}{2} \right) + \frac{r_z}{f_z} \cdot (\rho_{i+1} - \rho_i + \xi_{i_l+1} - \xi_{i_l} + h_{\min}) \quad (2.57)$$

where:  $h_{\min}$  – minimum undeformed chip thickness,  $\xi_{i_l}$  was assumed to be a sequence of independent random variables with uniform distribution of probability where the mean value equals 0 and the variance is  $D^2(\xi)$ . When  $\xi_{i_l}$  are independent random variables, then the profile of a modeled surface is no longer a periodic curve; it is said to be a stochastic process algebra.

To determine the parameter  $Ra$  of a surface described by Eq. (2.58), it is necessary to define a functional for a set of the stochastic process algebras.

The arithmetic mean profile deviation (given by the function  $y(x)$ ) from the mean line position  $\bar{y}$  at the elementary length  $l_e$  is determined from the relationship:

$$Ra = \frac{1}{l_e} \int_0^{l_e} |y(x) - \bar{y}| dx \quad (2.58)$$

Then, the position of the mean line is established from the following equation:

$$\bar{y} = \frac{1}{l_e} \int_0^{l_e} y(x) dx \quad (2.59)$$

Squaring both sides of relationship (2.58) and applying Schwarz inequality, it is possible to determine the parameter  $Ra$  of the modeled surface. Then, we get:

$$Ra^2 = \left[ \frac{1}{l_e} \int_0^{l_e} |y(x) - \bar{y}| dx \right]^2 \leq \frac{1}{l_e} \int_0^{l_e} [y(x) - \bar{y}]^2 dx =$$

$$= \frac{1}{l_e} \int_0^{l_e} [y(x)]^2 dx - \frac{2}{l_e} \bar{y} \int_0^{l_e} y(x) dx + \frac{1}{l_e} \bar{y}^2 \int_0^{l_e} dx$$
(2.60)

and after transition to the limit with  $l_e \rightarrow \infty$  :

$$Ra^2 \leq \left[ \overline{y^2} - \bar{y}^2 \right]$$
(2.61)

This inequality can be transformed into the following equality:

$$Ra = \theta \sqrt{\overline{y^2} - \bar{y}^2} \quad \text{for } \theta \in (0, 1)$$
(2.62)

where:  $\theta$  – form factor of the modeled profile.

In order to derive the equation to be used for determining the parameter  $Ra$ , it is required to establish the quantities  $\bar{y}$  and  $\overline{y^2}$  :

$$\bar{y} = \lim_{l_e \rightarrow \infty} \frac{1}{l_e} \int_0^{l_e} [y(x)] dx = \lim_{n \rightarrow \infty} \frac{1}{n \cdot f_z \cdot z} \cdot \sum_{i_l=0}^n \int_{b_{i_l}}^{b_{i_l+1}} \left[ \frac{1}{2r_z} (x - f_z \cdot i_l)^2 + \rho_i + \xi_{i_l} \right] dx$$
(2.63)

$$\overline{y^2} = \lim_{l_e \rightarrow \infty} \frac{1}{l_e} \int_0^{l_e} [y(x)]^2 dx = \lim_{n \rightarrow \infty} \frac{1}{n \cdot f_z \cdot z} \cdot \sum_{b_{i_l}}^{b_{i_l+1}} \left[ \frac{1}{2r_z} (x - f_z \cdot i_l)^2 + \rho_i + \xi_{i_l} \right]^2 dx$$
(2.64)

Substituting the integration limits (2.56) and (2.57) into Eqs. (2.63) and (2.64) and performing (2.56) calculations while neglecting moments of the variables  $\xi_{i_l}$ , an order higher than the second one as well as the power of these moments and the sum of the variables  $\rho_i$  in even powers, higher than the second as low values of a higher order, we got:

$$\bar{y} = \frac{f_z^2}{24r_z} + \frac{r_z h_{\min}^2}{2f_z^2} - \frac{r_z}{f_z^2} \left[ D^2(\xi) + D^2(\rho) \left( 1 - \cos \frac{2\pi}{z} \right) \right]$$
(2.65)

$$\begin{aligned} \overline{y^2} = & \frac{f_z^4}{320r_z^2} + \frac{h_{\min}^2}{8} + \frac{r_z^2 h_{\min}^4}{4f_z^4} + \frac{3}{4} \left[ D^2(\xi) + D^2(\rho) \left( 1 + \frac{1}{3} \cos \frac{2\pi}{z} \right) \right] + \\ & + \frac{r_z^2 h_{\min}^2}{f_z^4} \left[ D^2(\xi) + D^2(\rho) \left( 1 - \cos \frac{2\pi}{z} \right) \right] \end{aligned} \quad (2.66)$$

Performing transformations and calculations, we obtained:

$$\begin{aligned} Ra = & \left\{ \frac{f_z^4}{972r_z^2} + \frac{5}{81} h_{\min}^2 + \frac{50}{81} \left[ D^2(\xi) + D^2(\rho) \left( 1 + \frac{1}{5} \cos \frac{2\pi}{z} \right) \right] + \right. \\ & \left. + \frac{40r_z^2 h_{\min}^2}{27f_z^4} \left[ D^2(\xi) + D^2(\rho) \left( 1 - \cos \frac{2\pi}{z} \right) \right] \right\}^{\frac{1}{2}} \end{aligned} \quad (2.67)$$

This is an equation relevant for  $f_z > \sqrt{2r_z h_{\min}}$ .

A general relationship will be applied to calculate the parameter  $Ra$  for  $\sqrt{r_z h_{\min}} < f_z \leq \sqrt{2r_z h_{\min}}$ , as well as for the case of  $f_z \leq \sqrt{r_z h_{\min}}$ , i.e. when part of the material is removed with the  $k$ -th cutter of the multicutter tool. A profile obtained by cutting with small feed rates when the area of unremoved material is partly smoothed with the  $k$ -th cutter is shown in Figure 2.36.

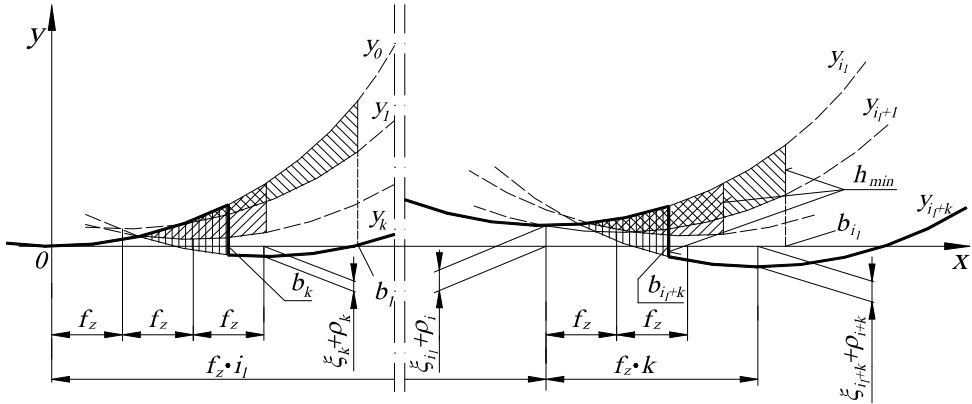


**Fig. 2.36.** Lateral roughness profile of a surface face-milled with a low feed rate  $f_z$  using round corner cutters with the radius  $r_z$ , due to relative displacements  $\xi_{i_1}$  of the tool and the workpiece and an instantaneous position of cutters due to a face run-out

The equation of the  $i_1$ -th parabola is given by relationship (2.54), while the equation of the  $(i_1 + k)$ -th parabola is written in the following form:

$$y_{i+k} = \frac{1}{2r_z} [x - f_z(i_l + k)]^2 + \rho_{i+k} + \xi_{i+k} \quad (2.68)$$

The position of point  $b_{i+k}$  (Fig. 2.36) was determined from:

$$y_{i_l}(b_{i+k}) - h_{\min} = y_{i+k}(b_{i+k}) \quad (2.69)$$

Substituting relationships (2.54) and (2.68) into Eq. (2.69) and performing certain transformations gives:

$$b_{i+k} = f_z \left( i_l + \frac{k}{2} \right) + \frac{r_z}{k \cdot f_z} (\rho_{i+k} - \rho_i + \xi_{i+k} - \xi_i + h_{\min}) \quad (2.70)$$

Similarly, the parameter  $Ra$  of the modeled surface can be calculated using the values of  $\bar{y}$  and  $\overline{y^2}$ :

$$\begin{aligned} \bar{y} &= \lim_{l_e \rightarrow \infty} \frac{1}{l_e} \int_0^{l_e} [y(x)] dx = \lim_{n \rightarrow \infty} \frac{1}{n \left( \frac{f_z \cdot k}{2} + \frac{r_z h_{\min}}{k \cdot f_z} \right) z} \times \\ &\times \sum_{i_l=0}^n \int_{f_z \cdot i_l}^{b_{i_l+k}} \left[ \frac{1}{2r_z} (x - f_z \cdot i_l)^2 + \rho_i + \xi_{i_l} \right] dx \end{aligned} \quad (2.71)$$

$$\begin{aligned} \overline{y^2} &= \lim_{l_e \rightarrow \infty} \frac{1}{l_e} \int_0^{l_e} [y(x)]^2 dx = \lim_{n \rightarrow \infty} \frac{1}{n \left( \frac{f_z \cdot k}{2} + \frac{r_z h_{\min}}{k \cdot f_z} \right) z} \times \\ &\times \sum_{i_l=0}^n \int_{f_z \cdot i_l}^{b_{i_l+k}} \left[ \frac{1}{2r_z} (x - f_z \cdot i_l)^2 + \rho_i + \xi_{i_l} \right]^2 dx \end{aligned} \quad (2.72)$$

Integrating, transforming, and neglecting low values of a higher order, we get:

$$\begin{aligned} \bar{y} &= \frac{f_z^2 k^2}{24r_z} + \frac{r_z h_{\min}^2}{6f_z^2 k^2} + \frac{h_{\min}}{6} - \frac{r_z}{f_z^2 k^2} \left[ D^2(\xi) + D^2(\rho) \left( 1 - \cos \frac{2\pi}{z} \right) \right] + \\ &+ \frac{4r_z^2 h_{\min}}{f_z^2 k^2 (k^2 f_z^2 + 2r_z h_{\min})} \left[ D^2(\xi) + D^2(\rho) \left( 1 - \cos \frac{2\pi}{z} \right) \right] \end{aligned} \quad (2.73)$$

$$\begin{aligned} \overline{y^2} = & \frac{f_z^4 k^4}{320 r_z^2} + \frac{3}{40} h_{\min}^2 + \frac{f_z^2 k^2 h_{\min}}{40 r_z} + \frac{r_z h_{\min}^3}{10 f_z^2 k^2} + \frac{r_z^2 h_{\min}^4}{20 f_z^4 k^4} + \frac{3}{4} D^2(\xi) \left[ 1 + \frac{4 r_z^2 h_{\min}^2}{3 f_z^4 k^4} \right] + \\ & + \frac{3}{4} D^2(\rho) \left[ 1 + \frac{4}{3} \left( \frac{r_z^2 h_{\min}^2}{f_z^4 k^4} + 4 \cos \frac{2\pi}{z} - \frac{r_z^2 h_{\min}^2}{f_z^4 k^4} \cos \frac{2\pi}{z} \right) \right] \end{aligned} \quad (2.74)$$

After the necessary transformations and calculations, it yields:

$$\begin{aligned} Ra = & \left\{ \left[ \frac{f_z^2 k^2}{18 \sqrt{3} r_z} + \frac{2 h_{\min}}{9 \sqrt{3}} \left( 1 + \frac{r_z h_{\min}}{f_z^2 k^2} \right) \right]^2 + \frac{50}{81} \left[ D^2(\xi) + D^2(\rho) \left( 1 + \frac{1}{5} \cos \frac{2\pi}{z} \right) \right] \right\} + \\ & + \frac{40}{81} \left[ \frac{r_z^2 h_{\min}^2}{f_z^2 k^2 (f_z^2 k^2 + 2 r_z h_{\min})} + \frac{2 r_z^3 h_{\min}^3}{f_z^4 k^4 (f_z^2 k^2 + 2 r_z h_{\min})} \right] \times \\ & \times \left[ D^2(\xi) + D^2(\rho) \left( 1 + \frac{1}{5} \cos \frac{2\pi}{z} \right) \right] \left. \right\}^{\frac{1}{2}} \end{aligned} \quad (2.75)$$

The relationship can be applied when the feed rate  $f_z$  ranges:

$$\sqrt{\frac{2}{(k+1)k}} r_z h_{\min} < f_z \leq \sqrt{\frac{2}{(k-1)k}} r_z h_{\min} \quad \text{for } k = 2, 3, 4, \dots$$

When no smoothing is required, and the area of unremoved material sculptured with subsequent cutters does not decrease, then  $k = 1$  is substituted into Eq. (2.75). As a result we get:

$$\begin{aligned} Ra = & \left\{ \left[ \frac{f_z^2}{18 \sqrt{3} r_z} + \frac{2 h_{\min}}{9 \sqrt{3}} \left( 1 + \frac{r_z h_{\min}}{f_z^2} \right) \right]^2 + \frac{50}{81} \left[ D^2(\xi) + D^2(\rho) \left( 1 + \frac{1}{5} \cos \frac{2\pi}{z} \right) \right] \right\} + \\ & + \frac{40}{81} \left[ \frac{r_z^2 h_{\min}^2}{f_z^2 (f_z^2 + 2 r_z h_{\min})} + \frac{2 r_z^3 h_{\min}^3}{f_z^4 (f_z^2 + 2 r_z h_{\min})} \right] \left[ D^2(\xi) + D^2(\rho) \left( 1 + \frac{1}{5} \cos \frac{2\pi}{z} \right) \right] \left. \right\}^{\frac{1}{2}} \end{aligned} \quad (2.76)$$

The relationship is relevant for the following feed rate:  $\sqrt{r_z h_{\min}} \leq f_z \leq \sqrt{2 r_z h_{\min}}$ .

Depending on the profile form, which results from the feed rate, several characteristic equations were derived. The relationships used for determining the parameter  $Ra$  of machined surfaces for the particular ranges of feed rates are given in Eqs. (2.67), (2.75) and (2.76).

Experiments have shown that when turning and milling with cutters characterized by various levels of wear  $VB_c$ , the rounded cutting edge radius  $r_n$  rose, and so did

the amplitude and variance ( $D^2(\xi)$ ) of relative T-W system vibrations, and this, accordingly, caused an increase in the roughness of surface. The wear of cutters leads to an increase in the rounded cutting edge and, consequently, to a rise in the cutting forces, which cause a growth in the amplitude of relative T-W system vibrations [63, 75].

In a cutting process when feed rates are high  $f_z > \sqrt{2r_z h_{\min}}$ , the member containing the feed  $\left( \frac{f_z^4}{972r_z^2} \right)$  plays an important role, as it includes the influence of

the cutter representation (2.67). It has been revealed that in such a case the effects of the stereometric-kinematic representation of cutters on the value of the parameter  $Ra$  is increasingly big. With an increasing feed rate, the influence of the cutter representation decreases (the member containing the feed decreases), and the members containing  $h_{\min}$  and  $D^2(\xi)$  and  $D^2(\rho)$  (2.76) begin to play a significant role.

Of importance is case 3 (2.75) occurring in cutting with small feed rates, i.e.  $f_z \leq \sqrt{r_z h_{\min}}$ . A series of equations relevant for the particular ranges of feed were derived for this case. This infinite series of equations was written with the aid of one recurrent relationship. In this case, during machining with small feed rates, some of the marks of unevenness left by the  $k$ -th cutter are smoothed. Equations (2.75) and (2.76) are complex and therefore inconvenient and impractical. Thus, it was necessary to substitute them with a simpler relationship shown in Table 2.1. The error resulting from this approximation in a most unfavorable theoretical case does not exceed 15%. However, for conditions of an after-machining process, it will range 1-5%, which is permissible [72]. From the simplified relationship it follows that for  $f_z \leq \sqrt{2r_z h_{\min}}$  the feed rate does not affect surface roughness considerably.

In practice, reducing the feed rate below the above mentioned value is not recommended, as it does not lead to a decrease in surface roughness, and for  $f_z \leq 100 \frac{e}{z}$  it may even cause its increase. It can be explained by the fact that for

small feed rates  $f_z \leq 100 \frac{e}{z}$ , the face run-out previously resulting in surface waviness will now cause and increase surface roughness. To decrease roughness, it is necessary to reduce  $h_{\min}$  and  $D(\xi)$ .

By applying sharp cutters with a minimum rounded cutting edge radius  $r_n$ , we are able to reduce the minimum undeformed chip thickness  $h_{\min}$ . It is undesirable to use such cutters intensively as this may lead to considerable wear.

The standard deviation of relative displacements  $D(\xi)$  can be reduced by decreasing the amplitude of relative displacements  $A_\xi$ , which makes the machining system more rigid and causes the attenuation of vibrations acting on the system. Moreover, it is crucial that the machining conditions be selected properly avoiding the occurrence of self-excited vibrations.

Similarly, applying the definition, we could establish the total height of the roughness profile  $Rt$ . The relationships shown in Table 2.2 were used to calculate  $Rt$  as well as  $Ra$ .

The generalized model can be used to develop individual models for each cutting operation. When surfaces are machined with a single-cutter tool, then in formulas (2.67), (2.75) and (2.76) as well as in the above tables, the members describing the influence of the run-out can be eliminated assuming that  $D^2(\rho) = 0$ .

Then, depending on the type of machining the equivalent radius  $r_z$  should be replaced with a suitable quantity. Thus, for example, for straight turning or facing as well as face milling with a rounded corner tool, we have  $r_z = r_\epsilon$ . It can be used also to forecast and control surface roughness in planing and chiseling, provided we employ tools with a rounded cutting edge having the radius  $r_\epsilon$ . This model of surface roughness constitution can be applied also in the operations of milling, turning, drilling, reaming, and counterboring of a cylindrical surface (with the counterbore circumference).

For oblique turning, the formulas should include the equivalent radius  $r_z$  described by relationship [72]:

$$r_z = \frac{(D - 2a_p)\cos^2 \kappa_r}{2(\tan^2 \lambda_s + \sin^2 \kappa_r)} \quad (2.77)$$

where:  $D$  – diameter of the workpiece,  $a_p$  – depth of cut,  $\kappa_r$  – tool cutting edge angle,  $\lambda_s$  – cutting edge inclination.

For a cylindrical milling operation, we should assume that  $r_z = d/2$ .

All in all, the developed models seem to be applicable in most sculpturing and finishing processes if tools with specified stereometry of cutters are used.

#### 2.4.2. FORECASTING THE PARAMETER $Ra$ FOR FACE MILLING WITH SPHERICAL TOOLS

The profile of a surface generated after a pass of the  $i$ -th cutter ( $i = 1, 2, 3, \dots, z$ ) during the  $l$ -th ( $l = 1, 2, 3, \dots, n$ ) revolution of the milling head moving along the  $x$ -axis with an assigned feed rate with relative vibrations and showing face run-out of cutters can be described applying the equation obtained by substituting  $r_z = d/2$  into Eq. (2.54):

$$y_i(x) = \frac{1}{d} \cdot (x - f_z \cdot i_l)^2 + \rho_i + \xi_i \quad (2.78)$$

where:  $d$  – diameter of cutters.

Figure 2.37 presents a lateral surface profile taking into account the factors described in section 2.4.1 during a single revolution of a milling head equipped with spherical cutters.

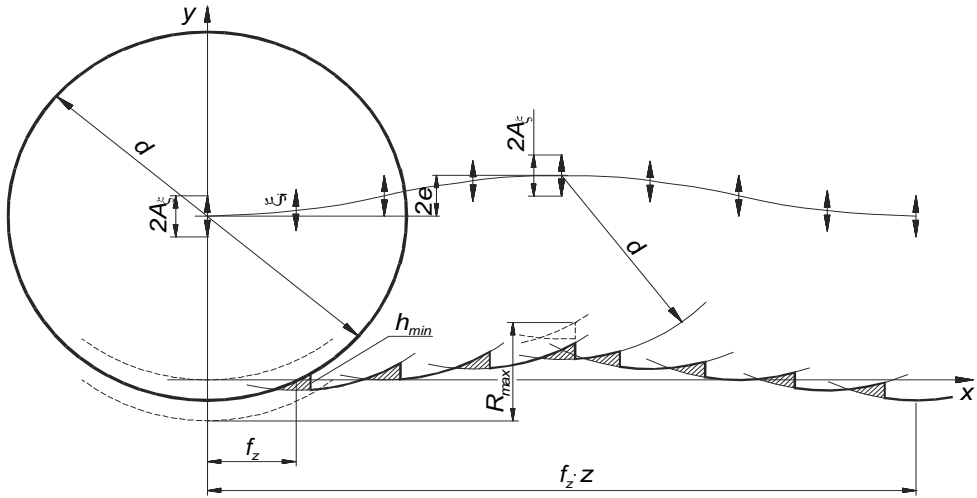


**Fig. 2.37.** Lateral microroughness profile of a surface face-milled with spherical tools with the diameter  $d$  applying the feed rate  $f_z$  due to relative vibrations of the tool and the workpiece  $\xi_{il}$  and an instantaneous cutter position owing to a face run-out  $\rho$  during one revolution

The mean arithmetic deviation of the profile (given by the function  $y_i(x)$ ) from the mean line will be established from relationship (2.67) assuming that  $D^2(\rho) = 0$ :

$$Ra = \sqrt{\frac{f_z^4}{243d^2} + \frac{5}{81}h_{\min}^2 + \frac{50}{81}D^2(\xi) + \frac{10d^2h_{\min}^2}{27f_z^4}D^2(\xi)} \quad (2.79)$$

Taking into consideration the above factors, it is possible to determine the total thickness of the surface roughness profile  $Rt$  (Table 2.2):

$$Rt = \frac{f_z^2}{4d} + \frac{h_{\min}}{2} \left( 1 + \frac{d \cdot h_{\min}}{2f_z^2} \right) + 2A_\xi \quad (2.80)$$

Equation (2.79) and (2.80) are relevant for  $f_z > \sqrt{dh_{\min}}$ . On the other hand, when feed rates per tooth range  $100 \frac{e}{z} \leq f_z \leq \sqrt{dh_{\min}}$ , the value of the parameter  $Ra$  will be (Table 2.1):

Moreover,

$$Ra = \sqrt{\frac{16}{243}h_{\min}^2 + \frac{60}{81}D^2(\xi)} \quad (2.81)$$

Accordingly, it is possible to determine the value of the parameter  $Rt$ :

$$Rt = \frac{f_z^2}{4d} + 2A_\xi + h_{\min} \quad (2.82)$$

When  $f_z \geq 100 \frac{e}{z}$ , the face run-out of cutters  $e$  results in surface waviness.

For small feed rates, on the other hand, i.e. when  $f_z < 100 \frac{e}{z}$ , the run-out will cause roughness, thus, according to Table 2.1 and Eq. (2.81), we get respectively:

$$Ra = \sqrt{\frac{16}{243} h_{\min}^2 + \frac{60}{81} \left[ D^2(\xi) + \frac{e^2}{2} \cdot \left( 1 + \frac{1}{5} \cos \frac{2\pi}{z} \right) \right]} \quad (2.83)$$

$$Rt = h_{\min} + 2A_\xi + 2e \quad (2.84)$$

**Table 2.1.** Generalized approximate formulas used for calculating the parameter  $Ra$  when applying tools with defined stereometry

Item	Feed range $f_z$	Approximate formula for calculating the parameter $Ra$
1	$f_z > \sqrt{2r_z h_{\min}}$	$Ra = \sqrt{\frac{f_z^4}{972r_z^2} + \frac{5}{81} h_{\min}^2 + \frac{50}{81} \left[ D^2(\xi) + D^2(\rho) \left( 1 + \frac{1}{5} \cos \frac{2\pi}{z} \right) \right] + \frac{40r_z^2 h_{\min}^2}{27f_z^2} \left[ D^2(\xi) + D^2(\rho) \left( 1 - \cos \frac{2\pi}{z} \right) \right]}$
2.	$100 \frac{e}{z} \leq f_z \leq \sqrt{2r_z h_{\min}}$	$Ra = \sqrt{\frac{16}{243} h_{\min}^2 + \frac{60}{81} D^2(\xi)}$
3.	$f_z \leq 100 \frac{e}{z}$	$Ra = \sqrt{\frac{16}{243} h_{\min}^2 + \frac{60}{81} \left[ D^2(\xi) + D^2(\rho) \left( 1 + \frac{1}{5} \cos \frac{2\pi}{z} \right) \right]}$

**Table 2.2.** Generalized formulas used for calculating the parameter  $Rt$  when applying tools with defined stereometry

Item	Feed range $f_z$	Formula for calculating the parameter $Rt$
1.	$f_z > \sqrt{r_z h_{\min}}$	$Rt = \frac{f_z^2}{8r_z} + \frac{h_{\min}}{2} \left( 1 + \frac{r_z h_{\min}}{f_z^2} \right) + 2A_\xi$
2.	$\sqrt{\frac{2}{(k+1)k} r_z h_{\min}} < f_z \leq$ $\leq \sqrt{\frac{2}{(k-1)k} r_z h_{\min}}$ $k = 2, 3, 4, \dots$	a) $100 \frac{e}{z} < f_z \leq \sqrt{r_z h_{\min}}$ $Rt = \frac{f_z^2 k^2}{8r_z} + \frac{h_{\min}}{2} \left( 1 + \frac{r_z h_{\min}}{f_z^2 k^2} \right) + 2A_\xi$
		b) $f_z \leq 100 \frac{e}{z}$ $Rt = \frac{f_z^2 k^2}{8r_z} + \frac{h_{\min}}{2} \left( 1 + \frac{r_z h_{\min}}{f_z^2 k^2} \right) + 2A_\xi + 2e$

Basing on relationships (2.79), (2.81) and (2.83), it was possible to develop a nomogram for forecasting the values of  $Ra$  in face milling with spherical cutters under conditions to be found in practice (Fig. 2.38).

Analyzing the curves in Figure 2.38, we can see that the influence of the feed rate  $f_z$  on the value of the parameter  $Ra$  is more and more considerable when the relative vibrations  $D(\xi)$  decrease. The value of the parameter  $Ra$  decreases with the feed rate  $f_z$  but only to a certain limit dependent on the relative vibrations  $D(\xi)$  and the minimum deformed chip thickness  $h_{\min}$  (curves 1 to 4). For a small feed rate, i.e.  $f_z < 100 \frac{e}{z}$ , the roughness increases even in jumps; this is caused by the fact that for these feed rates the face run-out of the cutters  $e$  leads to the constitution of roughness containing microirregularities (curves 1' to 4').

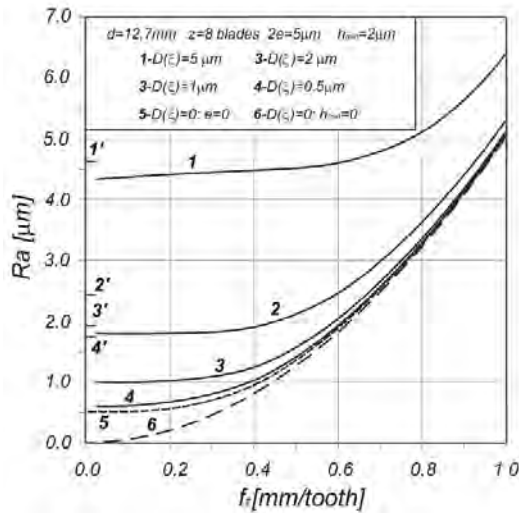


**Fig. 2.38.** Nomogram for forecasting the value of the roughness parameter  $Ra(f_z, D(\xi))$  for surfaces facemilled with rounded corner tools with the diameter  $d$

### 2.4.3. VERIFICATION OF THE MATHEMATICAL MODEL BASED ON THE EXAMPLE OF FACE MILLING MACHINING

The operation of the computerised test stand for registration and analysis of a lateral profile of the GSS was presented in Ref. [71]. The investigation involved milling specimens without any cooling or lubricating fluid at the F2-250 vertical knee-type milling machine, whose head was inclined at an angle of  $1^\circ$  so that a unidirectional GSS would be formed. Cubicoid-shaped specimens were made of 45 steel (180-200 HB hardness) and ŽL 200 cast iron (180-200 HB hardness).

The specimens were milled with a 160 mm diameter cassette head equipped with round RNGN 120400 T02020 inserts made of AZ-10 white ceramics and TWN black ceramics in the following conditions:

- speed of cutting  $v_c = (90.5-502.6)$  m/min,
- feed per blade  $f_z = (0.039-0.225)$  mm/blade,
- depth of cutting  $a_p = 0.5$  mm,
- number of cutting blades  $z = (1 \text{ and } 8)$  blades,
- width of milled specimens  $W = 110$  mm,
- rotational speed of the head  $n = (180-1000)$  revolution per min.

Surfaces machined in these conditions were analysed by registering their profiles and recording in the form of files by means of a computerized test stand. The registered lateral profiles of the surface micro-roughness were analysed after determining the standardised unilateral function of spectral power density (FSPD).

On the specimens milled in the specified conditions, the lateral roughness  $R_a$  was measured fifteen times in the direction of the feed by means of a computerized test stand [71]. The mean values of these measurements along with the confidence ranges for level 0.95 were given in these diagrams. For comparison purposes, the theoretical values of  $R_{ao}$  take into account tool representation and from the author's own model of  $R_{at}$  (Table 2.1) were also included in the diagram [72].

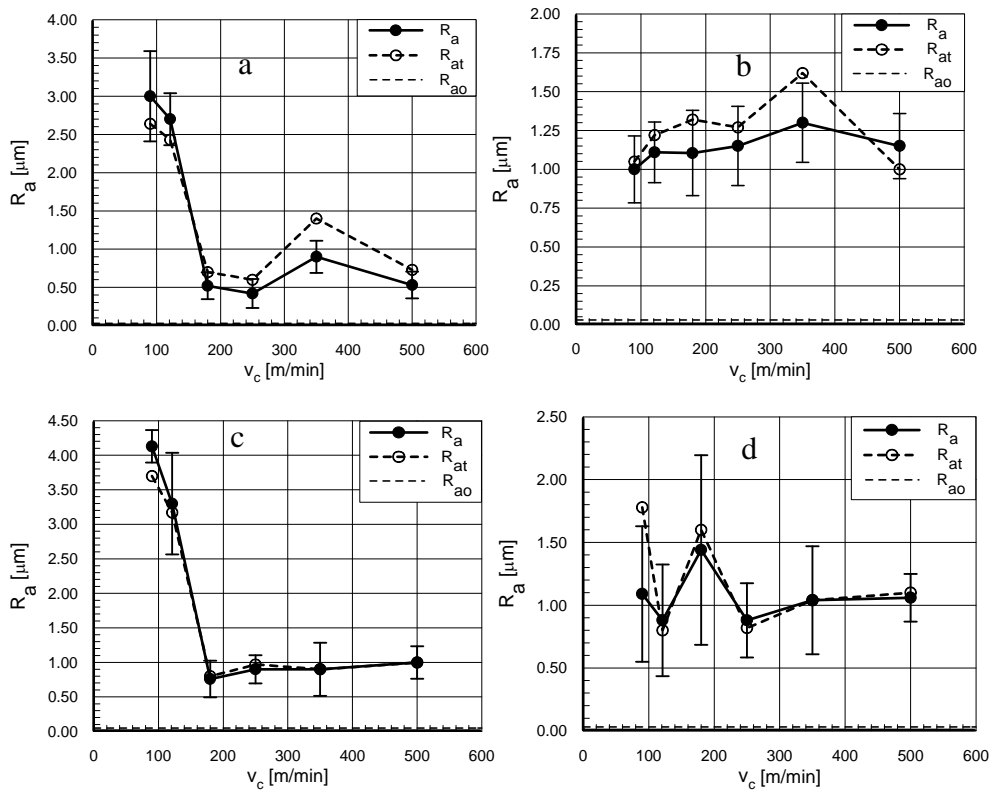


**Fig. 2.39.** Influence of the speed of cutting  $v_c$  on the surface roughness  $R_a$ . Comparison of the results of laboratory tests with the theoretical results. The machining conditions: blade material TWN, feed  $f_z = 0.078$  mm/blade, a) 45 steel,  $z=1$ ; b) Ž1200,  $z=1$ ; c) 45 steel,  $z=8$ ; d) Ž1200,  $z=8$

Figure 2.39 shows the influence of the speed of cutting,  $v_c$ , on the value of the parameter  $R_a$  and the results of laboratory tests compared with the theoretical results of  $R_{at}$  of surfaces milled with TWN ceramic blades.

Figure 2.40 shows the influence of the feed  $f_z$  on the surface roughness  $R_a$  and the results of laboratory tests with the theoretical values of  $R_{at}$  of surfaces milled with AZ-10 white ceramic blades. It was found that, in principle, the values of the parameter  $R_{at}$  determined on the basis of the author's own model are within the confidence ranges of the values measured on milled surfaces. However, the values of  $R_{ao}$  determined on the basis of relationship take into account only the tool representation differ from the real values of  $R_a$ . Hence the conclusion that the developed model provides a good description of the process of roughness constitution on surfaces face-milled with round blades. When machining 45 steel (Figs. 2.39a and c), an increase in the speed of cutting  $v_c$  caused a sudden decrease in the value of the parameter  $R_a$ , and then a slight increase at  $v_c = 180$  m/min or greater. When machining  $\check{Z}1200$  cast iron, the influence of the speed of cutting  $v_c$  is not big.

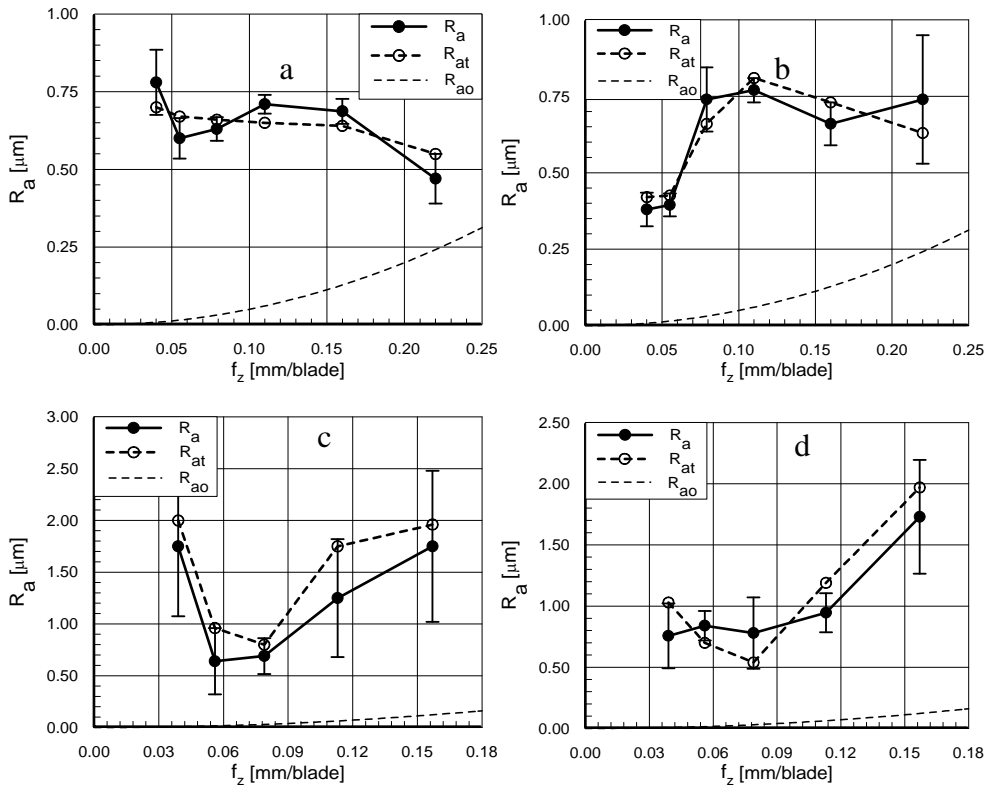


**Fig. 2.40.** Influence of the feed  $f_z$  on the surface roughness  $R_a$ . Comparison of the results of laboratory tests with the theoretical results. The machining conditions: blade material AZ-10, speed of cutting  $v_c=178.5$  m/min; a) 45 steel,  $z=1$ ; b)  $\check{Z}1200$ ,  $z=1$ ; c) 45 steel,  $z=8$ ; d)  $\check{Z}1200$ ,  $z=8$

Analysing Figure 2.40, one can see that if the feed goes down, the value of the parameter  $Ra$  falls to the minimum for  $f_z \approx 0.06$  mm/blade and then slightly goes up (with the exception of Figure 2.40a, where it rises first and then falls). Thus, the minimum surface roughness is obtained for the feed  $f_z \approx 0.06$  mm/blade.

The present study shows that:

1. The roughness of surfaces sculptured with multicutter tools, the cutters having specified stereometry is quantitatively affected by the cutting edge representation, the unremoved fragment of material, relative tool-workpiece system vibrations, the cutter run-out, and partly the tool wear.
2. There exists a general mathematical model for the constitution of surface roughness independent of the method of metal cutting using tools with specified geometry.
3. The vibrations of the tool-workpiece system, the cutter run-out (for milling), and the unremoved fragment of material constitute a limitation for surface roughness, thus it is necessary to reduce them to a minimum.
4. The feed rate is reported to have a considerable influence on the roughness of surfaces in face-milling only for high feed rates per tooth and small radii of the cutters. The influence becomes greater with an increase in the feed rate and a decrease in relative displacements as well as the minimum deformed chip thickness. The feed rate from the range  $100 \frac{e}{z} \leq f_z \leq \sqrt{2r_z h_{\min}}$  does not affect surface roughness in face milling.
5. It is recommended that a face milling operation should be performed with feeds per tooth being in the upper limit of or even slightly above the  $100 \frac{e}{z} \leq f_z \leq \sqrt{2r_z h_{\min}}$  range; applying lower values, we will fail to decrease surface roughness (and the feed rates  $f_z < 100 \frac{e}{z}$  will even increase it), and reduce the process capacity.
6. The values of the parameters  $Rat$  determined from the author's own model were within the confidence range of the measured values  $Ra$ . Hence the conclusion that the roughness  $Ra$  of surfaces face-milled with round blades, except from the blade mapping, affects considerably the non-removable part of the machining allowance, the relative vibrations of the tool and the work and the face milling of the blades.
7. An increase in the value of  $v_c$  for 45 steel leads to a decrease in the value of the parameter  $Ra$  and from  $v_c \approx 180$  m/min its stabilisation. The influence of  $v_c$  on the roughness  $Ra$  for cast iron is not clear. The influence of the feed  $f_z$  on the roughness  $Ra$  of surfaces milled with one blade is small. When machining  $\check{Z}1200$  cast iron with an 8-blade head, an increase in the feed  $f_z$  caused an in-

crease in the value of the parameter  $Ra$ . Smaller roughness was obtained after machining with inserts made of AZ-10 white ceramics. The surfaces machined with one blade were characterised by smaller roughness  $Ra$  than those machined with eight blades. It should be noted that the machining of highly efficient round ceramic inserts can be used as finishing because of low values of the parameter  $Ra$  (the minimum value of  $Ra \approx 0.4 \mu\text{m}$ ).

### Nomenclature

$A_{\xi}$ – amplitude of the tool-workpiece system vibrations, $\mu\text{m}$ ;	$\rho_i$ – instantaneous position of the $i$ -th cutter in relation to the workpiece due to cutter run-out, $\mu\text{m}$ ;
$D^2(\xi)$ – variance of the tool-workpiece system vibrations, $\mu\text{m}^2$ ;	$L$ – length of a measurement section, $\text{mm}$ ;
$D^2(\rho)$ – variance of the multicutter tool run-out, $\mu\text{m}^2$ ;	$l_e$ – length of elementary measurement section, $\text{mm}$ ;
$D$ – workpiece diameter, $\text{mm}$ , $\mu\text{m}$ ;	$Ra$ – arithmetic mean of roughness profile ordinates, $\mu\text{m}$ ;
$d$ – milling head cutter diameter, $\text{mm}$ , $\mu\text{m}$ ;	$Rt$ – total roughness profile height, $\mu\text{m}$ ;
$h_{\min}$ – minimum undeformed chip thickness, $\mu\text{m}$ ;	$r_{\varepsilon}$ – corner radius, $\text{mm}$ , $\mu\text{m}$ ;
$e$ – face (radial) run-out of cutters, $\mu\text{m}$ ;	$r_n$ – rounded cutting edge radius, $\text{mm}$ , $\mu\text{m}$ ;
$f$ – feed per revolution, $\text{mm/rev}$ , $\mu\text{m/rev}$ ;	$r_z$ – equivalent radius, $\text{mm}$ , $\mu\text{m}$ ;
$f_z$ – feed per tooth, $\text{mm/tooth}$ , $\mu\text{m/tooth}$ ;	$\lambda_s$ – tool cutting edge inclination;
$\kappa_r$ – tool major cutting edge angle;	$\bar{y}$ – mean value of the modeled profile, $\mu\text{m}$ ;
$\xi_{i_l}$ – instantaneous relative displacement of the $i$ -th cutter during the $l$ -th revolution due to tool-workpiece vibrations, $\mu\text{m}$ ;	$z$ – number of milling cutters or milling heads

## 2.5. THE ANALYSIS OF MECHANICAL CHARACTERISTICS OF FILAMENT BRUSH TOOL

*Slawomir Spadlo*

So far the machining process using filamentary metal brushes in the shape of disks has been used in surface machining to remove corroded layers, to prepare metal surfaces to be galvanized, and to produce surfaces of high adhesion to be coated with paint, glue, etc. Recently the process has been developed to include operations such as removing sharp edges and burrs [78], flashes and bosses from machine parts made of alloys of non-ferrous metals, as well as cleaning welds. Using brushes with densely packed filaments made of hard steel broadens the range of uses to include the micro-milling of ordinary constructional steels of low hard-

ness, which are machined with the tips of the filaments. To summarize, the typical uses of metal brush tools are limited to machining materials of a hardness lower than that of the material the filaments of the brush are made of.

Using filaments made of abrasive-grain-filled polymers allows the brushes to be used to machine the surfaces of materials of high hardness.

On analysis of the advantages of using brush filament tools the author suggests a new machining operation that combines mechanical, electrochemical, and electro-erosive processes acting on the machined item [82, 87, 88].

Thanks to the synergetic effect, this type of hybrid machining makes the metal removal process more cost-effective.

Soft machining parameters allow not only the removal of the excess material from large items of low stiffness but also the highly efficient volumetric machining of metals, alloys, and conductor-based composites.

The numerous uses of brush electrodes result from their characteristics [81, 92]:

- flexibility of individual filaments,
- type, shape, and packing density of the filaments,
- possibility of operation at various electrode deflection settings,
- large contact zone of the tool and the machined item,
- possibility of using the electrode until it is worn out,
- large working area of the hot electrode allowing the machining of both flat and complex-shape items.

Because of their construction brush electrodes are characterized by:

- uniform distribution of the filaments, which helps to form a discrete structure suitable for maintaining stable conditions in the machining zone,
- radial, axial, and tangential flexibility, which makes the filaments fit complex geometry surfaces easily thus permitting a uniform removal of surface layers without significantly changing the geometry of the machined part,
- easy disposal of the erosion by products from the discharge zone,
- suitability for automated operations.

The use of brushing tools in an automation environment will necessitate a clear understanding of important brush performance characteristics such as forces. An understanding of such characteristics is important, as surface preparation processes require a detailed knowledge of interrelationships between productivity of machining and brush operating conditions [89, 92]. For example, it is recognized that electrical discharges generated during electroerosion-mechanical processes are closely related to the mechanical characteristics of the filament [90].

### **2.5.1. STATICS INTERACTIONS AND KINEMATICS OF A SINGLE FILAMENT OF THE CIRCULAR BRUSH**

Since the elements of a disk brush tend to deform easily, the use of the brush in erosion mechanical machining changes the character of mechanical interactions with the machined surface in contrast to deformation-resistant electrodes. An increase in

the value of the pressure force at the filament tip as a function of displacement along the surface inevitably leads to a break in the anodic film and initiates discharges whose frequency can be determined, among others, by the vibrations of individual filaments of the electrode.

The mechanics of the movement and filament wire interactions with the machined surface is very complex. The wire becomes deformed in a way that is difficult to analyse. It is caused by confounded boundary conditions which allow only an approximate solution to the equation of its motion.

Only a tentative analysis of the interactions between the brush elements and the surface has been presented.

Let us consider a tentative analysis of a filament load. The basic assumptions are [79, 80]:

- inertial forces are neglected,
- the filament tip moves along a rigid surface.

Additionally, due to low packing density, interactions between individual wires are ignored. It is assumed that the filaments are placed radially from the hub centre and are restrained at the hub outside radius and obey Hooke's law [83-86, 91].

The filaments are straight before they come into contact with the machined surface. They are deflected perpendicularly to the axis of rotation, with the radial run-out of the disks being ignored.

Filament deflection is examined in a mobile reference system  $K \xi \eta$  (Fig. 2.41) where  $\eta = \eta(\xi)$  is its elastic deflection assuming that there is no influence of non-dilatational strain.

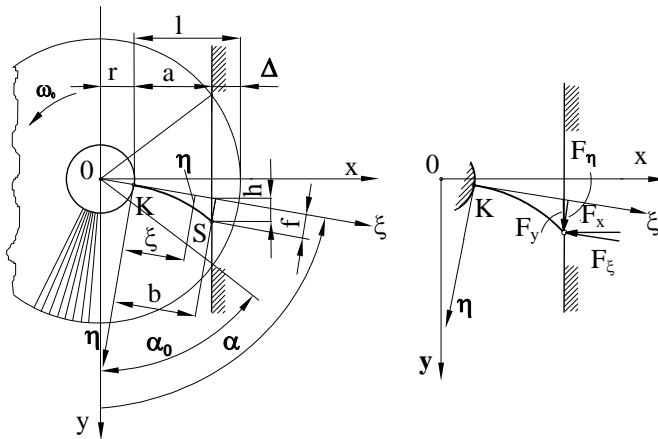


**Fig. 2.41.** Geometry of a single filament deformation

The differential equation of the bending line is:

$$EI \frac{\eta''}{(1+\eta'^2)^{3/2}} = F_\eta(b-\xi) + F_\xi[\eta(b) - \eta(\xi)] \quad (2.85)$$

where:  $EI$  – filament flexural rigidity,

$$\begin{aligned}\eta'(\xi) &= d\eta/d\xi, \\ \eta''(\xi) &= d^2\eta/d\xi^2, \\ 0 \leq \xi &\leq b.\end{aligned}$$

The geometry of the examined problem produces the following relationships:

$$\begin{aligned}h &= f / \sin \alpha \\ b &= \frac{a+r}{\sin \alpha} - r + h \cos \alpha = d + h \cos \alpha \\ d &= \frac{a+r}{\sin \alpha} - r\end{aligned}$$

We assume that:

$$\begin{aligned}F_y &= \mu F_x \\ F_\xi &= c_1 F_x, F_\eta = c_2 F_x \\ c_1 &= \sin \alpha - \mu \cos \alpha \\ c_2 &= \cos \alpha + \mu \sin \alpha\end{aligned}$$

where:  $\alpha = \omega_0 t$ ,  $\mu$  – coefficient of friction between the filament tip and the machined surface,  $\omega_0$  – angular velocity of the brush.

The function  $\eta(\xi)$  should also satisfy the following condition:

$$l - \int_0^b \sqrt{1 + [\eta'(\xi)]^2} d\xi = 0 \quad (2.86)$$

It is very difficult to obtain numerical solutions for equation (2.85) with constraint (2.86). Analytical solutions can be obtained if the values of  $\eta(\xi)$  are small enough to enable the linearization of the left-hand side of the equation (2.85).

The details of the solution of equation (2.85) with initial conditions:

$$|\eta(0)| = 0 \quad \text{and} \quad |\eta'(0)| = 0$$

and with the assumption that the wire tip (for  $\xi = b$ ) has point contact with the surface (then  $\eta''(b) = 0$ ) have been presented below.

We will examine a case of a single filament load under tentative conditions presented above. The deflection of the part is described in a mobile reference system  $K\xi\eta$  (Fig. 2.41). In that case  $\eta = \eta(\xi)$  is its elastic deflection with the assumption that there is no influence of non-dilatational strain.

An approximate analytical solution can be obtained if we assume that the values of  $\eta'(\xi)$  are small enough to enable the linearization of the left-hand side of equation (2.85), which is the case where:

$$\frac{l-a}{l} \ll 1$$

Then we assume that:

$$|\eta'(\xi)| \ll 1$$

Consequently, in place of equation (2.85) and (2.86) we can have

$$\left\{ \begin{array}{l} EI \left[ 1 - \frac{3}{2} \eta'^2(\xi) \right] \eta''(\xi) = [C_2(b - \xi) + C_1(f - \eta)] F_x \quad (2.85a) \\ l - b - \frac{1}{2} \int_0^b [\eta'(\xi)]^2 d\xi = 0 \quad (2.86a) \end{array} \right.$$

where:

$$f = \eta(b)$$

As a result of a subsequent approximation the above equations are replaced by:

$$\left\{ \begin{array}{l} EI \eta'' = [c_2(b - \xi) + c_1(f - \eta)] F_x \quad (2.87a) \\ \frac{1}{2} \int_0^b [\eta'(\xi)]^2 d\xi = l - b \quad (2.87b) \end{array} \right.$$

Furthermore, we will consider solutions for equations (2.87) valid only if  $l-a$  is small.

The first equation looks as follows:

$$\eta'' = [c_2 d + (c_2 \text{ctg} \alpha + c_1) f - c_2 \xi - c_1 \eta] \frac{F_x}{EI}$$

and we assign:

$$\omega^2 = \frac{c_1 F_x}{EI}, \quad \frac{F_x}{EI} = \frac{\omega^2}{c_1}$$

thus

$$\eta'' + \omega^2 = [c_2 d + (c_2 \text{ctg} \alpha + c_1) f - c_2 \xi - c_1 \eta] \frac{\omega^2}{c_1} - \frac{c_2}{c_1} \omega^2 \xi$$

because

$$c_2 \text{ctg} \alpha + c_1 = 1 / \sin \alpha$$

so

$$\eta'' + \omega^2 \eta = D - \frac{c_2}{c_1} \omega^2 \xi \quad (2.88)$$

where:

$$D = (c_2 d + h) \frac{\omega^2}{c_1} = \text{const} \quad (\text{does not depend on } \xi)$$

The solution to equation (2.88) with initial conditions:

$$\eta(0) = 0 \quad \text{and} \quad \eta'(0) = 0$$

and with the wire tip ( $\xi = b$ ) having point contact with the surface (then  $\eta''(b) = 0$ ) is:

$$\eta(\xi) = \frac{c_2(\alpha)}{c_1(\alpha)} \frac{1}{\omega} \left[ (1 - \cos \omega \xi) \text{tg} \omega b - (\omega \xi + \sin \omega \xi) \right] \quad (2.89)$$

where:

$$\omega^2 = \frac{c_1(\alpha) F_x}{EI}$$

The problem is intractable because:

- is unknown  $\omega$  (dependent on unknown  $F_x$ ),
- and  $b$  (dependent on  $h$  or  $f$ ).

We should require in (2.88) for  $\xi = b$  to be  $\eta(b) = f = h \cdot \sin \alpha$ , then we obtain:

$$h \sin \alpha = \frac{c_2(\alpha)}{c_1(\alpha)} \frac{1}{\omega} \left[ (1 - \cos \omega \xi) \text{tg} \omega b - (\omega \xi + \sin \omega \xi) \right] = \eta(b)$$

Thus, after employing geometric relationships, we obtain the following equation:

$$h = \frac{c_2 d (\text{tg} \omega b - \omega b)}{\omega b - c_2 \cos \alpha \text{tg} \omega b} \quad (2.90)$$

Condition (2.88) will be satisfied after employing (2.89), so the equation is re-written as:

$$\eta'(\xi) = \frac{c_2}{c_1} \left[ \frac{\cos \omega (b - \xi)}{\cos \omega b} - 1 \right]$$

then

$$\frac{1}{2} \int_0^b [\eta'(\xi)]^2 d\xi = \left( \frac{c_2}{2c_1} \right)^2 \left( \frac{1}{\cos^2 \omega b} - 3 \frac{\text{tg} \omega b}{\omega b} + 2 \right) \cdot b$$

employing

$$b = \frac{a + r}{\sin \alpha} - r + h \cos \alpha = d + h \cos \alpha$$

we obtain:

$$1 - \frac{a+r}{\sin \alpha} + r - h \cos \alpha = \left( \frac{1}{\cos^2 \omega b} - 3 \frac{\text{tg } \omega b}{\omega b} + 2 \right) \cdot b \quad (2.91)$$

Substituting (2.90) for (2.91) we obtain a transcendental equation with unknowns  $\omega b$ . Only the lowest roots of the equation calculated as a function of  $\alpha$  are physically feasible. These roots enable the value of  $\omega$  to be calculated.

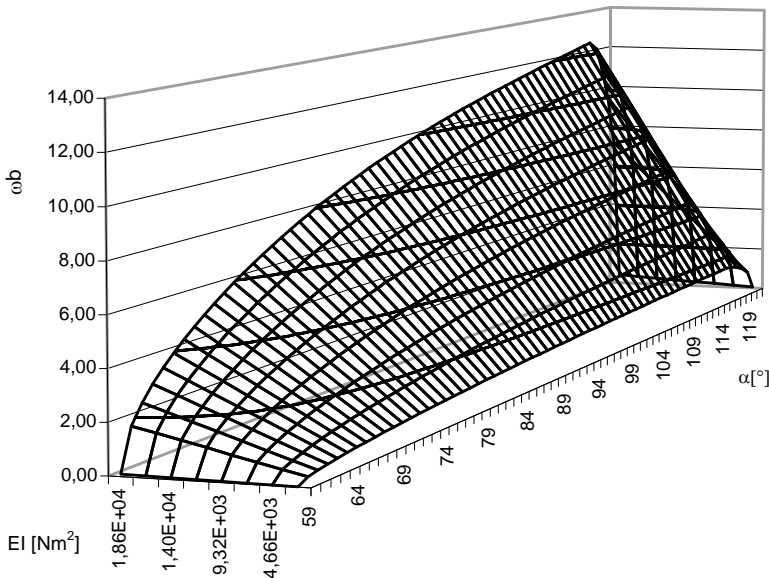
It applies to all the components of the interaction force, that is:

$$F_x = \frac{EI\omega^2}{c_1}, \quad F_y = \mu F_x$$

$$F_\xi = c_1 F_x, \quad F_\eta = c_2 F_x$$

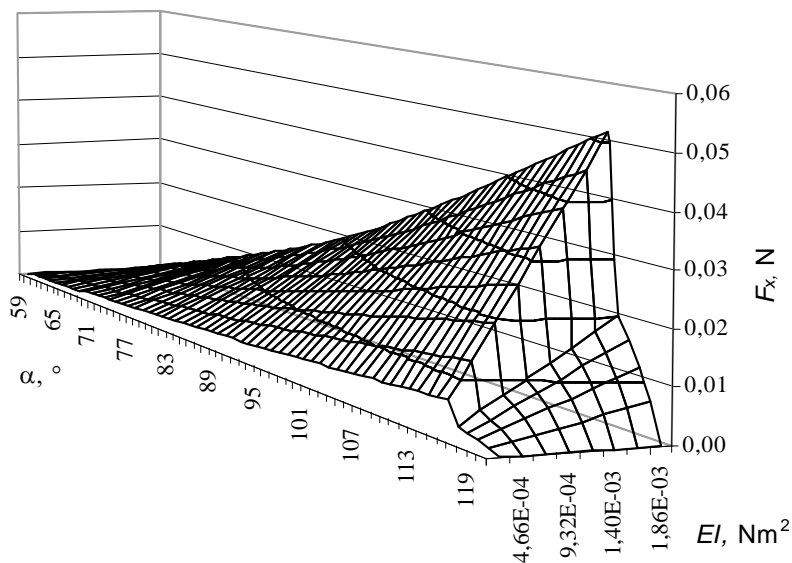
as well as the bending line for  $\eta(\xi)$ .

Figure 2.42 shows the relationship  $\omega b$  as a function of  $\alpha = \omega_0 t$  and filament flexural rigidity –  $EI$  with the following parameters:  $l = 0.05$  m,  $a = 0.04$  m,  $r = 0.02$  m,  $\mu = 0.5$ .



**Fig. 2.42.** Graph of changes in parameter  $\omega b$  as a function of the rotation angle and filament flexural rigidity –  $EI$

Graphs of the changes in the values of force components  $F_x$ ,  $F_y$ , as a function of the rotation angle and filament flexural rigidity –  $EI$  have been presented in Figures 2.43 and 2.44.



**Fig. 2.43.** The values of force component  $F_x$  interaction with the surface as a function of rotation angle  $\alpha$  and filament flexural rigidity –  $EI$

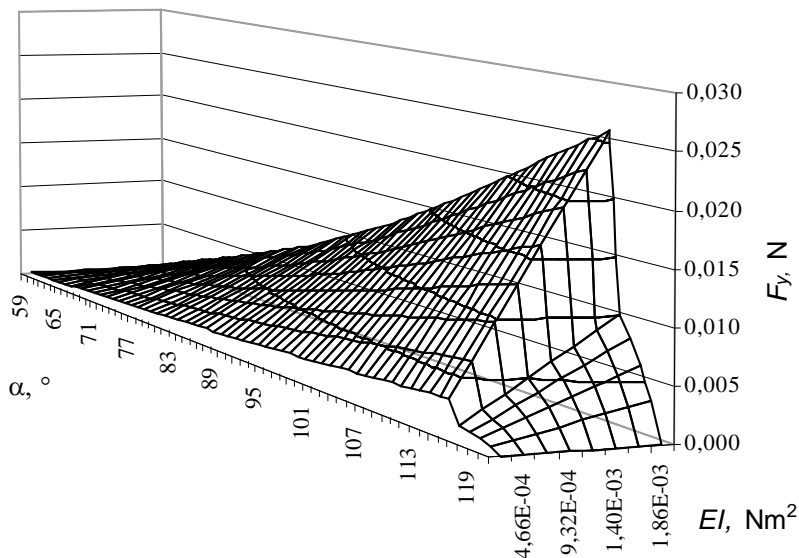


**Fig. 2.44.** The values of force component  $F_y$  interaction with the surface as a function of rotation angle  $\alpha$  and filament flexural rigidity –  $EI$

Graphs of the changes in the values of force components  $F\xi$ ,  $F\eta$  as a function of the rotation angle and filament flexural rigidity –  $EI$  have been presented in Figures 2.45 and 2.46.

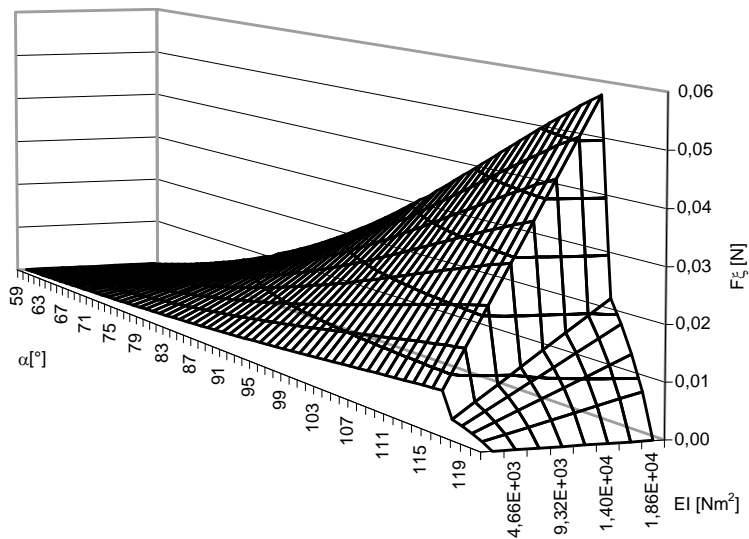


**Fig. 2.45.** The values of force component  $F_{\zeta}$  interaction with the surface as a function of rotation angle  $\alpha$  and filament flexural rigidity –  $EI$

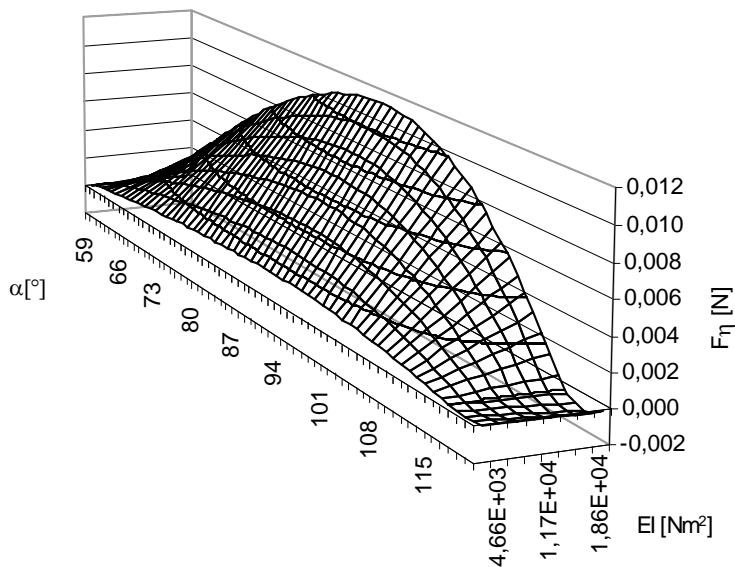


**Fig. 2.46.** The values of force component  $F_{\eta}$  interaction with the surface as a function of rotation angle  $\alpha$  and filament flexural rigidity –  $EI$

The changes in the relationship  $F_{\eta}$  as a function of angle  $\alpha = \alpha(t)$  have to be pointed out. At  $\alpha \approx 116^\circ$  the sign of the force is reversed. Consequently, the force causes the filament to straighten when it loses contact with the machined surface.

## 2.5.2. DYNAMICS OF A SINGLE FILAMENT OF A CIRCULAR BRUSH

The equation of the motion of a filament with its mass taken into account can be shown by coordinates  $K\xi \eta$  as an equation [79] describing relative motion. We assume that  $|\eta(\xi, t)| \ll 1$  and omit Coriolis inertial forces which are negligibly small in this case, to obtain:

$$EI \frac{\partial^4 \eta}{\partial \xi^4} + F_{\xi 1} \frac{\partial^2 \eta}{\partial \xi^2} + \rho A \frac{\partial^2 \eta}{\partial t^2} = -F_{\eta 1} \delta(\xi - b) + \rho A (r + \xi) \ddot{\alpha} \quad (2.92)$$

It can be shown that when inertial forces are neglected the equation can be rewritten as (2.87a). Forces  $F_\xi$  and  $F_\eta$  are marked  $F_{\xi 1}$  and  $F_{\eta 1}$  respectively because these are not the same forces as in the previous expressions.

Solutions have to be looked for with boundary conditions being:

$$\begin{aligned} \text{for } \xi(0) = 0 \text{ is } \eta(0, t) = 0, & \quad \text{and } \left. \frac{\partial \eta}{\partial \xi} \right|_{\xi=0} = 0, \\ \text{for } \xi = b(t) \text{ is } \left. \frac{\partial^2 \eta}{\partial \xi^2} \right|_{\xi=b(t)} = 0, & \quad \text{and} \\ & \quad \left[ EI \frac{\partial^3 \eta}{\partial \xi^3} + F_{\xi 1} \frac{\partial \eta}{\partial \xi} \right]_{\xi=b(t)} = -F_{\eta 1}, \end{aligned} \quad (2.93)$$

and initial conditions:

$$\eta(\xi, 0) = 0, \quad \left. \frac{\partial \eta}{\partial t} \right|_{t=0} = 0.$$

In addition, the earlier mentioned geometric conditions have to be met as well as condition (2.86). This boundary-initial problem cannot be solved by conventional methods. It is very hard to obtain even approximate numerical solutions for the equation.

If we assume that the filaments maintain contact with the machined surface, the following condition is satisfied:

$$\frac{1}{2} \int_0^b [\eta'(\xi)]^2 d\xi = l - b \quad (2.94)$$

It's very hard to obtain even approximate solutions for the equation.

This boundary-initial problem cannot be solved by conventional methods. Based on the solutions presented above, the Galerkin approximation was used. At  $\alpha = \omega_0 t$  the last component of equation (2.92) disappears.

Let's assume that the first approximation is

$$\eta(\xi, t) \approx Y(\xi) \cdot S(t) \quad (2.95)$$

where:

- value  $S(t)$  describes the shift of the filament tip towards axis  $\eta$  when is multiplied by  $Y(b)$ ,
- the function of  $Y(\xi)$  has been chosen arbitrarily; it satisfies conditions  $Y(0) = 0$  and  $Y'(0) = 0$  and will be integrated using the variable limits of  $0 - b(t)$ .

As a result, we obtain an ordinary differential equation containing variable coefficients because

$$b = b(\alpha) = b(t)$$

$$m_r(b) \cdot \ddot{S}(t) + k_r(b) \cdot S(t) = -F_{\eta 1} Y(b) \quad (2.96)$$

where:

$$m_r = \rho A \int_0^b Y^2(\xi) d\xi,$$

$$k_r = EI \int_0^b Y^{IV}(\xi) Y(\xi) d\xi + F_{\xi 1} \int_0^b Y^{II}(\xi) Y(\xi) d\xi,$$

whose solution should satisfy condition (2.94). Consequently, we obtain a system of two equations with two unknowns  $S(t)$  and  $b(t)$ .

Figure 2.47 shows a numerical solution for the equation describing filament tip displacement along the machined surface as a function of angle  $\alpha$  (being simultaneously a function of time  $\alpha = \omega_0 t$ ) for  $\rho A = 3.39 \cdot 10^{-4}$  kg/m, that is:

$$\begin{cases} \bar{y} = (r+1) \cos \alpha_0 - \frac{r+a}{\operatorname{tg} \alpha} - S(t) Y(b) / \sin \alpha & (2.97a) \\ \alpha_0 = \arcsin\left(\frac{r+a}{r+l}\right) & (2.97b) \end{cases}$$

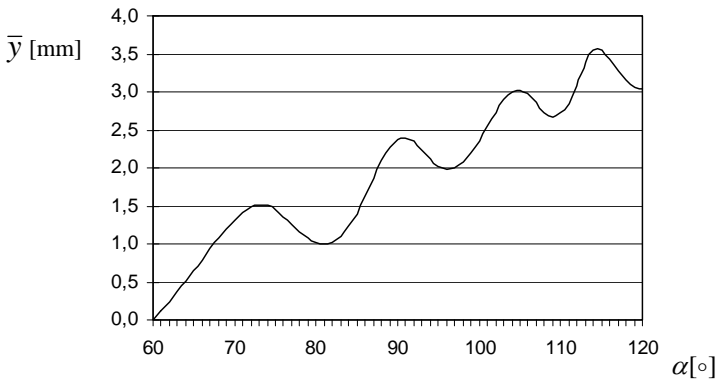


**Fig. 2.47.** Graph of the dynamic displacement of the filament tip along the line of contact with the surface as a function of the rotation angle of the disk  $\alpha(t)$

Equation (2.97a) can be rewritten as:

$$\bar{y} = R \cos \alpha_0 - \frac{r - \Delta}{\operatorname{tg} \alpha} - S(t)Y(b) / \sin \alpha ,$$

where:  $R$  – disk outside radius,  $\Delta$  – applied filament radial deflection value.

The figure shows that the movement of the filament along the machined surface is not monotonic. It demonstrates that the influence of the filament dynamics on its load can be quite considerable. The paper offers only a brief outline of the problem which requires further research.

The present study shows that:

1. Lower packing densities of filament wires diminish the effect of mutual filament support, thus making the brush more deformation-prone. It makes it possible to adjust the deflection ( $\Delta$ ) parameter within a wider range of settings, with the disk retaining its original size.
2. The pressure force the filament tip exerts on the surface along the displacement path increases in a non-linear manner, with its value suddenly dropping towards the end of the displacement path.
3. Upon analysis of the differential equation of a single filament displacement path it can be stated that:
  - changes of the force of the filament interactions with the surface are directly proportional to the changes of the filament stiffness, thus a solution for  $(EI)_1$  is also applicable to  $(EI)_2$ ,
  - the shapes of the bending line are identical if for a given position of a workpart (specified by angle  $\alpha$ ) the values of interaction forces  $(F(\alpha))i$  are proportional to the corresponding stiffness values of the elements  $(EI)i$ .

## **2.6. ELECTRO SPARK DEPOSITION AND LASER TECHNOLOGY IN SURFACE ENGINEERING**

*Norbert Radek*

The life of many machine parts can be significantly extended by enhancing the tribological properties of the surfaces. Better durability of surfaces can be achieved by coatings of appropriate materials. Coatings with various desired properties have been already developed and are already widely used with great economical benefits. The technologies that have been developed for this purpose are referred to as *Surface Engineering*.

There is an ever increasing requirement for low cost coatings with high quality tribological properties of its surfaces for wider applications with combined re-

quirements. Examples are machine elements subjected to severe conditions, such as friction and wear, corrosion, or exposure to high temperature. For example, coatings of shafts of rotating machinery have combined requirements. There is a need to increase the hardness of the surfaces rotating inside the bearings to resist wear, and increase the load capacity of the surface, while the core of the shaft must retain its original plasticity, in order to prevent failure due to brittle cracking under the impact forces in operating machinery. In addition, the coating must have good bonding to the substrate material of the machine element in order to avoid undesired peeling (delamination). It has been already realized that heterogeneous surfaces, are advantageous for such combined requirements. They are designed to have the desired distribution of composition and gradients of various properties, such as microhardness, along the thin width of the coating.

There are many methods for surface coatings such as electroplating, plasma spraying. Very thin layers can be deposited by vapor deposition. Various surface treatment techniques have been developed to improve the desired properties of the deposited layers, based on the substrate material. One important low cost method is the electro-spark deposition (ESD), which has been recognized and widely applied as an economically effective surface coating [93-95]. It is already widely used process for its expedient way of achieving the desired properties of surfaces. ESD has been known by several other terms such as *spark hardening*, *electric spark toughening*, and *electro-spark alloying*.

Electro-spark coatings are widely used to increase surface hardness for wear resistance [96, 97]. It includes important applications such as artificial implants, or cutting tool inserts [98]. It is used to protect components operating at high temperature, such as in nuclear reactors, combustion chambers, and turbine engines [99]. In addition, it is widely used to rebuild worn or corroded components, such as shafts in machines, ship propeller components, casting moulds and exhaust system. The coatings can be deposited using low cost, manually operated equipment, or robotized systems.

There is continuous effort to improve the properties of electro-spark deposited coatings. One method is laser treatment where a laser beam is used for surface polishing, surface geometry formation, surface sealing or for homogenizing the chemical composition of the coatings deposited [95, 100-102].

In this study, it is shown that if the process is properly applied, the advantages of laser-treated electro-spark coatings can include further improvements in the following directions:

- lower roughness,
- lower porosity,
- better adhesion to the substrate,
- higher wear and seizure resistance,
- higher fatigue strength due to the occurrence of compressive stresses on the surface, and
- higher resistance to corrosion.

ESD is a pulsed-spark micro-welding process which utilizes high-current electrical pulses with duration of  $10^{-4}$  to  $10^{-8}$  second to deposit an electrode material on a metallic substrate so as to produce an exceptionally fine-grained, homogeneous and metallurgically-bonded surface coating to the selected substrate while keeping the base bulk material with its original mechanical properties [94, 96, 97, 103]. Liberated energy, as a result of spark, leads to an extremely high temperature causing fusion and vaporization of electrode and substrate materials and producing a desired surface coating. These momentary heating-cooling impulses in periodical sequence are producing deep physical-chemical transformation in the surface of substrate. Intense spark heating produces extremely steep temperature gradients in the substrate's surface and results in extremely rapid quenching of micro volumes of the surface materials leading to the formation of an extraordinary fine grained microstructure, and/or amorphous structured coatings.

ESD technology also provides a low heat input and distortion free substrate; could be applicable to complex shapes for nearly all metals and ceramics; could form different surface alloys of high performance, can tailor desired surface properties independently from the bulk properties; nearly any cermets or alloys can be deposited; no needs for special chambers and areas with controlled atmosphere; equipment available from portable and inexpensive devices to fully automatic and computer controlled workstation.

Two stage deposition techniques, namely a rough and fast deposition followed by a fine deposition at normal speed usually are applied in order to achieve designed thickness and satisfied surface finish while keeping less heat affection on the substrate. Starting from 1970's, with the development of ESD low cost equipment and increased understanding of the process mechanism, different type of coatings have been applied to meet rigorous demands of performance and consistency, However ESD's process capability, various surface properties produced by the process, deposition mechanism, obtained microstructure, and bonding mechanism of deposited layers to the substrate are beyond thorough understanding.

As mentioned above, there is a need for further development to achieve combined properties. Many applications required better adhesion of ESD layer to the substrate, combined with better wear and corrosion resistance. Considerable improvement has been achieved by introduction of heterogeneous approach [104, 105]. It means, producing multilayer coatings, such as high adhesion of the low-melted bottom layer, combined with high abrasion resistance of the top layer containing carbides. If the deposition procedure of multilayer coatings is determined properly, surface roughness can be considerably decreased.

Currently, researchers suggest that this second treatment is insufficient and should be accompanied by next following finish treatment capable to produce extremely steep temperature gradients in the very substrate's surface in order to make so-called heterogeneous surfaces [106]. Heterogeneous surface is formed in selective areas having different microfinish, physico-mechanical or physico-chemical properties. This surface could be produced by applying more than one technology, or by combi-

nation of ESD and electron-beam machining, laser-beam forming or thermo chemical treatment [107, 108]. Any post ESD processing provides local selective heating and quenching and consequently, because of local alloying, diversified hardness and surface finish. Properly developed heterogeneous surface could be wear, corrosion or fatigue resistant. Surface with diversified micro geometry and surface finishing could provide required or desired load carrying ability.

For distance, an obtained cavity after laser erosion will form alloyed crater with edges having high mechanical properties. These edges after meeting a counter part during rubbing, depending on craters density on the surface will accept the main load while a crater's valleys will collect all produced debris developed during friction. This effect should, in turn, change the content of lubricants, reduce the friction, friction coefficient and will improve the wear resistance.

The goal of this paper is to investigate the heterogeneous wear resistant surfaces produced by ESD coating with post finishing by laser treatment. In order to achieve this goal the following objectives are met: selection of substrate-coating couple, design of surface treatment sequence; selection of process parameters; investigation of obtained surface topography, surface finish, microstructure, distribution of applied coated elements along the coating depth and micro-mechanical properties in order to make further understanding of the mechanism and metallurgical essence of the applied coating as well as equipment performance.

### 2.6.1. METHODOLOGY

In this research Cu-Mo coating were deposited on a low carbon content steel (AISI 1045) substrate. This type of coatings was selected because of it high wear resistance in various applications where a functional surface should possess, in addition, high heat, fatigue, thermal shock and delaminating resistance.

The selected coatings were applied just in the atmosphere air, using an electro-spark deposition of 1 mm diameter wires of Cu-Mo alloy (50% and 50%, respectively). The electro spark deposition used is a modernized device (ELFA-541) that operated as listed below.

- current intensity  $I = 16$  A,
- feeding rate  $V = 0.5$  mm/s;  $0.65$  mm/s,
- electrode head speed  $n = 4200$  rpm,
- number of coating passes  $L = 2$ ,
- condenser capacity  $C = 0.47$   $\mu$ F,
- “make” duration  $T_i = 8$   $\mu$ s,
- “break” duration  $T_p = 32$   $\mu$ s,
- frequency  $f = 25$  kHz.

The produced heterogeneous coatings were eroded by laser beam after the electro spark deposition. The laser surface treatment was performed by an Nd:YAG laser (impulse mode), model BLS 720, and operating in the pulse mode under the following conditions:

- laser spot diameter,  $d = 0.462\text{-}0.739$  mm,
- laser power,  $P = 10\text{-}150$  W,
- beam shift rate,  $V = 1200$  mm/min,
- nozzle-sample distance,  $h = 1$  mm,
- pulse duration,  $t_i = 0.8$  ms, 1.2 ms, 1.48 ms, 1.8 ms, 5.5 ms, 8 ms,
- frequency,  $f = 8$  Hz.

A typical methodology used for surface analysis was established by using optical image analyzer, scanning electron microscopy SEM with energy dispersive spectrometer (EDXA), Vickers microhardness tester, and computer controlled surf-analyzer with computer data acquisition. This equipment was used to measure the surface finishing as well as other mechanical properties of the applied coating on the outer surface and properties distribution inside the coating. All metallographic examinations were carried out on samples polished and etched by Nitol.

The Vickers microhardness tests, along the depth cross section of all zones, as shown in Figure 2.53, used 40 g load, while for crater cavity cross section, 100 g load was applied (Fig. 2.54).

## 2.6.2. RESULTS AND DISCUSSION

Surface topography of produced by ESD and followed by laser spot treatment specimens is shown on Figure 2.48. Coated substrate by ESD has a matt appearance with “small craters” due to local roughening by individual sparks. Noticeable features are pores and erosion pits on the surface, in particular for EDS treated surface at 0.5 mm/sec EDS applicator speed, as shown in Figure 2.48a. Surface roughness was measured by using a group of parameters:  $Ra$ ,  $Rz$ ,  $Rq$ ,  $Ry$ ,  $Rsk$  and  $tp$ . Some parameters, such as  $Ra$  and  $Rz$  have been increased by the ESD over 10 times in comparison with the original surface.

Here,

$Ra$  = roughness average

$Rz$  = average maximum height of the profile

$Rq$  = root mean square roughness

$Ry$  = maximum height of the profile

$Rsk$  = skewness

$tp$  = bearing length ratio

However, comparison of the bearing length ratio,  $tp$  (Fig. 2.49, curve B) shows that the surface of Sample 1 (for head applicator speed of 0.5 mm/sec) produces less porosity and surface skewness, indicating that this surface will be able to provide higher load carrying capacity and improved wear resistance may be expected. However, unlike sample 1, the outer surface of Sample 2, curve C (head applicator speed 0.65 mm/sec) indicates higher outer surface roughness with sharp and long asperities, and increased wear, and lower bearing load carrying capacity is expected. Surface roughness results for various ESD treatments are summarized in Table 2.3.

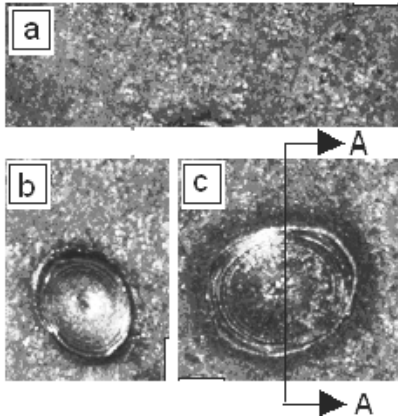


**Fig. 2.48.** Surface topography produced by ESD and laser treatment (x50): a) EDS treated surface at 0.5 mm/sec applicator speed (Sample 1); b), c) laser treated surface with craters of Sample 1: (b) 20 W; (c) 100 W

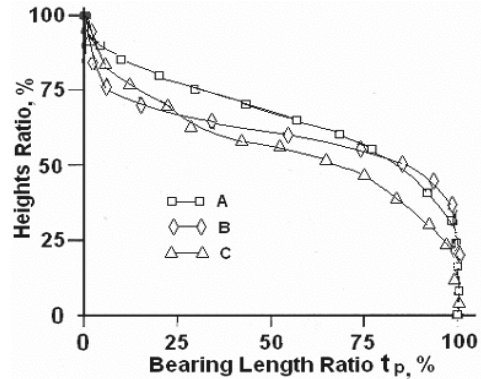


**Fig. 2.49.** Bearing length ratio for differently treated surfaces by ESD: A – just machined substrate; B – ESD coating with head applicator speed 0.5 mm/sec; C – ESD coating with head applicator speed 0.65 mm/sec

**Table 2.3.** Surface roughness parameters

Specimens	$R_a$ , $\mu\text{m}$	$R_q$ , $\mu\text{m}$	$R_z$ , $\mu\text{m}$	$R_y$ , $\mu\text{m}$	$R_{sk}$
Original as machined surface – curve A	0.36	0.45	2.28	1.25	-0.58
ESD treated surface, Fig. 2.48a, Sample 1 – curve B	3.01	4.07	23.84	23.99	-0.61
ESD treated surface, Sample 2 – curve C	3.90	4.92	30.35	30.88	-0.54

A 3D macrogeometry of the developed heterogeneous surface eroded by the laser craters for the used specimens with build in 2-D crater cross section A-A (Fig. 2.48c) is shown on Figure 2.50a, b.

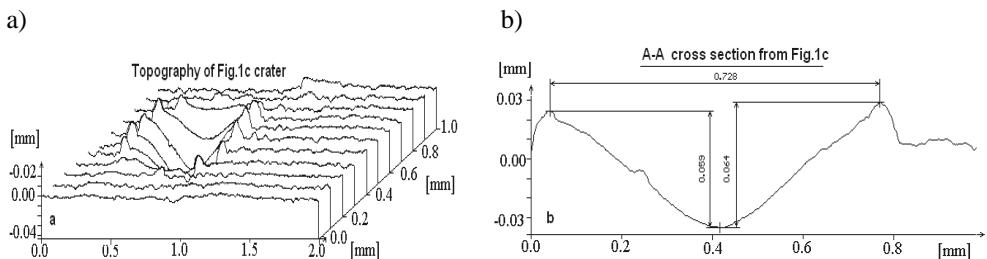


**Fig. 2.50.** Macrogeometry and cross section of eroded by laser crater: a) 3D crater topography; b) A-A cross section on Figure 2.48c

As can be concluded from these built graphs crater edges are sharp and are advanced up to 0.03 mm above an average height, just treated by ESD surface, what

is within a range of tolerances for designed clearance fit. The average size of the crater shown on Figure 2.48c produced by laser power 100 W has diameter about 0.7 mm and the total depth about 0.06 mm. The crater is going below so-called “ground zero level” by down to 0.030 mm.

For instant, crater displayed on Figure 2.48b, produced by laser power 20 W has diameter about 0.05 mm and depth of 0.015 mm. Produced crater profile (picks and valleys) and also order of craters location, depending on the required or desired surface performance, could be controlled and adjusted to acceptable level. As can be seen from Figure 2.51, relationship of the eroded cavity diameters and related cavity depth mainly depends on the laser power and pulse duration.

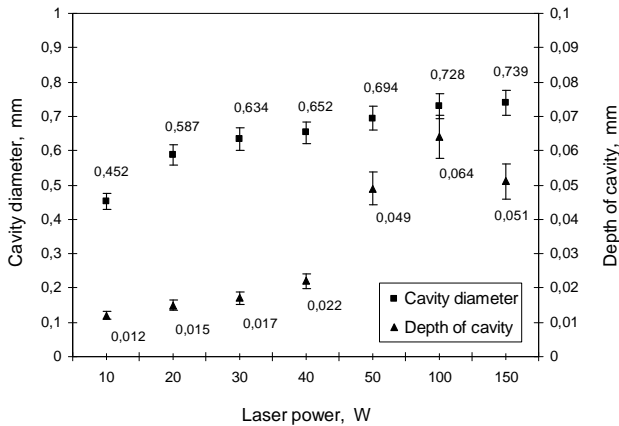


**Fig. 2.51.** Relation of laser craters depth and laser power

As shown in the Figure 2.52, the general feature of ESD coating is a two-zone microstructure made of a fusion and substrate zones. Interface of these zones has a thin heat affected lamella (HAZ). Top outmost surface of the fusion zone has a white lamella. The fusion zone is resistant to etching and appears dark, featureless while substrate zone is slightly etched and appears lighter showing modified structures with respect to bulk material. Figure 2.52a shows a microstructure and EDXA profiles of a deposited by ESD Cu-Mo coating. In this specimen the fusion zone is divided into three main layers. Cracking can be observed from these microstructures. Cracking exists along the first white lamella while new formed alloyed phases with microcracks are along the second lamella penetrated into the substrate zone. Cracking occurs because of solidification due to tensile stresses resulting from differential expansion in the steep thermal gradients associated with the ESD treatment. These developed tensile stresses at the presence of stress raisers in microstructure produce cracking of non ductile deposited layers. Considering Mo and Cu high concentration in the top fusion zone (Fig. 2.52a) and eutectic formation in microvolumes of alloyed substrate during solidification could be also a good reason for cracking in macro volumes of deposited coatings. Cracking starts mainly because of forming new alloyed phases having limited solubility. These phases are brittle and in tension environment they initiate cracks.

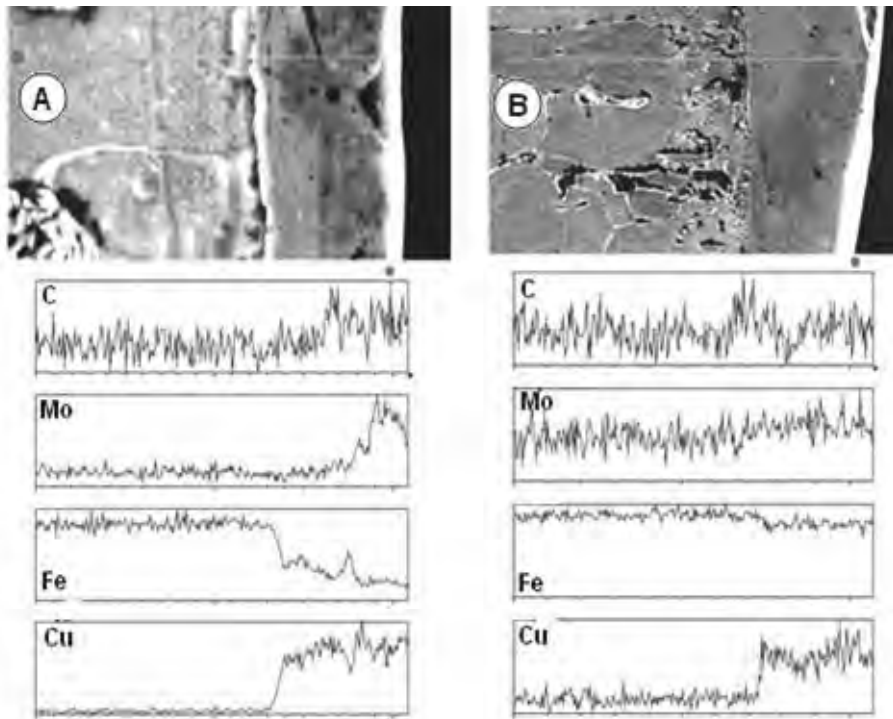


**Fig. 2.52.** Micrographs and concentration distribution of elements by EDXA detection along electron beam path: a) distribution of tested elements for ESD sample 1 (x5000); b) distribution of tested elements for laser-eroded sample 1 (x1000)

The outmost layer ( $\sim 8 \mu\text{m}$  thick) approximates to the composition of the electrode materials where beyond this layer concentration of Cu and Mo drops sharply following along with gradual decrease of C and increase of Fe. Such gradient transition of C and Fe indicating on diffusion effect considered to be negligible in ESD treatment. The whole distribution of elements: C, Fe, Mo, and Cu along 27-30  $\mu\text{m}$  depth are observed on Figure 2.52a.

The bottom layer of the fusion zone in interface with substrate ( $\sim 7 \mu\text{m}$  thick) or the HAZ zone has nearly the same composition as the substrate bulk material. This layer is produced by just substrate components because coating components do not get into the bulk of this layer due to exceptionally short heating duration and rapid solidification. Its high resistance to etching indicates on extremely fine grains structure or even amorphous nature.

On scrutiny, the fusion line made of merging co-grains indicates on a good bonding effect. The compositional homogeneity across the fusion line contributes a lot to the good bonding. The bottom part of the specimens has developed columnar microstructure because of powerful diffusion flux through grain boundaries during ESD heating. This zone at a depth of  $\sim 10\text{-}12 \mu\text{m}$  seems really homogeneous and extends continuously over the substrate.

The specific characteristics of each ESD coating are quite different depending upon the materials system, environment media, manipulating methods, process parameters and control.

The post finished specimen by laser erosion, as shown in Figure 2.52b, has also a two-zone structure made of a fusion and substrate zones divided into three characteristic layers. The outmost layer ( $\sim 7 \mu\text{m}$  thick) is made of dark white edged block layer similar to that of electrode materials. This layer without visible porosity is forming a homogeneous layer of the heterogeneous surface with white almost featureless, not etched edges of extreme properties. Concentration distribution of all controlled elements in this layer is almost maximum. This zone seems really homogeneous and extends continuously over the substrate. Interface between substrate and this homogeneous layer represents the HAZ zone ( $\sim 40 \mu\text{m}$  thick) and inherited visible extra-large pores and micro cracks and divides the fusion zone and substrate providing sufficiently good bonding with fusion zone. The heat input into substrate because of extremely short spark life duration and small volumes of deposited melting pools is not significant. This fact brings to lower level of cracks development during coating and solidification. Porosity occurs because of insufficient overlapping of ESD traces and laser eroded spots produced during side by side deposit during reciprocated vibration of the electrode in basic and finish coating. At the same time, porosity can appear at interface between substrate and deposited layers if the deposited layers consisted of electrode materials have a significantly different melting points than a substrate material. In this case solidification started at the surface of melted pool will finish at interface or on substrate surface when substrate material is still in liquid state.

The bottom part of this specimen about  $50 \mu\text{m}$  has developed columnar microstructure which could be resulted by powerful diffusion flux occurred through grain boundaries during post finishing by laser strike erosion. Its EDXA profiles have steps of concentration followed by distribution gradients to the bulk material, indicating clearly the diffusion effect and formation of new alloy phases.

Comparison of two types of the developed surfaces indicates on much thicker coatings produced in heterogeneous version. Fusion zone in Figure 2.52b representing remelted zone produced by laser strike of ESD coating became about 3 times thicker, homogeneous crack free structure carrying much higher hardness readings. Overall, these produced layers are shown desirable features like homogeneous appearance, big thickness and transition gradients of components. Therefore good surface performance can be expected. Porosity can be eliminated by proper planning of deposition process and selection of deposited electrode material together with reliable process parameters. Process of coating by ESD and post finishing by laser can be fully automated it is why reproducibility of obtained coating is very high.

The microhardness test results concerning the Cu-Mo coating before and after laser treatment is presented in Figure 2.53. After the indentation was made on metallographic specimens parallel in three zones: the coating, the remelted coating, and the heat affected zone. The original material was also tested. The electro-spark depo-

sition process caused some changes in the material. Laser treatment had a favorable effect on the changes in the microhardness of the electro-spark deposited coatings.

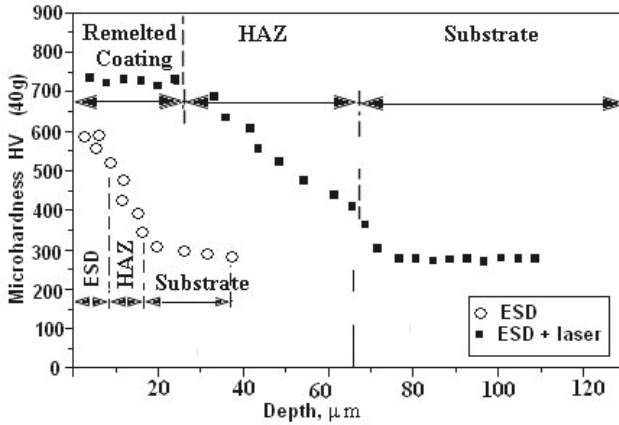


**Fig. 2.53.** Microhardness distribution along all zones for ESD and ESD plus laser eroded specimens

In Figure 2.54, a microhardness-profile is shown along the depth of obtained craters measured across the cross section shown on Figure 2.48c.

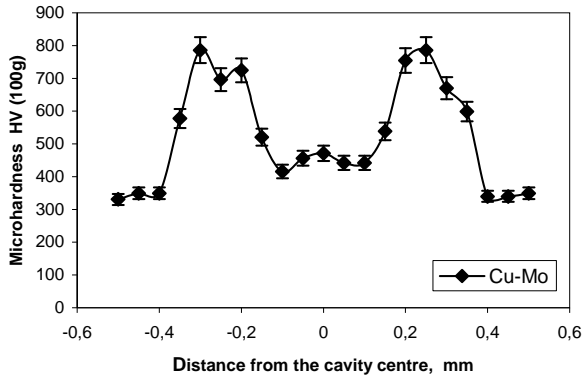


**Fig. 2.54.** Microhardness distribution along crater cross section

The surface of this cross section was treated by ESD and then post finished by laser erosion. Its microhardness profile reveals distribution of properties from the fusion zone into the bulk materials. It is shown that there is a soft region in the bottom valley of the fusion zone while a big increase is achieved across a fusion line. Since the samples were deposited by a two-stage process, the softening effect can be caused by insufficient alloying and reheat affection. This saying is confirmed already by the microstructural examination which shows very limited penetration of alloy components into the bottom fused layer. The thermal cracks presence, due to rapid solidification, could increase their contributions toward the low hardness values. The micro-

hardness profile shows gradient transition from outmost surface to the bulk materials while the variation in the outmost layer reveals the non-uniformity and the existence of micro cracks. The highest hardness value of about 800 HV achieved for the melted zone during the laser process is due to the fast quenching effect of highly alloyed surface. By comparison, surface softening effect near the bottom of the fusion line is achieved due to a milder extent so that better bonding can be expected.

Moreover, the microhardness values above the fusion lines present less variation corresponding to the concentration distribution in the EDXA profiles. Therefore, the formation of compounds and effect of diffusion can be confirmed. Measured average microhardness of the craters tips of about 800 HV, HAZ zone about 650 HV and substrate of 300 HV shows that the hardness of the working surface could be almost tripled by preparation of the heterogeneous surface.

The present study shows that:

The present study shows that a significant improvement of the tribological properties of heterogeneous surfaces can be achieved by an appropriate laser treatment. Detailed outcomes of the present study are summarized as follows:

1. Heterogeneous surface is made by ESD coating and post finished selectively by laser erosion.
2. Developed surface has fusion and substrate structural zones. The fusion zone presents of great interest and comprises of three layers. The outmost layer approaches quenched like structure and exhibit homogeneity and high micro hardness readings.
3. The middle layer shows the transition gradients of composition and properties with formation of certain new phases or compounds in some material systems, and can be taken as a major transitional layer due to alloying and diffusion.
4. The bottom layer is made of fused but non-alloyed bulk region and may include diffusion region at the upper part of the layer. The heat-affected zone is thin and seems friendly.
5. ESD surface achieves a metallurgically bonded coating of high bonding strength. It can be of good resistance to wear and corrosion or have other properties depending upon material systems applied.
6. Surface alloying predominates ESD process while reactive diffusion plays roles especially in the fusing state.
7. Microcracking and porosity seem inherent to ESD process. But they can be minimized through optimization of process parameters, process control and appropriate selection of electrode material. Porosity produced when insufficient overlapping is occurred during side by side layoff deposit during basic or finished coatings.
8. ESD surface produces better fullness and skewness indicating that this surface will be able to provide higher load carrying capacity and better wear resistance may be expected.

9. Electrode melting rate and produced alloy solidification rate should be kept under control in order to achieve large volumes of deposited coating layers and lowered heat impact on the substrate.
10. Air does not seem to be a very friendly atmosphere for ESD process due to the consequent oxidation which is usually unwelcome for many material systems.
11. ESD process using multi-tool headers for increased productivity shows good reproducibility and quality, can be completely automatic or used with or computer controlled.
12. Laser treatment of ESD coatings resulting in crater formation made the surface stronger and more resistant to wear.
13. Surface topography examination suggests that in order to obtain desired surface roughness additional research should be done to define some influence of material systems, manipulation method, process parameters and control as the main factors in determining the surface features.

## **2.7. TRIBOLOGICAL PROPERTIES OF PLASMA AND HVOF SPRAYED COMPOSITE COATINGS**

*Wojciech Żórawski*

Nowadays most machines require applying liquid lubricants on interacting surfaces, which allow us to achieve extremely favorable operating conditions in a friction pair. This assures long life and reliability of machine parts. It is often necessary, however, to employ a suitable lubrication system with seals and heat exchangers, which reduce the system reliability and increase its weight. Furthermore, it is essential to control the quality and quantity of the lubricant, and, as a result, occasionally, refill it. If the system fails to operate properly, excessive use of the lubricant may lead to a machine break-down. Moreover, liquid lubricants cannot be used under extreme operating conditions, e.g. high temperature, vacuum, very high unit pressure or aggressive medium [109].

The above-mentioned drawbacks do not occur if solid lubricants are applied. They are highly desirable whenever liquid lubricants cannot be used, e.g. in the electronic, food or textile industries. A friction pair with a solid lubricant requires no maintenance. Solid lubricants are also recommended in equipment operating under difficult conditions where access is limited, for instance, in orbiting stations. Of great significance is the ecological aspect too, as liquid lubricants may cause contamination of the environment.

There are two groups of methods for applying a solid lubricant into a sliding pair. Group One involves depositing a coating, for instance, by rubbing, pasting or varnishing the surfaces in contact, or applying the CVD, PVD or laser techniques

[2-5]. The life of a deposited coating depends on the method of deposition and the operating conditions. As soon as the coating is worn out, it is necessary to reapply it, which may be a little troublesome.

Group Two includes applying composite materials with a matrix containing a solid lubricant. This can be achieved by sintering or thermal spray [6-12]. The main advantage of such a solution is the constant presence of a solid lubricant at the interface. The amount of the lubricant evenly spread in the matrix material has a significant influence on the tribological properties of the coating. This is related to the process of formation of a stable film, which will not take place if the composite contains an insufficient amount of a solid lubricant [13]. Too much of it, on the other hand, may cause an increase in the coefficient of friction, a considerable decrease in the mechanical properties and a shorter life of the composite.

The aim of this work is to study the microstructure and coefficient of friction of plasma and HVOF thermally sprayed composite coatings with an NiCrBSi matrix and  $Fe_2O_3$  as a solid lubricant.

### 2.7.1. EXPERIMENTAL INVESTIGATION

The NiCrBSi powder produced by AMIL GmbH denoted by 1060.0 (Fig. 2.55a) with the following chemical composition (%) Ni – 70.51, Cr – 17.8, B – 3.1, Si – 4.2, Fe – 3.4, C – 0.85, O<sub>2</sub> – 0.14 was selected to constitute the composite matrix. From Figure 2.55a it can be seen that the particles are spherically shaped, which is characteristic of highly alloyed nickel based powders to be obtained by a gaseous spray method. Coatings produced from powders with such chemistry by remelting or plasma or HVOF thermal spray possess high resistance to wear, hence their wide application. NiCrBSi powders are deposited separately or as ingredients of blends. The presence of boron and carbon improves coating hardness, and this results from the formation of chromium, boron or iron carbides, as well as hard metallic compounds of boron and chromium in the alloy.

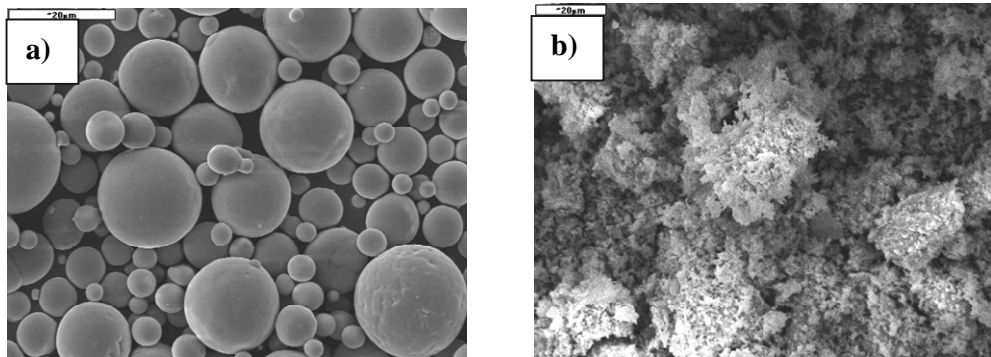


**Fig. 2.55.** Morphology of grains: a) NiCrBSi, b)  $Fe_2O_3$

In an NiCrBSi/Fe<sub>2</sub>O<sub>3</sub> composite coatings, iron oxide becomes the lubricant, as it possesses the desired properties i.e. a hexagonal crystal structure. For the testing purposes was employed purified iron oxide normally used as a chemical reagent with tiny, flaky, yet enhanced particles (Fig. 2.55b). The structure promotes agglomeration of particles, which makes it difficult to feed the powder to a spray gun.

The examination of the particle size distribution was carried out by means of the Sympatec GmbH HELOS laser analyzer (Fig. 2.56a, 2.56b).

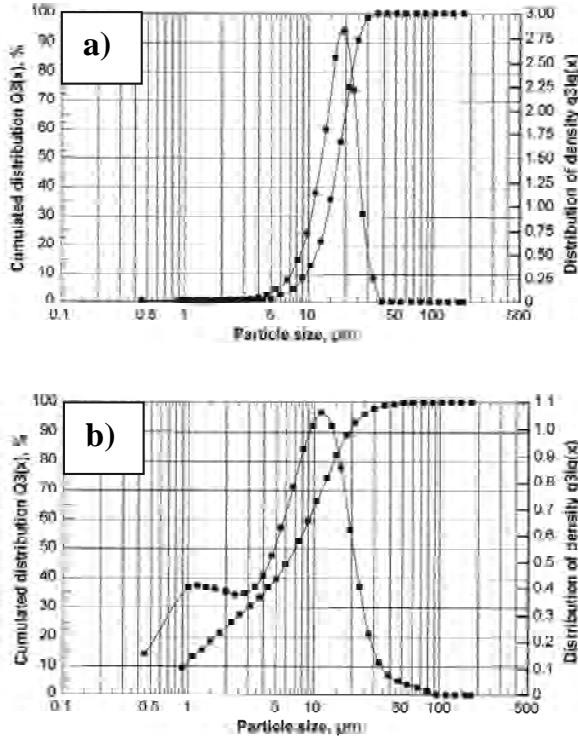


**Fig. 2.56.** Particle size distribution: a) NiCrBSi, b) Fe<sub>2</sub>O<sub>3</sub>

Plasma spraying belongs to semi-molten state surface coating techniques and basically consists of the injection of selected powders into a direct current plasma jet, where they are molten, accelerated and directed onto the substrate surface. The coatings are actually splats of molten droplets instantly solidified on the substrate surface because of its lower temperature. The principles of plasma spraying are shown in Figure 2.57.

During the process of supersonic (HVOF – High Velocity Oxy-Fuel Flame) spraying a material is discharged to form a coating by means of a special gun (Fig. 2.58). The fuel and oxygen burnt inside the gun produce a hot gas stream, the energy of which makes it possible for the material particles to travel with a high velocity of about 2.100 m/s, one that is unavailable in other technologies of thermal spraying.

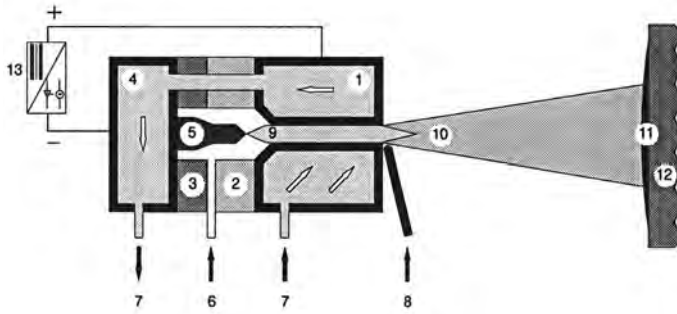


**Fig. 2.57.** Plasma spraying principles: 1 – anode, 2 – insulation, 3 – center section, 4 – rear section, 5 – cathode, 6 – plasma gas, 7 – water cooling, 8 – powder, 9 – electrical arc, 10 – plasma jet, 11 – coating, 12 – workpiece, 13 – generator

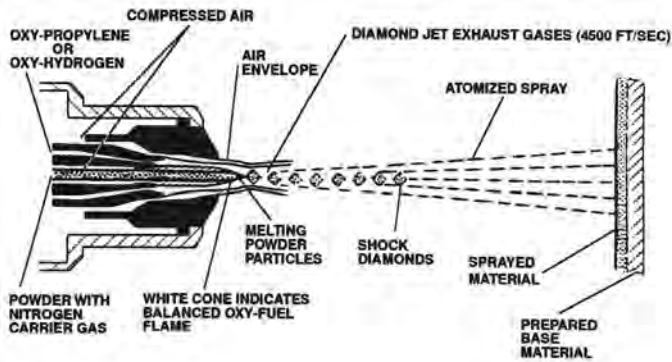


**Fig. 2.58.** Schematic diagram of the Diamond Jet gun

The plasma spray process was carried out with the Plancer PN-120 gun equipped with the Thermal Miller 1264 powder feeder. The plasma generated for plasma spraying incorporated a mixture of argon (primary plasma gas) and hydrogen (secondary plasma gas), the latter constituting 7%. The plasma spray parameters are given in Table 2.4. The HVOF thermal spray process was performed using the Sulcer Metco Diamond Jet gun supplied with propane and oxygen. The HVOF spray parameters are shown in Table 2.5.

**Table 2.4.** Plasma spraying parameters

Parameter	Value
Current, A	550
Voltage, V	55
Plasma gas pressure, MPa	0.7
Spraying distance, mm	100
Powder feeding rate, g/min	28

**Table 2.5.** HVOF spraying parameters

Parameter	Value
Oxygen flow, NI/min	265
Propane flow, NI/min	74
Air flow, NI/min	374
Spraying distance, mm	150
Powder feeding rate, g/min	94

For the metallographic examination, the coatings were deposited on thin flat samples in low-carbon steel with dimensions of 50x25x5 mm, whereas for the tribological test the coatings were deposited on ring-shaped samples in low-carbon steel with dimensions of  $\phi 46\text{mm} \times \phi 25\text{mm} \times 6\text{ mm}$ . Before the spray, the substrate had to be degreased and grit blasted with electrocorundum EB-12 at a pressure of 0.5 MPa. The height of the coatings after grinding was 0.3 mm.

The structure and the chemical composition of the coatings were analyzed by means of the JSM-5400 scanning microscope equipped with the ISIS 300 Oxford (EDS) microprobe. The phase composition of the powders and the coatings was determined with the Bruker D-8 Advance diffractometer.

The T-01 M ball-on-disc type tester was used to determine the coefficient of friction for the NiCrBSi and Fe<sub>2</sub>O<sub>3</sub> plasma and HVOF sprayed coatings. The schematic diagram of the tester operation is presented in Figure 2.59. The ball in bearing steel LH 15 had a diameter of 1/4". The testing involved applying a computer to aid in registering and controlling the action of the friction force in the function of time.

The parameters for the T-01M tester were as follows:

- load  $Q = 4.9\text{ N}$ ,
- linear velocity  $v = 1\text{ m/s}$ ,
- test duration  $t = 1\text{ h}$ .

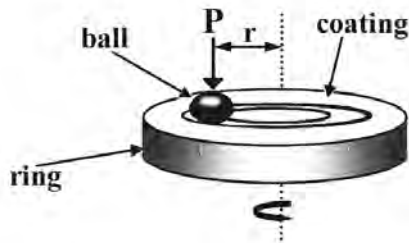


*Fig. 2.59. Principle of operating of the tribological tester T-01 (ball-on-disc type)*

## 2.7.2. RESULTS AND DISCUSSION

Plasma sprayed NiCrBSi + 50%vol. Fe<sub>2</sub>O<sub>3</sub> composite coatings have visible oxide strips between the highly deformed lamellae (the dark phases in Fig. 2.60a), as is the case of alloy powder spray coatings containing no iron oxide. The linear analysis (Fig. 2.60c) showed that the amount of iron and oxygen in the coatings had increased while the amount of the other constituents had decreased. The dark phase is identified with iron oxide. An increased amount of iron and oxygen can be observed also in the thin oxide films, which testifies that iron oxide is predominant there. The local analysis of this phase shows that there is a great number of peaks of iron and oxygen. The other alloying constituents are present in the dark phase, yet the number of their peaks is negligible. The local analysis of the white phase, on the other hand, shows an increased amount of nickel and the other constituents of the NiCrBSi powder. Studying the coating images and their chemical composition, one can easily discover that by plasma spraying of the NiCrBSi +

50%vol.  $\text{Fe}_2\text{O}_3$  mixture we obtain a composite coating. The matrix produced by spraying metallic powder contains iron oxide occurring in the form of lamellae, which vary in height. HVOF NiCrBSi + 50%vol.  $\text{Fe}_2\text{O}_3$  composite coatings have hardly visible short oxide strips between slightly deformed lamellae (Fig. 2.60b), as is the case of spraying of pure alloy powder. Between the lamellae we report a large area of the dark phase. The linear analysis shows (Fig. 2.60d) that there is a considerable increase in the amount of iron and oxygen, and, at the same time, a significant decrease in the amount of nickel, chromium and silicon. From that analysis as well as a local analysis it is clear that this is iron oxide. The dark phase on the left, however, shows no increase in the amount of iron or oxygen, yet there is a considerable decrease in the amount of the other constituents of the NiCrBSi powder. The changes in the component intensity confirm the occurrence of pores. The local analysis of the white phase proves a greater intensity of the peaks of nickel than in the case of a plasma sprayed coating. The changes in the element level are less varied, which is illustrated by iron. This implies less intensive phase transitions of the NiCrBSi powder during the HVOF spray process. Due to high particle velocity and different particle sizes, the  $\text{Fe}_2\text{O}_3$  content in an HVOF coating can be lower than that in a plasma sprayed coating.

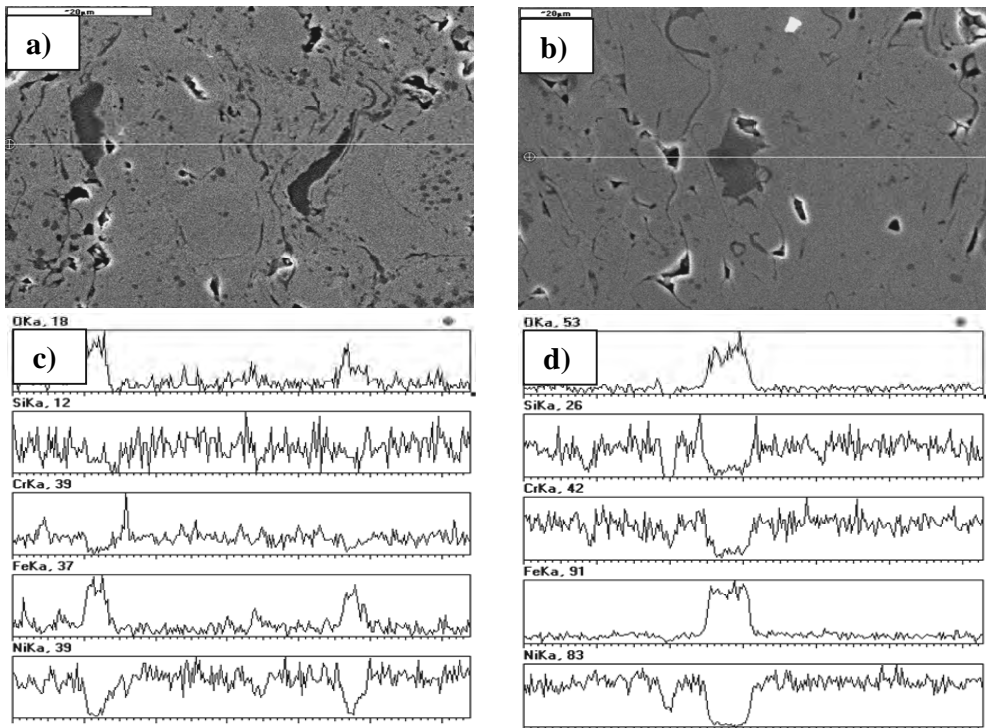


**Fig. 2.60.** Microstructure of: a) plasma sprayed NiCrBSi + 50%vol.  $\text{Fe}_2\text{O}_3$  coating, b) HVOF sprayed NiCrBSi + 50%vol.  $\text{Fe}_2\text{O}_3$  coating, c) linear analysis of plasma sprayed NiCrBSi + 50%vol.  $\text{Fe}_2\text{O}_3$  coating, d) linear analysis HVOF sprayed NiCrBSi + 50%vol  $\text{Fe}_2\text{O}_3$  coating

The phase composition of the NiCrBSi, Fe<sub>2</sub>O<sub>3</sub>, and NiCrBSi + 50% vol. Fe<sub>2</sub>O<sub>3</sub> powders and of the coatings produced from them was thoroughly analyzed (Table 2.6) in order to identify all the changes and differences resulting from the applied thermal spray process and the percentage of composite ingredients. The fundamental phase in the NiCrBSi powder and the NiCrBSi thermal spray coatings was nickel, due to high nickel content, i.e. 70.51%. After identifying displaced high-angle diffraction lines, one can assume that they are represented by the nickel lattice based solid solution phase. The other components include hard crystals of borides and silicides, of which only the Ni<sub>2</sub>B phase is present in all the lamellae. These phases impart good wear resistance properties of the coatings.

**Table 2.6.** Phase composition of powders and sprayed coatings

Material	Spraying	Phase composition
Powder NiCrBSi	without spraying	Ni(Me), Cr <sub>3</sub> Si, Ni <sub>31</sub> Si <sub>12</sub> , Ni <sub>2</sub> B, Cr <sub>5</sub> B <sub>3</sub> , CrB
Coating NiCrBSi	PLASMA	Ni(Me), Ni <sub>31</sub> Si <sub>12</sub> , Fe <sub>2</sub> O <sub>3</sub> – maghemite, Ni <sub>2</sub> B,
Coating NiCrBSi	HVOF	Ni(Me), Cr <sub>3</sub> Si, Ni <sub>31</sub> Si <sub>12</sub> , Ni <sub>2</sub> B, Cr <sub>5</sub> B <sub>3</sub> , CrB,
Powder Fe <sub>2</sub> O <sub>3</sub>	without spraying	Fe <sub>2</sub> O <sub>3</sub> – hematite
Coating Fe <sub>2</sub> O <sub>3</sub>	PLASMA	Fe, Fe <sub>3</sub> O <sub>4</sub> , Fe <sub>2</sub> O <sub>3</sub> – hematite
Coating Fe <sub>2</sub> O <sub>3</sub>	HVOF	Fe <sub>3</sub> O <sub>4</sub> , Fe <sub>2</sub> O <sub>3</sub> – hematite
Coating NiCrBSi + 50% obj. Fe <sub>2</sub> O <sub>3</sub>	PLASMA	Ni(Me), FeNi, Ni <sub>2</sub> B, Cr <sub>3</sub> Si, Ni <sub>16</sub> Cr <sub>6</sub> Si <sub>7</sub> , Cr <sub>5</sub> B <sub>3</sub> , Cr <sub>3</sub> Si, CrB <sub>2</sub> , Ni <sub>2</sub> O <sub>3</sub> , Fe <sub>2</sub> B, Fe <sub>3</sub> O <sub>4</sub> , Fe <sub>2</sub> O <sub>3</sub> – maghemite
Coating NiCrBSi + 50% obj. Fe <sub>2</sub> O <sub>3</sub>	HVOF	Ni(Me), FeNi, CrB, Ni <sub>2</sub> B, Cr <sub>5</sub> B <sub>3</sub> , B <sub>4</sub> Si, Ni <sub>3</sub> Si Fe <sub>3</sub> O <sub>4</sub> , Fe <sub>2</sub> O <sub>3</sub> – hematite, maghemite

In the case of plasma sprayed NiCrBSi coatings, the Cr<sub>3</sub>Si, Cr<sub>5</sub>B<sub>3</sub> or CrB phases were not identified. HVOF thermally sprayed NiCrBSi coatings showed no changes in the phase composition compared with that of the powder. Identical types of phases and negligible changes in their relative contents were reported in both diffraction patterns. The influence of temperature on the phase composition of the coating material is most visible for Fe<sub>2</sub>O<sub>3</sub>, which was identified as hematite. From a considerable difference in the intensity of all peaks of hematite in the powder and the deposited coatings it is clear that, in the spray stream, hematite is transformed into magnetite, the latter not present in the powder material. Since the peaks of hematite are very low, it is found that its presence in the deposited coating is negligible. A lower temperature HVOF stream causes only a partial transforma-

tion of hematite into magnetite. The number of magnetite peaks in an HVOF coating is much smaller than in a plasma sprayed coating, thus we can conclude that its content is very low. In both plasma and HVOF sprayed NiCrBSi + 50%vol. Fe<sub>2</sub>O<sub>3</sub> coatings, there is a new, FeNi, phase, which was not present in the analyzed lamellae. This is a result of the reaction of nickel with iron from iron oxide. The other phases in the coatings applied by both methods are Ni<sub>2</sub>B and Cr<sub>5</sub>B<sub>3</sub>. By comparing their relative intensity, we see that the FeNi phase is greater in the HVOF coating. The plasma coating, on the other hand, contains greater Ni<sub>2</sub>B and Cr<sub>5</sub>B<sub>3</sub> phases, the new phases of Cr<sub>3</sub>Si, CrB<sub>2</sub>, Ni<sub>2</sub>O<sub>3</sub>, and Fe<sub>2</sub>B, as well as magnetite, Fe<sub>3</sub>O<sub>4</sub>, and of maghenite, the latter not reported in the Fe<sub>2</sub>O<sub>3</sub> powder.

The diffractometry shows that the HVOF thermally sprayed NiCrBSi + 50%vol. Fe<sub>2</sub>O<sub>3</sub> coatings contain magnetite, Fe<sub>3</sub>O<sub>4</sub>, and both polymorphs of iron oxide, Fe<sub>2</sub>O<sub>3</sub>, hematite and maghenite, the latter not being present in the coating produced from the Fe<sub>2</sub>O<sub>3</sub> powder. The new phases identified in this coating are boron silicide, B<sub>4</sub>Si, and nickel silicide, Ni<sub>3</sub>Si.

Coefficient of friction studies were done using an experimental design PS/DS-P:2<sup>4-1</sup> (Table 2.7 and Table 2.8) in order to study the effect of 4 factors (in the case of each spraying technique) on a given property (roughness) with minimum number of experiments.

**Table 2.7.** Experiment for plasma spraying

Factors	Amount of Fe <sub>2</sub> O <sub>3</sub> , %	Gas pressure, MPa	Current intensity, A	Spraying distance, mm	Coefficient of friction, $\mu$
Code	$x_{p1}$	$x_{p2}$	$x_{p3}$	$x_{p4}$	$y_p$
Base level	30	0.7	550	100	–
Interval	10	0.1	50	20	–
Upper level (+)	40	0.8	600	120	–
Lower level (–)	20	0.6	500	80	–
Experiment 1	–	–	–	–	0.235
2	+	+	–	–	0.09
3	+	–	+	–	0.105
4	+	–	–	+	0.10
5	–	+	+	–	0.125
6	–	+	–	+	0.165
7	–	–	+	+	0.105
8	+	+	+	+	0.075

**Table 2.8.** Experiment for supersonic spraying

Factors	Amount of Fe <sub>2</sub> O <sub>3</sub> , %	Oxygen flow rate, l/min.	Propane flow rate, l/min	Spraying distance, mm	Coefficient of friction, $\mu$
Code	$x_{h1}$	$x_{h2}$	$x_{h3}$	$x_{h4}$	$y_h$
Base level	30	265	74	150	–
Interval	10	15	10	15	–
Upper level (+)	40	280	84	165	–
Lower level (–)	20	250	64	135	–
Experiment 1	–	–	–	–	0.23
2	+	+	–	–	0.07
3	+	–	+	–	0.11
4	+	–	–	+	0.12
5	–	+	+	–	0.11
6	–	+	–	+	0.14
7	–	–	+	+	0.14
8	+	+	+	+	0.08

This method gives only the direct effects of the factors on a considered property and factors have to be independent, which means that the variation of a given factor does not lead to an uncontrolled variation of another. The four independent factors considered in the case of each spraying technique. Iron oxide amount added to the NiCrBSi matrix, gas pressure, current intensity and spraying distance were changed in experiment during plasma spraying. In the process of supersonic spraying as main factors iron oxide amount added to the NiCrBSi matrix, flow rate of oxygen, flow rate of propane and spraying distance were considered. Plan of 8 experiments, lower and upper levels of factors and their combinations are presented in Table 2.7 and Table 2.8, respectively for plasma and supersonic spraying. Details of this statistical experiment are described elsewhere [123].

On the base of measurements regression equations were determined. In the case of plasma spraying (designations, see Table 2.7):

$$y_p = 0.125 - 0.033x_{p1} - 0.125x_{p2} - 0.02x_{p3} - 0.01x_{p4} \quad (2.98)$$

for supersonic spraying (designations, see Table 2.8):

$$y_h = 0.114 - 0.024x_{h1} - 0.019x_{h2} - 0.009x_{h3} - 0.0006x_{h4} \quad (2.99)$$

Analysis of both equations let to conclude that in the case of plasma spraying (eq. (2.98)) the most important factor influenced on coefficient of friction is pressure of

plasma gas. Coefficient of friction of supersonic sprayed coatings (eq. (2.99)) depends on content of  $\text{Fe}_2\text{O}_3$  in the mixture with NiCrBSi powder and oxygen flow rate.

The present study shows that:

1. By blending the NiCrBSi and  $\text{Fe}_2\text{O}_3$  powders characterized by different particle size distribution and morphology (the former being full, spherical in shape, the latter having a flaky, fuzzy structure), and then plasma or HVOF spraying them over a substrate, we can obtain a composite coating containing the two compounds.
2. The microstructure of coatings depends on the applied thermal spray process. Plasma sprayed coatings have a highly deformed lamellar structure interspersed with very thin oxide inclusions. HVOF coatings, on the other hand, exhibit little deformation of particles and thicker oxide films.
3. Compared with plasma coatings, HVOF composite coatings show lower coefficient of friction, which is strongly influenced by content of  $\text{Fe}_2\text{O}_3$  in the mixture with NiCrBSi powder and oxygen flow rate. Pressure of plasma gas is the factor which extremely decided about coefficient of friction of plasma sprayed coatings.

## 2.8. ANALYSIS OF RESIDUAL STRENGTH AFTER FATIGUE IN FIBROUS COMPOSITE USING MARKOV CHAINS MODEL

*Rafal Chatys, Yury Paramonov, Mārtiņš Kleinhofs*

Investigation of degradation of residual strength after fatigue is of vital importance to the reliability of aircraft structures. A lot of papers are devoted to this problem. Fine discussion of the state-of-the-art phenomenological residual strength models is provided in [124] with references of 49 papers. So it is no good once again to repeat the review of these works. Only we mention the main weakness of these works. The distribution of static strength, the fatigue curve, and the accumulation of fatigue damages under a program loading are often described by poorly interconnected theories and hypotheses. The distribution of static strength is usually analyzed by the Weibull or lognormal distributions, while the fatigue curve is described by formal regression dependences, for example, by exponential equation:

$$K\sigma_{\max}^b N = 1 \quad (2.100)$$

where:  $\sigma_{\max}$  – being the maximum cycle stress,  $K$  and  $b$  – the experimentally derived  $S - N$  parameters.

We see no connection of this (and similar equations) with static strength distribution.

The summation of fatigue damages under a program loading, as a rule, is carried out by using the Palmgren-Miner hypothesis and its modifications. For example, in [125], containing a brief review of 50 studies, for describing the condition of failure at a single change in the loading mode, the equation

$$(n_1 / N_1)^{\alpha_1} + (n_2 / N_2)^{\alpha_2} = 1 \quad (2.101)$$

was suggested, where  $n_1$  and  $n_2$  are the numbers of loading cycles;  $N_1$  and  $N_2$  are the average fatigue life at the first and second loading levels;  $\alpha_1$  and  $\alpha_2$  are constants.

Similarly, in [124] for description of residual strength  $X(n)$  after  $n$  fatigue cycles, really, some (nonlinear) modification of linear Bourtman and Sahu [126] model are used. For example the following equation is considered:

$$X(n) = X(0) - (X(0) - \sigma_{\max})(n / N)^k \quad (2.102)$$

Corresponding the cumulative distribution function (cdf) for  $X(n)$  was developed, using Weibull distribution for  $X(0)$

$$F_{X(n)}(x) = 1 - \exp \left( - \left( \frac{x - (n / N)^k \sigma_{\max}}{\beta(1 - (n / N)^k)} \right)^\alpha + \left( \frac{\sigma_{\max}}{\beta} \right)^\alpha \right) \quad (2.103)$$

where:  $a$ ,  $\beta$  being parameters of Weibull cdf :  $F(x) = 1 - \exp(-(x / \beta)^a)$ .

For offered in [124] model, which is referred to as OM model,  $k = k_1 \exp(k_2 n / N)$ . But in conclusion of [124] it is said, that “even though the OM in most cases predict satisfactory the residual strength it requires a considerable experimental effort for implementation and do not consistently produce safe prediction”.

All considered in [124] models really give the deterministic phenomenological description of degradation of residual strength. And it seems that without deep probabilistical analysis we can not get the solution of the problem. Also it is very difficult problem, we should try to find solution.

In authors publications [127, 128] the last version of mathematical model based on the Markov chains theory (MCh-model) was described (more simple versions are described in [129-132]). It provides, from unified positions, a tool for a coordinated description of the distribution of static strength, the fatigue life, for evaluating the residual strength and residual fatigue life after some preliminary fatigue loading. It can not be said, that the problem is solved already, but by analysis of specific numerical examples it was shown that this model deserves to be studied more circumstantialy and that development of this model can be productive.

In this paper we make test of this model using dataset reported in special OPTIMAT BLADES testing program documents [133-136]. It is shown again that studied MCh-model gives reasonable result.

In section 2 we remind the main ideas of this model. In section 3 we consider its application to mentioned above dataset. In Conclusion the analysis of this experience is given.

### 2.8.1. MODEL OF ACCUMULATION OF FATIGUE DAMAGES BASED ON THE MARKOV CHAIN THEORY, WITH ACCOUNT OF MATRIX PLASTICITY

It is assumed that the fatigue failure of a test specimen occurs after the destruction of some its critical microvolume (CMV) consisting of perfectly elastic (brittle) longitudinal fibers (bundles) (the elastic part) and a matrix where plastic deformations accumulate during cyclic loadings (the plastic part) (Fig. 2.61).

(We should note that, except for the longitudinal elements, the plastic part includes all other composite components, i.e., the matrix itself and all the layers with stackings different from the longitudinal one!).

We assume that, if the number of elastic elements in the CMV able to take up the longitudinal load decreases by  $r_R$  during the cyclic loading, the elastic part of the specimen breaks down, which is followed by the failure of the specimen as a whole.

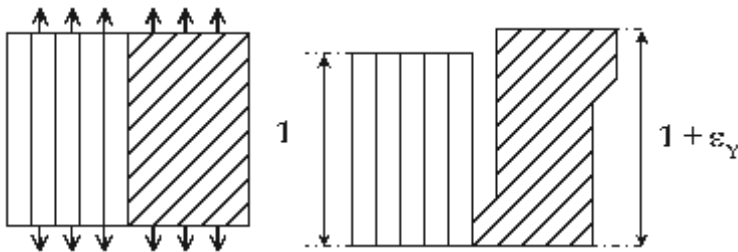


**Fig. 2.61.** Model of the critical microvolume of a composite under a load and after removal of the load. Explanations in the text

The slanted hatching in Figure 2.62 symbolically points to the possibility of accumulating an irreversible plastic strain. If it exceeds some level  $\varepsilon_Y$ , the failure of the CMV and the specimen as a whole occurs. We emphasize that this graphic image, as applied to a composite, should be understood symbolically. It is more suitable for metals, where the accumulation of plastic strains is associated with some “act of flow” (for metals – a shift over slip planes). We will assume that an individual act of flow, in the mathematical description of the process, leads to a respective change in the state of MC, while in the physical description – to the appearance of a constant plastic strain  $\varepsilon_{Y1}$ . The failure of CMV takes place after the accumulation of a “critical” number of such acts  $r_Y$ , i.e., after the accumulation of a critical plastic strain, the relation  $\varepsilon_{YC} = \varepsilon_{Y1} r_Y$  is valid, where  $\varepsilon_{YC}$  and  $r_Y$  are model parameters. Since the elastic and plastic parts are integrated in a unit, the

accumulation of plastic strains (irreversible deformation of the plastic part) leads to the appearance of residual stresses: tension in the elastic and compression in the plastic part of the specimen.

Let us associate the process of gradual failure of a specimen with a stationary Markov chain whose set of states is determined by the number of broken elastic elements and the number of acts of flow. The matrix of transition probabilities is presented as a totality of  $(r_Y + 1)$  blocks with  $(r_R + 1)$  states within each of them. Then, the indices of input and output states,  $i$  and  $j$ , respectively, can be expressed in terms of the corresponding local indices  $i_Y, i_R, j_Y$ , and  $j_R$  by the formulas

$$i = (r_R + 1)(i_Y - 1) + i_R; \quad j = (r_R + 1)(j_Y - 1) + j_R \quad (2.104)$$

Table 2.9 shows an example of (symbolic) filling of the matrix for the case where  $r_Y = r_R = 2$ .

**Table 2.9.** Example of the Matrix Structure of Transition Probabilities

		$j_Y$	$1$			$2$			$3$		
		$j_R$	$1$	$2$	$3$	$1$	$2$	$3$	$1$	$2$	$3$
$i_Y$	$i_R$	$i \setminus j$	$1$	$2$	$3$	$4$	$5$	$6$	$7$	$8$	$9$
$1$	$1$	$1$	$p_{R0}p_{Y0}$	$p_{R1}p_{Y0}$	$p_{R2}p_{Y0}$	$p_{R0}p_{Y1}$	$p_{R1}p_{Y1}$	$p_{R2}p_{Y1}$	$p_{R0}p_{Y2}$	$p_{R1}p_{Y2}$	$p_{R2}p_{Y2}$
	$2$	$2$	$0$	$p_{R0}p_{Y0}$	$p_{R1}p_{Y0}$	$0$	$p_{R0}p_{Y1}$	$p_{R1}p_{Y1}$	$0$	$p_{R0}p_{Y2}$	$p_{R1}p_{Y2}$
	$3$	$3$	$0$	$0$	$1$	$0$	$0$	$0$	$0$	$0$	$0$
$2$	$1$	$4$	$0$	$0$	$0$	$p_{R0}p_{Y0}$	$p_{R1}p_{Y0}$	$p_{R2}p_{Y0}$	$p_{R0}p_{Y1}$	$p_{R1}p_{Y1}$	$p_{R2}p_{Y1}$
	$2$	$5$	$0$	$0$	$0$	$0$	$p_{R0}p_{Y0}$	$p_{R1}p_{Y0}$	$0$	$p_{R0}p_{Y1}$	$p_{R1}p_{Y1}$
	$3$	$6$	$0$	$0$	$0$	$0$	$0$	$1$	$0$	$0$	$0$
$3$	$1$	$7$	$0$	$0$	$0$	$0$	$0$	$0$	$1$	$0$	$0$
	$2$	$8$	$0$	$0$	$0$	$0$	$0$	$0$	$0$	$1$	$0$
	$3$	$9$	$0$	$0$	$0$	$0$	$0$	$0$	$0$	$0$	$1$

In this case the destruction of a specimen occurs if two longitudinal elements fail (event A), or two acts of flow accumulate (event B), or events A and B take place simultaneously. To these events there correspond absorbing states of the Markov chain. In the example considered, there are  $(r_Y + 1)(r_R + 1) = 9$  such states. The symbols  $p_{R0}, p_{R1}$ , designate the probabilities of failure of the corresponding numbers of elastic (rigid) elements;  $p_{Y0}, p_{Y1}$ , are the probabilities of the corresponding

numbers of acts of flow (yielding). In the present study, we assume that the number of elastic elements destroyed in one step has a binomial distribution. If we have  $n_R$  still undestroyed elements, the probability of failure  $k_R$  of additional elements is found by the formula

$$p_R(i, j) = \binom{n_R}{k_R} (F_R(S_R(i_R, i_Y)))^{k_R} (1 - F_R(S_R(i_R, i_Y)))^{n_R - k_R}, \quad (2.105)$$

where:  $n_R = r_R - i_R$ ,  $k_R = j_R - i_R$  at  $0 \leq k_R \leq n_R$ ,  $1 \leq n_R \leq (r_R - 1)$  and  $F_R(\cdot)$  is the cumulative distribution function (cdf) of the strength of undestroyed elastic elements;  $S_R(i_R, i_Y)$  is the stress in the elastic part when the process is at an  $i$ -th state.

The probability of the fact that, at the same state of the process, the additional number of acts of flow will be equal to  $k_Y$ , is described by a similar formula:

$$p_Y(i, j) = \binom{n_Y}{k_Y} (F_Y(S_Y(i_R, i_Y)))^{k_Y} (1 - F_Y(S_Y(i_R, i_Y)))^{n_Y - k_Y} \quad (2.106)$$

where:  $n_Y = r_Y - i_Y$ ,  $k_Y = j_Y - i_Y$  at  $0 \leq k_Y \leq n_Y$ ,  $1 \leq n_Y \leq (r_Y - 1)$  and  $F_Y(\cdot)$  is the cdf of the yield point;  $(j_Y - 1)$  is the number of acts of flow;  $S_Y(i_R, i_Y)$  is the stress in the plastic part; the number of preceding acts of flow is  $(j_Y - 1)$ , and the number of already destroyed elastic elements is  $(j_R - 1)$ .

We will also assume the lognormal distribution for yield points of the plastic part:

$$F_X(x) = \Phi((x - \theta_0) / \theta_1), \quad (2.107)$$

$$F_Y(y) = \Phi((y - \theta_0) / \theta_1)$$

where:  $X$  and  $Y$  are the natural logarithms of the ultimate strength of elastic elements and of the yield point of the plastic part, and  $\Phi(\cdot)$  is the function of standard normal distribution.

The local stress is a function of the normal stress applied, the number of already destroyed elastic elements, and the number of preceding acts of flow. Let the initial value of the critical cross section examined be equal to  $f = f_R + f_Y = 1$ , where  $f_R, f_Y$  are cross sections of the elastic and plastic parts, respectively. After the break-down of  $i$  elastic elements, the new value of this cross section is equal to  $f_{Ri} = f_R \cdot (1 - i / r_R)$ . The cross-sectional area of the plastic part does not vary, but its length depends on the number of acts of flow. If both the parts operate within

the limits of elasticity, we can write the following equations of equilibrium and compatibility:

$$\begin{cases} S_R \cdot f_R + S_Y \cdot f_Y = S \cdot f \\ \frac{S_R}{E_R} = \frac{S_Y}{E_Y} \end{cases} \quad (2.108)$$

where:  $S$  – the average normal stress;  $E$  – the elastic modulus;  $R, Y$  – indices of the elastic and plastic parts, respectively.

If the lengths of both the parts are equal,

$$S_R = S \cdot f / (f_R + f_Y \cdot E_Y / E_R) \quad (2.109)$$

$$S_Y = S \cdot f / (f_Y + f_R \cdot E_R / E_Y) \quad (2.110)$$

But if acts of plasticity have occurred and the length of the plastic part is  $l_Y = 1$  instead of its initial length  $l_Y = (1 + \varepsilon_Y)$ , residual stresses arise in both parts of the specimen at the zero external loads, which are determined from the system of equations

$$\begin{cases} \Delta S_R \cdot f_R = \Delta S_Y \cdot f_Y \\ 1 + \frac{\Delta S_R}{E_R} = (1 + \varepsilon_Y) \left( 1 - \frac{\Delta S_Y}{E_Y} \right) \end{cases} \quad (2.111)$$

The solution of this system (within the limits of elasticity) makes it possible to write

$$\Delta S_R = E_R \cdot \varepsilon_Y / (1 + (1 + \varepsilon_Y) f_R E_R / f_Y E_Y) \quad (2.112)$$

$$\Delta S_Y = E_Y \cdot \varepsilon_Y / (1 + \varepsilon_Y + f_Y E_Y / f_R E_R) \quad (2.113)$$

Let us assume that the elongation of the plastic part is proportional to the number of plasticity acts:  $\varepsilon_Y = \varepsilon_{Y1} \cdot (i_Y - 1)$ ,  $i_Y = 1, \dots, r_Y$ , where  $\varepsilon_{Y1}$  is a model parameter.

By renumbering the states, the matrix of transition probabilities can be reduced to the form

$$P = \begin{bmatrix} Q & R \\ 0 & I \end{bmatrix} \quad (2.114)$$

where  $I$  is the unit matrix and  $0$  is the matrix consisting of zeros. Then, if the process starts from the first state, the distribution function for the number of steps in the Markov chain before absorption,  $T_A$ , is given by

$$F_{T_A}(t, S, \eta) = aP^t b, \quad t = 1, 2, 3, \dots \quad (2.115)$$

where  $a$  is a row vector with the structure  $(1, 0, 0, \dots, 0)$ ;  $b$  is a column vector of type  $(0, \dots, 0, \dots, 1, \dots, 1)'$ , with the number of unities equal to the number of absorbing states.

In what follows, for definiteness, loading by a pulsing cycle is assumed,  $S$  is the maximum (nominal) stress of the cycle, and  $\eta = (r_Y, r_R, \varepsilon_{Y1}, \dots)$  is the vector-parameter (its components are parameters of the structure of matrix  $P$ , parameters of distribution functions of strength and plasticity limits, ...). In the general case, it may be assumed that one step of Markov chain corresponds to  $k_M$  cycles; then  $k_M$  is also a component of the vector  $\eta$ .

Using the formulas of the theory of finite Markov chains [137], we obtain that the column vector of average numbers of steps before the absorption, whose components correspond to different initial states, is

$$\tau = N \cdot \xi \quad (2.116)$$

where  $N = (I - Q)^{-1}$ ,  $\xi$  is a column vector filled with unities.

The corresponding vector of variances is

$$\tau_2 = (2N - I)\tau - \tau_{sq} \quad (2.117)$$

where  $\tau_{sq}(i) = (\tau(i))^2$ ,  $i \in I_A$ , and  $I_A$  is the set of indices of absorbing conditions.

The matrix of absorption probabilities is

$$B = \{B_{ij}\} = NR \quad (2.118)$$

where  $B_{ij}$  is the probability of completion of the process at an  $j$ -th absorbing state if the initial one is an  $i$ -th irreversible state.

These formulas to the full are of importance in a program loading. In a cyclic loading with a constant cycle stress, we are interested only in the first components of the vector  $\tau$  and  $\tau_2$  and in the first row of the matrix  $B$ , which correspond to the beginning of Markov chain from the first irreversible state. The components of the first row of the matrix  $B$  show the probabilities of various failure modes (through the destruction of elastic elements, or an inadmissible elongation of the plastic part of the specimen, or their combination).

The fatigue life  $t_p(S)$  (the number of cycles) corresponding to the probability of failure  $p$  under an initial normal stress  $S$  (the  $p$ -quantile fatigue curve) is found from the formula

$$t_p(S) = k_M F_{T_A}^{-1}(p; S, \eta) \quad (2.119)$$

Notice that the knowledge of cdf (2.101) allows us to calculate the average fatigue life  $E(T(S))$  at an arbitrary  $S$  and, with known experimental data for constructing the fatigue curve, to estimate the parameter  $\eta$  by using either the nonlinear method of least squares or the method of maximum likelihood. These questions are treated in [129, 130].

The matrix  $P$  is a function of  $S$ . Therefore, the quantity

$$F_{\sigma_t}(x) = aP^t b \quad (2.120)$$

where  $x = S$ , determines the probability of failure of specimens in  $t$  steps ( $(k_M t)$  cycles, where  $k_M$  – is the number of cycles equivalent to one step of MC) at a stress equal to  $S$ , i.e., it determines the distribution function of residual strength (in this case, the fatigue limit at a fixed restricted number of cycles ( $k_M t$ ) in fatigue tests).

The vector of probabilities on the states of Markov chain after loading ( $S_1, n_1$ ), i.e., after  $n_1$  steps with a stress  $S_1$ , is defined as

$$\pi_{S_1 n_1} = (1, 0, \dots) P_1^{n_1} \quad (2.121)$$

The last  $(r_Y + 1 + r_R)$  components of this vector define the absorption probabilities of the Markov process at the states corresponding to failure of the specimen.

The residual strength  $\sigma_{n_1}$  after loading ( $S_1, n_1$ ), i.e., after  $n_1$  steps with a stress  $S_1$ , of course, is measured only on unfailed specimens. The corresponding components of the vector of distribution of probabilities on the nonabsorption (irreversible) states of the Markov chain are

$$\pi_{S_1 n_1}^*(k) = \pi_{S_1 n_1}(k) / \sum_{m=1}^{m^*} \pi_{S_1 n_1}(m) \quad (2.122)$$

where:  $\pi_{S_1 n_1}(k)$ , and  $k = 1, \dots, m^*$  – are components of the vector  $\pi_{S_1 n_1}$ ;  $m^* = (r_Y + 1)(r_R + 1) - (r_Y + 1 + r_R)$  – is the total number of non absorption (irreversible) states. The last  $(r_Y + 1 + r_R)$  components of the vector  $\pi_{n_1}^*$ , corresponding to the absorption states, are obviously equal to zero, since here we consider only specimens not failed upon the preliminary loading.

For such specimens, the distribution function of the stress  $\sigma_{n_1}^{II}$  at which absorption in one step in the Markov chain occurs (which corresponds to failure of a specimen in  $k_M$  cycles), has the form

$$F_{\sigma_{n_1}}(x) = \pi_{S_1 n_1}^* P(x)b \quad (2.123)$$

where:  $x \geq S_1$ ,  $P(x)$  – is the matrix of transition probabilities at  $S = x$ . If  $k_M$  is equal to unity or is relatively small, relation (2.103) determines the distribution of the residual strength.

The notion “relatively small” has to be defined more exactly during the accumulation of practical experience in using the model for processing experimental data. In general case, the function  $F_{\sigma_{n_1}}(x)$  determines the distribution of a conservative estimate of residual strength since, obviously, the destruction in one cycle requires a greater load than in  $k_M$  cycles.

Formulas (2.121)-(2.123) are easily generalized for the case where the residual strength is investigated after some arbitrary sequence of loadings  $(S_1, n_1)$ ,  $(S_2, n_2), \dots, (S_r, n_r)$ :

$$\pi_{(S_1, n_1), \dots, (S_r, n_r)} = (1, 0, \dots) P_1^{n_1} \dots P_r^{n_r} \quad (2.124)$$

$$\pi_{(S_1, n_1), \dots, (S_r, n_r)}^*(k) = \pi_{(S_1, n_1), \dots, (S_r, n_r)}(k) / \sum_{m=1}^{m^*} \pi_{(S_1, n_1), \dots, (S_r, n_r)}(m) \quad (2.125)$$

$$F_{\sigma_{(S_1, n_1), \dots, (S_r, n_r)}}(x) = \pi_{(S_1, n_1), \dots, (S_r, n_r)}^* P(x)b \quad (2.126)$$

For example, after the application of a load  $(S_2, n_2)$  with an increased value of stress, subsequent to a “normal” load  $(S_1, n_1)$ , we have to assume  $r = 2$  in Eqs. (2.124)-(2.126).

## 2.8.2. NUMERICAL EXAMPLE

In [133-136], results of 17 fatigue tests at  $R = 0.1$  and results of 33 residual strength tests for 3 different stress levels (48.5; 63.6 and 78.3 MPa) of preliminary loading in frame of OPTIMAL BLADES testing program of the OB UD material are reported. ISO standard specimens, [+45/-45]s, were therefore used. We see that in this case there are not straight longitudinal items (fibers or strands). But if we consider the described model just as nonlinear regression model we can try to make fitting of fatigue and residual strength experimental data using this model.

In Figure 2.62 we see the fitting of the fatigue data and in Figure 2.63 the residual strength and corresponding “prediction” using MCh-model and fatigue parameter estimates are shown. In Table 2.10 we see parameters of the model, which was used for these calculations.

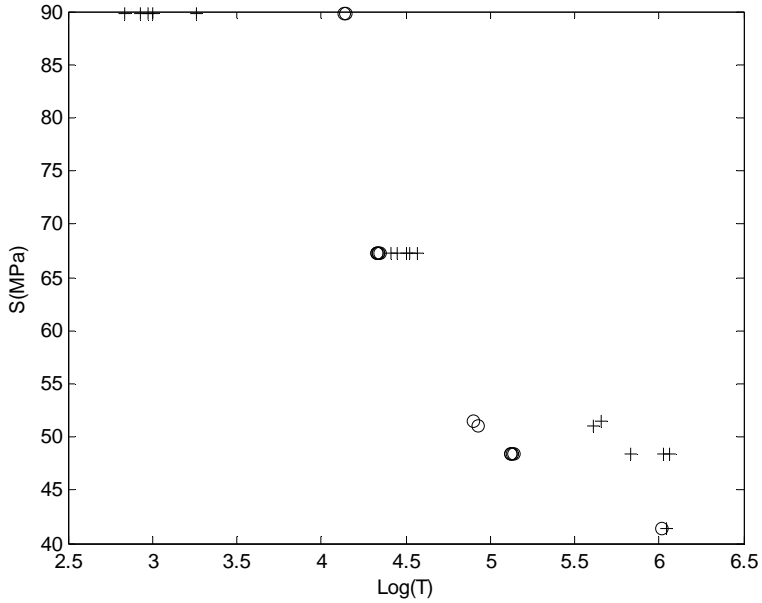


**Fig. 2.62.** Results of fatigue life tests at approximately pulsating ( $R = 0.1$ ) loading (+) according to [133] and the calculated estimates of mathematical expectations of the respective order statistics (O)

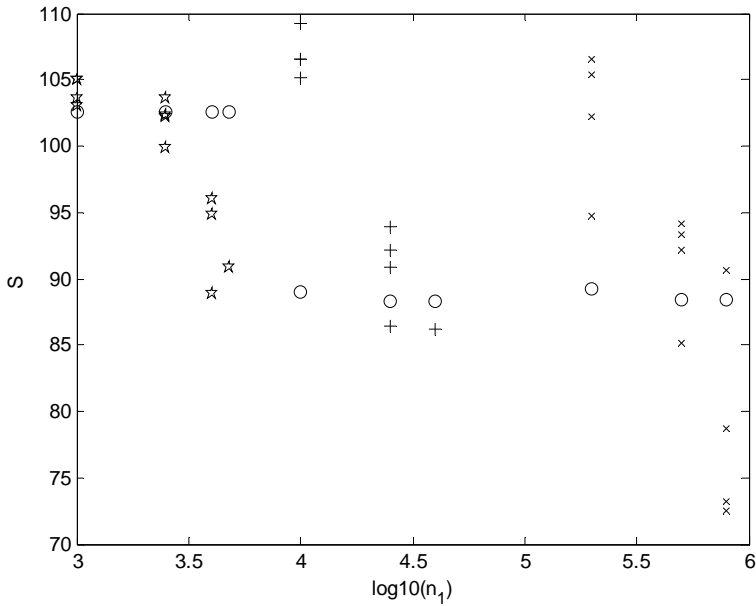


**Fig. 2.63.** Experiment (+) and estimates of the average residual strength vs the duration of preliminary loading with three stress levels (78.3 (\*); 63.6 (+) and 48.5 (x) MPa)

**Table 2.10. Parameters of the Model**

Parameters	
Number of longitudinal elements in the elastic part of critical microvolume, $r_R$	20
Number of elongation “steps” in the plastic part of critical microvolume, $r_Y$	10
Ultimate total relative elongation of the plastic part, $\varepsilon_Y$	0.2
Relative area of the elastic part, $f_R$ ( $f_Y = 1 - f_R$ )	0.21
Elastic modulus of longitudinal elastic elements, $E_R$ , MPa	79.000
Elastic modulus of the plastic part, $E_Y$ , MPa	5.000
Average value of the (natural) logarithm of the strength of longitudinal elastic elements, $\theta_{0R}$ ( $\exp(\theta_{0R})$ )	5.7038 (300 MPa)
Standard deviation of the (natural) logarithm of the strength of longitudinal elastic elements, $\theta_{1R}$	0.2
Average value of the (natural) logarithm of yield point of the plastic part of critical microvolume, $\theta_{0Y}$ ( $\exp(\theta_{0Y})$ )	4.0943 (60 MPa)
Standard deviation of the (natural) logarithm of yield point of the plastic part of critical microvolume, $\theta_{1Y}$	0.2
Number of cycle’s equivalent to one step of Markov chain, $k_M$	6934

Note. In parentheses, values according to the linear scale are given.

The present study shows that:

1. An analysis of the calculation results obtained shows that the considered model reasonably describes the “lower part” of the fatigue curve and mean value of residual strength.
2. The mathematical model suggested, from unified positions, gives a tool for consistently analyzing the distribution of static strength, the data for constructing the fatigue curve, and the prediction of distribution of residual strength under a program loading. The model is too simple to be able to exactly predict the fatigue life based on the data of static strength. In essence, it is model of nonlinear regression, but as distinct from, for example, the Weibull model of fatigue curve, the parameters of the model suggested can be interpreted as parameters of distribution of the local static strength. After estimating these parameters according to the data of fatigue curve, the model can be used for predicting the distribution function of residual strength after fatigue loading (in [127] it is shown that the model can be used for “prediction” fatigue life under program fatigue loading and for “prediction” residual fatigue life after some preliminary fatigue loading).
3. The model considered is most suitable for describing the processes with pulsating loading cycles. But using some method of “converting” of some cycle with arbitrary  $R = \sigma_{\min} / \sigma_{\max}$  into “equivalent” pulsating loading cycles (see, for example, [138]) this model can be extended to arbitrary loading cycles.

4. The determination of parameters of the model of nonlinear regression (the parameter  $k_M$  is easily found by using the methods of linear regression) is a serious problem. The search for its efficient solution is the subject of a special investigation. Therefore, at present, it seems likely that the model considered here cannot yet be recommended for “industrial” applications. However, it is of interest not only for student studies, but also for a serious scientific investigation, since it gives a sufficiently informative “translation of mathematics into physics”. And it deserves to be studied more circumstantially.

## REFERENCES

- [1] Vollertsen F.: *Mechanisms and Models for Laser Forming*, Laser Assisted Net Shape Engineering, Proceedings of the 26<sup>th</sup> International CIRP Seminar on Manufacturing Systems - LANE '94, Meisenbach-Verlag Bamberg 1994, pp. 345-360.
- [2] Taira S., Ohtani R.: *High Temperature Strength of Materials*. Metallurgy Publishers, Moscow 1986.
- [3] Frąckiewicz H., Mucha Z., Gradoń R., Kalita W.: *Method of bending metal objects with an energy beam*. United States Patent No. 5 719 374 (17.02.1998).
- [4] Steen W.: *Laser Material Processing*. Springer-Verlag London Limited 2003, pp. 301-325.
- [5] Mucha Z.: *Analytical modelling of laser plate bending by use of temperature gradient and buckling mechanisms and their experimental verification*. LANE 2007 (Laser Assisted Net Shape Engineering 5) volume 1, M. Geiger, F. Vollertsen (eds), Meisenbach-Verlag, Bamberg 2007, pp. 619-630.
- [6] Mucha Z.: *Modelowanie i eksperymentalne badania kształtowania laserowego materiałów konstrukcyjnych*. (Modelling and Experimental Investigations of Laser Forming of Construction Materials) (in Polish) Editor: Kielce University of Technology, Kielce 2004.
- [7] Li W., Yao Y.L.: *Laser Forming with Constant Line Energy*, Int. J. Advanced Manufacturing Technology, Springer-Verlag, Vol. 17 (2001), pp. 196-203.
- [8] Rykalin N., Uglov A., Kokora A.: *Laser Machining and Welding*. Mir Publisher, Moscow 1978.
- [9] Ashby M.F., Easterling K.E.: *The transformation hardening of steel surfaces by laser beams*. I. Hypoeutectoid steels. Acta Metall. Vol. 32, No. 11 (1984), pp. 1935-1948.
- [10] Mucha Z., Widłaszewski J.: *Physical Foundations of Laser Thermal Forming*. Invited Paper in Proceedings of the 1<sup>st</sup> International Conference on New Forming Technology, CNFT, Harbin China, September 6-9, 2004, Eds. Harbin Institute of Technology Press, pp. 235-240.
- [11] Klocke F., Demmer A., Dietz C.: *Laser-assisted metal forming*. Proceedings of the 30<sup>th</sup> International CIRP Seminar on Manufacturing Systems -LANE'97 (Laser Assisted Net shape Engineering 2), M. Geiger, F. Vollertsen (eds), Meisenbach-Verlag, Bamberg 1997, pp. 81-92.
- [12] Holt J.: *Contraction as a Friend in Need*. Joseph Holt 1938.
- [13] Holt R.E.: *Flame Straightening Basics*. Welding Engineer, Sept. 1965, pp. 49-53.

- [14] Holt R.E.: *Primary Concepts for Flame Bending*. Welding Journal, June 1971, pp. 416-424.
- [15] Avent R., Mukai D.: *Heat-straightening repairs of damaged steel bridges*. A manual of practice and technical guide. US Department of Transportation. Report No. FHWA-IF-99-004, 1998.
- [16] The National Shipbuilding Research Program, Line heating. U.S. Department of Transportation, Maritime Administration in cooperation with Todd Pacific Shipyards Corporation, USA, November 1982.
- [17] Scully K.: *Laser line heating*. Journal of Ship Production 3, 1987, 4, pp. 237-246.
- [18] Masubuchi K., Maumoto I.: *Study on Metal Working by High Power Lasers*. Proceedings of the 2nd International Conference on BEAM Technology, V. 2, 1985, 20.
- [19] Namba Y.: *Laser Forming in Space*. Proceedings of the International Conference On Lasers '85 (Las Vegas, NV, USA. Soc. Opt. & Quantum Electron., 2-6 Dec. 1985), C. P. Wang (Ed.), STS Press, McLean 1986, pp. 403-407.
- [20] Frąckiewicz H., Mucha Z., Trąmpczyński W., Baranowski, A. Cybulski A., Kottler, W.: *Bleche und Platten mit dem Laser formen*. Laser-Praxis (1990), pp. 111-113.
- [21] Hoving W.: *Accurate Manipulation using Laser Technology*. Proceedings of the European Symposium on Laser and Optics and Manufacturing, München, 16-20 June 1997. In Lasers in Material Processing, Leo H.J.F. Beckmann (Editor), Proceedings of SPIE (The International Society for Optical Engineering), Vol. 3097, pp. 284-295 (1997).
- [22] Vollertsen F.: *Mechanisms and Models for Laser Forming*. Proceedings of the 26th International CIRP Seminar on Manufacturing Systems - LANE '94 (Laser Assisted Net Shape Engineering), Editors: M. Geiger, F. Vollertsen. Meisenbach-Verlag, Bamberg (1994), pp. 345-360.
- [23] Steiger E.: *Führungsloses Justieren der Mittelkontaktfedern des Kleinrelais D2 in einem Pulslasersystem*. Siemens Components 22 (1984) 3, pp. 135-137.
- [24] Martin R., Kohler G. (SIEMENS AG): *Automatisiertes Justieren in der Feinwerktechnik*. Patent DE2918100. Date of application 1979-05-04. Date of patent 1980-11-13.
- [25] Hanebuth H., Hamann Chr.: *Prazisionsmontage und -justage mit dem Laserstrahl in der Elektronikproduktion*. In: Geiger M., Otto A. (Editors); Laser in der Elektronikproduktion & Feinwerktechnik, LEF'99. Publisher: Meisenbach Bamberg, 1999, pp. 141-155. ISBN: 3-87525-118-0.
- [26] Hoving W., van Dooren J.P. (PHILIPS ELECTRONICS NV): *Method of adjusting the switch-gap in a reed switch*. Patent EP0731978, Filed 1994-10-04. Publication date 1996-04-11.
- [27] Verhoeven E.C.M., de Bie H.F.P., Hoving W.: *Laser Adjustment of Reed Switches: Micron Accuracy in Mass Production*. Proceedings of the LEF'99 Conference (Laser in der Elektronikproduktion & Feinwerktechnik), Eds.: M. Geiger, A. Otto, Meisenbach Bamberg, 1999.
- [28] Hoving W.: *Accurate manipulation using laser technology*. Proceedings of the LANE 2001 (Laser Assisted Net Shape Engineering 3, International Conference), Eds.: M. Geiger, A. Otto, Meisenbach-Verlag Bamberg 2001, pp. 113-124.
- [29] Murata A., Mukae H., Maegawa T., Higashionji M., Okada T. (MATSUSHITA ELECTRIC IND CO LTD): *Rotary Head Adjuster*. European Patent Application, EP 0488 658 A2. Publication date 1992-06-03. Published also as US5341256.

- [30] Maegawa T., Murata A., Mukae H., Higashionji M. (MATSUSHITA ELECTRIC IND CO LTD): *Azimuth Adjusting Method for Magnetic Head*. United States Patent US 0052 5685 0A. Publication date 1993-10-26. Published also as JP5073866.
- [31] Press release Matsushita, Laser Adjustment Technology for Video Heads. JETRO, 95-12-002-08, Dec. 1995.
- [32] Hoving W., van Hout J.A., Grooten M.A., van Rens P.Ch., Koster M.P., Westerhof M. (PHILIPS ELECTRONICS NV): *Method of mutually displacing at least two parts of an actuator; and actuator for use in such a method*. European Patent EP0638895. Publication date 1995-02-15. Published also as United States Patent, US 5572895.
- [33] Müller B., Huber A., Geiger M.: *Sub-micron accuracy of assembled systems by laser adjustment*. In: Geiger, M. (Hrsg.): Proc. of the 6th Int. Conf. on Technology of Plasticity ICTP 1999 (ICTP). Berlin : Springer, 1999, pp. 1049-1550.
- [34] Geiger M., Huber A., Müller B.: *Basic Actuator Geometries for Laser Adjustment Process*. In: McKeon P., Corbett J., Bonis M., Sartori S., Kunzmann H., Week M., Brinksmeier E., Preuß W., Riemer O. (Eds.): *Precision engineering nanotechnology*, 1st Int. Conf. and General Meeting of the European Soc. for Precision Engineering and Nanotechnology (EUSPEN), BIAS Bremen, 1999, pp. 526-529.
- [35] Miyamoto I.: *Challenge to advanced laser materials processing in Japanese industry*. RIKEN Review No. 50 (January, 2003): Focused on Laser Precision Microfabrication (LPM 2002), pp. 20-28.
- [36] Jurgenson R., Danielson R.C., Lien B.D., Lewandowski M.S. (HUTCHINSON TECHNOLOGY, USA): *In-stack adjustable magnetic head suspension*. Patent US5995335. Filed 1997-06-27. Publication date 1999-11-30.
- [37] Singh G.P., Arya S.P., Krajnovich D.J., O'Sullivan T., Alexopoulos P.S., Lee C.-K. (International Business Machines Corporation): *Laser Apparatus and Method for Adjusting the Gram Load Static Attitude and Flying Height of a Slider in a Head Suspension Assembly*. Patent US5712463. Publication date 1998-01-27. Published also as US6011239.
- [38] Matsushita N. (FUJITSU LTD): *ABS Shape Correction Method for Slider of Magnetic Head, and ABS Shape Correction Apparatus for Slider of Magnetic Head*. Patent Application Publication US2001056334. Publication date 2001-12-27. Published also as US6546355, JP2002008338.
- [39] Mei Y., Mou J., Egbert D.E., Ma L. (SEAGATE TECHNOLOGY LLC): *Slider Having Adjusted Transducer Recession and Method of Adjusting Recession*. Patent Application Publication US20050047017. Publication date 2005-03-03.
- [40] Matsushita N.: *Laser micro-bending for precise micro-fabrication of magnetic disk drive components*, Proc. SPIE 5063 (2003), pp. 24-29.
- [41] Tam A.C., Poon C.C., Crawforth L.: *Laser Bending of Ceramics and Application to Manufacture Magnetic Head Sliders in Disk Drives*. ANALYTICAL SCIENCES, April 2001, Vol. 17 Special Issue, 2001, The Japan Society for Analytical Chemistry, pp. 419-421.
- [42] Koster M.P., Semmeling R.A.E.M. (PHILIPS ELECTRONICS NV): *Method of mutually displacing at least two parts of an actuator, and actuator suitable for use in such a method*. Patent BE1007436. Filed 1993-08-11. Publication date 1995-06-13.

- [43] Olowinsky A.M., Bosse L.: *Advances in laser beam micro forming for micropositioning*. Proceedings of the International Congress on Applications of Lasers and Electro-Optics ICALEO 2003, LMF, Section D, pp. 23-37.
- [44] Widłaszewski J.: *Modeling and experimental investigations of thermo-elastic-plastic deformations of the two-bridge actuator*. PhD Thesis. Institute of Fundamental Technological Research of the Polish Academy of Sciences, 2009.
- [45] Hoving W., Verhoeven E.C.M.: *High-precision micro-assembly using laser-adjustment*. Laser in der Elektronikproduktion & Feinwerktechnik - LEF 2000. Editors: M. Geiger, A. Otto. ISBN: 3-87525-123-7. Publisher: Meisenbach Bamberg, 2000, pp. 165-174.
- [46] Geiger M.: *Laser forming - the forming of metal using a laser beam*. ICMEN 2002 - 1st International Conference on Manufacturing Engineering. Austrian Research Centre, Seibersdorf Research GmbH, 2002.
- [47] Fraunhofer Institut Lasertechnik, Performance and Results, Annual Report 2002.
- [48] Müller B., Ströl K., Mehnert A. (AIFOTEC AG Fiberoptics): *Justierverfahren, insbesondere Laser-Justierverfahren und hierfür geeigneter Aktor*. Patent DE 10128827. Filed 2001-06-15. Publication date 2003-01-09.
- [49] Ossowski A., Widłaszewski J.: *Laser control of frame microstructures*. NATO Advanced Research Workshop SMART-98. In: Smart Structures. Eds.: J. Holnicki-Szulc, J. Rodellar, Kluwer Academic Publishers 1999, pp. 255-264.
- [50] Auracher F., Hanebuth H., Wittmann J., Hamann Ch. (Infineon Technologies AG): *Adjusting apparatus and method for its adjustment*. Patent US6614605. Publication date 2.9.2003.
- [51] Schmidt M., Dirscherl M., Rank M., Zimmermann M.: *Laser micro adjustment - from new basic process knowledge to the application*. Journal of Laser Applications, Vol. 19, No 2 (2007), pp. 124-132.
- [52] Huber A., Müller B., Meyer-Pittroff F.: *Laserstrahljustieren als Innovation für die Montage von Mikrosystemen*. Vollertsen F., Kleiner M. (Eds.), Idee – Vision – Innovation, Meisenbach, Bamberg, 2001, pp. 275-286.
- [53] Antoszewski B. i inni, 2008: *Projekt badawczy nr 4 T07B 04730*.
- [54] Erdemir A.: *Review of engineered tribological interfaces for improved boundary lubrication* – Tribology International 38 (2005), pp. 249-256.
- [55] Etsion I.: *State of the Art in Laser Surface Texturing*. Transaction of the ASME January 2005, Vol. 127.
- [56] Etsion I., Halperin G.: *A laser surface textured hydrostatic mechanical seal*. Sealing Technology (March 2003), pp. 6-10.
- [57] Kovalchenko A., Ajayi O., Erdemir A., Fenske G., Etsion I.: *The effect of laser surface texturing on transitions in lubrication regimes during unidirectional sliding contact*. Tribology International 38 (2005), pp. 219-225.
- [58] *Laser structuring – optimum tribosystems through functionally optimized surfaces* – Available from [www.gehring.de](http://www.gehring.de)
- [59] Sameera Ch., Bharat B.: *Effect of peak radius on design of W-type donut shaped laser textured surfaces*. Wear 230 (1999), pp. 118-123.

- [60] Wakuda M., Yamauchi Y., Kanazaki S., Yasuda Y.: *Effect of surface texturing on friction reduction between ceramic and steel materials under lubricated sliding contact* – Wear 254 (2003), pp. 356-363.
- [61] Yu X.Q., He S., Cai R.L.: *Frictional characteristics of mechanical seals with a laser textured seal face*. Journal of Materials Processing Technology 129(2002), pp. 463-466.
- [62] Zhou L., Kato K., Vurens G., Talke F.E.: *The effect of slider surface texture on flyability and lubricant migration under near contact conditions*. Tribology International 36 (2003).
- [63] Bonifaćio M., Diniz A.E.: *Correlating tool wear, tool life, surface roughness and tool vibration in finish turning with coated carbide tools*. Wear, Vol. 173(1994), pp. 137-144.
- [64] Góts I., Zajac J., Vojtko I.: *Vorrichtung zum Messen des Abnutzungsgrades von Schneidwerkzeugen*. Technische Messen, č.1. (1995), pp. 8-11.
- [65] Grzesik W.: *Podstawy skrawania materiałów metalowych* (Fundamentals of metal cutting), Wydawnictwa Naukowo-Techniczne, Warszawa 1998.
- [66] Jang D.Y., Choi Y.G., Kim H.G., Hsiao A.: *Study of the correlation between surface roughness and cutting vibrations to develop an on-line roughness measuring technique in hard turning*. International Journal of Machine Tools and Manufacture, Vol. 36, No. 4 (1996), pp. 453-464.
- [67] Kawalec M.: *Skrawanie hartowanych stali i żeliwa narzędziami o określonej geometrii ostrza* (Machining of hardened steel and cast iron using tools with specified geometry of cutters). Wydawnictwo Politechniki Poznańskiej, seria Rozprawy, No. 234, Poznań 1990.
- [68] Lin S.C., Chang M.F.: *A study on the effects of vibrations on the surface finish using a surface topography simulation model for turning*. International Journal of Machine Tools & Manufacture No. 38(1998), pp. 763-782.
- [69] Lin R., Koren Y.: *Efficient tool-path planning for machining free-form surfaces*. Transactions of the ASME, Journal of Manufacturing Science and Engineering, Vol. 118(1996), pp. 20-28.
- [70] Liubimov V., Oczos K.: *Wybrane zagadnienia kształtowania nierówności powierzchni w procesach obróbkowych* (Selected problems of surface roughness formation in machining processes), Mechanik No. 3 (1997), pp. 81-84.
- [71] Miko E.: *Konstytuowanie mikronierówności powierzchni metalowych obrobionych narzędziami o zdefiniowanej stereometrii ostrzy* (Determination of the microirregularities on metallic surfaces sculptured by cutting tools with defined stereometry), Monografie, Studia, Rozprawy, No. 46, Kielce 2004.
- [72] Miko E.: *Stanowiska badawcze do diagnozowania stanu frezarki i procesu frezowania czołowego* (Model measuring stand for testing the state of a milling machine and a face milling process). Metrologia i Systemy Pomiarowe, Tom V, Z. 3, Warszawa 1998, s. 183-200.
- [73] Peterka J.: *A New Approach to Calculating the Arithmetical Mean Deviation of a Profile during Copy Milling*. Journal of Mechanical Engineering, Vol. 50, No. 12 (2004), pp. 594-597.
- [74] Wawrzyniak W., Strelow B.: *Feindreihen gerätebautypischer Werkstoffe mit hochharten Schneidstoffen*. Feingerätetechnik, Vol. 29, No. 5 (1980), pp. 208-210.

- [75] Wilkinson P. et al.: *Surface finish parameters as diagnostics of tool wear in face milling*. Wear, Vol. 205 (1997), pp. 47-54.
- [76] Zhang G.M., Kapoor S.G.: *Dynamic generation of machined surface. Part I: Description of a random excitation system*. Transactions of the ASME. Journal of Engineering for Industry, Vol. 113 (1991), pp. 137-144.
- [77] Żebrowski H.: *Konstituowanie technologicznej warstwy wierzchniej w procesie toczenia z podwyższonymi prędkościami skrawania* (Constituting the outer layer in the turning process with increased cutting speeds), Mechanik No. 11 (1998), pp. 686-692.
- [78] Duwell E.J., Bloecher U.: *Deburring and Surface Conditioning with Brushes Made with Abrasive Loaded Nylon Fiber*, Society of Manufacturing Engineers, Technical Paper MR83-684, Dearborn, MI. 1983.
- [79] Gutowski R., Swietlicki W.A.: *Dynamika i drgania układów mechanicznych*. PWN, Warszawa 1986.
- [80] Gere J.M., Timoshenko S.P.: *Mechanics of Materials*, Second Edition, Wadsworth, Inc., Belmont, California, pp. 351-355, pp. 414-415, 1984.
- [81] Hollowell R.: *Hybrid Force/Position Control for Robotic Light Machining*, Robotics and Remote Systems Conference, Charleston, SC, 1989.
- [82] Nowicki B., Pierzynowski R., Spadło S.: *New Possibilities of Machining and Electrodischarge alloying of Free-Form Surfaces*, Journal of Materials Processing Technology, vol. 109, No. 3 (2001), pp. 371-376.
- [83] Osiecki J., Spadło S.: *Dynamika drucika szczotki tarczowej*. Zeszyty Naukowe Politechniki Rzeszowskiej - 1993, nr 117, ser. Mechanika, Zeszyt 38, s. 214-220.
- [84] Osiecki J., Spadło S.: *A model of mechanical interactions of a brush electrode with a flat surface*, Proc. of 9th Int. Sci. Conf. on Production Engineering. Computer Integrated Manufacturing and High Speed Machining, Croatian Association of Production Engineering, Lumbarda 2003, pp. IV066-IV072.
- [85] Osiecki J.: *Poprzeczne drgania lufy armatniej*, Zeszyty Naukowe WSO, Rok XXXIV(19), Toruń 2001, s. 230-244.
- [86] Seide P.: *Large Deflections of a Simply Supported Beam Subjected to Moment at One End*, ASME Journal of Applied Mechanics, Vol. 51 (1984), pp. 519-525.
- [87] Spadło S.: *Complex Shape Surface Finishing Process*, Patent PL 172559 (1997).
- [88] Spadło S.: *Experimental Investigations of the Brush Electro-Discharge Mechanical Machining Process – BEDMM*. Advances in Manufacturing Science and Technology. Quarterly Polish Academy of Science, Vol. 25, No. 3 (2001), pp. 117-135.
- [89] Spadło S.: *Comparative studies of brush electrodischarge machining with electrodes of alloy steel and tungsten*. Advanced Manufacturing Systems and Technology, International Centre for Mechanical Sciences (CISM), Courses and Lectures, No. 437, Springer – Verlag Wien New York, 2002, pp. 515-524.
- [90] Spadło S.: *Theoretical-experimental aspects of electroerosion-mechanical machining*. Published by Technical University in Kielce, 195 p., Kielce 2006 (in polish).
- [91] Timoshenko S.P., Gere J.M.: *Theory of Elastic Stability*, Second Edition, McGraw-Hill, Inc., London 1961, pp. 76-81.
- [92] Wick C., Veilleux R.F.: *Mechanical and Abrasive Deburring and Finishing*, SME Tool and Manufacturing Engineers Handbook, Chapter 16, Vol. 3, 1985.
- [93] Lazarenco B.R., Lazarenco N.I.: *Electric Erosion of Metals*, Gosenergoizdat, 1, 1944.

- [94] Agarwal A., Dahotre N.: *Pulse electrode deposition of superhard boride coatings on ferrous alloy*, Surface and Coatings Technology 106 (1998), pp. 242-250.
- [95] Radek N.: *Producing coatings with varied properties using the electro spark deposition and laser treatment methods*, Doctoral dissertation, Kielce University of Technology, Poland 2006.
- [96] Chen Z., Zhou Y.: *Surface modification of resistance welding electrode by electro-spark deposited composite coatings: Part I. Coating characterization*, Surface and Coatings Technology 201 (2006), pp. 1503-1510.
- [97] Ribalko A.V., Sahin O.A.: *A modern representation of the behaviour of electrospark alloying of steel by hard alloy*, Surface and Coatings Technology 201 (2006), pp. 1724-1730.
- [98] Brown E.A., Sheldon G.L., Bayoumi A.E.: *A parametric study of improving tool life by electrospark deposition*, Wear 138 (1990), pp. 137-151.
- [99] U.S. Patent No. 5071059 Method for joining single crystal turbine blade halves, 1991.
- [100] Antoszewski B., Radek N., Tarelnik W., Wajs E.: *Electro discharge and laser texturing of sliding face of mechanical seals*, IX Internationale Conference HERVICON-2005, Sumy, Ukraine, t. 3, pp. 115-123.
- [101] Radek N., Wajs E., Luchka M.: *The WC-Co electrospark alloying coatings modified by laser treatment*, Powder Metallurgy and Metal Ceramics 3-4 (2008), pp. 197-201.
- [102] Radek N., Szalapko J.: *Tribological properties of electro spark molybdenum coatings after laser treatment*, Problems of Tribology 1 (2006), pp. 76-81.
- [103] Liu J., Wang R., Qian Y.: *The formation of a single-pulse electrospark deposition spot*, Surface and Coatings Technology 200 (2005), pp. 2433-2437.
- [104] Johnson R.N.: *Tribological Coatings for Liquid Metal and Irradiation Environments*, Conference Proceedings on Coatings and Bimetals for Aggressive Environments, ASM, 1985, pp. 113-123.
- [105] Dubrovsky R., Xu T.: *Electro-Spark Deposition Technology for Durability*, Proc. Of 9<sup>th</sup> Intern. Conf. on CAD, CAM, Robotics, and Factories of the Future, Newark, 1993, pp. 57-61.
- [106] Antoszewski B.: *Influence of laser and plasma modification on surface properties of sliding and rubbing components*, Technical University of Kielce, 17, Kielce 1999, pp. 39-52.
- [107] Antoszewski B., Radek N.: *Shaping of heterogeneous surfaces of laser treated electro-spark coatings*, Materials of EDM School, Warsaw, Notebook 10 (2004), pp. 15-20.
- [108] Radek N., Szalapko J.: *Manufacture of heterogeneous surfaces by electro spark deposition and laser beam*, Herald of Aeroenginebuilding 2 (2006), pp. 208-210.
- [109] Donnet C., Erdemir A.: *Historical developments and new trends in tribological and solid lubricant coatings*. Surface and Coatings Technology Volume: 180-181, Complete, March 1, 2004, pp. 76-84.
- [110] Zhang, Guoyuan; Yuan, Xiaoyang; Dong, Guangneng;: *The tribological behavior of Ni-Cu-Ag-based PVD coatings for hybrid bearings under different lubrication conditions*. Tribology International Volume: 43, Issue: 1-2, January - February, 2010, pp. 197-201.

- [111] Wu J.-H., Phillips B.S., Jiang W., Sanders J.H., Zabinski J.S., Malshe A.P.: *Bio-inspired surface engineering and tribology of MoS<sub>2</sub> overcoated cBN–TiN composite coating*. Wear Volume: 261, Issue: 5-6, September 20, 2006, pp. 592-599.
- [112] Zhu M.H., Zhou Z.R.: *An investigation of molybdenum disulfide bonded solid lubricant coatings in fretting conditions*. Surface Coatings and Technology, vol. 141, 2001, p. 240-245.
- [113] Guo Baogang, Zhou Jiansong, Zhang Shitang, Zhou Huidi, Pu Yuping, Chen Jianmin: *Phase composition and tribological properties of Ti–Al coatings produced on pure Ti by laser cladding*. Applied Surface Science Volume: 253, Issue: 24, October 15, 2007, pp. 9301-9310.
- [114] Showaiter N., Youseffi M.: *Compaction, sintering and mechanical properties of elemental 6061 Al powder with and without sintering aids*. Materials and Design Volume: 29, Issue: 4, 2008, pp. 752-762.
- [115] Renevier N.M., Hampshire J., Fox V.C., Witts J., Allen T., Teer D.G.: *Advantages of using self-lubricating hard wear resistant MoS<sub>2</sub>-based coatings*. Surface and Coating Technology, vol. 142-144, 2001, pp. 67-77.
- [116] Mindivan Harun: *Wear behavior of plasma and HVOF sprayed WC-12Co+6% ETFE coatings on AA2024-T6 aluminum alloy*. Surface & Coatings Technology Volume: 204, Issue: 12-13, March 15, 2010, pp. 1870-1874.
- [117] Huang Chuanbing, Du Lingzhong, Zhang Weigang: *Preparation and characterization of atmospheric plasma-sprayed NiCr/Cr<sub>3</sub>C<sub>2</sub>–BaF<sub>2</sub>–CaF<sub>2</sub> composite coating*. Surface & Coatings Technology Volume: 203, Issue: 20-21, July 15, 2009, pp. 3058-3065.
- [118] Fanning Ch.E., Blanchet T.A.: *High-temperature evaluation of solid lubricant coatings in a foil thrust bearing*. Wear Volume: 265, Issue: 7-8, September 20, 2008, pp. 1076-1086.
- [119] Wang Hai-dou, Xu Bin-shi, Liu Jia-jun, Zhuang Da-ming, Wei Shi-cheng, Jin Guo: *The iron sulfide coatings prepared by plasma spraying and their friction-reduction performance*. Surface & Coatings Technology Volume: 201, Issue: 9-11, February 26, 2007, pp. 5286-5289 .
- [120] Vetter J., Barbezat G., Crummenauer J., Avissar J.: *Surface treatment selections for automotive applications*. Surface and Coating Technology, 200 (2005), pp. 1990-1993.
- [121] Barbezat G.: *Advanced thermal spray technology and coating for lightweight engine blocks for automotive industry*. Surface and Coating Technology, 200 (2005), pp. 1962-1968.
- [122] Yang Hyunseok, Lee Changhee, Hwang Soon Young: *The effect of nano-sized Cr<sub>2</sub>O<sub>3</sub> addition on the characteristics of NiCr–Cr<sub>2</sub>O<sub>3</sub>–Ag–BaF<sub>2</sub>/CaF<sub>2</sub> coating*. Surface & Coatings Technology Volume: 201, Issue: 1-2, September 12, 2006, pp. 38-44.
- [123] Polański Z.: *Metodyka badań doświadczalnych*. Wydawnictwo Politechniki Krakowskiej. Kraków 1984.
- [124] Philippidis T.P., Passipoularidis V.A.: *Residual strength after fatigue in composites: Theory vs. experiment*, International Journal of Fatigue 29 (2007), pp. 2104-2116.

- [125] Found M.S., Quaresimin M.: *Two-stage fatigue loading of woven carbon fiber reinforced laminates*. Fatigue Fract Eng Mater Struct 2003; 2, pp. 17-26.
- [126] Broutman L.J., Sahu S.: *A new theory to predict cumulative fatigue damage in fiber-glass reinforced plastics*. Composite materials: testing and design (2nd Conference). ASTM STP, 497, 1972, pp. 170-88.
- [127] Парамонов Ю.М., Клейнхоф М.А., Парамонова А.Ю.: *Марковская модель связи распределения статической прочности и усталостной долговечности волокнистого композита*. Механика композитных материалов. 5(2006), pp. 615-630.
- [128] Paramonov Yu., Andersons J., Kleinhofs M., Paramonova A.: *Markov model for analysis of residual tensile strength of fiber composite*. Mechanic of composite materials, 44(2008)4, pp. 559-568.
- [129] Paramonova A.Yu., Kleinhof M.A., Paramonov Yu. M.: *Binomial version of Markov model of fatigue life of composite with two reasons for failure*. AVIATION 8(2004)2, pp. 15-20.
- [130] Парамонов Ю.М., Клейнхоф М.А., Парамонова А.Ю.: *Вероятностная модель усталостной долговечности композита для аппроксимации кривой усталости*. Механика композитных материалов. 6(2002)37, pp. 741-750.
- [131] Kleinhof M., Paramonov Yu., Paramonova A.: *Regression model based on Markov chain theory for composite fatigue curve approximation*, Acta et Commentationes Universitatis Tartuensis de Mathematica, 8(2004), pp. 143-153.
- [132] Парамонов Ю.М., Клейнхоф М.А., Парамонова А.Ю.: *Оценка параметров кривой усталости композитного материала*. Механика композитных материалов 1(2005)41, pp.109-120.
- [133] OPTIMAT BLADES, Reliable Optimal Use of Materials for Wind Turbine Rotor Blades, Contract no. ENK6-CT-2001-00552. Available from (2001-2006): <http://www.ecn.nl/optimat/>.
- [134] Philippidis TP, Assimakopoulou T.T., Passipoularidis V.A., Antoniou A.E.: *Static and Fatigue Tests on ISO Standard  $\pm 45^\circ$  Coupons, OB\_TG2\_R020\_UP*, August 2004. Available from: <http://www.kcwmc.nl/optimatblades/Publications>.
- [135] Philippidis T.P., Assimakopoulou T.T., Antoniou A.E., Passipoularidis V.A.: *Residual Strength Tests on ISO Standard  $\pm 45^\circ$  Coupons, OB\_TG5\_R008\_UP*, July 2005. Available from: <http://www.kcwmc.nl/optimatblades/Publications>.
- [136] Philippidis T.P., Assimakopoulou T.T., Antoniou A.E., Passipoularidis V.A.: *Residual Strength Tests on ISO Standard  $\pm 45^\circ$  Coupons, Main Test Phase II, OB\_TG2\_R037\_UP*, June 2006. Available from: <http://www.kcwmc.nl/optimatblades/Publications>.
- [137] Kemeny J.G., Snell J.L.: *Finite Markov Chains*, Van Nostrand, Princeton, N.J., 1966.
- [138] Shokrieh M.M., Taheri-Behrooz F.: *A unified fatigue life model based on energy method*. Composite structure 75(2006), pp. 444-450.